Transport de graviers à faible contrainte : impact de l'arrangement et de l'infiltration du lit par des sédiments fins

Emeline Perret

▶ **To cite this version:**

Emeline Perret. Transport de graviers à faible contrainte : impact de l'arrangement et de l'infiltration du lit par des sédiments fins. Fluids mechanics [physics.class-ph]. Université de Lyon, 2017. English. NNT : 2017LYSE1223 . tel-01737702

HAL Id: tel-01737702
https://theses.hal.science/tel-01737702

Submitted on 19 Mar 2018

HAL is a multi-disciplinary open access archive for the deposit and dissemination of scientific research documents, whether they are published or not. The documents may come from teaching and research institutions in France or abroad, or from public or private research centers.

L'archive ouverte pluridisciplinaire **HAL**, est destinée au dépôt et à la diffusion de documents scientifiques de niveau recherche, publiés ou non, émanant des établissements d'enseignement et de recherche français ou étrangers, des laboratoires publics ou privés.

N° d'ordre NNT : 2017LYSE1223

THÈSE DE DOCTORAT DE L'UNIVERSITÉ DE LYON

opérée au sein de
l'Université Claude Bernard Lyon 1

École Doctorale ED162
Mécanique, Énergétique, Génie civil, Acoustique

Spécialité de doctorat : Mécaniques des fluides

Soutenue publiquement le 18/10/2017, par :
Emeline Perret

Transport of moderately sorted gravels at low bed shear stresses : impact of bed arrangement and fine sediment infiltration

---

Transport de graviers à faibles contraintes : impact de l'arrangement et de l'infiltration du lit par des sédiments fins

---

Manuscrit en anglais / Manuscript in English

Devant le jury composé de :

Le Hir Pierre, Directeur de recherche, IFREMER	Rapporteur
Soares Frazao Sandra, Professeure, Université Catholique de Louvain	Rapporteure
Dewals Benjamin, Professeur Associé, Université de Liège	Examinateur
Le Bouteiller Caroline, Ingénieure de recherche, Irstea	Examinatrice
Camenen Benoît, Directeur de recherche, Irstea	Directeur de thèse
Berni Céline, Chargée de recherche, Irstea	Co-encadrante de thèse
El kadi Abderrezzak Kamal, Ingénieur, EDF R&D LNHE/LHSV	Co-encadrant de thèse

Remerciements/acknowledgements

C'est avec beaucoup de plaisir et d'émotions que je rédige ces pages de remerciements. Il est important pour moi de pouvoir exprimer ma gratitude envers l'ensemble des personnes qui m'ont suivie, épaulée, conseillée, supportée et aidée au cours de ces trois dernières années. Sans elles, ce travail de thèse n'aurait pas été possible. Je tiens à m'excuser par avance auprès des personnes que je ne citerai pas directement mais qui ont tout de même apporté leurs graviers à l'édifice durant cette thèse.

Pour commencer, je tiens à remercier Magali Jodeau qui a su m'accueillir dans le monde de la recherche et m'initier au transport sédimentaire lors de mon stage de fin d'étude. Magali, tu m'as donné l'envie de poursuivre dans ce domaine et grâce à toi, j'ai eu connaissance de ce projet de thèse qui m'a tout de suite intéressée. Merci pour tout.

J'aimerais ensuite remercier Irstea pour m'avoir permis de faire cette thèse ainsi que tous les co-financeurs de ce projet : EDF, l'agence de l'eau AE-RMC, et l'OSR.

Je tiens aussi à remercier les membres du jury de ma thèse pour avoir accepté d'évaluer avec minutie et grand intérêt mon manuscrit de thèse: Pierre Le Hir, Sandra Soares Frazao, Benjamin Dewals et Caroline Le Bouteiller. De plus, je tiens à leur exprimer ma gratitude par rapport à leurs remarques et discussions intéressantes lors de la soutenance. Ces dernières ont permis d'apporter une plus-value à ce travail.

J'adresse également mes remerciements aux membres de mon comité de suivi de thèse qui ont été d'une grande aide dans la définition des objectifs de la thèse et son orientation: Philippe Belleudy, James Cooper, Alain Recking, Jean-Réné Malavoi, Albert Herrero, André Paquier, ainsi que mes encadrants. Mes remerciements s'étendent aussi à Graeme Smart qui, lors de ses courts séjours en France, m'a accordé de son temps et m'a donné de précieux conseils.

Durant ma thèse, j'ai eu la chance d'avoir des encadrants et directeur investis qui m'ont guidée avec patience dans mes recherches: Céline Berni, Kamal el Kadi Abderrezzak et Benoît Camenen. Je tiens à les remercier pour ces trois années qui ont été intenses et rythmées par de nombreuses réunions,

discussions, relectures d'articles et débats. J'ai pu compter sur eux et je leur en suis reconnaissante. Leurs avis ont beaucoup compté pour moi et je tiens à souligner que j'ai énormément appris à leurs côtés. Céline, j'ai vraiment apprécié travailler avec toi et tiens à te remercier pour ta disponibilité, ta bienveillance, ton soutien scientifique et tes encouragements. Tes idées pertinentes et nos discussions improvisées dans ton bureau (ou dans le lieu calme qu'est le hall hydraulique) ont largement contribué à faire de cette thèse ce qu'elle est aujourd'hui. Benoît, je tiens à te remercier pour tout ce que tu as fait pour moi durant ces trois années et pour l'ensemble de tes remarques et conseils (même si je ne les ai pas toujours suivis ...). J'aimerais également te remercier de m'avoir donné la possibilité de communiquer mes travaux à l'étranger et d'effectuer des expériences de laboratoire au Canada. J'en garde de merveilleux souvenirs. Céline et Benoît, je tiens également à vous remercier pour vos nombreuses relectures de la thèse qui vous ont conduits à savoir les numéros de figures du manuscrit par coeur. Kamal, merci de m'avoir suivi, même à distance, et d'avoir fait l'intermédiaire entre les besoins opérationnels et la recherche. Grâce à toi, j'ai pu avoir un regard plus concret sur mes résultats et intégrer à ma thèse une vision opérationnelle. Les expériences de terrain sur l'Arc organisées avec EDF m'ont également beaucoup apporté.

Je souhaite également remercier l'équipe métrologie d'Irstea Lyon-Villeurbanne pour son aide précieuse durant mes expériences de laboratoire et de terrain. Je remercie également Sylvie Nicaise (Irstea Aix-en-Provence) et Khedidja Abbaci (Irstea Lyon-Villeurbanne) pour leur assistance lors de la phase de caractérisation des propriétés des sédiments utilisés. Plus particulièrement, je tiens à exprimer ma gratitude envers Alexis Buffet pour son support et son aide technique. Alexis, tu as toujours répondu présent, et avec gentillesse, lorsque j'avais besoin d'aide durant mes expériences. Une grande partie de la quantité de données expérimentales présentes dans ce manuscrit est là grâce à toi, à ton professionnalisme et à ton efficacité. Je suis fière du duo que l'on a pu former pendant ces dernières années et du travail que l'on a accompli.

Ces trois ans de thèse ne se résument pas seulement à de la science; ils sont également synonymes de belles rencontres. Je tiens à dire merci

aux équipes *hydraulique des rivières*, *métrologie*, *hydrologie des bassins versants* et *poldif* pour m'avoir intégré aussi rapidement à Irstea. La bonne humeur et l'ambiance qui règne au sein du laboratoire a largement contribué au bon déroulement de ma thèse. J'aimerais remercier plus particulièrement: Musaab, membre indispensable du bureau 167 et grand maître du ping-pong, pour son soutien et nos fous rires; Sheng, mon super partenaire de discussions HH, pour tous les bons moments que l'on a pu partager et pour sa bonne humeur; Lily-Rose, mon acolyte, pour tous les moments que l'on a passé à Irstea ou ailleurs; Albert, partenaire de danse certain soir et partenaire d'expériences dans le canal la journée, pour avoir su m'épauler dès le début de ma thèse; Victor, grand maître du canal large, pour son aide et sa bienveillance; Tristan, roi de l'orthographe, pour son aide dans le hall hydraulique; et Pierre Exiga, pour son aide apportée au projet durant son stage de fin d'étude. Enfin, merci à tous mes autres collègues pour ces trois belles années: Delphine (co-chasseuse de trésors), Laurie (et Gandalf), Valentin (le Baratineur), Yassine et Alexandre (les nouvelles recrues), Lucie (l'américaine), Sylvain (le grand théoricien), Camille (ex-chef du bureau IRIP), Sébastien, Jérôme, Benjamin, Lionel, Adrien, Marc, Marina, Martin, François, Grégoire, Aurélien B. et D., Violaine, Laura, ...

Je tiens à adresser une mention particulière à mon fiancé Louis qui m'a toujours encouragée et n'a jamais douté de moi. Merci également à ma famille et mes amis pour leur soutien.

Un grand merci à tous, et à vous aussi lecteurs, pour l'intérêt que vous portez à mon travail.

Transport of moderately sorted gravels at low bed shear stresses: impact of bed arrangement and fine sediment infiltration

Abstract

This PhD thesis aims to understand gravel dynamics in Alpine rivers at low bed shear stress using laboratory experiments. Alpine river beds are often poorly sorted and composed of sediments ranging from clay to pebble. To understand interactions between these classes is an issue for predicting bedload rate. Original laboratory experiments were performed in a 18 m long and 1 m wide flume, under unsteady flows. Two types of bed were investigated: unimodal and bimodal beds. A particular attention was paid to the bed construction, which was conducted in order to obtain a nature-like bed with different bed arrangements and degrees of clogging. Unimodal beds were made of moderately sorted gravels with different bed surface arrangements. Bimodal beds were made of moderately sorted gravels in which fine sediments (sand or silt) were infiltrated. Gravel rate was found to be impacted by the bed arrangement degree, the fine sediment concentration within the transport layer and the changes in bed properties due to fine sediment presence (bed cohesion, bed permeability). The more packed the bed is; the more difficult it is to move gravels. The more concentrated in fine sediments the transport layer is; the easier the transport of gravels is. The shape of fine sediments can also be an important factor for modifying the gravel rate. The presence of cohesive fine sediments within the bed matrix reduces significantly the gravel rate. A phenomenological diagram was built to recap the different processes controlling gravel transport. It provides a description of the overall bed responses to a hydrograph. Based on this diagram, a methodology and recommendations were proposed to help understanding, estimating and interpreting gravel transport in Alpine rivers. The methodology was discussed and applied to a field case made on the Arc River. We also suggest a new dimensionless analysis for the construction of a new bedload predicting model involving parameters describing bed arrangement, bed properties and fine sediment presence.

Keywords: sediment transport; fine sediment clogging; bed arrangement; incipient motion; laboratory experiments.

Transport de graviers à faibles contraintes : impact de l'arrangement et de l'infiltration du lit par des sédiments fins

Résumé étendu

Ce travail de thèse a pour objectif de mieux comprendre la dynamique des graviers au sein des rivières alpines. Ces rivières sont souvent composées d'une large gamme de sédiments, allant des argiles aux galets. Ces différentes classes sédimentaires peuvent intéragir entre elles, ce qui peut rendre difficile l'estimation du transport d'une de ces classes (ex: le gravier). De plus, ces rivières sont fortement anthropisées ce qui modifie significativement leur état naturel d'équilibre (ex: la rivière de l'Arc-en-Maurienne est fortement contrainte par des digues et régulée par des barrages). Les conditions hydrauliques des rivières alpines sont souvent proches des conditions de mise en mouvement des graviers, que cela soit dans le chenal ou sur les bancs. Ces conditions sont les plus fréquentes durant l'année et contribuent de manière non négligeable à la dynamique de la rivière. C'est pourquoi, nous avons choisi d'étudier le transport de graviers à faibles contraintes ou à relativement faibles contraintes.

Cette étude est basée sur des expériences en laboratoire, réalisées dans le canal inclinable de 18 m de long et de 1 m de large, d'Irstea Lyon-Villeurbanne. Une attention particulière a été portée sur la réalisation des lits de graviers dans notre canal. En effet, ils ont été crées dans le but d'approcher au mieux la configuration des lits de rivières alpines, c'est-à-dire avec différents arrangements et degrés de colmatage du lit par des sédiments fins (cohésifs ou non). Deux types de lits ont été étudiés: des lits unimodaux et des lits bimodaux. Les lits unimodaux sont composés de graviers modérément triés avec divers arrangements de surface (lâche ou arrangé). Les lits dits lâches sont faits à la main et sans compaction. Les grains sont disposés aléatoirement dans le canal. En revanche, les lits dits arrangés sont des lits organisés qui ont été soumis à la force de l'eau. Des structures ou formes de fond peuvent se former sous l'action de l'eau. Les lits bimodaux sont constitués d'une matrice de graviers modéremment triés dans laquelle des sédiments fins se sont infiltrés (soit du sable, soit des sédiments fins de type limons). Dans le cas d'un lit sables/graviers, le sable s'infiltre seulement en surface formant un bouchon. En revanche, dans le cas d'un lit de limons/graviers, le limon s'infiltre du bas vers le haut sur toute la profondeur de la matrice grossière. Après avoir

créé ces lits, des expériences de transport de graviers ont été conduites en écoulements instationnaires. Les conditions hydrauliques suivent un hydrogramme symétrique montant et descendant représentant un petit événement de crue ou un scénario de chasse de barrage. Quinze expériences ont été menées au total, dont sept sur lits lâches, trois sur lits arrangés, cinq sur lits infiltrés par des sédiments fins.

Nos expériences ont permis de mettre en avant les processus clés régissant la mise en mouvement des graviers. Deux approches ont été choisies pour cette étude: à l'échelle globale et à l'échelle locale.

L'étude à l'échelle globale a montré que le transport de graviers était contrôlé à la fois par la force de l'écoulement mais aussi par la mobilité du lit. La résistance à l'écoulement (autrement dit la rugosité hydraulique) et la mobilité du lit (autrement dit la contrainte de mise en mouvement) sont toutes deux impactées par l'arrangement de surface, par la quantité de sédiments fins dans la couche de transport (couche où les interactions entre sédiments grossiers et fins s'effectuent) et par les changements de propriétés géotechniques du lit dues à la présence de sédiments fins (perméabilité ou cohésion/consolidation du lit). Plus le lit est arrangé, plus le transport de graviers est difficile. Nos expériences ont montré que même un faible arrangement du lit peut entraîner de fortes modifications au niveau du transport solide. Une méthode a été développée dans le but de caractériser l'arrangement initial de la surface du lit. Cette méthode est basée sur la mesure topographique du lit. Grâce à l'analyse de l'ensemble des élévations du lit, différents critères peuvent être calculés et ceux-ci peuvent permettre de classer le lit en fonction de son arrangement (lit lâche ou lit arrangé). Les critères de surface sont la rugosité des grains, le degré d'armurage, la taille des formes du lit et des différentes structures ainsi que l'orientation des grains présents en surface. La présence de sédiments fins cohésifs dans la matrice grossière réduit fortement le transport des graviers. Les sédiments fins non cohésifs, eux, ont un effet lubrificateur sur les graviers. Plus la concentration en sédiments fins dans la couche de transport est forte, plus le transport de graviers est augmenté. Cette concentration est directement liée au mode de transport des sédiments fins (charriage ou suspension) et à leur distribution dans la matrice grossière.

L'étude à l'échelle locale a montré que le transport solide était seulement régi par la force de l'écoulement. Elle montre également que seul l'arrangement local impacte la structure de l'écoulement. Selon cette analyse, le transport est contrôlé seulement par la contrainte de cisaillement locale (la friction du grain). L'analyse locale doit être poursuivie pour vérifier ces hypothèses émises avec une base de données limitée.

Nos observations expérimentales nous ont permis de developper un modèle phénoménologique récapitulant les différents processus contrôlant le transport de graviers. Il décrit le comportement des graviers dans les différentes configurations étudiées. Basé sur ce modèle, une méthode a été proposée pour aider à comprendre, estimer et interpréter le transport de graviers. Cette méthode a été appliquée et discutée sur un cas de terrain realisé sur la rivière de l'Arc. Elle peut être aussi utilisée pour ajuster la contrainte de mise en mouvement en fonction de l'état initial du lit dans les différents modèles numériques.

Grâce à nos experiences, nous avons pu proposer une nouvelle analyse dimensionnelle qui est une première étape avant de construire un nouveau modèle de transport sédimentaire. Cette analyse prend en compte des paramètres décrivant l'arrangement du lit, les propriétés géotechniques du lit et la présence de sédiments fins. La plupart des modèles existants ne prennent pas en compte ces effets.

Mots-clefs: transport sédimentaire; charriage; colmatage; arrangement du lit; mise en mouvement; laboratoire.

Notations

Abbreviations

ADV	Acoustic Doppler Velocimeter
DEM	Digital Elevation Model
FS	Fine sand
G	Gravel
GRP	Ground Reference Points
GSD	Grain Size Distribution
H&L	Hurther & Lemmin
LSPIV	Large Scale Particle Image Velocimetry
Ms	Medium silt
PDF	Probability Density Function
PIV	Particle Image Velocimetry
PST	Phase-Space Threshold
S	Sand
SS	Sweet Spot
SNR	Signal Noise Ratio
TKE	Turbulent Kinetic Energy
US	Ultrasonic Sensors

Symbols

a	Major axis of the fitted ellipse formed by the 2D structure function contour line [m]
a_g	Grain major axis [m]
a_j	Coefficient depending on Vectrino II geometry used to evaluate the Doppler noise [-].
A	Particle projected area on the photograph [m^2]
A_D	Deposit area on the DEM [m^2]
A_E	Erosion area on the DEM [m^2]
A_R	Aspect ratio of the grain [-]
b	Minor axis of the fitted ellipse formed by

	the 2D structure function contour line [m]
b_g	Grain minor axis [m]
b_j	Coefficient depending on Vectrino II geometry used to evaluate the Doppler noise [-].
c_f	fine sediment concentration [g/L]
$c^*_{f\text{-TL}}$	Dimensionless volumetric fine sediment concentration within the transport layer [-]
C_D	Friction coefficient [-]
C_i	Surface average concentration of moving particles on the image [-]
C_I	Circularity index [-]
$C_{I\text{-c}}$	Circularity index of coarse sediments [-]
$C_{I\text{-f}}$	Circularity index of fine sediments [-]
C_{TKE}	Empirical constant value used in the TKE-method [-]
C_u	Bed consolidation indicator [kPa]
$C_{u\text{-sat}}$	Bed consolidation indicator measured for water-saturated bed [kPa]
$C_{u\text{-20-30\,\%}}$	Bed consolidation indicator measured when bed water content is about 20 - 30 % [kPa]
d	Diameter of fine sediment [m]
d_a	Arithmetic mean size of the sediment mixture [m]
d_g	Geometric diameter of fine sediments [m]
d_i	Diameter such as i % of grains are finer by weight (for fine sediments) [m]
D	Grain diameter [m]
D^*	Dimensionless grain diameter [-]
D_b	Second-order structure function [m^2]
D^*_b	Dimensionless second-order structure function [-]
D_G	Gravel diameter [m]
D_{gX}	Geometric diameter of the sample X [m]
D_i	Diameter such as i % of grains are finer by weight (for gravels) [m]
D_{mix}	Representative diameter of the bed mixture [m]
D_s	Scissometer reel diameter [m]

D_t	Grain travel distance [m]
D_x and D_y	Longitudinal and transverse dimensions of the camera range, respectively [m]
e	Void ratio [-]
$E_{\overline{\tau^*_{\text{ref}}}}$	Maximum deviation of τ^*_{ref} with respect to the average $\overline{\tau^*_{\text{ref}}}$ [%]
$E(z)$	Expected value of bed elevation z [m]
f	Fine sediment content within the gravel matrix [-]
f_c	Cone factor specified by the norm (penetrometer test) [-]
f_G	Proportion of gravels in the bed [%]
$f_{\max}$	Maximum fine sediment content that the gravel pores can contain [-]
F_A	Buoyant force [N]
F_b	Stabilising force applied on the bed [N]
F_f	Force of the fluid [N]
F_L	Lift force [N]
F_r	Froude number [-]
F_s	Sand content [-]
g	Gravitational acceleration [m.s^{-2}]
G	Force of gravity [N]
h	Flow depth [m]
h_p	Penetration distance during the penetrometer test [m]
h_s	Height of infiltrated fine sediments [m]
H_s	Scissometer height [m]
H_x, H_y	Hurst exponents of x- and y-directions, respectively [-]
i (or j, k)	index [-]
I_b	Global bed slope [-]
I_c	Channel slope [-]
$I_{\text{fit,i}}$	Fitted longitudinal bed slopes [-]
I_l	Local bed slope [-]
J	Energy slope [-]
k	Bed permeability [m^{-2}]
k_s	Hydraulic roughness [m]

k_{scisso}	Spring stiffness of the scissometer [N.m/°]
K	Strickler coefficient [$m^{1/3}/s$]
K_g	Strickler coefficient representing grain roughness [$m^{1/3}/s$]
K_h	Hydraulic conductivity [$m.s^{-1}$]
K_u	Kurtosis of bed elevation PDF [-]
l_A	Width of areas explored for computing bed surface criteria at local scale [m]
L	Channel length [m]
L_A	Length of areas explored for computing bed surface criteria at local scale [m]
$L_{j,k}$	Longitudinal distance between two points j and k (used in the local slope calculations) [m]
m_r	Ratio between spatial lags and measurement steps in the transverse direction used to compute D_b [-]
M	Number of measured elevation points in the transverse direction on the DEM patch [-]
M_p	Mass penetrating the sample during the penetrometer test [g]
M_D	Total mass of deposited gravel [kg]
M_E	Total mass of eroded gravel [kg]
M_f	Fine sediment mass in the sample [g]
M_G	Mass of gravels collected in baskets [kg]
M_{sample}	Total sample mass [g]
M_{tot}	Total gravel mass transported during an experiment [kg]
n	Number of measurements [-]
n_r	Ratio between spatial lags and measurement steps in the longitudinal direction used to compute D_b [-]
N	Number of measured elevation points in the longitudinal direction on the DEM patch [-]
n_p	Number of moving particles on an image [-]
p_X	Porosity of the sample [-]
p_f	Porosity of the fine sediments [-]
p_G	Porosity of the gravels [-]

p_m	Porosity of the sediment mixture [-]
P	Particle projected perimeter on the photograph [m]
P_c	Clay percentage [%]
q_s	Bedload rate per unit of width [$m^2.s^{-1}$]
q_s^*	Dimensionless bedload rate [-]
$q_{s\text{-ref}}$	Reference bedload rate [$m^2.s^{-1}$]
$q_{s\text{-ref}}^*$	Dimensionless reference bedload rate
Q	Water discharge [$L.s^{-1}$] or [$m^3.s^{-1}$]
$Q_{\text{ref-F}}$	Reference flow discharge at the falling hydrograph limb [$L.s^{-1}$] or [$m^3.s^{-1}$]
$Q_{\text{ref-R}}$	Reference flow discharge at the rising hydrograph limb [$L.s^{-1}$] or [$m^3.s^{-1}$]
R^2	Coefficient of determination
R_b	Auto-correlation function [m^2]
R_h	Hydraulic radius [m]
Re	Reynolds number [-]
Re^*	Particular Reynolds number [-]
Re_k	Permeability Reynolds number [-]
R_I	Roudness index [-]
R_o	Rouse number [-]
s	Relative grain density [-]
S_k	Skewness of bed elevation PDF [-]
S_t	Student coefficient [-]
t	Time [s]
t_{image}	Time interval between two recorded images [s]
$T0$ - $T5$	Specific time in the diagram [s]
T_c	Time of bedload collection (manual method) [s]
T_f	Final time in the diagram [s]
T_r	Fine sediment residence time [h]
$T_{s\text{-max}}$	Maximal torsional moment applicable on a sample during the scissometer test [N.m]
u	Instantaneous longitudinal velocity [$m.s^{-1}$]
u'	Longitudinal turbulent fluctuations [$m.s^{-1}$]
$\overline{u}$	Time-average longitudinal velocity [$m.s^{-1}$]

u^*	Friction velocity [m.s^{-1}]
u^*_{DS}	Friction velocity calculated with the depth-slope equation [m.s^{-1}]
u^*_{Log}	Friction velocity calculated with the log-method [m.s^{-1}]
u^*_{Re}	Friction velocity calculated with the Re-method [m.s^{-1}]
u^*_{TKE}	Friction velocity calculated with the TKE-method [m.s^{-1}]
U	Local depth-averaged longitudinal velocity [m/s]
U_s	Local longitudinal surface velocity [m/s]
UCS	Unconfined compressive strength [KN/m^2]
UCS^*	Dimensionless unconfined compressive strength [-]
v	Instantaneous transverse velocity [m.s^{-1}]
v'	Transverse turbulent fluctuations [m.s^{-1}]
$\overline{v}$	Time-average transverse velocity [m.s^{-1}]
V_D	Volume of deposited gravel [m^3]
V_E	Volume of eroded gravel [m^3]
V_v	Void-space volume of a sediment sample [m^3]
V_p	Average velocity of the particles on the camera field [m.s^{-1}]
V_t	Total volume of a sediment sample [m^3]
w	Instantaneous vertical velocity [m.s^{-1}]
w'	Vertical turbulent fluctuations [m.s^{-1}]
$\overline{w}$	Time-average vertical velocity [m.s^{-1}]
w_1, w_2	Two instantaneous vertical velocities measured by the Vectrino II [m.s^{-1}]
w'_1, w'_2	Two vertical turbulent fluctuations measured by the Vectrino II [m.s^{-1}]
$\overline{w_1}$, $\overline{w_2}$	Two time-average vertical velocities measured by the Vectrino II [m.s^{-1}]
w_s	Settling velocity [m.s^{-1}]
W	Channel width [m]
W^*	Dimensionless transport rate [-]
x	Longitudinal direction [m]
x_0	Longitudinal distance defined by the ellipse on the contour plot [m]

x_{Ar}	Adjustment applied on τ^*_{ref} in case of bed arrangement [%]
x_{Cu}	Adjustment applied on τ^*_{ref} in case of cohesive fine sediment presence [%]
x_{cf1}	Adjustment applied on τ^*_{ref} in case of the presence of a seal of non cohesive fine sediments [%]
x_{cf2}	Adjustment applied on τ^*_{ref} in case of the presence of non cohesive fine sediments infiltrated from the bottom-up [%]
y	Transverse direction [m]
y_0	Transverse distance defined by the ellipse on the contour plot [m]
z	Vertical direction [m]
z_{bed}	Bed level [m]
Z_0	Roughness length determine with the velocity profile [m]
Z_L	Height of the logarithmic layer [m]
Z_R	Height of the roughness layer [m]

α	Average angle between emitter and receivers of the Vectrino II [rad]
α_j	Angle between emitter and receivers of the Vectrino II, j=[1:4] according to the considered beam device [rad]
δ_x, δ_y	Sampling intervals in the x- and y-directions for calculating D_b, respectively [m]
Δ_{x0}, Δ_{y0}	Longitudinal and transverse scales of bed roughness, respectively [mm]
δz_{surf}	Water surface uncertainty [m]
Δ_x, Δ_y	Measurement steps in the x- and y-directions for calculating D_b [m], respectively
Δz_{bed}	Bed level change [m]
κ	Von Karman constant $\kappa = 0.4$ [-]
μ	Water dynamic viscosity [kg/m/s]
μ_k	k-order centered distribution moment [mm^k]
ν	Water viscosity [m^2.s^{-1}]
Φ	Angle of rotation of the ellipse relative to the

	flow direction detected using a contour plot [°]
Φ_{rad}	Angle of rotation of the ellipse relative to the flow direction detected using a contour plot [rad]
ρ	Water density [kg.m^{-3}]
ρ_s	Gravel mass density [kg.m^{-3}]
σ_g	Geometric standard deviation of the GSD [-]
σ_j	Doppler noise [m^2/s^2]
σ_{1-3}, σ_{2-4}	Doppler noise associated to beam 1 and 3 or to beam 2 and 4, respectively [m^2/s^2]
σ_s	Bedload thickness [m]
$\sigma_{z\text{-surf}}$	Standard deviation of the water surface measurements [m]
σ_z	Standard deviation of bed elevations [m]
σ_{zg}	Geometrical grain roughness [m]
σ_{zl}	Longitudinal bedform roughness [m]
σ_{zt}	Transverse bedform roughness [m]
τ	Bed shear stress [Pa]
τ^*	Dimensionless bed shear stress [-]
τ'	Shear stress due to grain resistance [Pa]
τ'_K	Shear stress due to grain resistance estimated using Manning Strickler relationship [Pa]
τ'^*_K	Dimensionless shear stress due to grain resistance estimated using Manning Strickler relationship [-]
τ'_l	Shear stress due to grain resistance estimated using local measurements [Pa]
τ'^*_l	Dimensionless shear stress due to grain resistance estimated using local measurements [-]
τ''	Shear stress due to bedform or bed irregularity resistance [Pa]
τ_c	Critical bed shear stress for the cohesionless sediment having size equal ot the arithmetic mean size of the cohesive sediment mixture [Pa] (Kothyari and Jain, 2008)
τ_{cc}	Critical bed shear stress for the cohesive sediment mixture [Pa] (Kothyari and Jain, 2008)
τ_{cr}	Critical bed shear stress [Pa]
τ^*_{cr}	Dimensionless critical bed shear stress [-]

τ_{ref}	Reference bed shear stress [Pa]
τ^*_{ref}	Dimensionless reference bed shear stress [-]
$\overline{\tau^*_{\text{ref}}}$	τ^*_{ref} average [-]
$\tau^*_{\text{ref-F}}$	Dimensionless reference bed shear stress during the falling limb [-]
$\tau^*_{\text{ref-R}}$	Dimensionless reference bed shear stress during the rising limb [-]
τ_t	Turbulent stress [Pa]
τ_ν	Viscous stress [Pa]
$\theta_{s\text{-max}}$	Maximal rotation angle during the scissometer test [°]
$\theta_{(\overline{u},\overline{v})}$	Rotation angle of the device in the plan $(\overline{u},\overline{v})$ [rad]
$\theta_{(\overline{u},\overline{w})}$	Rotation angle of the device in the plan $(\overline{u},\overline{w})$ [rad]
υ_g	Equivalent volume for spherical particle $[m^3]$

Contents

Notations XIV

I Introduction **1**

1 Introduction **3**

1.1 General context 3

1.1.1 Why study sediment transport? 3

1.1.2 Morphology and sediment transport in mountain rivers 4

1.2 Bedload predictions 7

1.2.1 Grain motion 7

1.2.2 Existing formulations 9

1.2.3 What are the variables influencing the onset of motion? 12

1.2.4 Uncertainties on the bed shear stress estimation 14

1.3 Objective and scientific approach 15

II Materials and methods **19**

2 Materials **21**

2.1 Experimental facility 21

2.2 Instrumentations 22

2.2.1 Ultrasonic sensors 23

2.2.2 Acoustic Doppler Velocimeter 25

2.2.3 Laser-scanner 26

2.3 Bed material characteristics 28

2.3.1 Grain size characteristics 28

2.3.2 Geotechnical properties 30

3 Experimental set-up **34**
3.1 Protocol introduction 34
3.2 Preparation of the beds 36
3.2.1 Clean gravel bed formation 36
3.2.2 Infiltrated gravel bed formation 39
3.3 Protocol for the sediment transport experiment 42
3.4 Link with the field 48

4 Gravel transport measurements **49**
4.1 Bedload estimation using manual collection 49
4.2 Bedload estimation using video measurements 50
4.2.1 Measurement procedure 51
4.2.2 Image processing analysis 52
4.2.3 Validity tests 55
4.3 Bedload estimation using topographic measurements 58

5 Bed characterization **60**
5.1 Digital elevation model 60
5.2 Direct measurements 61
5.2.1 Bed slope measurements 62
5.2.2 Bed surface grain size distribution 63
5.2.3 Fine sediment content on the bed surface 64
5.3 Indirect measurements 65
5.3.1 PDF analysis 65
5.3.2 Variogram analysis 68

6 Velocity measurements **75**
6.1 Analysis of the raw data 76
6.2 Despiking method 78
6.3 SNR and correlation filters 79
6.4 Bottom interference 80
6.5 Doppler noise correction 80
6.6 Device rotation correction 83

6.7 Signal decorrelation influence 85

7 Bed shear stress calculations 87
7.1 Methods 87
7.1.1 Depth-slope equation 87
7.1.2 Logarithmic law method - log method 88
7.1.3 Reynolds stress method - Re method 89
7.1.4 Turbulent kinetic energy - TKE method 90
7.2 Sensitivity of the friction velocity estimation to the bed position 92
7.3 Recommendations 94

III Results 97

8 Gravel dynamics at the global scale 99
8.1 Literature review on transport of poorly sorted sediments at low bed shear stresses 99
8.2 Dynamics over an unimodal gravel bed 103
8.2.1 General results 103
8.2.2 Hysteresis effect 109
8.2.3 Impact of bed arrangement 110
8.3 Dynamics over an infiltrated bed 118
8.3.1 General results 118
8.3.2 Hysteresis effect 123
8.3.3 Impact of geotechnical bed properties 124
8.3.4 Importance of fine sediment concentration 127
8.4 Summary of the results and methodology for bedload prediction 128
8.4.1 Summary of the results 129
8.4.2 Methodology/recommendations for bedload prediction 132
8.5 Bedload rate estimation using existing models 138
8.5.1 One-state formulations 138
8.5.2 Two-state formulations 140

9 Hydrodynamics at the local scale 142
9.1 Identification of the spatial variability 142

9.1.1 Impact of the bed spatial variability on friction velocity 143
9.1.2 Impact of the bed spatial variability on velocity and turbulent profiles . . . 147
9.1.3 Impact of the bed spatial variability on sediment transport experiments . . . 151
9.2 Local dynamics of unimodal beds . . . 153
9.2.1 Impact of bed arrangement on friction velocity . . . 153
9.2.2 Impact of the bed arrangement on velocity and turbulent profiles . . . 156
9.3 Local dynamics of infiltrated beds with Ms sediments . . . 159
9.3.1 Impact of the fine sediment presence on friction velocity 159
9.3.2 Impact of the fine sediment presence on velocity and turbulent profiles . . . 163

10 In situ Application - Arc River 166
10.1 Introduction . . . 166
10.2 Site presentation and field experimental set-up . . . 167
10.2.1 Location of field measurements . . . 167
10.2.2 Field experimental set-up . . . 168
10.3 General hydro-dynamical results . . . 172
10.3.1 Flushing event hydrographs . . . 172
10.3.2 Water levels and depths . . . 174
10.3.3 Surface velocities over the gravel bar . . . 176
10.3.4 Bed shear stresses over the gravel bar . . . 181
10.4 Gravel dynamics . . . 187
10.4.1 Observed movements . . . 187
10.4.2 Comparisons with laboratory results . . . 197

IV Conclusions and prospects 199

11 Conclusions and prospects 201
11.1 General conclusion . . . 201
11.1.1 Approach at the global scale . . . 202
11.1.2 Approach at the local scale . . . 203

11.1.3 Toward a general understanding of gravel transport . . 205
11.1.4 Summary of the controlling parameters 207
11.2 Prospects 209
11.2.1 Improvement of the flow and sediment transport descriptions at local scale 210
11.2.2 Improvement of the methodology for improving bedload prediction 211
11.2.3 Impact of bedload rate on fine sediment transport . . . 216
11.2.4 Improvement of restoration operations 216
11.2.5 Use of different material 216

Bibliography **217**

V Appendices **239**

A Experimental data **241**

B Bed surface characteristics **247**
B.1 L-G-1 experiment 247
B.2 P-G-1 experiment 254
B.3 L-G-2 experiment 261
B.4 P-G-2 experiment 268
B.5 L-G-3 experiment 275
B.6 P-G-3 experiment 282
B.7 L-G-4 experiment 289
B.8 L-G-5 experiment 296
B.9 H-G/Ms-5 experiment 303
B.10 L-G-6 experiment 310
B.11 P-G/Ms-6 experiment 317
B.12 L-G-7 experiment 324
B.13 H-G/S-7 experiment 331
B.14 H-G/Ms-9 experiment 338

C Doppler noise and variance correction **345**

Part I

Introduction

Chapter 1

Introduction

1.1 General context

1.1.1 Why study sediment transport?

Rivers are not only sources of risks such as floods or bridge instabilities, but also are essential for drinking purposes, agriculture (irrigation), navigation and for energy production. They were first simply defined as a moving mass of water but today, we know that river systems are worth to study both hydraulics and sediment dynamics. Flow and sediments are in constant interactions: flow is responsible for sediment transport that leads to morphological changes within the bed; and these changes impact the flow, etc.

In natural conditions, a river is considered at equilibrium when the sediment supply is equal to what can transport the flow (Lane, 1955). Then, sediment transport occurs without changing significantly the original river morphology. If a perturbation occurs (natural such as floods or anthropogenic such as engineering structures), the river answers with bed modifications (bed aggradation, bed degradation, bank erosion) in order to search for a new equilibrium.

Bed erosion and its causes has been extensively studied this past few decades because is largely connected to ecological or socio-economic issues (Galay, 1983; Schumm, 2005; MacArthur et al., 2008). Indeed, as a conse-

quence of bed erosion, engineering structures can become unstable, environment and fish habitat can be altered, and problems of deposition can appear at the downstream part of the river. Schumm (2005) assesses that bed erosion can come from different causes, such as geologic, geomorphic, climatic, hydrologic, animal or human causes. Lots of anthropogenic activities alter the natural morphological evolution of the rivers (MacArthur et al., 2008), such as the exploitation of dams, the river channelization and the river dredging.

All these issues makes challenging the understanding of sediment transport for engineering purposes. Today, the evaluation of solid transport remains uncertain and complex because it depends on numerous parameters, such as grain size and form, bed morphology, bed slope, water depth, boundary roughness, bed material, hydraulics conditions, etc.

1.1.2 Morphology and sediment transport in mountain rivers

In this thesis, we will focus on anthropogenic mountain rivers such as the ones found in the Alps. In this part, we will recap the specificity of such rivers.

Morphology in anthropogenic rivers

Many anthropogenic constructions affect the morphology of mountain rivers. Due to a growing population, water resources of many rivers are over-exploited. Lots of them are now channelized or regulated by dams to protect urbanization and roads from floods and to product electricity (Irwin and Whiteley, 1983; Brooker, 1985; Booth, 1991). The main effect of channelization is that the river becomes narrower, deeper and steeper (Schumm et al., 1984). In that case, the in-channel flow and velocity increase and bed incision appears. In addition, the straightening of the rivers prevents meandering and reduces the ecosystem variability. Numerous previous works have noticed a decrease in fish species after an operation of channelization (Huet and Timmersmans, 1976; Swales, 1980). Less shelters and spawning areas for fishes are present in case of constraint rivers implying a loss of biodiversity (Wasson et al., 1998).

The channelization also accelerates the sediment transfer to the downstream part of the rivers that can create deposition problems.

Cross-sectional structures such as dams alter the sediment transport in mountain rivers (Williams and Wolman, 1984; Morris and Fan, 1998). The sediments transported from upstream are stopped and stocked within the reservoir. This causes a sediment deficit downstream of the dam that can lead to a progressive erosion of the downstream reach (Ligon et al., 1995; Schmidt and Wilcock, 2008). The deposits of sediments within the reservoir increase the risk of flood and also lead to a reduction in the storage volume of the reservoir. Dam presence also regulates the flow in the downstream reach which is generally only sufficient to mobilize fine grains leading to the creation of an armored bed surface (Parker et al., 1982). To increase the dam efficiency, flushing events are regularly scheduled. During the flushing events, a large amount of fine sediments are released and might infiltrate the downstream river reach that could disturb and degrade the aquatic habitat (Wood and Armitage, 1997) by making exchanges between bed subsurface and surface impossible (nutriment, oxygene). This past few years, there was an increased awareness of the potential impacts of dams on environment (Pizzuto, 2002; Ligon et al., 1995; Kondolf, 1995; Kondolf et al., 2014; Dany, 2016). Suggestions were proposed to manage dams and conduct operations such as flushing events with more respect to the environment (controlled release of sediments).

These rivers are also subject to dredging operations to allow for fluvial navigation, or to recover raw materials for engineering constructions. Dredging of river beds is a main cause of river erosion (Lagasse, 1986). They can be carried out in dams or in channelized rivers with the aim of enlarging the river volume to rapidly evacuate floods. These operations largely impact the river morphology.

Sediment transport in mountain rivers

River beds in mountains are often made of poorly sorted material (cohesive or non-cohesive) with grain sizes ranging from clay to pebble (Miller, 1958; Montgomery and Buffington, 1997), namely varying between few micrometers

to decimeters (see the classification of Wentworth, 1922). All these classes of material can thus be in interaction making more difficult the transport rate estimation. Figure 1.1.1 shows an example of bed material variability that can be found in French Alpine rivers (gravel bar of the Arc-en-Maurienne river).

Figure 1.1.1: Photograph of the bed material found on a gravel bar in the Arc-en-Maurienne river. The size of the Wolman patron located on the bed surface is equal to 40 cm.

Coarse sediments (pebble, gravel) are generally transported as bedload whereas fine sediments (silt, clay) are transported in suspension only (Figure 1.1.2). Sand particles can be transported either as bedload or as graded suspended load according to hydraulic conditions. For these reasons, no interaction between fine and coarse sediments is generally considered. Yet, it seems that their movement is linked (Curran and Wilcock, 2005; Kothyari and Jain, 2008). The coarse sediments might impact the transport of fine sediments, and vice-versa. For instance, the bed roughness generated by the presence of coarse sediments can change during their transport and impact the flow turbulence and thus can influence the particles in suspension (Wilson, 1966; Recking et al., 2008). In addition, the presence of fine sediments infiltrated within a matrix of coarse sediments can increase or reduce the bedload rate (Wilcock et al., 2001; Kothyari and Jain, 2008, among others). The coexistence of fine and coarse sediments within the bed river make thus difficult the understanding of sediment transport.

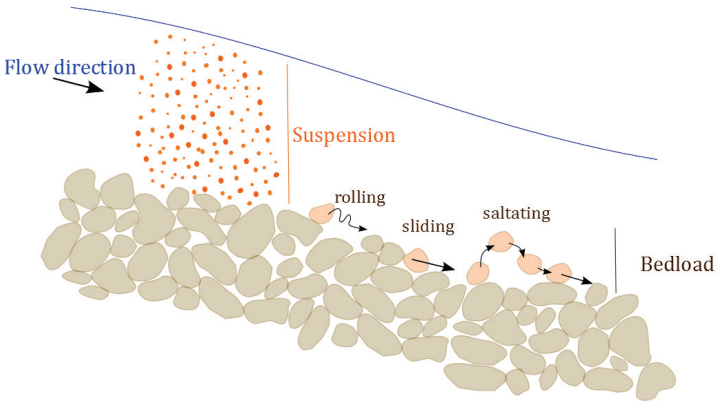

Figure 1.1.2: Transport modes of coarse (bedload) and fine sediments (suspension) within a gravel-bed river.

In our study, we are interested in gravel-bed rivers which are largely present in the Alps. Gravel-bed rivers were studied for decades: Buffington and Montgomery (1997) gave an exhaustive review on experimental and in-situ studies performed on gravel beds and highlighted the complexity of understanding the gravel transport, especially in case of poorly sorted sediments.

The distribution of fine sediments within the bed matrix is often inhomogeneous, making the bedload rate estimation even more difficult. Numerous studies were conducted to understand the mechanisms of fine sediment infiltration (Gibson et al., 2009; Wren et al., 2011) but to our knowledge, none focused on the impact of these infiltrated sediments on bedload rate. For stream restoration and management of regulated mountain rivers, it is crucial to understand the transport of multi-modal beds.

1.2 Bedload predictions

1.2.1 Grain motion

The movement of a grain is essentially driven by the flow and constrained by the bed stability. The force F_f due to the flow on a particle of diameter D

is proportional to the shear stress at the bed level τ generated by the flow velocity gradient and to the surface of the particle:

$$F_f \propto \tau D^2 \tag{1.1}$$

where D is the grain diameter.

The bed stability, or more precisely the force F_b, is defined as the distributions of the dislodging forces, which individual grains can resist before moving (Tait, 1993):

$$F_b \propto (G_n - F_A) \tag{1.2}$$

where G_n is the normal gravity force and F_A is the buoyant force (principle of Archimedes). Figure 1.2.1 recaps the forces involved in the grain motion.

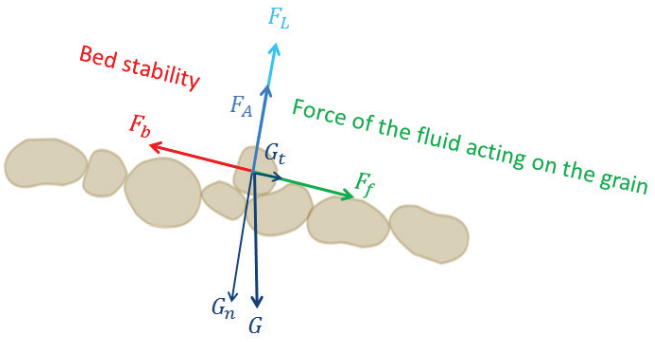

Figure 1.2.1: Forces involved in the grain motion. G is the gravity force; subscript n and t denote the normal and transverse directions, respectively; F_A refers to the buoyant force; F_L is the lift force; F_f is the flow force and F_b is the stabilising force (bed stability).

The flow needs to overcome the stabilising forces applied on the bed to move grain (Shields, 1936). This describes a deterministic approach which supposes that the transition between no motion and initiation of grain motion is discontinuous. The discontinuity is referred to the threshold for incipient motion.

Another approach, namely the stochastic approach, supposes that the transition between no motion and initiation of grain motion is continuous and that the threshold for incipient motion does not really exist in a macroscopic point of view. Over a rough gravel bed, the flow is turbulent composed

of a succession of turbulent events with different magnitudes and randomly distributed over time, such as sweeps and ejections. This stochastic flow character and the grain-grain interactions control the sediment transport (Einstein, 1937; Paintal, 1971; Ancey et al., 2008; Ancey et al., 2015; Houssais et al., 2015). The sediments moves intermittently according to the event magnitude and duration.

1.2.2 Existing formulations

To study the bedload transport using the stochastic approach, data at local scale are needed. However, in most of studies, only data at global scale (i.e. average over specific zone) are available. That is why, most of the bedload predicting formulae remain based on deterministic approaches which focus on the transport at global scale.

Historically, the bedload predicting models are based on the evaluation of the excess bed shear stress (Meyer-Peter and Müller, 1948; Wilson, 1966; Fernandez - Luque and van Beek, 1976; Wong and Parker, 2006; Buscombe and Conley, 2012). The excess bed shear stress is a comparison between the bed shear stress τ exerted by the fluid and the critical bed shear stress τ_{cr} needed for the sediment initiation of motion representing the stabilising force. Once the bed shear stress exceeds the critical bed shear stress ($\tau > \tau_{cr}$), the movement happens. The bed shear stress is often analysed in its dimensionless form, also called the Shields number (τ^*) (Shields, 1936). It represents the ratio between the hydraulic force and the submerged weight of the sediment:

$$\tau^* = \frac{\tau}{(\rho_s - \rho)gD} \tag{1.3}$$

where g is the acceleration of gravity, ρ_s and ρ are sediment and water density, respectively, and D is the grain size.

The bedload rate is also studied in its dimensionless form, q_s^*:

$$q_s^* = \frac{q_s}{\sqrt{(s-1)gD^3}} \tag{1.4}$$

where q_s is the bedload rate and $s = \rho_s/\rho$ is the relative grain density.

As an example of bedload predicting model, here is the well-known empirical model of Meyer-Peter and Müller (1948):

$$q_s^* = 8(\tau^* - \tau_{cr}^*)^{3/2} \tag{1.5}$$

where τ^* is the dimensionless bed shear stress and τ_{cr}^* is the dimensionless critical bed shear stress equal to 0.047 according to Meyer-Peter and Müller (1948).

τ_{cr}^* is the value at which the transport begins which is practically impossible to measure directly. Its definition is related to the definition of the onset of motion which has been subjected to numerous debates. No universal definition exists (Lavelle and Mofjeld, 1987; Dey, 1999; Beheshti and Ataie-Ashtiani, 2008). Figure 1.2.2 represents a revised version of the Shields diagram (van Rijn, 1984) which shows τ_{cr}^* as a function of the dimensionless grain diameter $D^* = [g(s-1)/\nu^2]^{1/3} D$, where ν is the water viscosity. All data reported by Buffington and Montgomery (1997) were plotted in Figure 1.2.2, as well as the Soulsby and Whitehouse (1997) curve which is often used to fit the revised Shields diagram. Data follow the overall shape of the Soulsby and Whitehouse (1997) curve:

$$\tau_{cr}^* = \frac{0.24}{D^*} + 0.055\,[1 - \exp(-0.02D^*)] \tag{1.6}$$

However, a significant scatter is present. For a given D^*-value, τ_{cr}^* can vary up to one order of magnitude. It reveals the difficulty of τ_{cr}^* prediction.

Small errors in τ_{cr}^* determination can lead to large errors in bedload rate estimation with excess bed shear stress models. When $\tau^* >> \tau_{cr}^*$, models like Meyer-Peter and Müller (1948) model predict fairly the bedload rate. However, they fail at low transport where bedload becomes highly intermittent (Camenen and Larson, 2005). Unfortunately, these conditions of low transport are the most frequent in natural streams. Figure 1.2.3, taken from Camenen and Larson (2005) study, shows bedload rate as a function of the ratio τ^*/τ_{cr}^*. It presents a comparison between bedload data and predicting formulas, such as the one of Meyer-Peter and Müller (1948). For excess bed shear stress formulas, the threshold was set at 0.04. The breakdown of

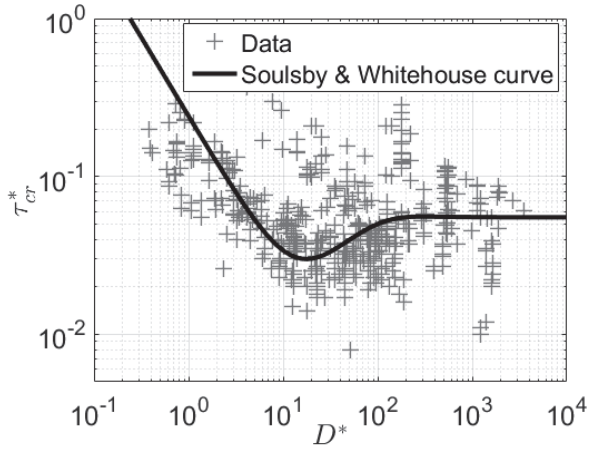

Figure 1.2.2: Shields number versus the dimensionless grain size (data from Buffington and Montgomery, 1997). The fit curve corresponds to Equation 1.6.

excess bed shear stress models is noticeable at low transport and seems to be linked to the estimation of the threshold of motion itself. The plot of the Meyer-Peter and Müller (1948) formula is very steep and non-linear at low transport. Even after having highlighted this problem, the use of such models remains predominant and convenient in engineering studies.

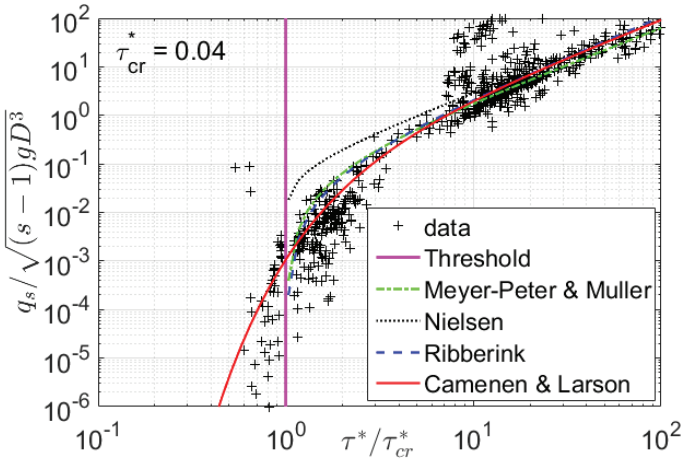

Figure 1.2.3: Comparison between bedload rate data and bedload rate predicted using different bedload models as presented in Camenen and Larson (2005).

Some authors suggests improving the bedload predictions at low transport by introducing models based on the ratio $\tau^*_{\text{ref}}/\tau^*$ where τ^*_{ref} is the di-

mensionless reference bed shear stress (Wilcock and Crowe, 2003; Camenen and Larson, 2005; Recking, 2010). Such formulations allow prediction at low sediment transport. The relationship of Camenen and Larson (2005) which is based on an exponential relationship is given as an example:

$$\frac{q_s(t)}{\sqrt{(s-1)gD^3}} = 12\tau^{*1.5}\exp\left(-4.5\frac{\tau^*_{\text{ref}}}{\tau^*}\right) \tag{1.7}$$

The Equation 1.7 is represented in Figure 1.2.3. τ^*_{ref} is a surrogate for τ^*_{cr} and refers to the bed shear stress that produces a low but measurable reference transport rate $q_{s\text{-ref}}$ (Wilcock et al., 2009). $q_{s\text{-ref}}$ is defined arbitrarily. As for τ^*_{cr}, τ^*_{ref} depends on the grain diameter as suggested by the revised Shields diagram, but also on other variables, such as bed slope, bed arrangement, presence of fine sediments.

To sum up, no universal and accurate formulae exists. Most of the existing formulations for q^*_s are functions of a term which represents the flow resistance and a term which represents the bed stability. The flow resistance is often described using the bed shear stress τ and the bed stability is characterized either by the dimensionless critical bed shear stress τ^*_{cr} or by the dimensionless reference bed shear stress τ^*_{ref}:

$$q^*_s = f(\tau^*, \tau^*_{cr}) \tag{1.8}$$

or

$$q^*_s = f(\tau^*, \tau^*_{ref}) \tag{1.9}$$

One can wonder which parameter between the flow resistance and the bed stability is the more important to study to improve the estimation of q_s.

1.2.3 What are the variables influencing the onset of motion?

A grain having a given size, shape and density can be transported differently according to the bed arrangement on which it lies. Bedload displays a strong dependence with grain protrusion, imbrication, compaction and presence of structures or bedforms (Fenton and Abbott, 1977; Brayshaw et al., 1983;

Kirchner et al., 1990; Hassan et al., 2006; Guney et al., 2013; Masteller and N.J., 2017). The bed arrangement plays a significant role on the onset of motion. Bed arrangement will change according to the history of the stream, so does the sediment incipient motion (Reid et al., 1985; Monteith and Pender, 2005; Turowski et al., 2011).

The presence of multi-sized grains on the bed can also impact the onset of motion. It is now well-established that transport of a given particle over a poorly sorted bed material differs from the transport over a well-sorted bed material. In bed material with multiple size fractions, finer particles can be hidden by coarser particles. The latter are then more exposed to the flow making their motion easier. The concept of hiding-exposure was developed to assess for the position of a grain relative to another grain having a different size (Egiazaroff, 1955; Ashida and Michiue, 1972; Parker and Klingeman, 1982; Proffitt and Sutherland, 1983; Wu et al., 2000). The transport of multi-sized grains remains an up-to-day issue, particularly the transport of bimodal bed material. When gravels are in presence of fine sediments, their incipient motion can either be enhanced (Ikeda and Iseya, 1988; Wilcock et al., 2001) or reduced (Kothyari and Jain, 2008).

Several studies have related a potential impact of the river bed slope or the relative roughness (k_s/h, where k_s is the hydraulic roughness and h is the water depth) on the incipient motion (Shvidchenko and Pender, 2000; Armanini and Gregoretti, 2005; Lamb et al., 2008; Recking, 2009; Prancevic and Lamb, 2015). The effect of bed slope on bedload is controversial in the literature. Chiew and Parker (1994) showed that τ^*_{cr} decreases with increasing bed slope. They attributed this behavior to an increase in gravitational component in the downstream direction. Others found that τ^*_{cr} increases with increasing bed slope (Shvidchenko and Pender, 2000; Mueller et al., 2005; Lamb et al., 2008; Recking, 2009). For instance, Mueller et al. (2005) showed using field measurements performed on 45 different streams that τ^*_{cr} varies from 0.025 to 0.035 for rivers with slope ranging from 0.001 to 0.006 or from 0.06 to 0.12 for steeper rivers with slope ranging from 0.02 to 0.05. This augmentation remains partially explained. Most of the researchers argued that, at high slope, stable bed structures and bedforms appear leaving less energy for bedload transport (Shvidchenko and Pender, 2000). Others

related this augmentation to change in relative roughness with increasing slope (Lamb et al., 2008; Recking, 2009; Camenen, 2012). Indeed, at high slope, the water depth is lower and often close to the height of the largest grain. The flow structure and its turbulence are different according to the ratio k_s/h which affects the bed shear stress and consequently the bedload rate.

These variables are crucial for bedload prediction. They seem to impact both the flow resistance and the bed stability. This makes harder the understanding of the mechanisms governing the bedload.

1.2.4 Uncertainties on the bed shear stress estimation

We have seen that physical processes can affect bed stability and so lead to uncertainties in bedload estimation but this uncertainty can also results from the estimation of the bed shear stress itself. The bed shear stress will inform about the flow resistance on the bed. Bed shear stress can also change according to the previous mentioned physical processes. Several methods exist to determine and calculate it. Some of them are presented in this manuscript (Section 7). Bed shear stress values obtained with these methods need to be compared with caution. Indeed, some of them inform about global bed shear stresses, also called total bed shear stresses, whereas the others describe local bed shear stresses, at the grain scale.

It is important to remind that total bed shear stress τ can be divided into a shear stress due to the grain resistance τ' and one due to the resistance of bedforms or bed irregularities τ'' (e.g. structures, clusters, ripples, preferential flow pathways). According to many authors, (Meyer-Peter and Müller, 1948; Camenen and Larson, 2005; Petit et al., 2015), τ' is responsible for the bedload transport. Unfortunately, in most studies, no indication is given about bedforms making difficult the estimation of τ''. Buffington and Montgomery (1997) estimated in their review about gravel-bed rivers that τ'' can vary between 10 to 75 % of the total bed shear stress according to the bed configuration. Considering this variation, if we compare local bed shear stress with total bed shear stress, the difference can be significant. This might impact the result of a bedload prediction.

Most of the time, the bed shear stresses were evaluated using methods describing global values. To be able to compare these values with local values, one should apply corrective coefficients in order to take into account the bedform impact (see Buffington and Montgomery, 1997). Even with these corrections, error in bedload estimation can be significant.

1.3 Objective and scientific approach

The main objective of this thesis is to examine gravel dynamics at low bed shear stress over moderately or poorly sorted bed materials representative of mountain rivers using laboratory experiments. This work is intended to find the main parameters governing gravel transport. In particular, effects of the bed structure on flow resistance and bed stability will be clearly distinguished. Using original laboratory data, a method and some recommendations that will help to improve the prediction of bedload at low bed shear stress are proposed. This work intend to answer the following questions:

- How can we reproduce a bed representative of natural mountain streams in laboratory?
- How can we improve bedload predicting models at low transport rate?
- Which parameters between bed stability and flow resistance are the most critical for bedload prediction?
- What are the processes controlling bedload rate at local and global scales?
- How can we calculate the bed shear stress and estimate a reference bed shear stress in case of arranged beds with presence of fine sediments?
- What is the impact of bed arrangements and presence of fine sediments on the flow resistance and the bed stability? And how the flow resistance and the bed stability changes affect the bedload rate?
- What is the impact of presence of cohesive fine sediments on bedload rate?

This study is based on experimental results collected in a 18 m long flume in the laboratory of Irstea Lyon-Villeurbanne. Different types of beds (i.e. diverse bed arrangements and degrees of clogging) will be investigated to study bedload in configurations close to what can be found in mountain rivers. We will focus on packed and infiltrated with fine sediments beds, which are often observed at the downstream end of dams in mountain rivers. The dynamics of a given material (gravel) forming the structure of the beds is studied over beds having different compositions. This work will be carried out at low bed shear stress in order to focus on conditions close to the gravel incipient motion. These conditions are frequent in rivers and generate a non negligible amount of transported sediments over a year (Camenen et al., 2011). To complete this work, different sediments (different sizes, non-cohesive and cohesive) and numerous measurement devices (laser-scanner, Acoustic Doppler Velocimeter, ...) are available.

The manuscript is organized as follows:

- In the first part, the context and the different issues associated to this study are presented .
- In the second part, the procedure retained to create gravel beds representative of mountain rivers is explained and the experimental set-up is described. Particular attention was paid to perform reproducible and comparable experiments. Tools and methods necessary to process and analyse the data such as the bed surface characterization method are also presented.
- Results are presented and discussed in the third part. Experimental results are analysed at different scales (global and local) to understand the mechanisms and processes involved in gravel transport. Focus is set on the bed arrangement influence as well as on the impact of fine sediment presence. Main factors impacting gravel transport are discussed, apart from bed slope which is not investigated in our study. Previous bedload predicting models are tested on our data. Using the experimental observations, recommendations are given for improving bedload prediction and then discussed with an in-situ experiment conducted on the Arc-en-Maurienne river.

- Main conclusions of the thesis are recapped in the last part. Suggestions are given for further works on bedload analysis over poorly sorted bed material.

Part II

Materials and methods

Chapter 2

Materials

2.1 Experimental facility

Sediment transport experiments were carried out in a 18 m long, 1 m wide and 0.8 m deep tilting flume, located in the Hydraulic and Hydromorphology Laboratory (HHLab) of Irstea Lyon-Villeurbanne, France (Figure 2.1.1). The channel slope is adjustable from 0 % to 5 %. The channel is made of glass allowing for visual observations. A closed recirculating system can be used to supply clear water or a mixture of water and fine sediments (up to 0.5 mm in diameter) in the flume. The water is pumped up from a tank located in the basement to the upstream end of the channel.

The flume has a working length of 17 m (Figure 2.1.2). A honeycomb is placed at the flume inlet to break turbulent structures generated by the entering flow. The flow depth is controlled by a 1 m-long weir with adjustable slope and height, installed at the downstream end of the flume. The weir is used to ensure the flow uniformity. The flow was qualified as uniform when its free surface was approximately parallel to the longitudinal bed profile. The weir settings were determined after several trials. In our experiments, the flow depth was the same (within $\pm$ 1 cm) at every sections of the channel located between 6 and 18 m downstream of the flume inlet.

An automated mobile platform is set on two rails running along the channel sides, parallel to the channel bottom (Figure 2.1.1a). The platform can move in various directions: longitudinal (x), transverse (y) and perpendic-

(a) Tilting flume **(b)** Feeding system

Figure 2.1.1: Photographs of the main experimental installations: tilting flume with the automated platform (a) and feeding system (b).

ular to the bottom (z). The origin of the axes is located at the right side of the upstream end of the flume, at the bottom channel. All measuring devices are installed on this platform, such as ultrasonic sensors (US) measuring the water surface, an Acoustic Doppler Velocimeter (ADV) measuring the flow velocity and turbulence and a laser-scanner measuring the bed topography. The platform movements and the measurements are synchronized and recorded using a home-made LabVIEW program.

Recently, a feeding system was installed at the upstream end of the tilting flume (Figure 2.1.1b). It is constituted of a sediment reservoir and a conveyor belt. The system can feed the flume continuously and uniformly along the channel width with diverse sediments (large gravel to fine sand particles) and feeding rates.

2.2 Instrumentations

The devices used during experiments are described in the following sections: the ultrasonic sensors, the acoustic Doppler velocimeter and the laser scanner.

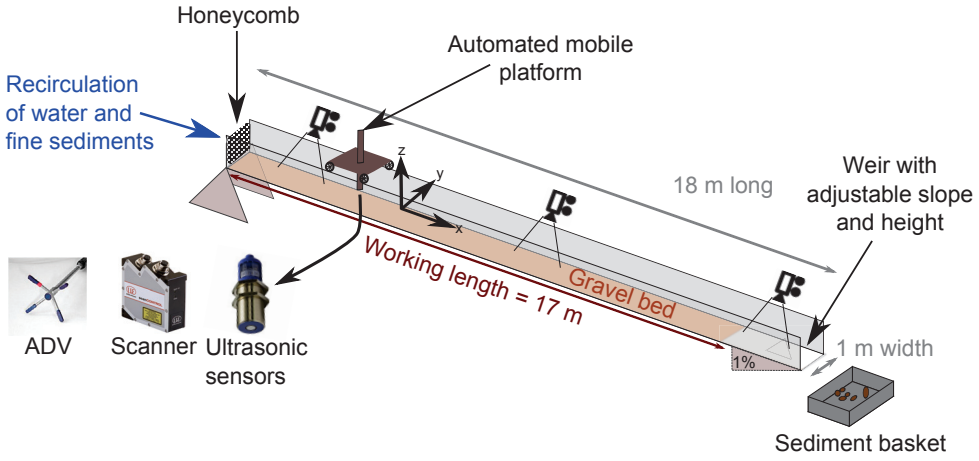

Figure 2.1.2: Scheme view of the experimental set-up, installed in HH-Lab Irstea Lyon-Villeurbanne.

2.2.1 Ultrasonic sensors

Ultrasonic sensor (US) is a non-intrusive instrument able to measure the distance between its sensor and an object (fluid or solid). US transmits a short ultrasonic pulse and measures the time between the emission and the reception of the pulse echo on the object. The distance is computed from this travel time.

In this study, US were used to determine the water surface or bed level. The water surface was measured using three ultrasonic sensors (Microsonic mic +130/IU/TC) installed on the automated platform (Figure 2.1.2) and spaced apart from each other in the longitudinal direction by 40 or 50 cm. Multiplying the number of ultrasonic sensors enabled to cover a larger zone during the experiments. The mobile platform was programmed to measure water surface at specific locations along the flume center line (every meters). The measuring time was set to 30 seconds per location with a frequency of 50 Hz (about 1500 measurements). The water surface measurements at a given location were then time-averaged. 30 seconds were sufficient to obtain a converged signal and to smooth the potential water surface fluctuations. The waterline along the channel was estimated using all these measurement points. Uncertainty related to the water surface measurement, δz_{surf}, was

estimated of about 0.1 mm, based on data from several experiments:

$$\delta z_{\text{surf}} = S_t \frac{\sigma_{z\text{-surf}}}{\sqrt{n}} \tag{2.1}$$

where δz_{surf} is the water surface measurement uncertainty, S_t is the Student coefficient, $\sigma_{z\text{-surf}}$ is the standard deviation of the data set and n is the number of measurements.

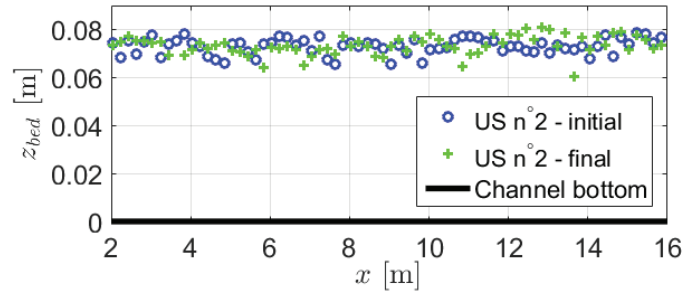

(a)

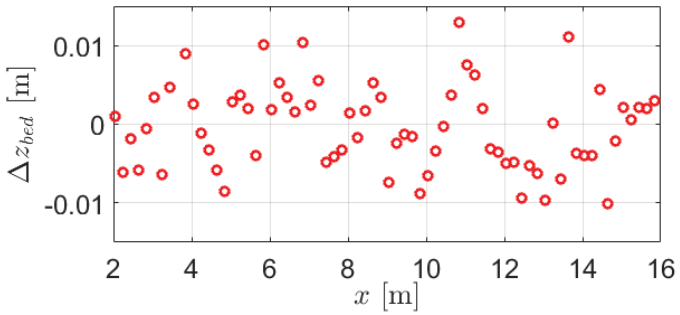

(b)

Figure 2.2.1: (a) Example of US data of initial and final bed levels at the flume centerline for an experiment performed on a loose gravel bed. (b) Differences between initial and final bed levels. Deposit ($\Delta z_{\text{bed}} < 0$) and erosion ($\Delta z_{\text{bed}} > 0$) zones can be identified.

Using the same devices and procedure once the channel is drained, initial and final bed surface elevations were measured at same locations as the water surface. The flow depth h was estimated as the difference between the measured water surface and bed surface, considered as the average between the initial and final measured bed elevations. Bed level measurements could not be carried out when water was flowing in the flume. Comparing initial

and final bed states of all our experiments, we noticed that the bed level change can reach up to 10 mm, namely just a little larger than the median gravel size (D_{50} =6.8 mm) (Figure 2.2.1). The uncertainty linked to the water depth measurement was at least of the order of the gravel size, because of the uncertainty linked to the bed level determination.

2.2.2 Acoustic Doppler Velocimeter

Velocities were measured using a Nortek Acoustic Doppler Velocimeter (ADV) (Vectrino II). The ADV is a profiling velocimeter that provides measurements of the 3D-velocity at high rates (frequency up to 100 Hz). It consists of a central transmitter that is surrounded by four receivers. It measures along a sampling volume (cylinder of 6 mm in diameter and 3.5 cm in length) starting 4 cm away from the transmitter with a vertical resolution of 1 mm. Figure 2.2.2 shows the main characteristics of the device.

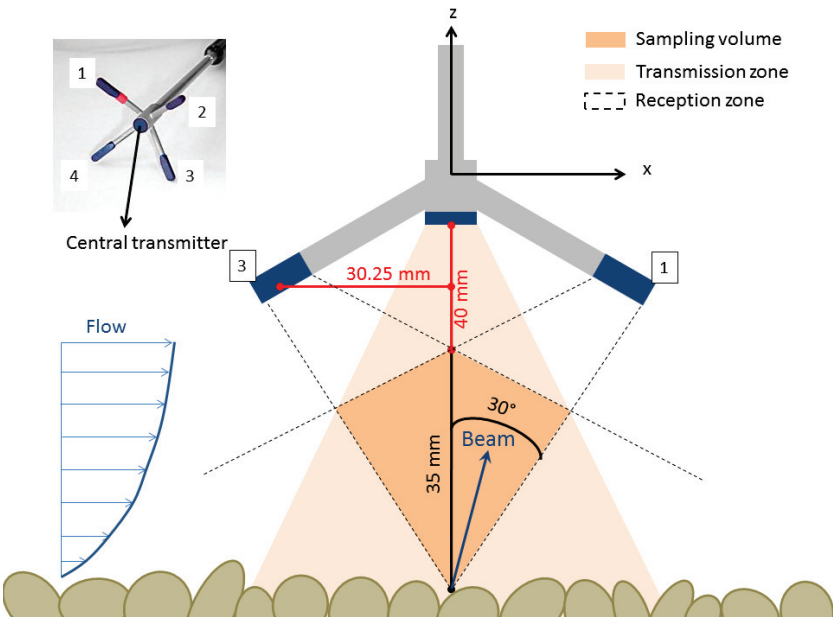

Figure 2.2.2: Overview of the main characteristics of the Vectrino II showing its range of measurement, its configuration and its geometrical aspects. The Vectrino II photograph was taken from the Nortek website.

Velocity measurement is based on Doppler effect. A sound wave is transmitted to particles (or impurities) in motion in the water. The sound wave

is then reflected back to the device with a frequency shift proportional to the velocity of the moving particles. The flow velocity is assumed to be equal to the particle velocity. It is thus important to make sure that particles within the flow are small enough with a negligible fall velocity before starting the measurement. In our case, particles were either impurities initially present in the water or very fine sediments in suspension within the water column. These sediments will be presented in the Section 2.3.

Four velocity values can be obtained with the Vectrino II. The raw velocities, directly measured by the ADV receivers, are located along the bisector between the receivers and the transmitter (Figure 2.2.2). A transformation matrix provided by the manufacturer is applied to compute velocities in the reference coordinates (x, y, z) from beam velocities. The longitudinal and vertical instantaneous velocities u and w_1 are deduced from the signal provided by receivers 1 and 3. Similarly, the transverse and second vertical instantaneous velocities v and w_2 are calculated using receivers 2 and 4. With a sufficient sampling time (at least 3 minutes), time-average velocities can be computed ($\overline{u}$, $\overline{v}$, $\overline{w_1}$ and $\overline{w_2}$) along with their associated turbulent fluctuations (u', v', w_1' and w_2'). According to device manufacturer, it is expected that $\overline{w_1} = \overline{w_2}$.

One of the advantages of this device is that the measurement is quick, at high-frequency and along a whole profile of around 3.5 cm. The ADV seems to be adapted for dynamic experiments, involving sediment transport for example. Indeed, the ADV is able to record the position of the bed using the point of maximum echo intensity received by the central transmitter. This can be useful for experiments on mobile beds. In addition, with this device it is possible to detect a grain passage and its impact on the velocity profile.

2.2.3 Laser-scanner

Tools measuring 3D bed surfaces have been recently developed, such as bed profilers, laser-scanners and stereo-photogrammetry techniques. Laser-scanner appears to be one of the most precise device for measuring bed topography (Bertin and Friedrich, 2014).

The scanControl 2900 was used in this study (vertical resolution of 2 μm

and around 1280 measurement points per laser profile, i.e 2D zone lightened by the scanner) and placed on the mobile platform to cover a large zone (Figure 2.1.2). Bed topography is determined lighting a 2D zone with a red laser. The light is reflected diffusely by the bed and detected by the device sensor. Bed elevation is estimated using the propagation time of the light from the transmitter to the bed and back to the receiver. The set of bed elevation profiles is then gathered on the same plot to draw bed topography (Figure 2.2.3). The signal is able to cross the water surface but its accuracy is largely reduced under water. Indeed, a part of the red light can be reflected by the water surface or absorbed by the water. This problem is accentuated if fine particles are present in the water. In this study, topography measurements were conducted before and after experiments (i.e. when the water was drained). In some locations, measurements were repeated to check bed elevation profile overlapping (Figure 2.2.3).

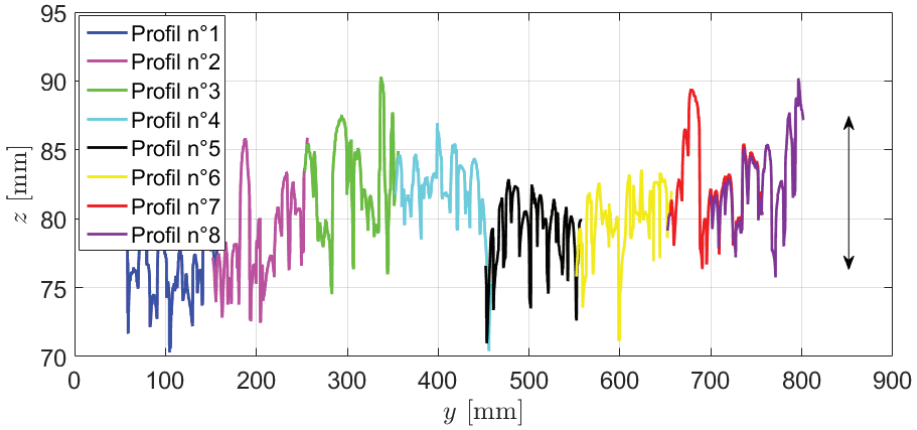

Figure 2.2.3: Initial topography of a transect located at around 8.6 m from the upstream end of the flume of a loose gravel bed. Each color corresponds to one profile measured using the laser scanner. The line with the double black arrows informs about the typical size of the used sediment.

2.3 Bed material characteristics

2.3.1 Grain size characteristics

Different sediments were used to create beds within the flume. Bed materials were chosen to be consistent with those found in mountain gravel-bed rivers, namely with a wide range of grain sizes. In this study, we chose to study bimodal materials as well as unimodal material for reference. In the following, D and d denote diameters of the coarse and fine sediments of the bed material, respectively.

Unimodal beds were composed of moderately sorted gravel particles (G). Bimodal beds were made of the same gravel matrix infiltrated with fine sediments. Three types of fine sediments were used: two were cohesionless (sand (S) and artificial fine sand (FS)), and one was cohesive (medium silt (Ms)).

Cumulative grain size distributions and main characteristics of the used sediments are presented in Figure 2.3.1 and in Table 2.1, respectively. Gravel particles, originally from crushed rocks, were quite angular with $D_{50} = 6.8\,\mathrm{mm}$ (where D_i is the diameter such as, i % of grains are finer by weight) and with a relative density of 2.65. Sand particles were well-sorted and natural, with $d_{50} = 813\,\mu\mathrm{m}$. Fine sand (FS) particles consisted of non-cohesive glass beads with $d_{50} = 66\,\mu\mathrm{m}$. Medium silt (Ms) particles were formed of cohesive glass powder with $d_{50} = 40\,\mu\mathrm{m}$. Sizes of FS particles and Ms particles were similar but the two types of fine sediments were different in nature (cohesive or not).

The grain size distribution (GSD) of the fine sediments was obtained using a laser granulometer (CILAS 1190). The GSD of the gravel particles was determined by sieving three gravel samples of 1 kg each.

Photographs were taken to show shapes of the different sediments (Figure 2.3.2). Post-processing these images with ImageJ software, several shape indexes were calculated. Around fifty particles of each sediment material were analysed to get statistically relevant indexes. It is important to precise that the analysis were done in 2D. We neglect the grain thickness and assume that the grain is orientated in a way that we have access to its major (a_g) and minor axes (b_g). It is common to use the circularity index (C_I), the aspect ratio (A_R) and the roundness index (R_I) to characterize a particle

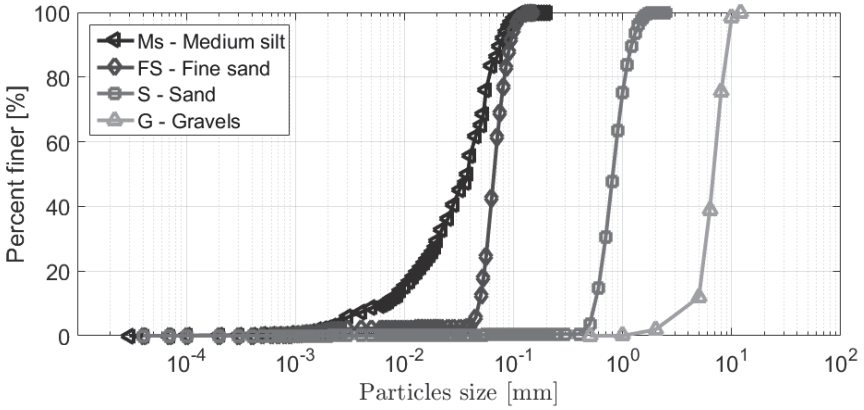

Figure 2.3.1: Cumulative GSD of the different sediments used in this study.

Table 2.1: Main characteristics of the sediments.

Grain	D_{16}, d_{16} (mm)	D_{50}, d_{50} (mm)	D_{84}, d_{84} (mm)	σ_g (-)	w_s (m/s)	C_I (-)	A_R (-)	R_I (-)
G	5.13	6.8	8.78	1.3	0.34	0.84	1.4	0.71
S	0.602	0.813	1.12	1.4	0.11	0.84	1.5	0.70
FS	0.051	0.066	0.087	1.3	$3.6.10^{-3}$	0.99	1.0	0.97
Ms	0.0097	0.040	0.067	2.6	$1.3.10^{-3}$	0.75	1.8	0.63

D_i and d_i are the coarse or fine diameters such as i % of grains are finer by weight,respectively [mm]; σ_g is the geometric standard deviation ($\sigma_g = \sqrt{D_{84}/D_{16}}$); w_s is the settling velocity computed with Soulsby (1997) Equation; C_I is the circularity index; A_R is the aspect ratio; R_I is the roundness index.

shape (Blott and Pye, 2008; Durafour et al., 2015). These parameters are given by the following equations:

$$C_I = 4\pi \frac{A}{P^2} \tag{2.2}$$

$$A_R = \frac{a_g}{b_g} \tag{2.3}$$

$$R_I = \frac{4A}{\pi a_g^2} \tag{2.4}$$

where A is the area of the particle projected on the image, P is the perimeter of the projected area of the particle, a_g and b_g are the major and minor axis of the ellipse fitting the grain shape, respectively.

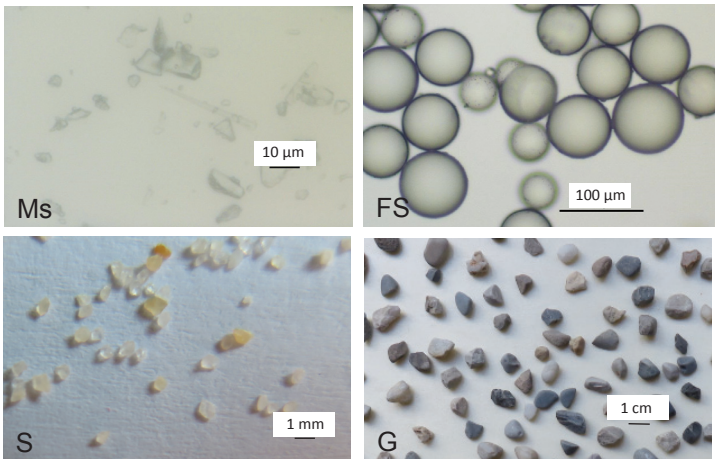

Figure 2.3.2: Photographs showing the particle shape of each used sediment material. Photographs of Ms and FS were taken with a microscope.

The circularity index measures the 2D grain shape deviation from a perfect circle (i.e. changes in form, symmetry or grain roughness). $C_I = 1$ is associated to a perfect circle. In case $C_I \approx 0$, this indicates an increasingly distorted shape. The aspect ratio is related to the grain elongation ($A_R > 1$), representing the ratio between the major and minor axes of the particle fitted ellipse. The roundness index R_I defines the sharpness of the grain (particle edge roughness) independently of its global form. $R_I = 1$ corresponds to a smooth grain. The lower R_I is, the rougher the grain is.

2.3.2 Geotechnical properties

Table 2.2 recaps the geotechnical properties of the used sediments or associated mixtures (porosity, permeability, hydraulic conductivity, consolidation, permeability Reynolds number). In this study, we will see that sediments in a gravel-sand bed rivers are not homogeneously distributed across the vertical direction. That is why, average geotechnical parameters of sand and gravel-sand mixture are not detailed in Table 2.2.

Properties of G/FS and G/Ms mixtures were determined assuming the bed matrix is composed of gravel particles in which fine sediments are in-

Table 2.2: Geotechnical characteristics of the studied mixtures.

Sediments	p_X [-]	k [m^2]	K_h [m.s^{-1}]	$C_{u\text{-sat}}$ [kPa]	$C_{u\text{-20-30\%}}$ [kPa]	Re_k [-]
G	0.42	$3.6.10^{-8}$	0.35	0	0	15.7
FS	0.40	$3.4.10^{-12}$	$3.4.10^{-5}$	0	11-12	0.15
Ms	0.56	$3.4.10^{-12}$	$3.3.10^{-5}$	2.4-28	250-500	0.15
G/FS	0.17	$1.9.10^{-11}$	$1.9.10^{-4}$	/	/	0.36
G/Ms	0.23	$6.7.10^{-11}$	$6.7.10^{-4}$	/	/	0.68

p_X is the bed porosity; k is the bed permeability; K_h is the hydraulic conductivity; $C_{u\text{-sat}}$ is the bed consolidation measured for water-saturated bed; $C_{u\text{-20-30\%}}$ is the bed consolidation measured when the bed water content is about 20-30 %; Re_k is the permeability Reynold number.

filtrated, clogging all the gravel pores. Porosity of unimodal bed materials were estimated by measuring the ratio V_v/V_t (where V_v and V_t are the void-space and total volumes (void + solid) of the sediment sample, respectively). Porosity of sediment mixtures were calculated using Equations 2.5 and 2.6.

$$p_m = p_G - f_{\max} \tag{2.5}$$

where p_m is the mixture porosity, p_G is the gravel porosity and $f_{\max}$ is the maximum fine sediment content that can contain the gravel pores (Ridgway and Tarbuck, 1968). $f_{\max}$ value is calculated following Leonardson (2010):

$$f_{\max} = p_G(1 - p_f)\left[1 - 2.35\frac{d_g}{D_{15}} + 1.35\left(\frac{d_g}{D_{15}}\right)^2\right] \tag{2.6}$$

where p_f is the fine sediment porosity and d_g is the fine sediment geometric diameter.

Bed permeability k was computed with the Kozeny-Carman relation:

$$k = \frac{p_X^3}{180(1 - p_X)^2} D_{gX}^2 \tag{2.7}$$

where p_X is the porosity of the sample and D_{gX} is the geometric diameter of the sample.

Hydraulic conductivity K_h was deduced from k (i.e. $K_h = kg/\nu$). The

permeability Reynold number, Re_k, was determined to classify the beds as permeable or impermeable and to characterize their influence on the flow structure (Breugem et al., 2006; Manes et al., 2009):

$$Re_k = \frac{\sqrt{k}u^*}{\nu} \tag{2.8}$$

where u^* is the friction velocity ($u^* = \sqrt{ghI_b}$). In Table 2.2, u^* was calculated for a standard case where h =0.07 m (the water depth) and I_b =0.01 (the global bed slope). The latter were typical values in our experiments. Values of Re_k are not constant in our experiments, since u^* varies; nevertheless they stay close to this first approximation.

For large Re_k ($>>1$), the bed behaves like a permeable bed. For $Re_k < 1$, the bed acts like impermeable bed. In our study, G/FS and G/Ms beds were considered impermeable whereas gravel beds were permeable.

Consolidation of fine sediments, C_u, was measured in the laboratory of Irstea Aix-en-Provence using two standardized mechanical tests: a penetrometer (French norms, XP CEN ISO/TS 17892-6, 2006) and a scissometer tests (French norms, NF P 94-072, 1995). In the penetrometer test, C_u corresponds to a dynamic penetration resistance, whereas in the scissometer tests, C_u is the sediment resistance to a rotational moment.

The penetrometer was composed of a metallic rod on which a standard cone was fixed as well as different masses according to the presumed sediment resistance (Figure 2.3.3a). The rod could translate vertically. Before starting the test, the cone tip was placed carefully on the sediment sample surface. Then, the rod was released and its fall distance was measured. C_u was computed using Equation 2.9.

$$C_u = \frac{f_c M_p g}{h_p^2} \tag{2.9}$$

where f_c is a cone factor specified by the norm, M_p is the mass penetrating in the sample (rod, cone and masses) and h_p is the penetration distance.

The scissometer was constituted of a reel fixed on a long rotative rod (Figure 2.3.3b). The reel was composed of 4 blades. The reel was inserted vertically in a fine sediment sample before rotating the device. A torsional

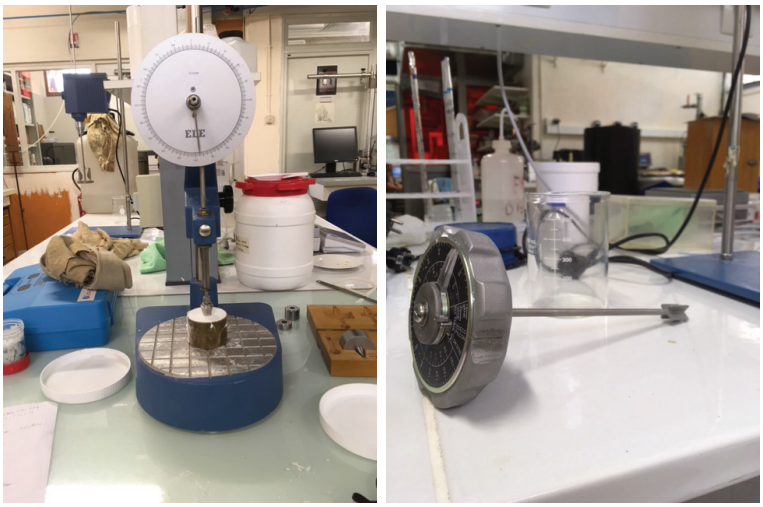

(a) Penetrometer **(b)** Scissometer

Figure 2.3.3: Devices used for measuring cohesion: (a) penetrometer and (b) scissometer.

moment was measured according to the imposed maximal angle of rotation ($\theta_{s\text{-max}}$). C_u was calculated as follows:

$$C_u = \frac{T_{s\text{-max}}}{\pi(0.5H_sD_s^2 + D_s^3/6)} \tag{2.10}$$

where $T_{s\text{-max}}$ is the maximal torsional moment applicable on the sample ($T_{s\text{-}max} = k_{\text{scisso}}\theta_{s\text{-max}}$), $\theta_{s\text{-max}}$ is the maximal rotation angle, k_{scisso} is the spring stiffness, H_s is the scissometer height and D_s is the reel diameter.

C_u reported in Table 2.2 are averaged values given by the two different tests. Tests were conducted on water-saturated ($C_{u\text{-sat}}$) and low water content ($C_{u\text{-20-30\%}}$) sediment samples. Values presented in Table 2.2 show that gravel, sand and fine sand particles are non-cohesive in comparison to the medium silt sediment. The consolidation increases with a decrease in moisture content. For Ms, C_u reaches values similar to those characterizing soft rocks ($C_u \geq 250\,\text{kPa}$) when the water content is low.

Chapter 3

Experimental set-up

3.1 Protocol introduction

In the past century, channel experiments were largely used to study and understand sediment transport. Experimental approaches were often chosen as the procedure and control were easier than in field campaigns (Garcia, 2008). The interest of using laboratory experiments is linked to the possibility of isolating a process controlling the others. However, the main limit is associated to the difficulty to reproduce conditions close to real rivers. In our protocol, particular attention was paid to approach closely regulated mountain rivers.

The transport of coarse particles moving as bedload (e.g. gravels, cobbles) was largely studied (Buffington and Montgomery, 1997). Historically, experiments were just performed on uniform sediments assuming that the bed material was mono-disperse (i.e. with a single representative particle size). Potential interactions between diverse grain size fractions were ignored. Lots of sediment transport capacity formulas were derived from these experiments (Meyer-Peter and Müller, 1948; Fernandez - Luque and van Beek, 1976; Parker et al., 1982, among others) and applied on rivers. Their uses became rapidly questioned for river beds composed of poorly or moderately sorted sediments.

Bedload transport for non-uniform sediments was then investigated (Parker and Klingeman, 1982; Proffitt and Sutherland, 1983; Wiberg and Smith,

1987; Wu et al., 2000), but still remains not fully understood. Numerous mechanisms are involved making its understanding difficult. Several experiments were conducted on disperse unimodal (Hassan and Church, 2000; Hassan et al., 2006; Guney et al., 2013; Ancey et al., 2015) and bimodal / multimodal bed material (Jackson and Beschta, 1984; Ikeda and Iseya, 1988; Wilcock and McArdell, 1993; Wilcock et al., 2001; Wilcock and Crowe, 2003; Curran and Wilcock, 2005; Curran, 2007; Jain and Kothyari, 2009; Li et al., 2016). They revealed some factors impacting bedload rate, such as grain exposure, degree of bed armoring, and presence of fine sediments. Our experiment approach was motivated by quantifying and clarifying the impact of these factors to take them into account in bedload models.

In previous studies, bimodal or multimodal bed material were quite homogeneous and man-made (Ikeda and Iseya, 1988; Wilcock et al., 2001; Curran and Wilcock, 2005; Jain and Kothyari, 2009). However, fine sediment distribution within natural bed is not necessarily homogeneous. Fine sediments can infiltrate at some locations of the river bed (Wood and Armitage, 1999). The final distribution of fine particles within the bed will depend on the fine to coarse diameter ratio (Gibson et al., 2009). The formation of an infiltrated bed and the associated mechanisms were largely studied (Gibson et al., 2009; Leonardson, 2010; Wren et al., 2011; Herrero and Berni, 2016), but the impact of infiltrated sediments on bedload rate still has to be explored. That is why we chose to conduct sediment transport experiments on infiltrated beds.

Laboratory experiments are generally performed under steady state conditions. However, most of the time, natural flows are highly unsteady over time. In addition, they do not generate important coarse bedload rates, except during floods. The conditions of low bedload are the most frequent and contribute substantially to the river dynamics. We looked for the same conditions in our experiments to better mimic natural rivers. Our measurements were realized under uniform and unsteady flow conditions (hydrograph). The choice of uniform flow was made to ensure a reliable and simple measurement of the bed shear stress.

Experiments can be divided in two parts. Firstly, experiments are performed on clean gravel beds to investigate the impact of bed arrangements on bedload rate. These experiments are considered as references for the sec-

ond part. Secondly, experiments are carried out on infiltrated beds formed by either gravel and sand or gravel and silt/clay to focus on fine sediment impact on bedload rate. Gravel matrix is the same in the two parts.

3.2 Preparation of the beds

Bedload transport experiments were conducted on several types of beds approaching natural river beds: clean gravel beds (unimodal beds) and gravel beds infiltrated with fine sediments (bimodal beds). Sketches and photographs of these beds are presented in Figure 3.2.1.

In the rest of this manuscript, beds will be identified using the following nomenclature:

- *bed arrangement of the gravel matrix*: L for loose, H for hybrid or P for packed;
- *sediments forming the bed material*: G for gravel, S for sand, FS for fine sand and Ms for medium silt.

For instance, L-G refers to a loose gravel bed and H-G/Ms refers to a hybrid bed composed of gravel and medium silt particles.

3.2.1 Clean gravel bed formation

Clean gravel beds (L-G, H-G and P-G) are composed of only one class of sediments: gravels. L-G beds denote loose, random and non-organized gravel beds that were not rearranged by antecedent flows. To create L-G beds, gravels were installed manually in the flume using a large scraper to obtain a 8 cm thick and flat bed surface, parallel to the flume bottom. In most of the previous studies, experiments were performed on these types of beds even if they are not representative of natural river beds.

P-G beds refer to packed and arranged gravel beds. In contrast to L-G beds, antecedent long flows over a gravel bed were necessary to create a P-G bed. P-G beds were realized in order to better mimic arrangement of gravel bed rivers. The most suitable way to recreate natural river beds in a laboratory is probably the water-worked bed methodology proposed by

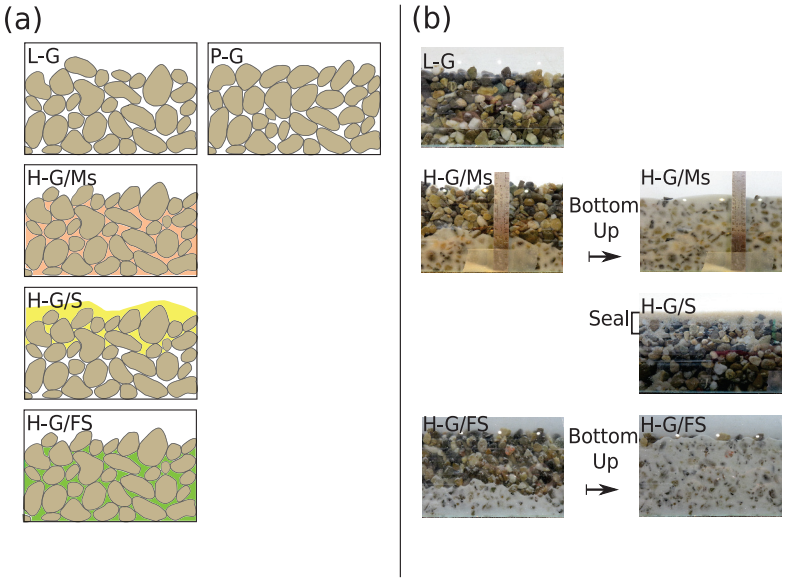

Figure 3.2.1: (a) Diagrams illustrating the different types of beds studied and (b) lateral photographs of the beds during (left) and at the end (right) of the infiltration phase.

Cooper and Tait (2009). The method consists in feeding sediments into a running flume to create the bed. Consequently, the subsurface and surface of the water-worked bed exhibit strong organization and complexity, close to those found in the field. However, such methodology is difficult to apply for forming a plane uniform bed in the channel during a limited time. Because the feeding system was not installed during the first two years of my PhD thesis, we use a different protocol in three steps using antecedent flows to form our packed gravel beds (Figure 3.2.2).

The P-G bed preparation followed three steps (see Figure 3.2.2). First, a L-G bed was installed manually in the flume (step (1)). Then, this bed was subjected to a typical flow hydrograph (step (2)) with increasing and decreasing steps of 5 L/s. At the end of this phase, a hybrid bed (H-G) was created, meaning a bed that had just experienced a flood during a short time. During step (2), the flow discharge $Q_{\text{ref-F}}$ producing a specified reference transport rate $q_{s\text{-ref}}$ at the falling hydrograph limb was determined. $q_{s\text{-ref}}$ denotes a low bedload rate that can be accurately measured considering the large uncer-

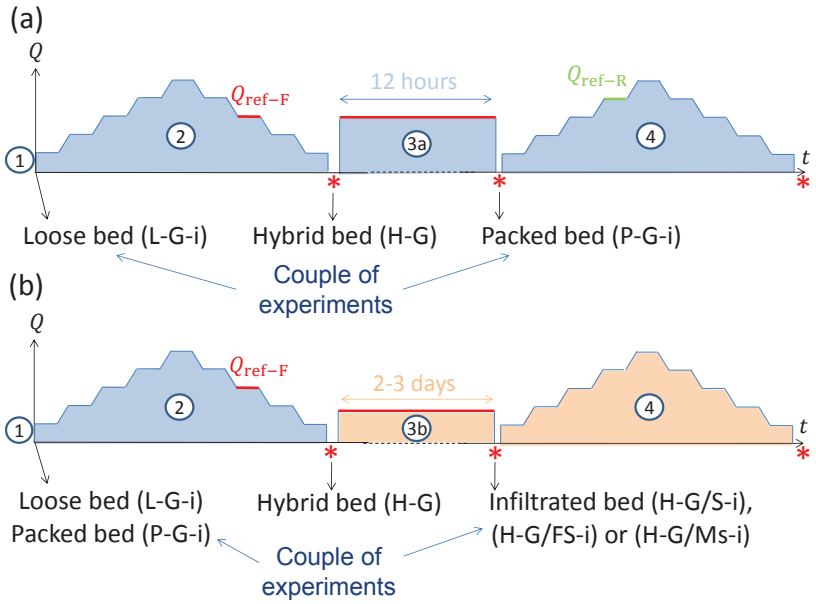

Figure 3.2.2: Experimental protocol from bed preparation to bedload experiment (a) for clean gravel beds and (b) for infiltrated gravel beds. Blue areas correspond to clear water flow while orange areas correspond to fine concentrated water flow. (1) denotes the bed installation, (2) and (4) refer to sediment transport experiments, (3a) and (3b) are bed arrangement phase and infiltration phase, respectively. The symbol * indicates a drained bed (can last a few days). $Q_{\text{ref-R}}$ and $Q_{\text{ref-F}}$ are the flow discharges for which the initiation of gravel motion (during the rising limb) and the cessation of gravel motion (during the falling limb) were observed, respectively.

tainty linked to bedload measurements at low bed shear stress. $q_{s\text{-ref}}$ was set at 1.325 $\text{g.m}^{-1}\text{.s}^{-1}$ and defines the gravel incipient motion. $Q_{\text{ref-F}}$ corresponds to the discharge for cessation of gravel motion on a hybrid bed. The reference discharge was not exactly the same between two experiments performed on a loose bed because we were not able to reproduce the exact same initial loose bed. This has been confirmed by laser scanner surveys of the bed surface. $Q_{\text{ref-F}}$ varied within the range of 60 - 65 L.s^{-1}. In the third (step (3a)), called arrangement phase, the flow recirculated at constant discharge equal to $Q_{\text{ref-F}}$ over the gravel matrix to enhance and organize a natural bed surface arrangement. This phase lasted several hours (approximately 12 hours). It was stopped when bedload rate became insignificant at the downstream end of the flume. We considered that the P-G bed is created at the end of step

(3a). Water was then drained out carefully from the flume, keeping intact the P-G bed surface organization. Since the P-G bed preparation was carried out with low gravel transport, the bed stabilized without significantly changing its longitudinal slope (variation was around 5 % on average according to the laser-scanner measurements). Laser scanner measurements also showed that grain arrangements were present on a H-G bed, although not as pronounced as for P-G bed.

Step (3a) is similar to a static armor layer creation in natural flow. In rivers, extended periods of low flows with reduced sediment supply occur. During these periods, the flow produces low bed shear stresses that entrain only the fine or unstable particles present on the bed surface. This leads to a coarsening of the bed surface, an increase in grain imbrications, and to the creation of grain patterns such as clusters or microforms (Brayshaw et al., 1983; Hassan and Church, 2000; Curran, 2010; Marion et al., 2003; Mao et al., 2011). These changes enhance the bed stability (Church et al., 1998). In our case, no strong bed surface coarsening was observed (Section 8.2.3). Therefore, we chose to qualify our beds as packed rather than armored.

3.2.2 Infiltrated gravel bed formation

Infiltrated beds (bimodal beds: H-G/Ms, H-G/FS, H-G/S) were not prepared by mixing homogeneously gravels and fine sediments as commonly done in previous studies (Hill et al., 2017). Instead, these bimodal beds were prepared by infiltrated fines into a H-G bed, thereby replicating natural vertical bed structures (Figure 3.2.1).

Figure 3.2.2 illustrates how an infiltrated bed was prepared. First, an initial bed (L-G or P-G) was subjected to a hydrograph (step (2)). That way, a hybrid bed was obtained. The bed is designated as hybrid when produced using a single hydrograph flowing either over a L-G bed or over a P-G bed. In step (3b), the infiltration phase started. We chose to carry out the infiltration phase over a hybrid bed because these beds are more reproducible in laboratory in terms of bed surface arrangements than loose beds. An infiltrated hybrid bed and a clean hybrid bed can thus be compared by focusing only on the effect of fine sediment presence and by excluding the

potential effects of changes in bed arrangement.

Two types of infiltration can be distinguished in rivers (Gibson et al., 2009): bottom-up, also called unimpeded static percolation (USP), and bridging (or sealing) (Figure 3.2.1). Bottom-up infiltration corresponds to an interstitial infiltration of fine sediments along the vertical within the bed matrix. However, bridging denotes a superficial infiltration of fine sediments in the upper part of the bed matrix. The fine distribution within the bed is controlled by the capacity of the coarsest fine grains to get through the finest coarse grains and can be predicted using the Gibson et al. (2009) criterion, which is based on D_{15}/d_{85}.

For the preparation of H-G/FS and H-G/Ms beds, a fine sediment-laden flow recirculated along the flume under flow conditions yielding no gravel motion. For these beds, the D_{15}/d_{85} ratio was larger than 150. According to Gibson et al. (2009), USP is the expected infiltration mechanism for $D_{15}/d_{85} \geq 15.4$, meaning that fine sediments should filled the beds from the bottom upwards. This behaviour was indeed observed in our experiments (see Figure 3.2.1). Part of fine suspended sediments penetrated into the gravel bed due to turbulent events and fell down by gravity (Hamm et al., 2011; Fries and Taghon, 2010). No fine particle got trapped at the surface due to the large difference in diameters between fine and coarse particles. The rest of fine suspended sediments remained in the water column and recirculated with water. In order to keep an approximately constant concentration during the infiltration phase (step (3b)), bags of fine sediments were added periodically in the water tank. The infiltration phase stopped when the bed was fully clogged, i.e. gravel matrix pores being fully filled by fines. The flow discharge was then cut off and the bed was carefully drained.

During the infiltration phase, photographs were taken at several locations along the flume length to evaluate the height of fine sediments infiltrated within the matrix over time and to verify the clogging. When the infiltration height was stable over time and reached the bed surface, we assumed that the bed was fully clogged (Figure 3.2.1). This assumption was verified in some dedicated experiments with combined in-bed samplings (cylinders). Cylinders were disposed into the beds at several locations and were filled with gravels before starting the bed preparation and the infiltration phase.

They were made of a 1 mm mesh grid allowing pore flows to pass through the gravel matrix. Cylinders were infiltrated in the same manner than the rest of the bed matrix. When the bed was clogged, water feeding was stopped, bed was carefully drained and cylinders were removed. A geotextile material placed initially at the cylinder bottom avoided fine sediment loss during the extraction from the bed. Vertical fine sediment contents within the gravel matrix, f, were calculated weighting each centimeter layers of the cylinders before and after washing gravels from fine sediments ($f = M_f/M_{\text{sample}}$, where M_f is the fine sediment mass in the sample and M_{sample} is the total sample mass). These contents were then compared to the maximal fine sediment content $f_{\max}$ that can accumulate the pores of the gravel matrix (Leonardson, 2010). When $f_{\max}$ was reached, the bed was considered fully clogged. $f_{\max}$ equals to 0.24 and 0.18 for FS and Ms sediments, respectively. Cylinder results showed that fine content vary between 0.15 at the surface to 0.24 at the bed bottom for FS sediments and between 0.14 at the surface to 0.18 at the bed bottom for Ms sediments. The lower bed parts were effectively clogged. However, the near bed surface was difficult to clog. In this region, flows turbulence was probably too strong avoiding fine particle settling. Figure 3.2.3 shows cylinder results and associated photograph analyses of a bed fully clogged with FS sediments. Fine content were measured twice: after one day of infiltration ($\approx$ 8 hours) and at the end of the infiltration (3 days $\approx$ 21 hours)), at two locations: around 6 and 9 m. The fine sediment height was deduced from photographs taken at the same location of the cylinders. Taking the stability of infiltration height as a criteria for characterizing a fully clogged bed was quite verified in that case.

For the preparation of H-G/S bed, a feeding system located at the flume entrance was used because sand was too coarse to recirculate within water. The feeding system supplied sand continuously and uniformly across the channel width. During step (3b), sand moved as bedload along the flume. Sand particles entered into the gravel matrix but were quickly trapped within the gravel pore spaces near the bed surface, thereby blocking infiltration deeper into the substrate and creating a bridge (or seal). This behaviour is consistent with Gibson et al. (2009) findings stating that bridging should occur for $D_{15}/d_{85} \leq 10.6$ (for the present H-G/S bed, D_{15}/d_{85} was equal to

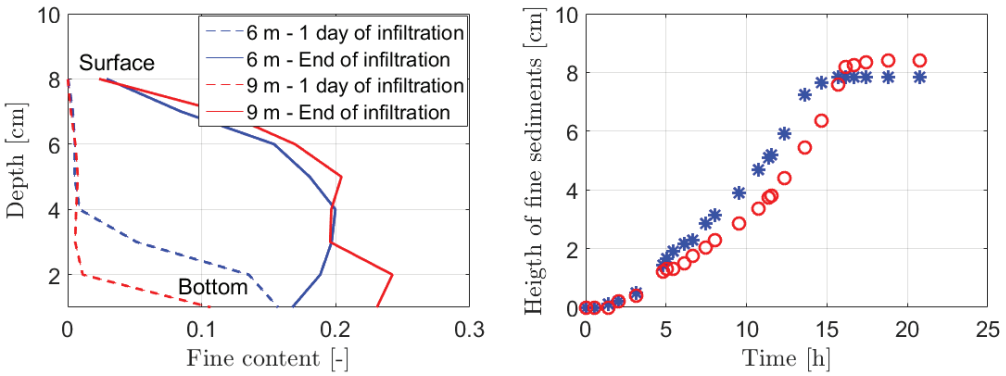

(a) (b)

Figure 3.2.3: (a) Fine content evolutions within the gravel bed deduced from cylinder measurements and (b) height of fine sediment infiltrated during an infiltration phase deduced from photograph analysis. Cylinders were located at 6 and 9 m from the flume upstream end. Photograph were taken at the same locations.

4.5). Step (3b) was stopped when a sand bridge at the surface was stable along the flume length. Flow and sand feedings were cut off and the bed was carefully drained. The stability was verified using photographs taken during the experiments which enabled to evaluate the temporal evolution of the infiltration depth. In case of sand presence, cylinders were not used because their analysis was subjected to large uncertainties.

3.3 Protocol for the sediment transport experiment

A sediment transport experiment consists in operating the flume with a stepped flow hydrograph while collecting transported gravel periodically at the flume downstream end, and while performing several hydraulic measurements (see Figure 3.2.2, step (2) and step (4)). Each experiment was denoted with its bed nomenclature completed by an experiment number i (Table 3.1). Two experiments sharing the same experiment number refer to one experiment couple, corresponding to two tests performed successively with no manual gravel bed re-installation. For example, a sediment transport

experiment conducted on a loose bed (step 2 in Figure 3.2.2) that was performed before a bed arrangement phase (step (3a)) forms a couple with the following sediment transport experiment performed on a packed bed (step 4) (e.g. L-G-1 followed by P-G-1). Similarly, two experiments conducted before and after the infiltration phase form a couple (e.g. L-G-5 and H-G/MS-5).

For all these experiments, the channel slope was set to 1 %. The selected hydrographs simulate unsteady flow events, and are characterized by symmetrical rising and falling limbs with steady and uniform flow intervals of 15 - 20 minutes and flow transitions of 5 minutes. The hydrographs are not continuous for practical reasons. Indeed, constant discharge plateaus were necessary to carry out a large number of measurements (e.g. water depth along the channel, local velocities and gravel transport rates) in a minimum of time. The hydrograph plateaus were chosen to be much shorter than the characteristic time for bed arrangement (several hours) (Church et al., 1998). That way, it is expected that the gravels will behave the same way as if the flow was truly unsteady. The flow should be unsteady from the point of view of the gravel sediments. It could be therefore interesting to perform experiments of gravel transport under continuous flow conditions (hydrographs without steady plateaus) and compare the bedload rate obtained in this case with the one obtained under discontinuous flow conditions. That way, one could verify that the chosen hydrograph does not impact the gravel behaviour. Similar hydrographs (i.e. magnitude, duration and sequencing) were used for all experiments in order to compare them, while isolating bed topography influence or fine sediment effect (see Appendix A). The hydrographs for experiments H-G/S-7 and H-G/Ms were slightly modified. For H-G/Ms experiments, the peak discharge of the hydrograph was increased because the presence of Ms particles reduced the gravel rate. For H-G/S-7, the hydrograph was reduced in time and magnitude because bedload rates were too high due to the presence of sand particles. Steady flow intervals and flow transitions were of 8 minutes and 4 minutes, respectively.

Before starting each sediment transport experiment, the surface of the studied bed was photographed and scanned. That way, a general view of the initial bed morphology and bed composition was obtained. Bed surface parameters (e.g. roughness, structure lengths, gravel preferential orientation)

were calculated using the laser-scanner data and the method presented in Section 5. Bed elevations were also measured with US at the centerline.

During the experiments, transported gravels were collected manually in the large rolling sieves and periodically (every 5 minutes or 4 minutes for H-G/S-7 experiment) at the downstream end of the flume. The transported gravels were then dried and weighed to deduce bedload temporal variations (per unit width), $q_s(t)$ (see Section 4.1). Level of the water surface was measured with ultrasonic sensors during each hydrograph plateau at every meter along the flume centerline; the averaged water depth h was then calculated. Two or three velocity measurements were made per steady hydrograph plateau at specific locations (around 7, 11 and 15 m) using the ADV located on the mobile platform (Figure 2.1.2). Locations were carefully selected to ensure a fully developed flow and to avoid the effects of the upstream end of the flume. The ADV sampling time was set to 3 minutes to have enough and a sufficient amount of data points for computing time-average velocities. During experiments involving fine sediments, side-view photographs were taken at 5 locations along the channel length to observe the fine sediment evolution within the bed and water column. The 5 locations were at around 7 m (right and left flume sides), 11 m (right and left flume sides) and 15 m upstream of the beginning of the channel. Photographs were taken at a 15 min frequency. The two sides of the channel were monitored to verify that the bed evolution was similar along the channel width. The fine sediment concentrations in the water column were measured in experiments involving Ms or FS fine sediments during every hydrograph plateaus. Samples of suspended material were taken simultaneously at the upstream and downstream ends of the flume. They were filtrated and weighed in our laboratory to obtain the fine particle concentration.

At the end of the sediment transport experiments, the bed was drained and a topographic survey and series of bed surface photographs were carried out to detect changes between initial and final bed states.

A total of fifteen bedload experiments were carried out among which ten were realized to investigate bed arrangement impact and five were conducted to examine the fine sediment effects. It important to know that these experiments are expensive in time and staff. Indeed, it takes one month to

realize an experiment couple (installation, bed creation, sediment transport experiment, cleaning, bedload sample analysis) and at least three people are necessary to perform a sediment transport experiment.

During the bedload transport experiments, we choose the shortest bedload sampling time possible for this installation in order to have the quasi-instantaneous bed response to flow change. Indeed, it is known that q_s highly fluctuates over time and that the results will probably depend on the selected bedload sampling time (Recking et al., 2012). This statement was verified by conducting complementary experiments at constant discharge during several hours and evaluating q_s variability according to different averaging time (Figure 3.3.1). Figure 3.3.1a shows that the bedload rate fluctuates over time and decreases significantly until reaching a stabilization zone in conditions of gravel starving. Once this stabilization zone is reached, the bed is considered arranged, armored or packed. Figure 3.3.1b presents the mean bedload rate computed over different times of bedload collection (from 5 min to 240 min). Mean bedload rate is highly sensitive to the sampling time. Due to the decrease in gravel rates, q_s can vary until more than 50 % if the sampling time is sufficiently long in comparison to the value obtained with a sampling time of 5 min. In our sediment transport experiments, steady hydrograph plateaus were sufficiently long to collect 3 or 4 bedload samples (except for H-G/S-7 experiment where only 2 samples were collected) and still short enough to minimize bed rearrangement. Repeating the measurements enabled to get reliable bedload data while detecting part of q_s time variability.

In our study, we characterize the gravel incipient motion using the gravel flux. The onset of gravel motion is assumed to occur when the gravel rate reaches a reference value. We set the reference transport rate for gravels at $q_{s\text{-ref}} = 5{\times}10^{-7}\,\mathrm{m^2/s}$ (=1.325 g/m/s). This arbitrary value is the same for all the experiments in order to compare them. The associated dimensionless bed shear stress is referred to the reference dimensionless bed shear stress τ^*_{ref}. It is clear that $q_{s\text{-ref}}$ should be adapted if another sediment was studied. For example, USWES (1935) studied sand sediments and related their onset of motion to an arbitrary low transport rate equal to $1.6{\times}10^{-7}\,\mathrm{m^2/s}$, which corresponds only to a few transported grains during 5 minutes in our case with gravels. To avoid this problem linked to sediment size, Parker

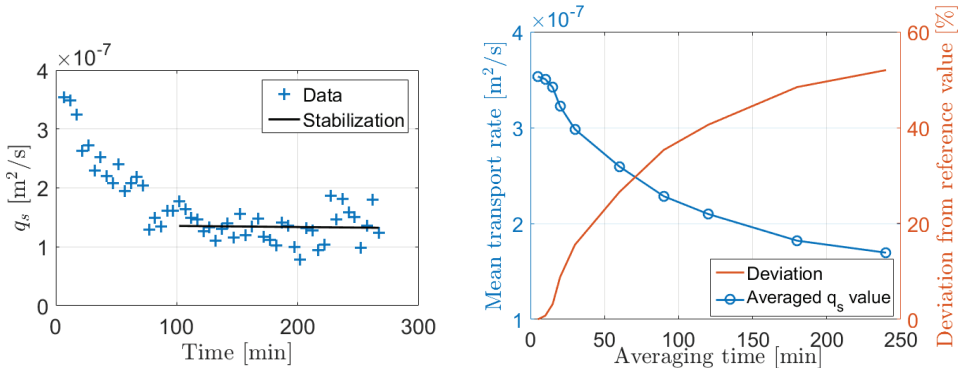

(a) Experiment results **(b)** Choice of averaging time

Figure 3.3.1: (a) Time variation of bedload rates obtained during a complementary experiment performed during more than 4 hours at constant discharge (Q =55 L/s), the bedload collection time was equal to 5 min. (b) Illustration of the mean bedload rate variations according to the chosen averaging times.

et al. (1982) suggested expressing the sediment incipient motion using a low dimensionless transport rate, $W^* = q_s^*/\tau^{*3/2}$. W^* depends on the Einstein (1942) bedload parameter ($q_s^* = q_s/(\sqrt{(s-1)gD^3})$ and the dimensionless bed shear stress τ^*. The value retained for incipient motion conditions was set to $W^* = 0.002$. Parker et al. (1982) definition was not chosen for our experiment because the transport rates associated to their dimensionless criterion ($W^* = 0.002$) were to small (of around 8×10^{-8} m^2/s) and subjected to large measurement uncertainties in our experiments. Our choice of taking $q_{s\text{-ref}}$ =5×10^{-7} m^2/s as the reference transport rate was strengthened after comparing our experimental data with the Shields curve (Figure 1.2.2). Our data agrees within 10 % of the Shields curve determined using the Soulsby and Whitehouse (1997) Equation.

Using this original protocol, we were able to measure for each experiments: the transport rate, the local bed shear stress, the global bed shear stress and the surface arrangement. Figures shown in Appendix A present typical data generated following bedload experiments. Table 3.1 recaps all the gravel transport experiments carried out during this thesis and their main conditions.

Table 3.1: Overview of all the conducted bedload experiments and their experimental conditions.

Exp.	I_c [-]	I_b [-]	Q [L/s]	h [cm]	F_r [-]	τ^* [-]	D_{50}/h [-]	Re^* [-]	c_f [g/L]
L-G-1	0.01	0.0101	45 - 70	6.6 - 8.4	0.85 - 1.16	0.058 - 0.073	0.081 - 0.10	542 - 610	0
L-G-2	0.01	0.0100	45 - 70	6.0 - 8.2	0.95 - 0.98	0.052 - 0.07	0.083 - 0.11	516 - 597	0
L-G-3	0.01	0.0100	45 - 75	6.4 - 8.4	0.88 - 0.98	0.056 - 0.072	0.081 - 0.11	533 - 605	0
L-G-4	0.01	0.0106	45 - 70	6.4 - 8.1	0.88 - 0.96	0.059 - 0.074	0.084 - 0.11	547 - 614	0
L-G-5	0.01	0.0103	45 - 75	6.4 - 8.0	0.88 - 1.06	0.057 - 0.07	0.085 - 0.11	540 - 598	0
L-G-6	0.01	0.0105	45 - 70	6.4 - 8.1	0.88 - 0.96	0.058 - 0.073	0.084 - 0.11	544 - 610	0
L-G-7	0.01	0.0106	45 - 70	6.3 - 8.3	0.90 - 0.93	0.058 - 0.076	0.082 - 0.11	544 - 623	0
P-G-1	0.01	0.0100	45 - 80	6.5 - 8.9	0.86 - 0.96	0.057 - 0.076	0.077 - 0.10	537 - 623	0
P-G-2	0.01	0.0104	45 - 75	6.5 - 8.6	0.86 - 0.95	0.059 - 0.077	0.079 - 0.10	547 - 624	0
P-G-3	0.01	0.0104	45 - 75	6.7 - 8.9	0.83 - 0.9	0.06 - 0.08	0.077 - 0.10	553 - 637	0
H-G/FS-8	0.01	0.0100	45 - 70	6.5 - 8.5	0.86 - 0.9	0.056 - 0.073	0.080 - 0.10	535 - 599	1.0
H-G/Ms-5	0.01	0.0105	45 - 75	6.4 - 8.6	0.88 - 0.95	0.059 - 0.078	0.079 - 0.11	547 - 629	1.5
H-G/Ms-6*	0.01	0.0104	45 - 75	6.4 - 8.7	0.88 - 0.93	0.058 - 0.078	0.078 - 0.11	544 - 628	1.7
H-G/Ms-9	0.01	0.0103	45 - 75	6.6 - 8.5	0.85 - 0.96	0.059 - 0.075	0.08 - 0.10	546 - 619	6.7
H-G/S-7	0.01	0.0091	40 - 65	5.0 - 7.2	1.07 - 1.14	0.04 - 0.056	0.094 - 0.14	447 - 534	NE

I_c is the channel slope; I_b is the bed slope; Q denotes the range of water discharge generated during the experiment; h refers to the range of water depth generated during the experiment; Fr is the Froude number; τ^* denotes the range of dimensionless bed shear stress generated during the experiment ($\tau^* = \tau/(g(\rho_s - \rho)D_{50})$); τ was calculated with the depth-slope equation ($\tau = \rho g h J$, where ρ is the water density); D_{50}/h is the range of relative roughness during the experiment; Re^* is the particular Reynolds number ($Re^* = u^* D_{50}/\nu$, where u^* was deduced from $u^* = \sqrt{\tau/\rho}$). c_f refers to the fine sediment concentration in the water. NE means that the value was not evaluated. * refers to the only experiment performed on an infiltrated hybrid bed resulted from an initial packed bed.

3.4 Link with the field

Although the objective of this study was not to scale with specific field sites, the consistence of the experimental set-up can be examined with regard to natural processes. The set-up scaled with alpine rivers in terms of Shields numbers (τ^*), relative roughness (D_{50}/h) and bed morphology planform (plane beds) (see Table 3.1). The studied flows were turbulent (Re >2000) and hydraulically rough ($Re^* > 70$). The Froude number F_r varied from 0.85 to 1.22 indicating that fluvial and torrential flows were studied. However, the used gravels were finer than the ones usually found in natural gravel bed streams with longitudinal slopes of 1 %. Median grain sizes are usually higher than 50 mm according to the river data base found on this website http://www.bedloadweb.com/data. Gravel particles were finer in our experiments because of experimental limitation in terms of maximum discharge ($Q = 110$ L/s). With coarser grains, we would not have a sufficient range of water discharge to generate measurable bedload rates. Accordingly, gravel sediments were chosen finer but still coarse enough to keep a significant size ratio between the gravel and fine sediments ensuring the fine sediment infiltration. These experimental conditions were chosen to approach the condition found on the Arc River, which is a French river highly studied in Irstea Lyon-Villeurbanne (Jodeau, 2007; Jaballah, 2013).

Chapter 4

Gravel transport measurements

In our experiments, we are interested in monitoring the gravel dynamics over various types of beds. During experiments, gravels are transported as bedload. Practical and reproducible techniques are needed in order to compare bedload rate of one experiment to another. Several methods were tested and three will be presented in details in this part. According to the technique, we will have information about the instantaneous bedload rate or about the averaged rate over different time periods (5 min or at the experiment time scale).

4.1 Bedload estimation using manual collection

Bedload rate was collected at the downstream end of the flume during a specific time period using large rolling baskets (Figure 4.1.1). The bottom of the baskets was covered with a mesh with an opening of 1 mm retaining all gravels (size range : 1 - 12 mm) while letting pass water and fine particles. That way, only the gravel particles were collected. Conditions in our experiments ensured that all gravels were transported as bedload, even the finer particles close to 1 mm. Samples of transported gravels were removed from the baskets, stocked, dried and weighed. The gravel rates is then deduced

using the following equation:

$$q_s = \frac{M_G}{T_c \rho_s W} \tag{4.1}$$

where q_s is the bedload rate per unit of width, M_G is the weight of gravels collected in the basket, T_c is the time of collection, ρ_s is the gravel density ($\rho_s = 2650\,\mathrm{kg.m^{-3}}$) and W is the channel width.

Figure 4.1.1: Large rolling baskets used to collect gravel rates.

This technique requires at least two persons and is time and effort consuming. Main advantage of this method stands in the fact that very small as well as high transport rates can be quantified accurately. However, the major drawback is that no instantaneous values of transport rate can be estimated.

4.2 Bedload estimation using video measurements

This method is based on image processing analysis of recorded frames of transported gravels. It was developed for two main reasons:

- case 1: to record the transport rate at the downstream end of the flume and compare it to the results of the manual collection;
- case 2: to measure the transport at different locations within the flume and verify the uniformity of bedload during our experiments.

The image processing analysis code was written in Matlab. The following parts detail the measurement procedure (Section 4.2.1), the method to compute bedload rate using recordings (Section 4.2.2) and the validity tests of the method (Section 4.2.3).

4.2.1 Measurement procedure

In case (1), a video camera was placed above the channel at the downstream end of the flume, recording the gravel movement over the long weir (Figure 4.2.1a). The weir was uniformly white facilitating the detection of the particles. The lighting was not optimal and non-homogeneous in the laboratory. Different sources of light created shades and object reflections in the recorded frames making difficult the particle detection. To limit this problem, black plates were installed on the flume sides and white light was projected from above with a certain angle.

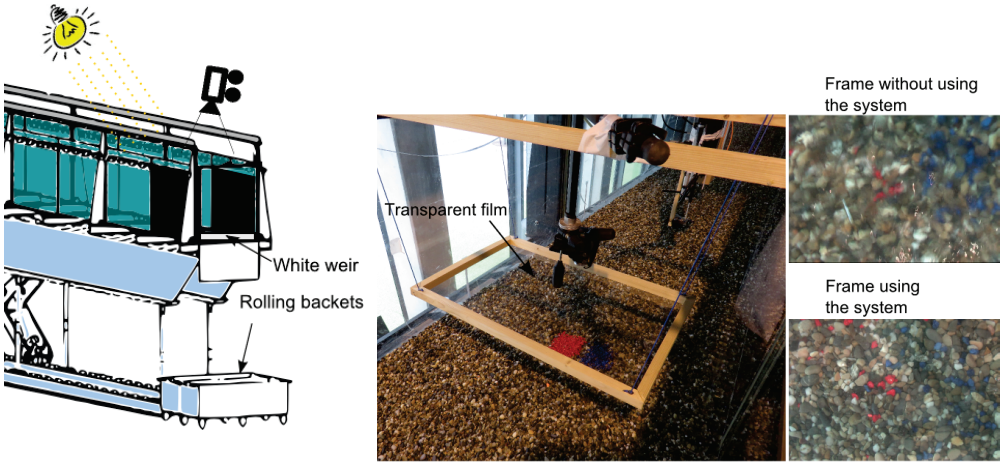

(a) case 1 **(b)** case 2

Figure 4.2.1: Installation for video measurements in case 1 (a) showing the video camera and light orientation and in case 2 (b) showing the system for avoiding free surface problems.

In case (2), a video camera and lights were installed in the same manner as described previously. The installation was moved at several locations of the channel during experiments (upstream, middle and downstream ends of

the flume). Transported gravels were not discernible from gravels forming the bed matrix because of the free-surface movements and light reflections. A system composed of a transparent film tightened and fixed to a wood-frame was built to override the free surface effect (Figure 4.2.1b). The system was delicately placed on the free surface before recording the transport rate.

4.2.2 Image processing analysis

In order to be post-processed, the recordings were separated in a succession of images. The time interval between two images was chosen in order to detect the particles movement and in order to limit the computation time: Δt_{image}=1/10 s, so 10 images per second. In order to convert pixels values in meters, it is important to place a scale in the video camera range. The video camera was placed accurately parallel to the flume bottom in order to avoid a step of image ortho-rectification. In function of the type of objective used, images may require rectification or correction from potential distortion. The images were then loaded in a Matlab code. The code was based on 3 steps:

- detection of the number of particles in motion,
- particle velocity calculation,
- sediment transport computation.

Number of moving particles - The process for evaluating the number of moving particles between two successive images is presented in Figure 4.2.2. First, a subtraction between two successive images was made. A new image was obtained showing zones of movement (colored zone) and a zone without movement (black zone). Colored areas correspond to particles either leaving the image or arriving. Using a color-threshold, two images were generated: one representing the arrived particles on the video camera range and one representing the left particles. These images were transformed into gray-level images in order to regionalize each object. Regionalization consists in finding pixels that belong to the same object and attributed them a single identifier. This leads to the creation of a region. Code focused on left particles because they were in motion. Indeed, arrived particles may

just represent the new location of the left particle. By counting the regions on the left particle image, the number of moving particles can be deduced. False regions corresponding to image noises (shadows, water-bubbles) were detected and removed automatically using a threshold filter on the area values of the obtained regions. Center coordinates of real regions were then saved.

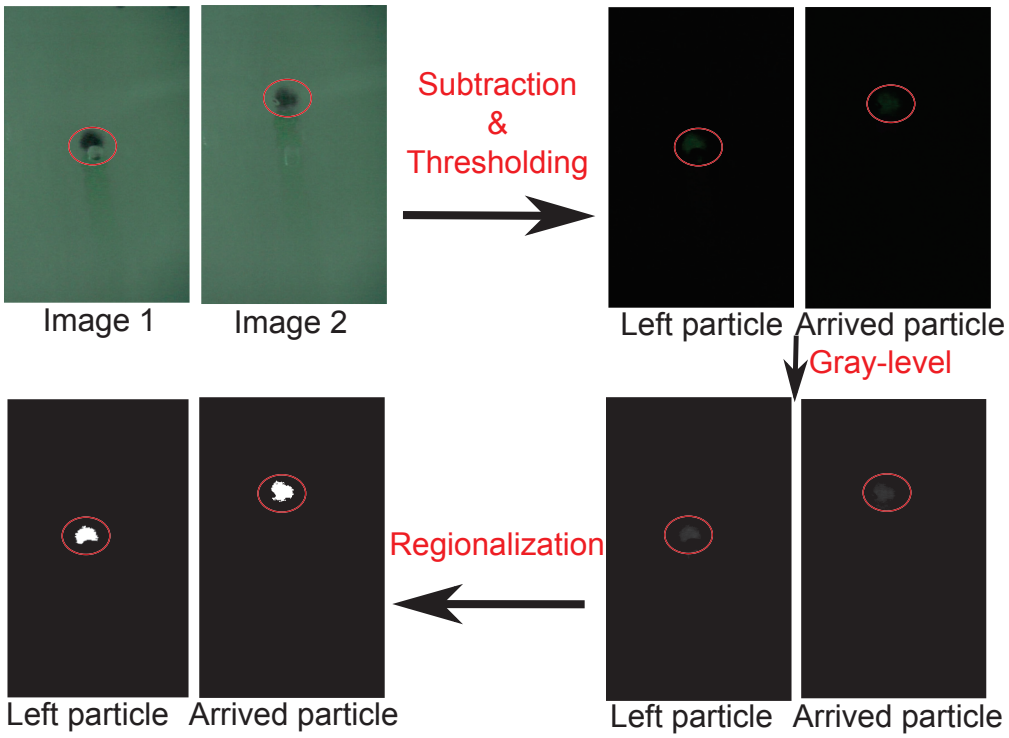

Figure 4.2.2: Illustration of the process for determining the number of moving particles between two successive images.

Particle velocity calculation - In a second step, the velocity of each particle in motion was calculated. To do so, we used the coordinate of each movement regions (left and arrived particles). Centers of left particles were compared with centers of arrived particles. If coordinates centers were close, we assumed that there were the same particles. The arrived particle was in fact the new position of the left particle. This assumption was valid if the movement between two frames was sufficiently low. A visual verification of this assumption was conducted on several random frames and was conclusive. Once left and arrived particles were correctly associated, the distance between them were computed using their coordinates. Each particle velocity was

deducted using the ratio between the particle covered distance and the time between each image. Then, we averaged all particles velocities to obtain an average velocity of the entire studied zone for a given time ($< V_p >$).

The association between left and arrived particles was not always simple. Four cases were encountered:

- The numbers of left and arrived particles were equal to zero. In that case, we set the solid transport to zero.
- The number of arrived particles is equal to the number of left particles. In that case, no particular operation was needed. We simply associated the neighboring particles.
- The number of left particles was larger than the number of arrived particles. Some particles left the image field under the flow influence. These particle were thus not associated with arrived particles and were called single particles. Because the movement was low between two images, we assumed that a single particle had just left the camera video range. To calculate its covered distance, we created a fictive arrived particle that had as streamwise center coordinate the maximum coordinate of the studied zone (i.e. upper edge of the image) and as cross-stream center coordinate the same than the single particle (uni-directional flow). Doing so, we probably underestimated some particles velocities and consequently the transport rate. Another possibility would have been to ignore these single particles. However, because the number of particles passing through the video camera range was low, we chose to keep every particles.
- The number of left particles was lower than the number of arrived particles. This means that some new particles reached the camera video range. This time, the new arrived particles cannot be associated to left particles. We decided to associate these new particles to fictive particles that had the bottom edge of the image as longitudinal coordinate and the same transverse coordinate as the new arrived particle because the movement was assumed low between two frames and flow was uni-directional.

Sediment transport computation - The instantaneous transport rate ($q_s(t)$, where t is the time) was computed using the average particle velocity and the concentration in gravels on the movement image (ratio between detected object area and total image area) at a given time t, assuming a bedload thickness equal to D_{50}:

$$q_s(t) = C_i(t) \langle V_p(t) \rangle D_{50} \tag{4.2}$$

$$C_i(t) = \frac{n_p(t) \upsilon_G}{D_x D_y D_{50}} \tag{4.3}$$

where $\langle V_p \rangle$ is the surface average velocity of moving particles between two specific frames, C_i is the surface average concentration of moving particles on the movement image, n_p is the number of moving particles on this image, D_x and D_y are the dimension of the camera range (longitudinal and transversal, respectively) and υ_G is the equivalent particle volume (here, particles were assumed to be spherical of $D_{50} = 6.8\,\text{mm}$, $\upsilon_G = 4/3\pi(D_{50}/2)^3$).

4.2.3 Validity tests

Several tests were conducted to verify the code efficiency. First, a test was performed in ideal conditions (i.e. on a dry bed, so without effect of the water surface). The code was able to detect all moved particles. In ideal conditions, the code is thus reliable.

Secondly, specific tests in real conditions were conducted. In case 1 where video were recorded on the white weir at the downstream end of the flume, the code was able to calculate the transport rate (Figure 4.2.3). Instantaneous calculated transport rate was visually verified between images by counting by eyes the number of moving particles and measuring their covered distance. A good agreement between number of particles detected by the code and by eyes was found. In addition, calculated average transport rate was compared with the one obtained with the rolling baskets. For example during a test-experiment at water discharge $Q = 70\,\text{L.s}^{-1}$, the average transport rate calculated with the code was about $4.7.10^{-7}\,\text{m}^2.\text{s}^{-1}$ whereas the one from manual collection was about $4.9.10^{-7}\,\text{m}^2.\text{s}^{-1}$. The recording was made during 1 min 30 and the manual collection time was 3 minutes. Video

camera range did not cover the whole width channel during experiment. Calculated transport rate might be therefore underestimated or overestimated if bedload rate was not perfectly uniform along the transverse. Although the image processing analysis gave us the instantaneous transport rate, the manual technique was retained. Indeed, the time to post-process the data was too long (3 h 20 for post-processing a video of 1 min 30). In addition, the data files would have been too heavy if the entire experiment was recorded.

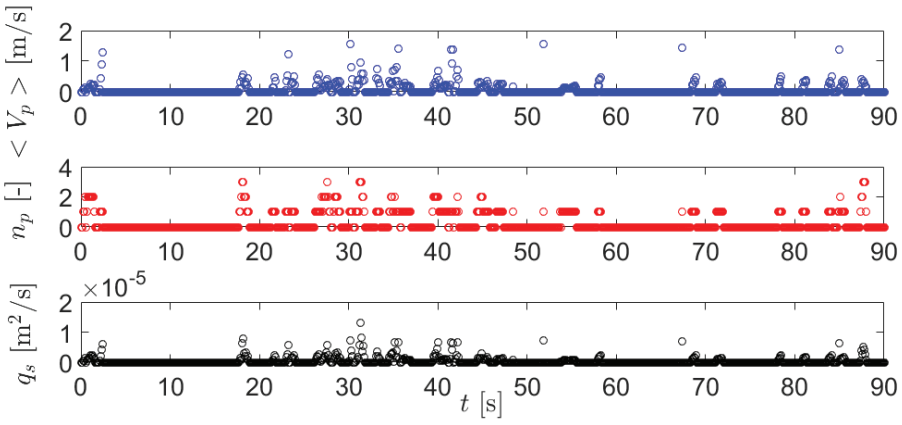

Figure 4.2.3: Results of image processing analysis of a 1 min 30 recording made during a specific test-experiment. Average particle velocity, number of moving particles, and instantaneous bedload rate are plotted as function of time.

In case 2, the code was not effective. First, the film system was difficult to adjust without disturbing bedload rate. Once it was wet, it seems that the bedload was accelerated even after profiling the wood frame of the film system. This acceleration was probably due to a compression of the water depth in the vertical direction from the film system. We decided to stop using this system and to make video measurements by eyes (i.e. recording images from above and counting the number of particles transported in the image). It was difficult with the moving free surface, especially at high flow discharges, but we managed to count moving particles and compute q_s in specific experiments to verify its longitudinal uniformity (case 2). Figure 4.2.4 shows a comparison between bedload rates obtained using the manual method at the downstream end of the flume and those obtained using the video measurements at several flume locations (around $x = 8$ m and $x = 17$ m). Sediment transport

with video measurements corresponds to sediment transport deduced from manual collection within 10 % error range. This means that gravel transport seems to be uniform along the channel at least in a large temporal averaging (1 min). However, some q_s measured with video deviates strongly from the ones obtained with manual collection (more than 50 %). These observations highlighted a problem of q_s non-uniformity across the channel width. Indeed, along the transect some preferential pathways can be created during an experiment due to the flow action. According to where the video camera was located, the transport rate could be quite different: overestimated if the video camera was located on a preferential bed pathways or underestimated if it was placed around a zone of no-movement. To avoid the transversal non-uniformity problem, we chose to focus on the manual technique (reference method), which measures q_s over the entire channel width. With material at our disposal, it was not possible to take video of the entire flume width with sufficient resolution.

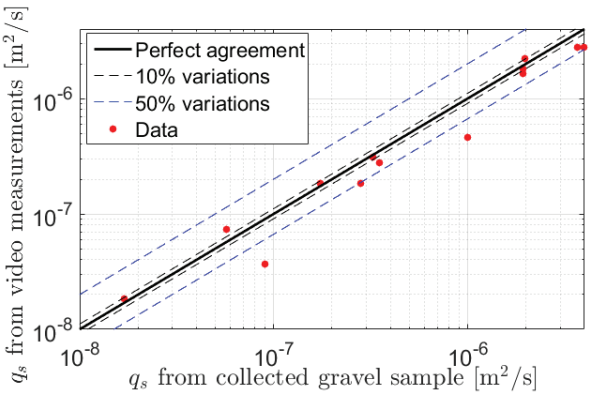

Figure 4.2.4: Comparisons between bedload rates obtained using manual measurements at the downstream end of the flume and using video measurements at several locations along the flume (case 2). Data were collected during several experiments performed on unimodal bed material.

4.3 Bedload estimation using topographic measurements

Erosion and deposition areas were detected by subtracting initial and final bed topographies (Figure 4.3.1). The total bedload rate, q_s [$m^2.s^{-1}$], was then deduced from the total gravel mass, M_{tot}, transported during an experiment:

$$q_s = \frac{M_{tot}}{T_{tot}\rho_s W} \tag{4.4}$$

where T_{tot} correspond to the time period of the sediment transport experiment and W is the channel width.

M_{tot} was estimated using the total mass of eroded (M_E) and deposited (M_D) gravel particles (Equations 4.5, 4.6 and 4.7).

$$M_{tot} = M_E - M_D \tag{4.5}$$

$$M_E = \rho_s V_E \tag{4.6}$$

$$M_D = \rho_s V_D \tag{4.7}$$

where V_E and V_D are the volumes of eroded and deposited gravels estimated from topographic measurements, respectively.

In some experiment, measurements of the quasi-totality of the bed surface were made with the laser scanner (transects of 70 cm from 1 to 16 m every 6 cm). In that case, the erosion/deposition pattern of one transect was assumed to be the same between this transect and the following one (i.e. 6 cm) in order to calculate the eroded/deposited gravel volume, V_E and V_D:

$$V_E = \sum_i 0.06(1 - p_G)A_{E\text{-i}} \tag{4.8}$$

$$V_D = \sum_i 0.06(1 - p_G)A_{D\text{-i}} \tag{4.9}$$

where i subscript denotes a specific transect and A_E and A_D are the erosion

and deposit areas of each transect, respectively:

$$A = \int_0^W (z_{b\,\text{initial}} - z_{b\,\text{final}})dy \tag{4.10}$$

When only longitudinal bed surveys were carried out, it was assumed that the same erosion/deposition pattern as the one of the center line was repeated along the channel width. Regarding Figure 4.3.1, one can see that this hypothesis is admissible. Indeed, the erosion/deposition pattern at the center line is representative to the global pattern of the channel. In that case, the volumes were estimated as follows: $V_E = A_{E\text{-c}}(1 - p_G)W$ and $V_D = A_{D\text{-c}}(1 - p_G)W$, where c subscript denotes the centerline.

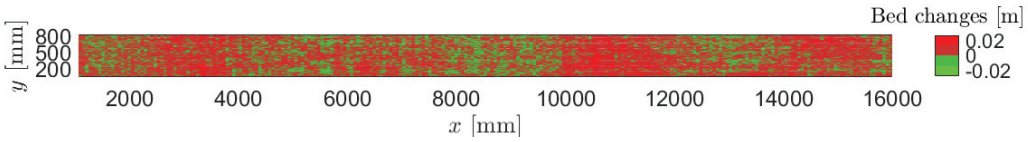

Figure 4.3.1: Erosion and deposit areas detected using laser-scanner bed surface topographies at the end of experiment conducted on a loose gravel bed (L-G-7). Red color corresponds to erosion area and green color corresponds to deposit area.

Estimations of M_{tot} were verified by comparing them with the total gravel mass collected using the manual technique. A variation of 10 - 15 % was generally found between values which also corresponds to the uncertainty of this method. For example, after the analysis of Figure 4.3.1, M_{tot} was 27 kg whereas the total gravel mass collected at the end of the channel was 30 kg. This difference could be reduced if the channel bed was totally surveyed with a higher resolution.

Chapter 5

Bed characterization

This chapter focuses on a method developed to characterize the bed with parameters describing its slope, its surface roughness, the orientation of its surface grains, the presence of fine sediments on its surface and its global arrangement. This method is based on 3D topographic bed surface measurements and considers the bed surface as a random field of bed elevations $z(x, y)$. This 3D-approach is increasingly used for gravel bed characterization (Marion et al., 2003; Aberle and Nikora, 2006; Cooper and Tait, 2009; Mao et al., 2011; Qin and Leung Ng, 2012). In this study, 3D measurements were carried out using the laser-scanner (see Chapter 2).

5.1 Digital elevation model

A digital elevation model (DEM) corresponds to a 2D or 3D-view of the bed surface elevations. DEM provides the basic data for bed characterization. Statistical tools, such as bed elevation probability density function (PDF) or variograms, were used to obtain bed characteristics (Nikora et al., 1998).

DEMs were produced from bed surface surveys covering diverse flume areas using the laser-scanner (Figure 5.1.1):

- Longitudinal DEMs representing bed elevations along a line of the center, right and left side of the channel;
- A set of transverse DEMs every 6 cm along the channel length giving

an overview of the entire bed surface and allowing for the detection of eventual bed-anomalies;

- Bed surface patch DEMs showing specific flume areas with high resolution (spacing of 1 mm in x-direction and 128 measurement points per centimeter in y-direction).

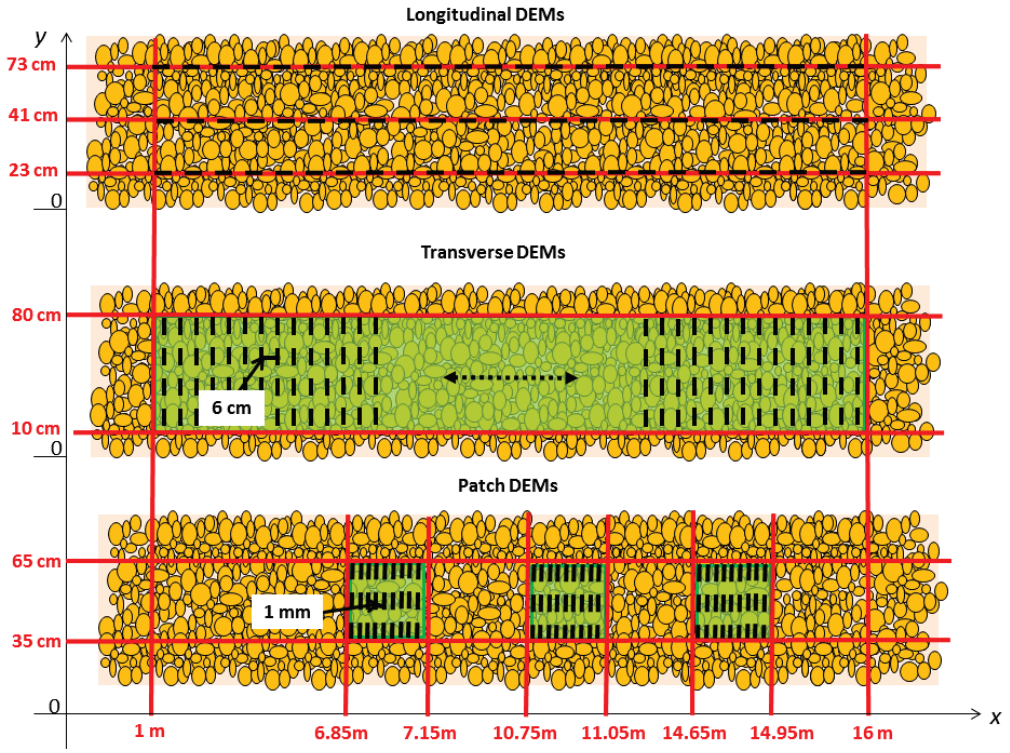

Figure 5.1.1: Schematic of the different bed surface areas surveyed by the laser-scanner as well as the measurement density.

5.2 Direct measurements

In this section, bed characteristics estimated directly from the DEM are presented. Photographs of the entire bed surface are also used to quantify the fine sediment content on the bed surface.

5.2.1 Bed slope measurements

Local and global bed slopes were estimated using longitudinal DEM measured at three locations: centerline, right and left sides of the flume. Figure 5.2.1 illustrates how the global bed slope is obtained. Data from 6 m to 16 m were fitted with a linear law. The first meters of the flume were not taken into account because they were located in an area where flow was not uniform during experiments. In addition, this area was significantly eroded during tests because of the absence of sediment feeding.

The global bed slope, I_b, was calculated using the average of the fitted longitudinal bed slopes, $I_{\text{fit},i}$, added to the channel slope value, I_c:

$$I_b = \left| \frac{\sum_{i=1}^{n} I_{\text{fit},i}}{n} - I_c \right| \tag{5.1}$$

where i refers to a specific longitudinal bed slope measurement (center, left or right side), n is the number of measured longitudinal profiles (here, $n = 3$) and I_c is the channel slope determined either by direct reading on a gradual scale located at the downstream end of the flume or by measuring the flume inclination using a ultrasonic sensor placed under the channel. The procedure was done for obtaining the initial and final global bed slopes.

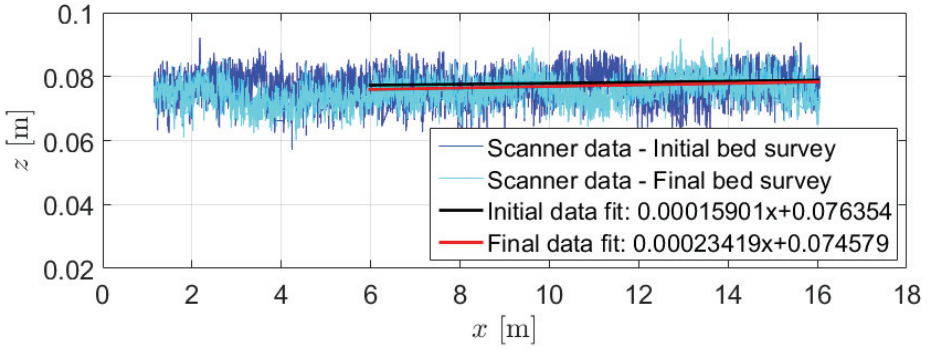

Figure 5.2.1: Longitudinal DEM showing initial and final bed profiles at the flume centerline for an experiment performed on a loose gravel bed (L-G-1). (Fits are used for determining global bed slopes.)

The local bed slopes, I_l, were computed after smoothing the laser-scanner data using a running average filter with a step of around $7 \times D_{50}$ which

smooths effectively the variation at the grain scale:

$$I_{l,jk} = \frac{z_{\mathrm{bed},j} - z_{\mathrm{bed},k}}{L_{jk}} - I_c \tag{5.2}$$

where $z_{\mathrm{bed},j}$ and $z_{\mathrm{bed},k}$ are bed levels at successive data points j and k, and $L_{j,k}$ is the longitudinal distance between them. I_l values vary largely around the mean bed slope (corresponding to the global bed slope). Figure 5.2.2 shows an example of I_l distribution for initial and final beds of an experiment performed on a loose gravel bed. The observations of the local scale inform about the grain inclination on the bed surface. The distribution of the final bed slopes is positively skewed (i.e. a larger range of positive local bed slopes), reflecting a potential grain imbrication on the bed. Grains of the bed surface overlap each other as tiles.

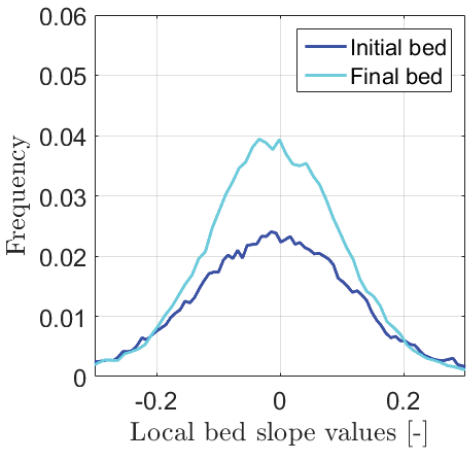

Figure 5.2.2: Example of local slope distributions computed along the channel length on initial and final beds of the same experiment as in Figure 5.2.1 (L-G-1).

5.2.2 Bed surface grain size distribution

Bed surface grain size distributions (GSD) were estimated using the Line-by-Number method (Fehr, 1987) on patch DEM images. Patch DEM images were used to estimate the GSD rather than real bed photograph for which shade and light problems were often present.

In the patch DEM images, grains were perfectly distinguishable because of the high measurement resolution (Figure 5.2.3). The Line-by-Number procedure consists in placing random lines over the bed surface patch DEM and measuring the sizes of grains in contact with these lines. This technique is non-intrusive, i.e. the bed arrangement is not modified after the measurement. Grain size measurements were made using the software ImageJ. To have representative GSD, at least 100 particles were measured per patch DEM image.

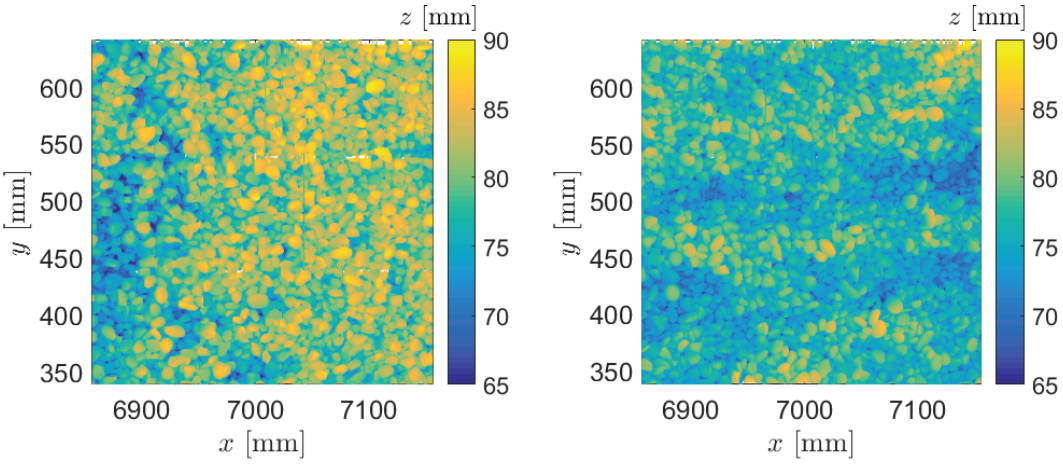

(a) Initial patch **(b)** Final patch

Figure 5.2.3: Bed surface patches DEM determined using (a) initial and (b) final bed topographic surveys of an experiment performed on a loose gravel bed at around x= 7 m (L-G-6).

5.2.3 Fine sediment content on the bed surface

Photographs of the entire bed surface were made, and then stitched together (with the software Image Composite Editor) to estimate roughly the proportions of each sediment fraction on the bed surface (fine/sand/gravel particles). Stitching was facilitating if clear patterns between photographs were recognizable. The stitched images enable to detect potential fine sediment patches formed during experiments, by eyes or using color thresholds on the images. Figure 5.2.4 shows two stitched images: one representing a gravel/sand bed and one representing a gravel/fine sediment bed.

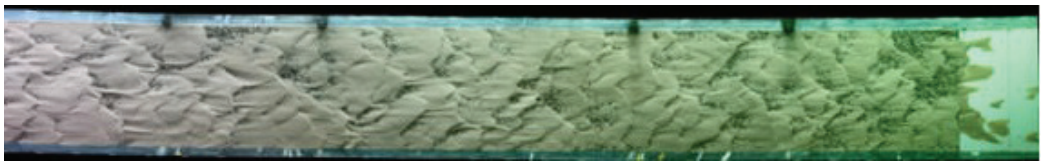

(a) Experiment with sand/gravel particles

(b) Experiment with medium silt/gravel particles

Figure 5.2.4: Stitched bed surface photographs of (a) a gravel-sand bed (H-G/S-7) and of (b) gravel-medium silt bed (H-G/Ms-6). For the sake of a better visualisation, only a part of the flume is presented here: between $x = 5\,\mathrm{m}$ from the upstream end of the flume and the downstream end of the flume (white weir).

5.3 Indirect measurements

Bed characteristics (e.g. bed roughness, bed structure, grain orientation, etc.) can be computed using statistical tools, such as the probability density function (PDF) of bed elevations around the mean bed level and variograms also called 2D-structure functions (Nikora and Walsh, 2004).

5.3.1 PDF analysis

Bed parameters deduced from the PDF are presented hereafter. Figure 5.3.1 illustrates the typical PDF obtained during experiments conducted on gravel beds with random organization. Diverse criteria can be deduced from this kind of figures, based on their shape and symmetric nature. Differences can be noticed between PDF describing the initial and final bed, which denote that bed arrangements are not the same at the beginning and at the end of the experiment.

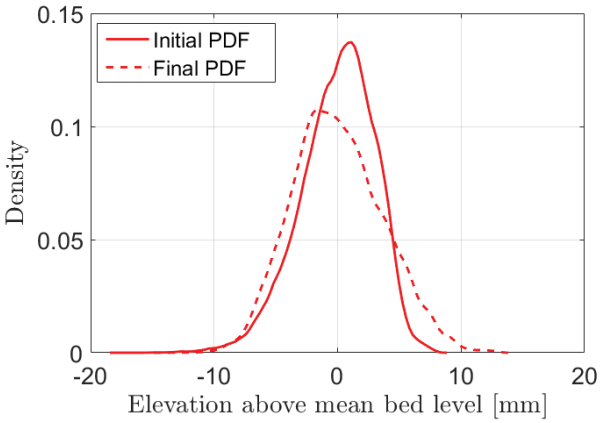

Figure 5.3.1: PDF of bed surface elevations before (initial) and after (final) an experiment performed on a loose gravel bed (L-G-2).

Roughness estimation

In our study, we chose the standard deviation σ_z of the PDF of bed elevations around the mean bed level (second-order moment) as the parameter representing the bed surface roughness. This roughness is geometric and different from the hydraulic roughness, k_s, even if a direct link probably exists between them. Lot of studies supposed that k_s is related to a geometric roughness that is often defined using a GSD characteristic percentiles (D_i) or percentile multiples of the bed material (Nikuradse, 1933; Yalin, 1977; Bathurst, 1985; Wiberg and Smith, 1991). However, using D_i as a geometric roughness means assuming that beds would have the same roughness as long as they are formed of the same grain mixture. This assumption might be verified for specific sediments involving no specific bed organization, but probably not for moderately sorted angular gravel sediments. Indeed, same gravel mixture can lead to several bed arrangements (Figure 5.3.1), having consequently different geometrical bed roughness (Aberle and Smart, 2003). The standard deviation of bed elevations seems to be a better geometric roughness indicator because can take into account potential bed arrangement changes.

Different roughnesses can be computed: the vertical grain roughness σ_{zg} and the vertical roughness of the longitudinal and transverse bed-forms (σ_{zl} and σ_{zt}). σ_{zg} was computed using bed elevations of patch DEM at the scale

of a laser-scanner profile (≈10 cm) to avoid assessing for bed forms roughness. On the contrary, σ_{zl} and σ_{zt} were calculated using bed elevations of longitudinal and transverse DEMs at the flume scale (≈ 15 m for longitudinal profiles and ≈ 70 cm for transverse profiles).

Degree of bed armoring

The development of a static armor layer occurs frequently in gravel-bed rivers (Hassan and Church, 2000). The static armor layer appears after an extended period of low flow condition combined with a reduced sediment supply over a poorly sorted gravel bed (e.g. downstream of dams) (Wilcock and DeTemple, 2005; Orrú et al., 2016). In our experiments, we will try to replicate this phenomenon. An armored bed corresponds to a bed which has a coarser bed surface than its sub-surface. Conventionally, the degree of bed armoring is defined using the armor ratio, which corresponds to the ratio between the mean diameters of the bed surface and sub-surface (Guney et al., 2013). Armoring is also related to changes in grain imbrication, arrangement as well as clusters, that are not quantified by the armor ratio (Tan, 2012).

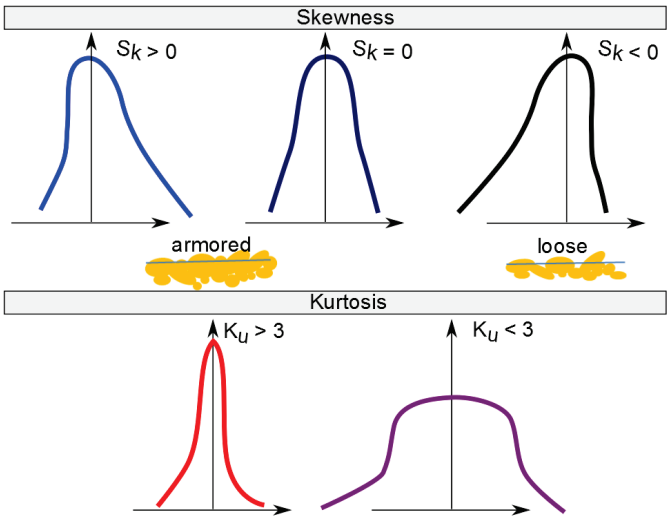

Figure 5.3.2: PDF shapes according to their values of skewness and Kurtosis.

Third-(skewness) and fourth-order (Kurtosis) distribution moments were chosen for characterizing bed armoring degree. The skewness S_k represents the symmetric or asymmetric nature of the PDF in comparison to a normal

distribution:

$$S_k = \frac{\mu_3}{\mu_2^{3/2}} \tag{5.3}$$

where $\mu_k = E((z - E(z)))^k$ is the k-order centered moment and $E(z)$ is the expected value of the bed elevation z.
$S_k = 0$ is attributed to a symmetric distribution around the mean bed values (Figure 5.3.2). Negative skewness is related to a PDF that is dilated to the left of the mean value. This means that the range of values lower than the mean bed level is larger than the one for values higher than the mean bed level. Negative skewness probably reflects presence of holes, emerged grains and random organization on the bed surface. Inverse behavior is observed when the skewness is positive. Positive skewness is associated to an armored or organized bed. In that case, the surface is smooth and coarse with several emerged grains. Small particles fill holes reducing bed elevation dispersion below the mean bed level.

The Kurtosis K_u characterizes the flatness or peakedness of the PDF shape (Figure 5.3.2) and can be used to describe the bed regularity:

$$K_u = \frac{\mu_4}{\mu_2^2} \tag{5.4}$$

For a normal distribution, $K_u = 3$. $K_u < 3$ means that the PDF has a bell-shape (i.e. wide flat distribution), so that the bed elevation values are strongly scattered around the mean bed level. This describes an irregular fluctuating bed surface. On the contrary, when $K_u > 3$ the PDF has a peak-shape assessing for a more regular bed surface.

5.3.2 Variogram analysis

In the past few years, second-order structure functions D_b have been used to characterize gravel or sand bed texture (Robert, 1988; Robert and Richards, 1988; Nikora et al., 1998; Marion et al., 2003; Nikora and Walsh, 2004; Aberle and Nikora, 2006; Cooper and Tait, 2009; Mao et al., 2011; Qin and Leung Ng, 2012). These functions are also called variograms in hydrogeology. They constitute an effective method to investigate the fractal properties of bed surfaces. The principle is to detect systematic patterns in a spatial

bed elevation distribution. D_b exhibits the correlation between elevations at various spatial scales in different directions:

$$D_b(\Delta_x, \Delta_y) = \sum_{i=0}^{N-n_r} \sum_{j=0}^{M-m_r} \frac{|z(x_i + n_r\delta_x, y_j + m_r\delta_y) - z(x_i, y_j)|^2}{(N - n_r)(M - m_r)} \tag{5.5}$$

where $\Delta_x = n_r\delta_x$ is the measurement step in the x direction, $\Delta_y = m_r\delta_y$ is the measurement step in the y direction, δ_x and δ_y are the sampling intervals in the x and y directions, respectively, N and M are the numbers of measured elevation points in the x and y directions, n_r and m_r are the ratios between measurement steps (Δ_x and Δ_y) and spatial lags (δ_x and δ_y) in each directions.

For random field, the second-order structure function and the auto-correlation function $R_b(\Delta_x, \Delta_y)$ are related as follows:

$$D_b(\Delta_x, \Delta_y) = 2(\sigma_z^2 - R_b(\Delta_x, \Delta_y)) \tag{5.6}$$

When the autocorrelation function tends to zero, $D_b^* = D_b/2\sigma_{zg}^2$ tends to 1 meaning that no correlation between bed elevations exists. $D_b^* = 1$ corresponds to randomly distributed bed elevations. However, when D_b^* tends to 0, total correlation exists between bed elevations. Values larger than 1 in D_b^* plot correspond to negative correlations.

Figure 5.3.3 shows two D_b^* plots obtained during our experiments. Figure 5.3.3a represents a typical plot for a bed with random organization. The plot shape has a flat plateau around the no-correlation value (= 1). In this case, correlation between bed elevations is rapidly lost at small lags. Figure 5.3.3b shows a typical plot for an organized bed. A slope is visible in the D_b^* plots before reaching a flat plateau at larger lags (plateau would have been more visible if the size of the patch was larger). This means that bedforms or bed structures are present on the bed surface.

Bed structure characterization

From D_b^* plots, different bed arrangement characteristic lengths can be deduced. Three distinct zones can be distinguished if we look at 1D-structure

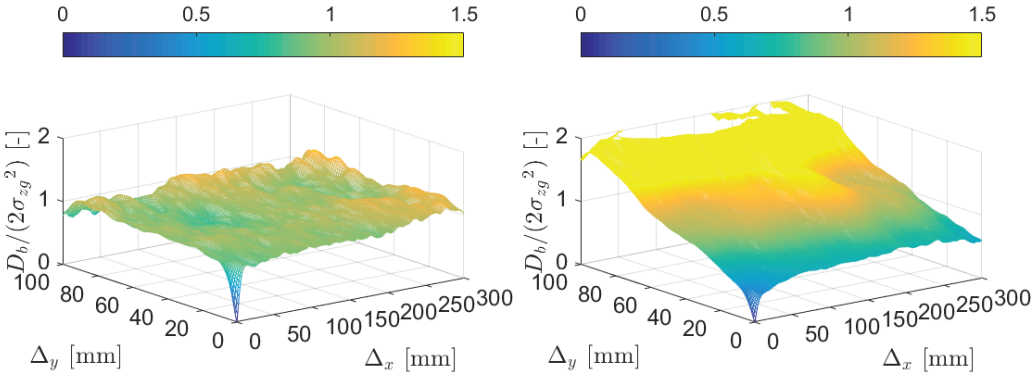

(a) Loose bed **(b)** Packed bed

Figure 5.3.3: Structure function plots obtained from bed elevation data of patch surveys: (a) D_b^* plots of unorganized bed (L-G-1) and (b) D_b^* plots of organized bed (P-G-2).

function associated plots, namely $D_b^*(\Delta_x = 0, \Delta_y)$ or $D_b^*(\Delta_x, \Delta_y = 0)$ (see Figure 5.3.4):

- a linear part at small lags (scaling region);
- a transition zone (region of bed-form characterization);
- a saturation zone at large lags ($D_b^* = 1$)

At small lags, the 1D-structure function can be approximated by a power function (Nikora et al., 1998):

$$\frac{D_b(\Delta_x, \Delta_y = 0)}{2\sigma_z^2} \approx \Delta_x^{2H_x} \tag{5.7}$$

$$\frac{D_b(\Delta_x = 0, \Delta_y)}{2\sigma_z^2} \approx \Delta_y^{2H_y} \tag{5.8}$$

where H_x and H_y are the Hurst exponents. These exponents assess for the rate at which the correlation decreases as the lag between bed elevations increases. H_x and H_y values are inversely proportional to the degree of bed surface complexity (Bergeron, 1996; Cooper and Tait, 2009). In our gravel-bed experiments, H_x and H_y range from 0.49 to 0.55 and from 0.51 to 0.56,

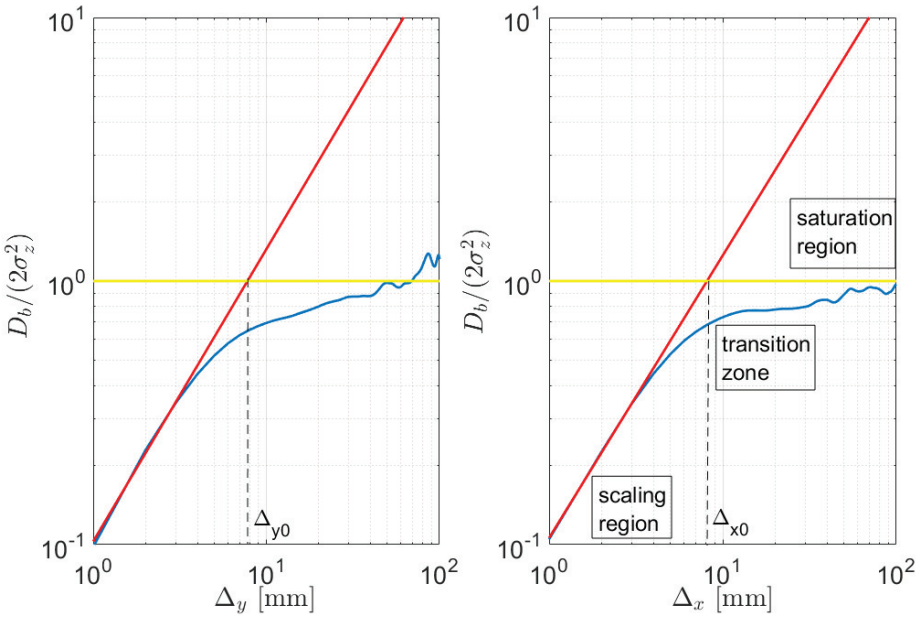

Figure 5.3.4: Typical 1D-structure function plots of a loose gravel-bed surface (L-G-1).

respectively (see Appendix A). These values are consistent with those found by Nikora et al. (1998).

The procedure to identify the longitudinal (Δ_{x0}) and transverse (Δ_{y0}) scales of bed structures is presented in Figure 5.3.4. They are quantified by plotting the 1D-structure functions in log-log scales and fitting the scaling regions with Equations 5.7 and 5.8 until reaching the asymptotes of no correlation considered equal to 1 (see the saturation region). Δ_{x0} and Δ_{y0} can be then estimated using the intersection between the fitted scaling region and the saturation asymptote (Figure 5.3.4). These parameters inform about bed structures at the grain scale. The length of the transition zone can also be used to have information about small-scale bed-form roughness.

Preferential grain orientation

Analyses of D_b^* contour plots provide information about preferential grain orientation and alignment. For gravel beds, contour line shapes at small lags (at the grain scale) can be either circular or elliptical. Circular shape indi-

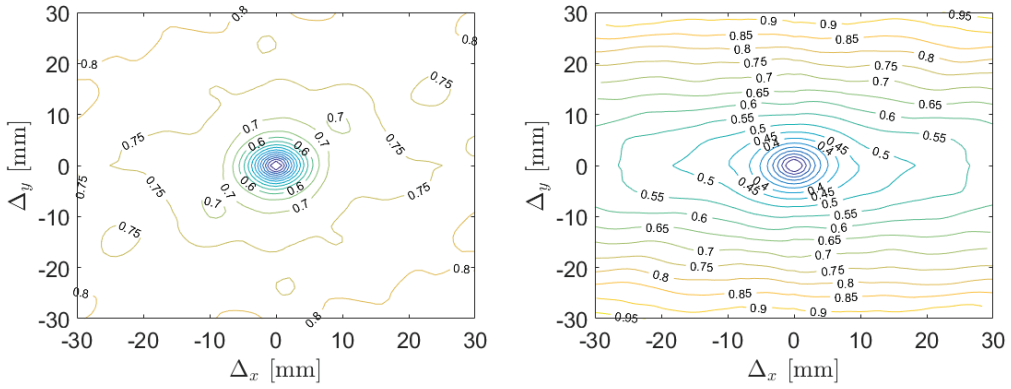

(a) Loose bed **(b)** Packed bed

Figure 5.3.5: Contour plots of the 2D structure function for (a) a loose (L-G-2) and (b) a packed bed (P-G-2).

cates that no prevalent grain direction is present. Elliptical shape suggests a preferential grain orientation in the direction of the ellipse main axis. Figure 5.3.5 shows examples of contour plots for a loose (non-organized) and a packed (organized) gravel beds. The grains on the loose bed were not preferentially orientated, whereas those on the packed bed were aligned in the flow direction.

To quantify the intensity of particle preferential orientation, the following variables obtained by fitting an ellipse on a specific contour line were used:

- Φ, the angle of rotation of the elliptical shape relative to the flow direction; It gives the average direction of the grains.
- a/b, the ratio between the major (a) and the minor (b) axes of the ellipse; The ratio a/b exhibits the magnitude of the effect. The higher the ratio is, the clearer is the preferential orientation.
- x_0/y_0, the ratio between the longitudinal (x_0) and transverse (y_0) distances defined by the ellipse. The ratio x_0/y_0 indicates the orientation and alignment of the grain main axis. When $x_0/y_0 > 1$, grain main axis is aligned in the flow direction. When $x_0/y_0 \approx 1$ and $a/b \approx 1$, no particular grain orientation is present on the bed surface. If $x_0/y_0 < 1$, the grain main axis is mainly oriented in the cross-stream direction.

Figure 5.3.6 shows the different variables and an example of a fitted ellipse of a specific contour line of a packed bed. The parameters are dependant on the selected contour line. Because we are interested in grain scale, we chose to focus on the first contour line that reaches the value of the median gravel diameter D_{50} in its transverse direction ($y_0 > D_{50}$).

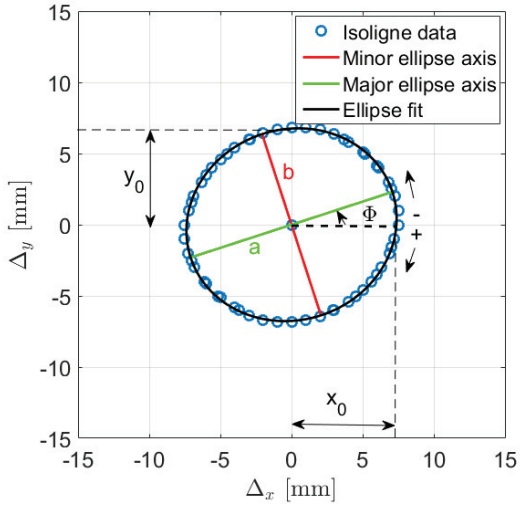

Figure 5.3.6: Fitted ellipse of the targeted contour line of a packed bed (P-G-1). Geometrical information describing the ellipse shape are reported.

Figure 5.3.7 presents the variations of parameters describing preferential grain orientation and alignment on a packed bed according to different fitted contour lines. Contour lines at larger lags informs about bedform or structure orientations and not about the grain orientation.

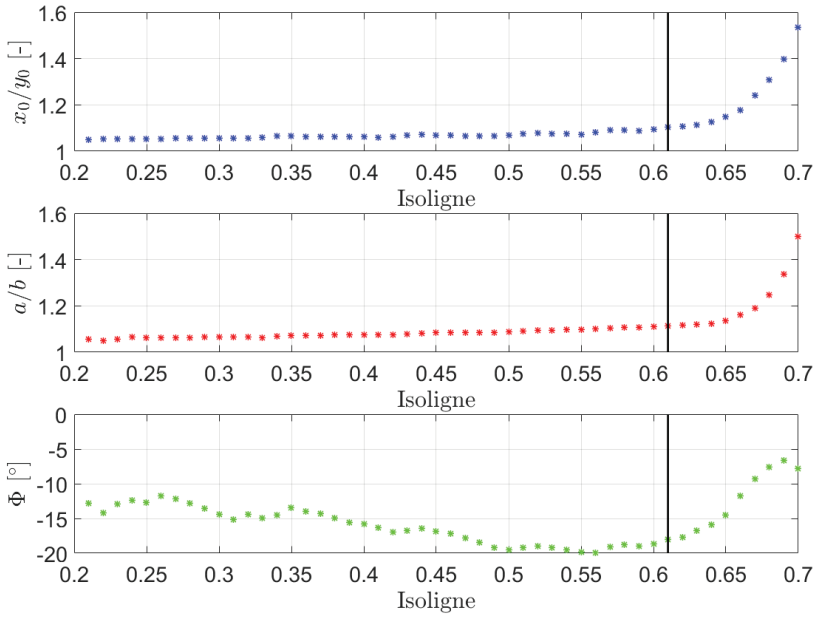

Figure 5.3.7: Variations of parameters defining preferential grain orientation and alignment according to different isolignes. Data are derived from an experiment performed on a packed bed (P-G-1). Black vertical line symbolizes the retained isoligne for post-processing the data.

Chapter 6

Velocity measurements

During the last decade, ADV probes and ADV profilers have been increasingly used for measuring velocity in field and laboratory because of its practicality. However, errors associated with these measurements are not always clearly detectable and taken into account. Different noise sources were identified and methods for correcting the ADV data were suggested (Nikora and Goring, 1998; Voulgaris and Trowbridge, 1998; Hurther and Lemmin, 2001; Goring and Nikora, 2002; Craig et al., 2011; MacVicar, 2014). Recent specific studies focused on the validity of ADV profiler data recorded close to the bed (Brand et al., 2016; Koca et al., 2017). For instance, Koca et al. (2017) conducted experiments in which they compared velocity profiles obtained with the PIV technique (Particle Image Velocimetry) and with the Vectrino profiler. Considering PIV measurements as references, they concluded that even after several noise corrections the Vectrino profiler data needed to be interpreted with caution.

Because the use of PIV was not a possibility in our study, only the Vectrino II was used. Special attention was paid to post-treat the Vectrino II data in order to obtain reliable velocity profiles. This chapter recaps all the process and recommendations established to improve the Vectrino II data and their interpretations.

6.1 Analysis of the raw data

Figure 6.1.1 shows an example of raw velocity and turbulence profiles measured using the Vectrino II during an experiment performed on a loose bed. The profile observations enable to detect several measurement problems. First, transverse and vertical velocity profiles are expected to be equal to zero in average, even if the measurement was not carried out along the entire water column. In this example, representative of all the measurements, the transverse and vertical velocities are equal to $-0.031\,\mathrm{m/s}$ and $-0.022\,\mathrm{m/s}$ in average, respectively. The deviation of $\overline{v}$ profile from zero might inform us of the potential presence of secondary currents in the channel transverse direction. The deviation of $\overline{w_1}$ and $\overline{w_2}$ profiles from zero is probably the reflect of a disorientation or misalignment of the device with the flow.

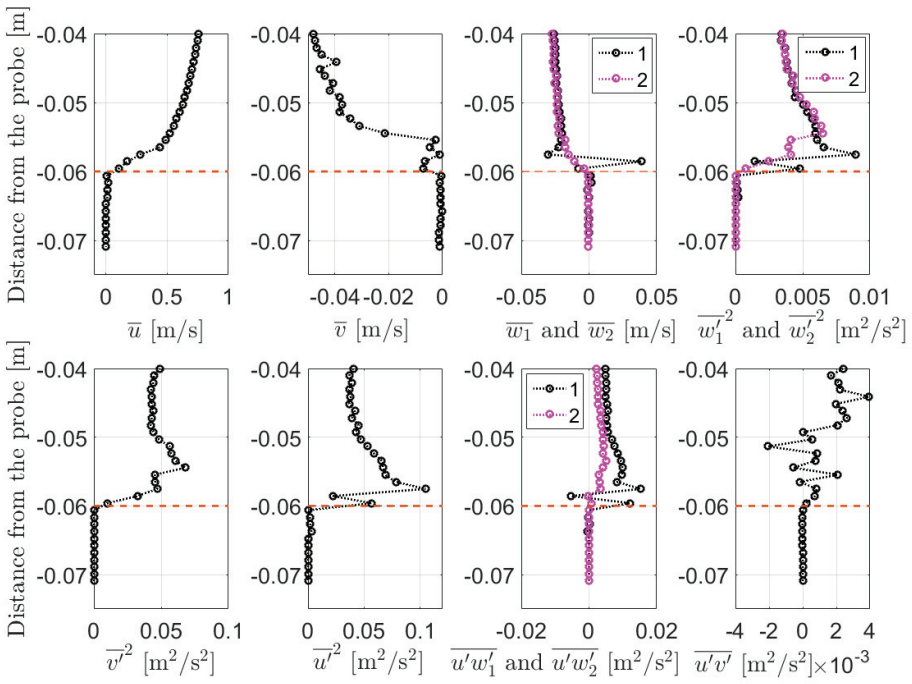

Figure 6.1.1: Examples of velocity and turbulence profiles measured using the Vectrino II. Data were obtained during experiment conducted on a loose gravel bed at 50 L/s (L-G-3). They are unfiltered and uncorrected. 1 and 2 refer to the two vertical velocity profiles (or turbulence components) measured with beams 1 and 3 and with beams 2 and 4, respectively. Orange dashed line represents the bed level.

Secondly, $\overline{w_1}$ and $\overline{w_2}$ are supposed to be equal because they both represent the time-average vertical velocity profile (see Section 2.2.2). However, they seem to have different behaviour near the bed (located close to 6 cm below the Vectrino II probe, in this particular case). Bottom interference might be present.

Thirdly, regarding the turbulence profiles and in particular $\overline{u'}$ and $\overline{v'}$, one can see that the profiles tend to bend and not follow the classical linear decrease approaching the water surface. This is probably due to noise contamination. In addition, as for $\overline{w_1}$ and $\overline{w_2}$, $\overline{w_1'}$ and $\overline{w_2'}$ should be similar. Some variations are clearly detectable impacting consequently the $\overline{u'w_1'}$ and $\overline{u'w_2'}$ profiles. It is thus necessary to apply correction on the data before interpreting the results.

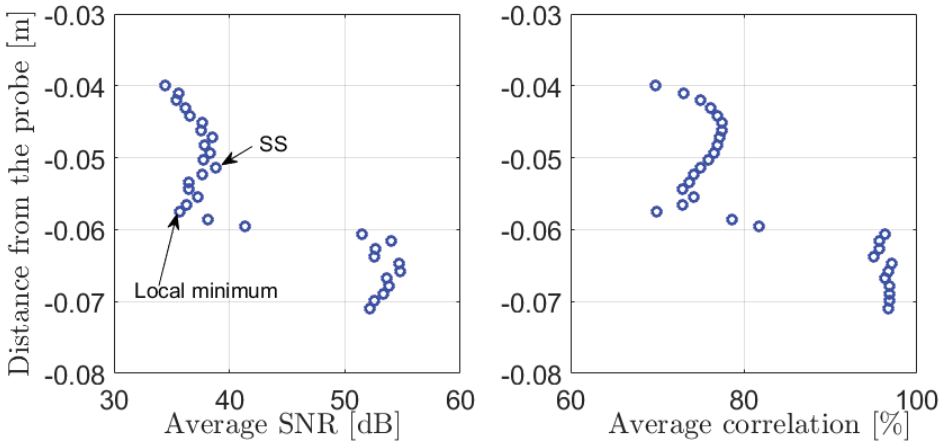

Figure 6.1.2: Examples of average SNR and average correlation profiles measured using all the Vectrino II beams. Data were obtained during the same experiment as in Figure 6.1.1 at 50 L/s (L-G-3). These data are unfiltered and uncorrected. *SS* indicates the location of the sweet-spot.

Figure 6.1.2 presents the average SNR (Signal Noise Ratio) and the average correlation profiles recorded by all the Vectrino II beams during the same experimental conditions as in Figure 6.1.1. It shows that the signal quality changes along the profile. This indicates that the data should be interpreted with caution. The profiles have a parabolic shape with a maximum reached around 50 - 52 mm from the probe for the SNR profile. The point of maximum SNR located between 50 - 52 mm is commonly called the

"'sweet spot"' (SS). It corresponds to the location where the measurement is the most reliable. At the lower end of the parabolas, the profiles reach local minimums and sharply increase, suggesting that we approach the bed.

To improve the data, we recommend to apply the following filters and corrections:

- a despiking filter as suggested by Goring and Nikora (2002);
- threshold filters for the SNR and for the correlation profiles;
- a correction for bottom interference;
- a correction for the Doppler noise;
- corrections for potential rotations of the device;
- a detection of the signal decorrelation influence on the measurements.

Details of each filters and corrections are given in the following sections.

6.2 Despiking method

Temporal series of velocity measurements are often contaminated by noise called spikes (Figure 6.2.1). Spikes are corrupted data present in a sample. Numerous causes can create spikes but ADV noise is still not fully understood (lack of impurities in the water, particles entering and leaving the sampling volume during the interval between sound pulses, turbulence at scales equal or smaller than the measuring volume causing particle scattering) (Nikora and Goring, 1998; Jesson et al., 2013).

A despiking method is an iterative process that identifies, removes, replaces the contaminated data (by NaNs in our case) and reconstructs a new and less corrupted signal. To post-treat our data, the despiking process initially developed by Goring and Nikora (2002), called Phase-Space Threshold method (PST) was used. The method is based on a 3D phase-space plot in which the velocity (u) and its derivatives (first (du/dt) and second (d^2u/dt^2)) are plotted against each other. A fictive ellipsoid with specific size, position and orientation is added to this plot. The ellipsoid center coordinates are the

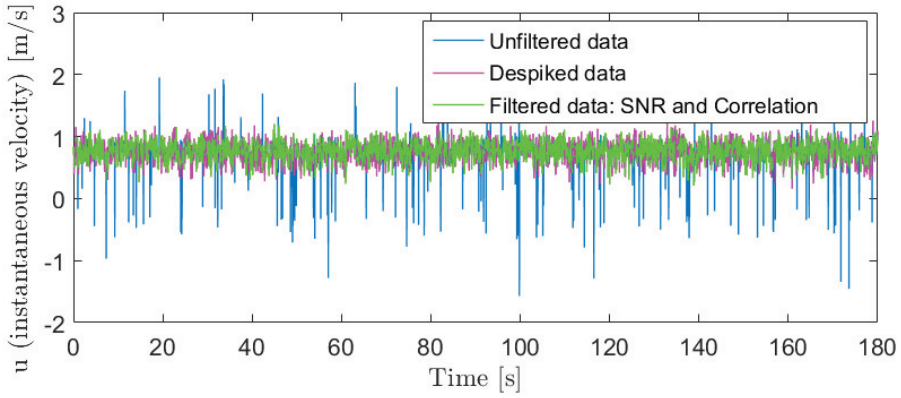

Figure 6.2.1: Comparison between raw, despiked and filtered (SNR and correlation thresholds) instantaneous longitudinal velocities. Data were recorded during the same experiment as in Figure 6.1.1 at 50 L/s (L-G-3), at a specific vertical location (first cell from the probe) during 180 s at 50 Hz. The despiking process was performed using the PST method of Goring and Nikora (2002).

means of u, du/dt and d^2u/dt^2. For each pair of variables, ellipse axis lengths and rotation angles are calculated. The points lying outside the ellipsoid are designated as spikes and replaced by new values based on the neighboring values or simply by NaNs. Once the new signal is reconstructed, a new ellipsoid is calculated. The process is then repeated until the number of spikes falls to zero. For further details, please refer to the publication of Goring and Nikora (2002).

Figure 6.2.1 shows the effect of the despiking process on the instantaneous velocity recorded during one of our experiments. After the despiking of this specific time-series, more than 4 % of data were removed.

6.3 SNR and correlation filters

Data were filtered according to their SNR and correlation values. The manufacturer (Nortek) suggests that data are reliable when their SNR are higher than 20 dB and their correlation values are higher than 70 %. Threshold filters were thus applied to remove values with bad SNR and poor correlation. Values were replaced with NaNs. Figure 6.2.1 presents data after threshold

filtering. In that specific case, more than 35 % of data were removed from the temporal series of the instantaneous longitudinal velocity. For the rest of the study, if more than 40 % of the data were removed after the filtering process, the data were not analysed and considered as inaccurate. Usually the removed data did not exceed 30 %.

6.4 Bottom interference

Close to the bed, the velocity measurements can be affected by bottom interference. They are not reliable and need to be removed from the velocity profile. To detect the interference region, the method suggested by Koca et al. (2017) was chosen. Comparing Vectrino profiler data with PIV data, they proved that the zone affected by bottom interference ended at the same distance than the location of the local minimum of the SNR profile (Figure 6.1.2). All the data below this local minimum will not be retained for the interpretation of the results. It is important to note that the vertical extent of the zone depends on the bed material properties (particularly on the bed porosity) and on the probe's proximity to the bed (Koca et al., 2017).

6.5 Doppler noise correction

The correction of Doppler noise in each velocity variances was performed using the Hurther and Lemmin (2001) method (H&L). This method is applicable if the device is correctly aligned with the flow during the measurements. It is based on the assumption that the measured variances of velocities can be decomposed into real variances and a noise term:

$$\overline{u'^2_{measured}} = \overline{u'^2_{real}} + a_j\sigma_j \tag{6.1}$$

$$\overline{v'^2_{measured}} = \overline{v'^2_{real}} + a_j\sigma_j \tag{6.2}$$

$$\overline{w'^2_{1\ measured}} = \overline{w'^2_{1\ real}} + b_j\sigma_j \tag{6.3}$$

$$\overline{w'^2_{2\ measured}} = \overline{w'^2_{2\ real}} + b_j\sigma_j \tag{6.4}$$

$$a_j = \frac{1}{2sin^2(\alpha_j)} \tag{6.5}$$

$$b_j = \frac{1}{2cos^2(\alpha_j)} \tag{6.6}$$

where, $\overline{u'^2_{measured}}$, $\overline{v'^2_{measured}}$, $\overline{w'^2_{1\ measured}}$ and $\overline{w'^2_{2\ measured}}$ are the measured variances, $\overline{u'^2_{real}}$, $\overline{v'^2_{real}}$, $\overline{w'^2_{1\ real}}$ and $\overline{w'^2_{2\ real}}$ are the real variances, σ_j is the Doppler noise associated with the device, a_j and b_j are terms calculated using the device geometry and particularly the angle α_j between the emitter and receiver, and j denotes a specific measurement cell (35 cells along 3.5 cm). $\overline{u'^2}$, $\overline{v'^2}$, $\overline{w'^2_1}$ and $\overline{w'^2_2}$ can be affected with Doppler noise (see Appendix C for more details).

To assess the noise that contaminates the variances, Hurther and Lemmin (2001) suggest investigating the covariance $\overline{w'_1 w'_2}$ that gives the true variance of vertical fluctuations without contamination by instrument noise:

$$\sigma_j = \left(\overline{w'^2_{1\ measured}} - \overline{w'_1 w'_2}\right) b_j^{-1} = \left(\overline{w'^2_{2\ measured}} - \overline{w'_1 w'_2}\right) b_j^{-1} \tag{6.7}$$

No noise contaminates the covariance because it is computed with uncorrelated beam velocities (see Appendix C). Equation 6.7 is valid for an ideal case. In other words if $\overline{w'^2_{1\ measured}} = \overline{w'^2_{2\ measured}}$ and if α_j are the same for each receivers.

Figure 6.5.1 shows the vertical velocity variance and covariance profiles measured during the experiment chosen as example. It clearly displays that the two vertical variances are not the same. The assumptions made for validating Equation 6.7 are thus not correct in our case. Two different noises can be calculated:

$$\sigma_{1\text{-}3} = \left(\overline{w'^2_{1\ measured}} - \overline{w'_1 w'_2}\right) b_j^{-1} \tag{6.8}$$

$$\sigma_{2\text{-}4} = \left(\overline{w'^2_{2\ measured}} - \overline{w'_1 w'_2}\right) b_j^{-1} \tag{6.9}$$

$\sigma_{1\text{-}3}$ and $\sigma_{2\text{-}4}$ correspond to the noises associated with the beam couple 1 - 3 (so, the noise contaminating $\overline{u'^2}$ and $\overline{w'^2_1}$) and with the beam couple 2 - 4 (so, the noise contaminating $\overline{v'^2}$ and $\overline{w'^2_2}$), respectively.

In addition, Figure 6.5.2a presents the geometric angles between emitter

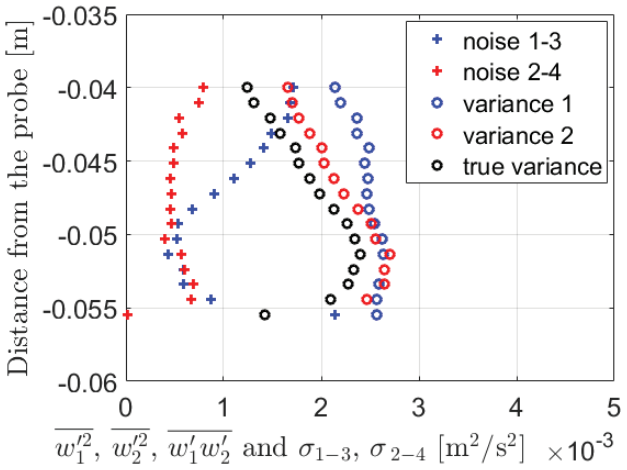

Figure 6.5.1: Profiles of variances and covariance of vertical velocity. Noise 1-3 and noise 2-4 are associated with the variance calculated with w_1 (variance 1) and with the variance calculated with w_2 (variance 2), respectively. The true variance corresponds to the covariance $\overline{w_1'w_2'}$. Data were extracted from the same experiment as in Figure 6.1.1 during measurements at 50 L/s (L-G-3).

and receiver for each receivers and each measurement cells. These angles were calculated using the transformation matrix beam/XYZ estimated and provided by the manufacturer of the device for each measurement cells. The transformation matrix can be written analytically as follows:

$$\begin{pmatrix} \sin(\alpha_1) & 0 & \cos(\alpha_1) & 0 \\ 0 & \sin(\alpha_2) & 0 & \cos(\alpha_2) \\ -\sin(\alpha_3) & 0 & \cos(\alpha_3) & 0 \\ 0 & -\sin(\alpha_4) & 0 & \cos(\alpha_4) \end{pmatrix} \begin{bmatrix} u \\ v \\ w_1 \\ w_2 \end{bmatrix} = \begin{bmatrix} b_1 \\ b_2 \\ b_3 \\ b_4 \end{bmatrix} \tag{6.10}$$

where α_1, α_2, α_3 and α_4 correspond to angles between emitter and receiver 1, 2, 3, and 4, calculated for each measurement cells, respectively (see Figure 6.5.2b which provides a definition sketch for these angles).

Figure 6.5.2a shows that the device is not perfect and that the angles between emitter and receivers for each measurement cells vary according to the considered receivers. To facilitate the correction phase, we choose to impose the same angles for each receivers during our calculations. The angles retained correspond to the average angles of all four receivers (angles

α presented on Figure 6.5.2a).

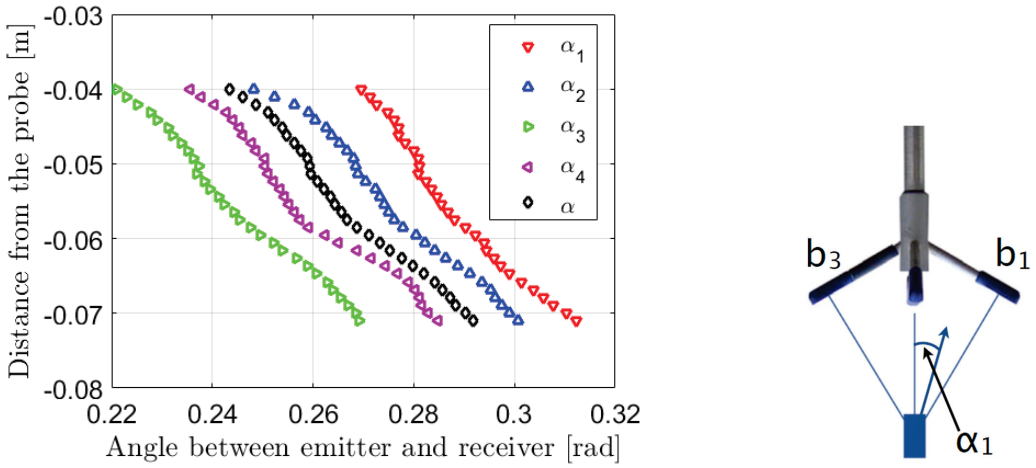

(a) (b)

Figure 6.5.2: (a) Values of geometric angles between emitter and receiver for each receivers and each measurement cells. α_1, α_2, α_3 and α_4 correspond to angles between emitter and receiver 1, 2, 3, and 4, respectively. α corresponds to the average angles. (b) Definition sketch for these angles.

Figure 6.5.3 shows the Vectrino II data after despiking, filtering and Doppler noise correction in comparison with the despiked and filtered data. The profile shape are now more consistent with the theory, in particular for $\overline{u'^2}$ which after correction decreases along the water column. The noise for $\overline{v'^2}$ does not seem to have been completely compensated.

6.6 Device rotation correction

It is very difficult, even in laboratory experiments, to set the Vectrino II in perfect alignment with the flow. Rotation in the plan (u, v) may lead to errors as well as rotation in the plan (u, w). These disorientation errors need to be quantified. Koca et al. (2017) showed that if the device is rotated of 1°, the turbulent kinetic energy profile and the Reynolds stress profile ($\overline{u'w'}$) vary of around 0.5 % and 4 %, respectively. Peltier et al. (2013) found that a device rotation of 2.5° involve a variation of 14 % for the Reynolds stress profile.

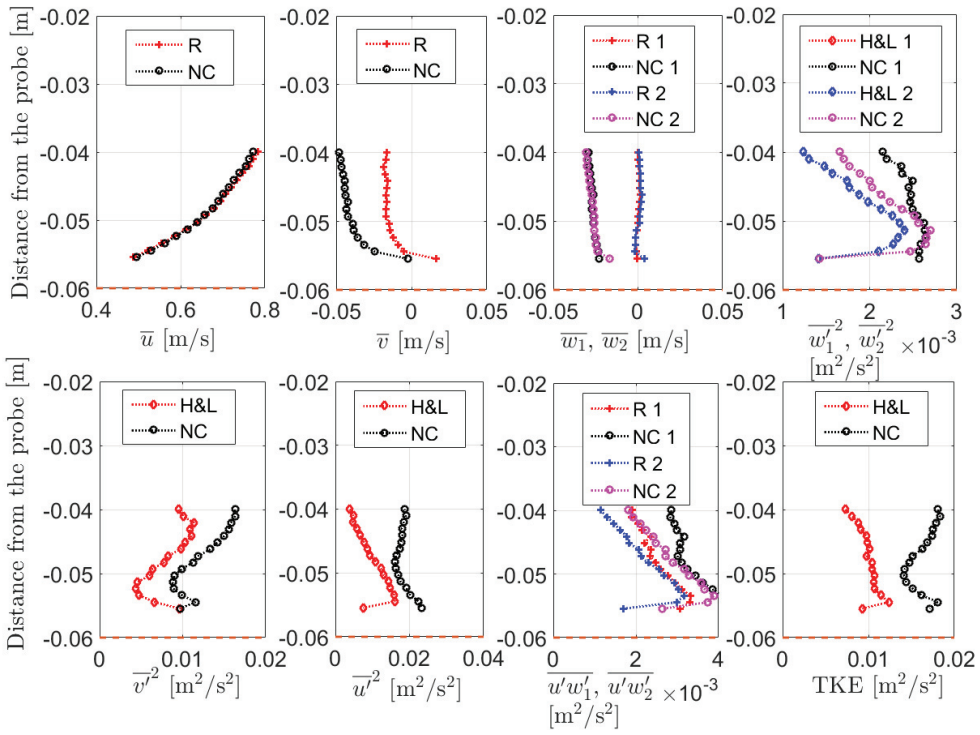

Figure 6.5.3: Examples of velocity and turbulence profiles measured using the Vectrino II. Data were obtained during the same experiment as in Figure 6.1.1 at 50 L/s (L-G-3). All data are despiked and filtered with the SNR and correlation thresholds. In the legend, *H&L* denotes data corrected with the Hurther and Lemmin (2001) method, *R* refers to data corrected of a potential device rotation and *NC* are not corrected data. 1 and 2 refer to the two vertical velocity profiles (or turbulent components) measured with beams 1 and 3 and with beams 2 and 4, respectively. *TKE* is the turbulent kinetic energy. Orange dashed line represents the bed level.

The rotation correction follows two steps. First, the data are corrected from potential rotation in the plan ($\overline{u}$, $\overline{v}$). Then, they are corrected of a second potential rotation in the plan ($\overline{u}$, $\overline{w}$). The rotation effect was estimated by calculating two rotation angles with the assumption that the time-average vertical velocity ($\overline{w}$) and the transverse velocity ($\overline{v}$) should be equal to zero in average:

$$\tan(\theta_{(\overline{u},\overline{v})}) = \frac{\overline{v}}{\overline{u}} \tag{6.11}$$

$$\tan(\theta_{(\overline{u},\overline{w})}) = \frac{\overline{w}}{\overline{u}} \tag{6.12}$$

where $\theta_{(\overline{u},\overline{v})}$ and $\theta_{(\overline{u},\overline{w})}$ are the rotation angles of the device in the plan ($\overline{u}$, $\overline{v}$) and ($\overline{u}$, $\overline{w}$), respectively.

Same rotation angles are affected for all the data. Indeed, the device was never moved during the thesis experiments. To minimize the effect of potential secondary currents, angles were calculated on the basis of spatially and time-average velocity profiles. The spatially and time-average profiles were obtained from 14 time-average individual profiles located along a channel transect.

After the first rotation, new velocities, called temporary velocity (tmp), are deduced:

$$\overline{u}_{\text{tmp}} = \overline{u}\cos(\theta_{(\overline{u},\overline{v})}) + \overline{v}\sin(\theta_{(\overline{u},\overline{v})}) \tag{6.13}$$

$$\overline{v}_{\text{tmp}} = -\overline{u}\sin(\theta_{(\overline{u},\overline{v})}) + \overline{v}\cos(\theta_{(\overline{u},\overline{v})}) \tag{6.14}$$

$$\overline{w}_{\text{tmp}} = \overline{w} \tag{6.15}$$

The second rotation is performed and the corrected velocities are deduced ($\overline{u_{\text{rotated}}}$, $\overline{v_{\text{rotated}}}$, $\overline{w_{\text{rotated}}}$):

$$\overline{u}_{\text{rotated}} = \overline{u}_{\text{tmp}}\cos(\theta_{(\overline{u},\overline{w})}) + \overline{w}_{\text{tmp}}\sin(\theta_{(\overline{u},\overline{w})}) \tag{6.16}$$

$$\overline{v}_{\text{rotated}} = \overline{v}_{\text{tmp}} \tag{6.17}$$

$$\overline{w}_{\text{rotated}} = -\overline{u}_{\text{tmp}}\sin(\theta_{(\overline{u},\overline{w})}) + \overline{w}_{\text{tmp}}\cos(\theta_{(\overline{u},\overline{w})}) \tag{6.18}$$

Figure 6.5.3 present the Vectrino II data after despiking, filtering and rotation correction in comparison with the despiked and filtered data. Due to the rotation correction, the time-average vertical and transverse profiles now approach zero in average. In addition, the correction has an effect on the Reynolds stress profiles by diminishing its global intensity.

6.7 Signal decorrelation influence

According to our knowledge, no method exists for correcting the decorrelation effect. It is still important to have it in mind when interpreting the results. Decorrelation between beam signals is caused by a decreasing overlap between beams (Figure 2.2.2). The maximum beam correlation is located at the sweet

spot that is why it is the most reliable data point. Size of overlap zone diminishes rapidly close to the probe and the bed. In this zone of decrease in overlap, some particles might be seen by only one beam. This leads to a loss in covariance between beam signals (Brand et al., 2016). Appendix C shows how variances and different turbulent components are calculated based on beam velocities. Regarding these calculations, one can see that some variances are more affected by signal decorrelation than others. $\overline{w_1' w_2'}$, $\overline{u' w_2'}$, $\overline{u'^2}$, $\overline{v'^2}$, $\overline{w_1'^2}$, $\overline{w_2'^2}$ are sensitive to the beam decorrelation because they are calculated using covariances between different beam velocities. However, $\overline{u' w_1'}$ is not affected by this problem. In addition, we have seen that $\overline{u' w_1'}$ was not contaminated by Doppler noise. It might be the most reliable variance.

Chapter 7

Bed shear stress calculations

The bed shear stress τ is a key parameter for understanding sediment transport and particularly bedload transport. It is often used to characterize the sediment incipient motion via the Shields parameter. Various methods are available to calculate or measure τ. Some of them are presented in the following section. In general, these methods are based on the determination of the shear velocity, $u^* = \sqrt{\tau/\rho}$.

7.1 Methods

7.1.1 Depth-slope equation

The most commonly used method is based on a force balance between the gravitational force and the friction force (Equation 7.1). This method is known as the depth-slope method. It can be used only in uniform flows. In that case, the estimated bed shear stress corresponds to a global reach-averaged bed shear stress.

$$\tau = \rho g R_h J \approx \rho g h I_b \tag{7.1}$$

where R_h is the hydraulic radius and J is the water slope.

7.1.2 Logarithmic law method - log method

The logarithmic law method (log-method) is a local method based on the analysis of the time-average longitudinal velocity profile and particularly its logarithmic region. It consists in detecting and approximating the log-region using the log-law (Equation 7.2).

$$\frac{\overline{u(z)}}{u^*} = \frac{1}{\kappa} \ln\left(\frac{z}{Z_0}\right) \tag{7.2}$$

where $\overline{u(z)}$ is the time-averaged longitudinal velocity at the height z, $\kappa = 0.41$ is the Von Karman constant and Z_0 is defined as the roughness length (the height at which the time-averaged longitudinal velocity will be equal to zero, if the logarithmic law would be applicable down to the bed).

From the fit of the profile with a log-law, the shear velocity and the roughness height are deduced. Figure 7.1.1 illustrates the log-method and its corresponding log-fit using velocity data of an experiment performed on a loose bed.

The first difficulty of this method is to detect correctly the logarithmic region within the profile. No universal way exists to determine its limits. It is important to note that on a rough bed, the time-average longitudinal velocity profile can be divided into two main layers: the inner and outer layers. The inner layer is composed of a roughness layer located just above the bed followed by a logarithmic layer. Several authors have made propositions to define the roughness layer height Z_R, so the beginning of the log-region; many are related either to the bed sediment diameters (D), a characteristic roughness length (Z_0) or to the water depth (h): $Z_R = 50Z_0$ (Townsend, 1976), $Z_R = 5D$ (Raupach et al., 1991), $Z_R = 3D_{84}$ (Wilcock, 1996), $Z_R = \sigma_z$ (Nikora and Goring, 2000) where σ_z is the standard deviation of the bed elevations, $Z_R = 0.05h$ (Smart, 1999). Concerning the logarithmic layer end (Z_L), Katul et al. (2002) and Smart (1999) suggested that the logarithmic layer ends at $Z_L < h/5$ and $Z_L < h/2$, respectively. The limits as defined by Smart (1999) were used in our study ($0.05h \leq$ log-region $\leq 0.5h$).

Another difficulty is related to the definition of the flow depth, so indirectly to the determination of the bed level z_{bed}. The flow depth is necessary

to locate the log-region and approximate correctly our velocity data. The definition of the flow depth is also very important when using the depth-slope equation method. In our experiments, the bed is rough, the sediments can be in motion and bedforms can appear; z_{bed} is thus complicated to detect and consequently h is also hard to estimate. As a first approach for z_{bed}, we choose to use the bed level detected by the Vectrino II.

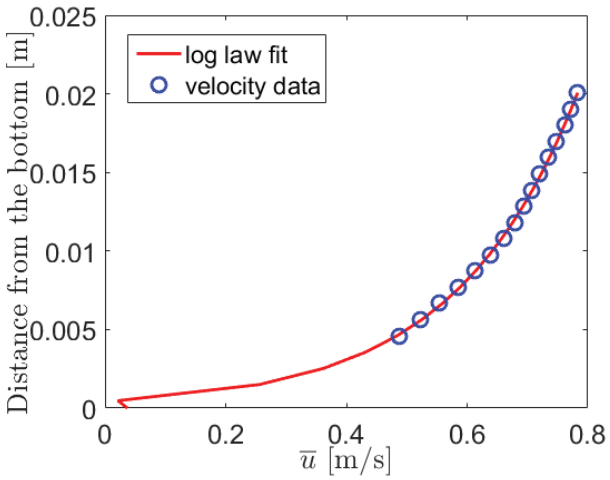

Figure 7.1.1: Estimation of the bed shear stress using the log-method. These data were obtained during the same experiment as in Figure 6.1.1 at 50 L/s (L-G-3).

7.1.3 Reynolds stress method - Re method

Shear velocity can be determined using turbulent velocities profile ($\overline{u'w'}$). The total shear stress can be defined by the following equation:

$$\tau = \tau_t + \tau_\nu = -\rho\overline{u'w'} + \mu\frac{du}{dz} \tag{7.3}$$

where μ is the water dynamic viscosity.
It can be decomposed into a turbulent stress (τ_t) and a viscous stress (τ_ν). Far from the bed, the viscous shear stress can be neglected. It can also be neglected closer to the bed in case of beds having rough boundaries. The shear stress varies linearly and decreases along the water column. Close to

the bed, the profile decreases rapidly reaching values close to zero at the bed level.

This local method consist in extrapolating the Reynolds stress profile ($-\overline{u'w'}$) to the bed level in order to deduce u^*:

$$u^{*2} \approx -\overline{u'w'}(z = z_{\text{bed}}) \tag{7.4}$$

As for the previous methods, the determination of the bed level z_{bed} is essential to compute an accurate friction velocity. As a first estimation, we choose to use the bed level detected by the Vectrino II. Figure 7.1.2 illustrates the Re-method using data collected with the Vectrino II. In Section 6.5 and 6.7, we see that the Reynolds stress profile $\overline{u'w'_1}$ is not contaminated by noise nor by signal decorrelation problems. The bed shear stress estimated using this profile is probably the most reliable.

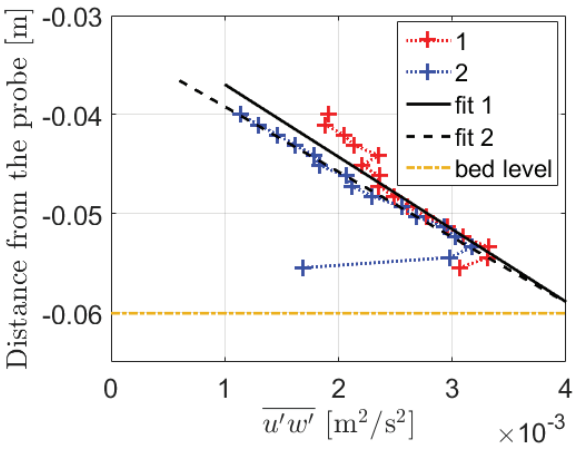

Figure 7.1.2: Estimation of the bed shear stress using the Re-method. These data were obtained during the same experiment as in Figure 6.1.1 at 50 L/s (L-G-3). In the legend, 1 and 2 refer to the Reynolds stress calculated with $\overline{w'_1}$ and with $\overline{w'_2}$, respectively. The horizontal dashed yellow line corresponds to the bed elevation.

7.1.4 Turbulent kinetic energy - TKE method

The turbulent kinetic energy profile (TKE) is increasingly used for estimating the local bed shear stress (Kim et al., 2000; Biron et al., 2004; Pope et al.,

2006; Wren et al., 2016). The TKE is defined as follows:

$$TKE = \frac{1}{2}(\overline{u'^2} + \overline{v'^2} + \overline{w'^2}) \tag{7.5}$$

where $\overline{u'^2}$, $\overline{v'^2}$ and $\overline{w'^2}$ are the velocity variances.

This method is empirical and largely used in oceanography. Simple relation between bed shear stress and the TKE were developed:

$$\tau = \rho C_{\text{TKE}} TKE \tag{7.6}$$

where C_{TKE} is an empirical constant value varying according to the studies (C_{TKE}=0.2 for Soulsby (1981), C_{TKE}=0.19 for Stapleton and Huntley (1995) (often used for gravel beds), and C_{TKE}=0.21 for Kim et al. (2000)). In this study, C_{TKE} =0.2 was chosen for the calculations. These values of C_{TKE} were estimated for specific levels within the water column and specific hydraulic conditions. Wren et al. (2016) do not confirm the constant proportionality seen in Equation 7.6. They found that C_{TKE} varies along the water column, and according to the particle size, the bed roughness and the presence or not of fine sediments within the bed. It is then important to keep in mind that this method may not be adapted for our study.

Some studies suggest taking a single value of TKE for estimating bed shear stress (for example, Biron et al. (2004) proposed to take the point at approximately $0.1h$). Because our measurements were not often reliable at the same point, we choose to linearly extrapolate the TKE profile to the bed level and take this value for the estimation of bed shear stress. The bed level is the one detected by the Vectrino II.

Figure 7.1.3 illustrates the TKE-method using data collected with the Vectrino II. The TKE profile is not affected by any device rotation. Indeed, the TKE is nothing but a norm. However, all the velocity variances used to calculate TKE are contamined by Doppler noise (see Section 6.5). This might introduce errors in the estimation of the bed shear stress.

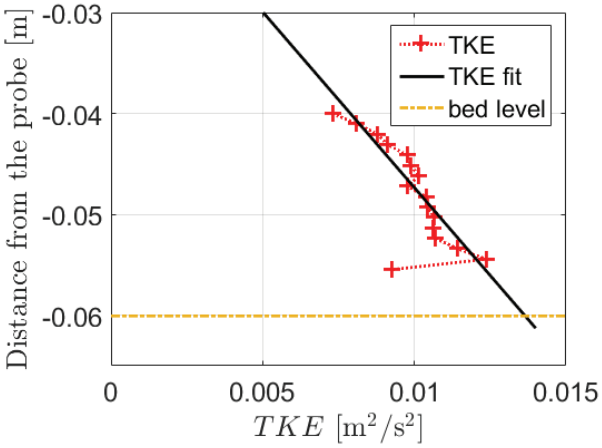

Figure 7.1.3: Estimation of the bed shear stress using the TKE-method. These data were obtained during the same experiment as in Figure 6.1.1 at 50 L/s (L-G-3). The horizontal dashed yellow line corresponds to the bed elevation.

7.2 Sensitivity of the friction velocity estimation to the bed position

Methods for friction velocity calculation are highly dependent on the chosen bed location. The position of the bed level is often difficult to measure precisely, especially during sediment transport experiments. Sensitivity studies are presented in Figure 7.2.1 for Re-method, in Figure 7.2.2 for TKE-method and in Figure 7.2.3 for the log-method. Sensitivity tests were performed using velocity and turbulence profiles performed during a specific experiment, where the topography around the velocity measurement was scanned. No gravel movement was detected during the experiment, in that way the exact position of the bed level was known. The bed location according to the scanner is reported on the Figures 7.2.1, 7.2.2 and 7.2.3.

For the case of Re-method, an error in bed level estimation of around +/- 5 mm leads to a maximum variation of +/-1.2 % for the bed shear stress value (Figure 7.2.1). For the TKE-method, an error in bed level estimation of around +/- 5 mm leads to a maximum variation of +/-3 % for the bed shear stress value (Figure 7.2.2). These two methods have thus a small dependence to the bed level position.

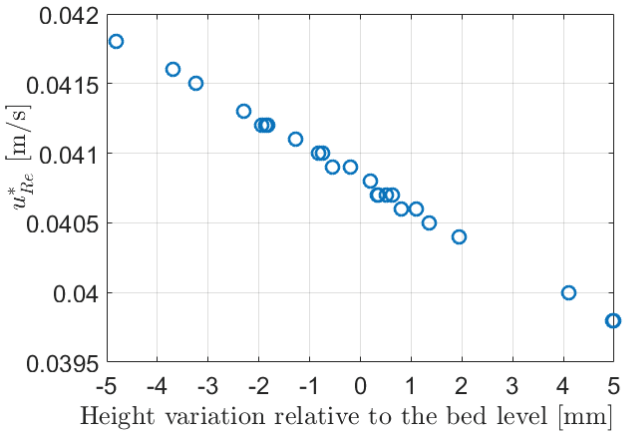

Figure 7.2.1: Friction velocities computed with the Reynolds stress method as a function of the chosen bed level location relative to the bed level estimated with the scanner measurement.

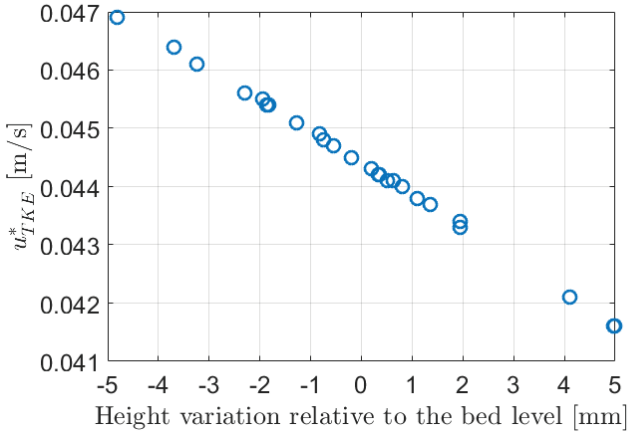

Figure 7.2.2: Friction velocities computed with the TKE-method as a function of the chosen bed level location relative to the bed level estimated with the scanner measurement.

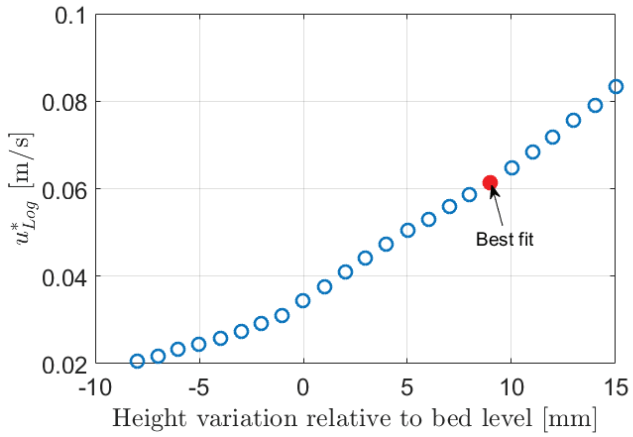

Figure 7.2.3: Friction velocities computed with the log-method as a function of the chosen bed level location relative to the bed level estimated with the scanner measurement. Red filled circle indicates the friction velocity obtained with a fictive bed level providing the best log-fit of the data.

This is not the case for the log-method. An error of 1 mm changes the friction velocity value by about 5 % (Figure 7.2.3). For application of the log-method, it is often advised to fit the experimental velocity data with the method of least squares by varying the bed level position. A fictive bed level that provides the best fit (best R^2) is then evaluated. If we consider the bed level equal to the fictive bed level, the bed shear stress value might vary by about 79 % in comparison to the value calculated when considering the bed level equal to the initial bed level measured by the laser-scanner. This sensitivity study shows that the use of the log-method during experiments on mobile beds remains questionable.

7.3 Recommendations

For the rest of the study, the bed shear stress estimated with the depth-slope method is kept for the global scale approach and the one estimated with the Re-method is chosen for the local scale approach. The global bed shear stress includes the skin and form drag whereas the local bed shear stress describes only the skin friction.

We recommend to use the Re-method because it is the less sensitive to

the bed position and because the $\overline{u'w'_1}$ profile is not contaminated by Doppler noise, but just impacted by rotation effect due to measurement device misalignment. We do not recommend the use of the log-method because of its high sensitivity to the bed level position, although it is the only one able to give estimate of the hydraulic roughness ($k_s = f(Z_0)$). The TKE-method should not be used because the TKE profile is too affected by Doppler noise.

Furthermore, the Re-method is a local method based on physical bases in contrast to the others. Indeed, the log-method is based on the assumption that the velocity profile can be fitted with a log law and the TKE-method is based on some empirical correlation between the TKE and the Reynold stress values. The value of C_{TKE} might not be constant or accurate for any type of beds (Wren et al., 2016).

Part III

Results

Chapter 8

Gravel dynamics at the global scale

This chapter focuses on the data resulting from the experiments of sediment transport presented in Section 3 in Table 3.1. Only the global results are presented here, i.e. the general results at the flume scale, with the aim of determining the properties influencing the gravel dynamics at low bed shear stresses and detecting the main parameters to take into account in gravel transport models. To compare experimental results, we will refer to a reference dimensionless bed shear stress characterizing condition of a given low but measurable gravel transport. A phenomenological description of the results is chosen to better apprehend processes governing the gravel dynamics.

8.1 Literature review on transport of poorly sorted sediments at low bed shear stresses

Few previous experimental studies have focused on the transport of poorly or moderately sorted sediments. Some of them were dedicated to understand the dynamics of unimodal and scattered GSD bed material under steady flows, such as beds composed of poorly or moderately sorted gravel particles (Hassan et al., 2006; Ancey et al., 2015). The main conclusion of these studies was that the bedload dynamics reaches an equilibrium state after a temporal

decline, if there was no coarse sediment feeding during the experiments. This decline was linked to the development of a static armor layer on the bed surface (Hassan and Church, 2000). The characteristics of the bed surface changed during its development, such as the number of emerged particles (Fenton and Abbott, 1977), the grain imbrication and compaction (Li and Komar, 1986), the bed structures and bedforms (Laronne and Carson, 1976; Brayshaw et al., 1983).

Bedload dynamics of unimodal beds during unsteady unidirectional flows was also explored (Hassan et al., 2006; Mao, 2012; Guney et al., 2013). Bedload rate hysteresis was highlighted, reflecting changes in bed surface complexity and organization during unsteady flows (Guney et al., 2013). All these experimental studies agreed that the antecedent flow history and initial degree of bed armoring are determinant for bedload rate prediction. These experimental observations were consistent with in-situ observations (Reid et al., 1985). Reid et al. (1985) noticed that in Turkey Brook River, for the same hydraulic conditions, sediment transport rates differed from the rise to the ebb of a flood. They showed that the bed shear stress for incipient motion was up to three times higher than the one for cessation of movement. They attributed this difference to the fact that the first mobilization of sediments required destruction of pebble clusters present initially on the bed surface. They thus associated these changes in critical bed shear stress for incipient motion and in sediment mobility to a change in bed surface arrangement during the flood. Depending on previous flows, the bed can become more or less armored. Large and short floods can strongly reduce bed stability, thus increasing sediment transport. Indeed, in that case, bed patterns or structures are broken, fine particles responsible of bed stability are preferentially transported, and the bed becomes looser. However, if the bed is submitted to a long period of medium floods, the bed stability will increase due to local particle rearrangements, which in turns reduces the sediment mobility. This field study raised the idea that it is important to take into account the bed shear stress history of the river when predicting bedload transport (Monteith and Pender, 2005; Ockelford and Haynes, 2013).

Other studies have examined the behaviour of bimodal beds, focusing on the behaviour of a bed composed of a coarse matrix with the presence of

fine sediments. It is now well-accepted that when fine sediments are present into a coarse matrix, the mobility of the coarse sediments can change drastically. Lots of studies investigated bed materials made of a sand and gravel mixtures (Beschta and Jackson, 1979; Jackson and Beschta, 1984; Ikeda and Iseya, 1988; Wilcock and McArdell, 1993; Wilcock et al., 2001; Wilcock and Crowe, 2003; Curran and Wilcock, 2005; Curran, 2007; Hill et al., 2017). Beschta and Jackson (1979) showed that by injecting finer particles (sand) into a coarser matrix (gravel), the mobility of the coarser grain increased. Following their work, similar studies were performed under different conditions and confirmed that the sand grains enhanced the coarser particle movements. Curran (2007) showed that the gravel particles mobility increased with an increase in sand supply, which was consistent with Ikeda and Iseya (1988) results. Wilcock et al. (2001) observed that the sand content has an important non-linear effect on gravel bedload rate. They found that gravel transport increased by orders of magnitude with 10 to 30 % of sand content present on the bed surface. Following these observations, Wilcock and Crowe (2003) developed a surface-base transport model for sand-gravel mixtures. Their model incorporates a hiding function and takes into account the non-linear effect of sand content present on the bed surface (Wilcock et al., 2001) by including it in the computation of the dimensionless reference bed shear stress:

$$\tau^*_{\text{ref}} = 0.021 + 0.015e^{-20F_s} \tag{8.1}$$

where F_s is the sand content.
Hill et al. (2017) showed that when fine sediments disappeared from the bed surface, the enhancement of the coarser grains was no longer apparent, even if fine sediments were still present within the bed matrix.

Tests on the influence of small gravels on larger gravels revealed also that their presence increased the coarser grain transport (Venditti et al., 2010). Nowadays, stream restoration programs increasingly use the addition of finer sediments into the river bed matrix in order to facilitate the coarse matrix transport (Sklar et al., 2009; Koll et al., 2010), even if the response of such fine sediment inputs is still not fully understood.

The general conclusion of all of these studies is that there is an undeniable

effect of lubrication from the finer sediments. This lubrication effect was often associated to a simple reduction in the overall bed grain size due to the presence of sand (Wilcock et al., 2001). Other studies suggested that the presence of fine sediments smoothed the bed surface, so reduced the bed roughness and consequently the skin friction (Ikeda and Iseya, 1988). The finer grains filling the bed surface interstices can also reduce the ability of coarser grains in motion to come to rest (Hill et al., 2017), implying larger travelling distance for the coarser grains.

Few laboratory and field studies explored the role of very fine sediments, such as silt or clay on gravel transport in rivers (Jain and Kothyari, 2009; Barzilai et al., 2013). Most of the previous investigations were carried to characterize sediment transport in estuaries (i.e mixture of clay/silt/sand) or in sewer systems (i.e. mixture of clay/silt/sand/gravel) (Mitchener and Torfs, 1996; Sutter et al., 2000).

Jain and Kothyari (2009) observed that gravel transport decreases with the increase in clay content. They noticed that large values of the clay percentage (P_c) and Unconfined Compressive Strength (UCS) of the sediment bed (i.e. parameter that reflects the resistance of the bed to compression, usually estimated using a soil mechanics test) significantly limit the bedload rate. It is important to specify that during their experiments gravel particles were in inter-contact.

Barzilai et al. (2013) realized a field study on the Nahal Eshtemoa river, which had undergone strong bed composition changes in few years. They observed that the value of bed shear stress necessary to put into motion the coarse particles has doubled and that the bedload transport has reduced following a large amount of silt and clay infiltration into the coarse matrix. The reduction in bedload was probably due to this presence of very fine sediments increasing the cohesion and consolidation of the bed matrix.

These laboratory and field observations are consistent with results found on clay/silt/sand mixture in estuaries. Generally, this kind of mixture depends on parameters such as clay type and percentage, water content in the cohesive fraction, undrained shear strength, unconfined compressive strength of the sediment mix and plasticity index. Clay or silt particles act as cement consolidating the bed material. Following these observations, Kothyari

and Jain (2008) proposed a relationship for determining incipient motion of cohesive sediment mixtures (τ_{cc}) based on bed material cohesion and clay percentage:

$$\frac{\tau_{cc}}{\tau_c} = 0.94(1 + P_c)^{3/2} e^{-1/6} (1 + 0.001 UCS^*)^{9/20} \tag{8.2}$$

where τ_c is the critical shear stress for the non cohesive sediment having size equal to the arithmetic mean size of the cohesive sediment mixture, e is the void ratio, P_c is the clay percentage, $UCS^* = UCS/((\rho_s - \rho)d_a)$ is the dimensionless unconfined compressive strength and d_a is the arithmetic mean size of the sediment mixture.

The understanding of the very fine and fine sediment influence on gravel transport is still an up-to-date challenge in river hydraulics. Our experiments were conducted on beds set to mimic mountain rivers, i.e. with diverse bed arrangements and inhomogeneous vertical distributions of fine sediments (cohesive or not). Generally, the previous studied mixtures were man-made and homogeneous as explained in Section 3.1. The presence of fine sediments inhomogeneously distributed within the bed river might impact the transport rate. Our experiments aim to examine the gravel movement of such beds. First part of the gravel dynamics analysis at global scale will focus on the influence of bed arrangement on bedload rate. Second part will present the influence of fine sediments on bedload rate.

8.2 Dynamics over an unimodal gravel bed

This section relates the results concerning the unimodal beds, called loose (L-G) and packed (P-G) beds according to their initial bed surface arrangement (see Section 3.2 for the experiment nomenclature).

8.2.1 General results

Figure 8.2.1 presents an example of flow and sediment transport time series during a couple of experiments. This example is representative of all other experiments performed on loose and packed unimodal beds. For further

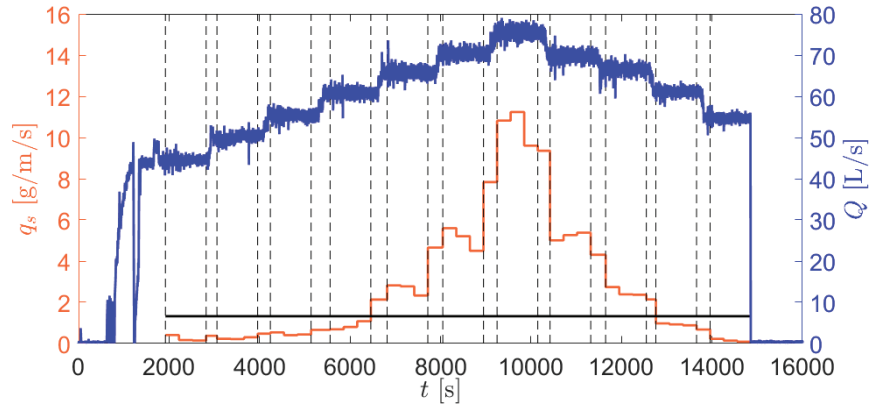

(a) L-G-3

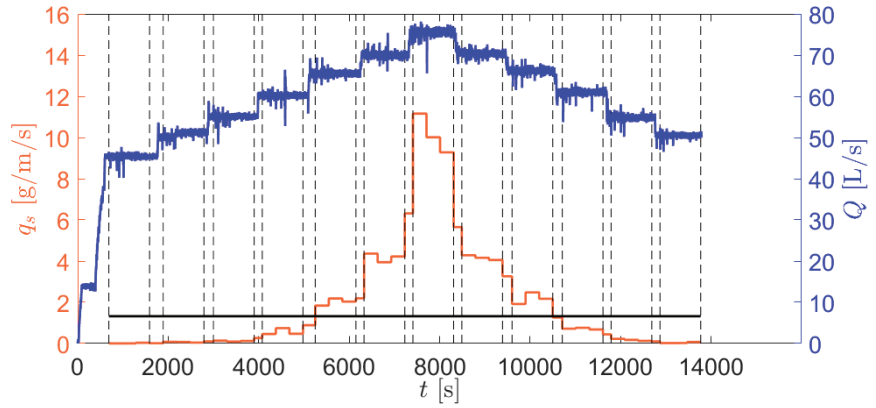

(b) P-G-3

Figure 8.2.1: Time variations of bedload (q_s) and flow (Q) rates for the experiment couple n° 3 (loose bed: L-G-3 and packed bed: P-G-3). Grid delimits steady states from transitions zones. Black horizontal line corresponds to the reference transport rate $q_{s\text{-ref}}$. The left axis refers to the bedload rate (orange) and the right axis refers to the water discharge (blue).

details on these experiments, please refer to Appendix A. During the L-G and P-G bed experiments, the bedload rate clearly increases and decreases with the water discharge. Hydrographs were chosen to be similar from one experiment to another (duration, magnitude and sequencing). The shape of the bedload evolution for experiments conducted on a loose bed and on a packed bed is similar with a single-peak shape. However, depending on the initial state of the bed (loose or packed), the bedload intensity differs. In addition, regarding a single experiment, differences between the rising and falling limbs in terms of bedload rates can be perceived. For example, for experiment L-G-3 (Figure 8.2.1a), the bedload rate is a little bit smaller during the falling limb compared to the rising limb. These differences will be analysed hereafter using another result representation.

Observing the results at the scale of hydrograph plateaus (see Figure 8.2.1 during steady states), one can evaluate a part of the temporal variability of the bedload rate (Recking et al., 2012). Indeed, one can observe some differences in the 5 min averaged bedload rates. The first bedload sample of a plateau if often higher than the others. This might reflect the temporal decline often observed in previous studies at constant discharge (Hassan et al., 2006; Guney et al., 2013).

Figure 8.2.2 presents all the results obtained for unimodal beds. It shows the dimensionless bedload rate q_s^*:

$$q_s^* = \frac{q_s}{\sqrt{(s-1)gD_{50}^3}} \tag{8.3}$$

as a function of the dimensionless bed shear stress τ^*:

$$\tau^* = \frac{\tau}{(\rho_s - \rho)gD_{50}} \tag{8.4}$$

In this Section, the dimensionless bed shear stress corresponds to a total dimensionless bed shear stress. τ^* calculated with the depth-slope equation is generally the one determined in the field (Section 1.2.4).

For the sake of clarity, the bedload rates during the flow transitions are not shown in Figure 8.2.2. The results related to rising and falling limbs are separated in order to capture any possible differences in bedload evolu-

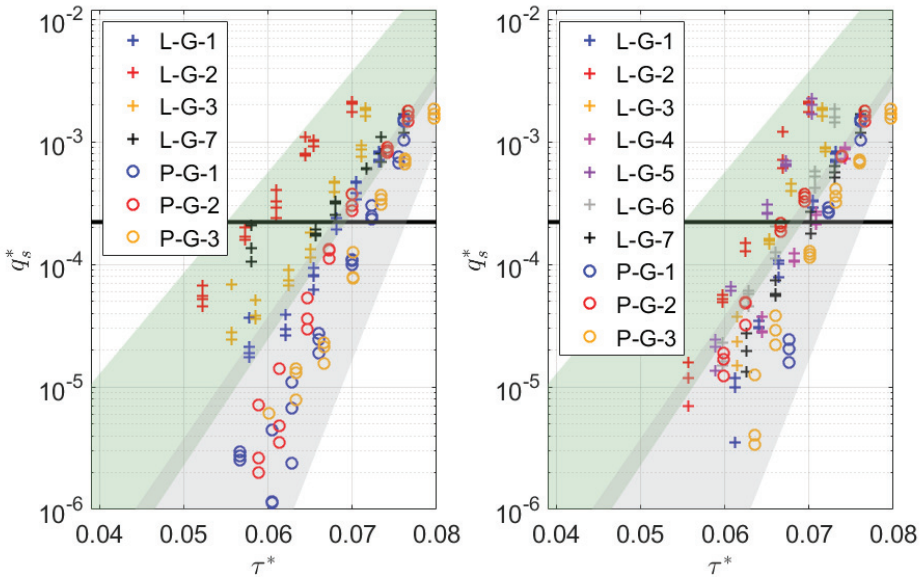

(a) Rising limb **(b)** Falling limb

Figure 8.2.2: Evolution of the dimensionless bedload rate as a function of the dimensionless bed shear stress for experiments performed on unimodal gravel beds with different bed arrangements: (a) at the rising limb and (b) at the falling limb. Green and grey shaded areas delimit data from experiments conducted on loose beds to data from experiments conducted on packed beds during the rising limb. These areas are reported on data at the falling limb. The black horizontal line corresponds to the dimensionless reference low transport rate $q^*_{s\text{-ref}} = 2.2\times10^{-4}$.

tion. Three or four q_s^* values are available for a given τ^* value (i.e. given flow discharge). These values correspond to the three or four bedload samples collected during each steady plateau. Regarding the results, one can see that a large scatter is present at very low bedload rates (i.e. different q_s^* values for the same τ^* value), making difficult the comparison between experiments. Indeed, at very low bed shear stresses, the bedload fluctuated substantially, making high-accuracy measurements delicate (Ancey et al., 2015). That is why, we added on the figure a dimensionless reference transport rate $q^*_{s\text{-ref}} = 2.2\times10^{-4}$ associated to a lower, accurate enough, measured bedload rate $q_{s\text{-ref}}$ =1.325 g/m/s. Above this reference limit, the scatter is reduced facilitating the result interpretation. The choice to set $q_{s\text{-ref}}$ =1.325 g/m/s as the reference transport rate is discussed in Section 3.3. One should have

in mind that $q_{s\text{-ref}}$ is seen in this study as a criterion for comparing our experiments and not as the true incipient motion.

The difference observed between L-G beds and P-G beds is significant during the rising limb. For a given q_s^* value, τ^* is globally lower for loose beds than for packed beds. The reference dimensionless bed shear stress τ^*_{ref} (i.e. the dimensionless bed shear stress needed for generating the bedload rate $q^*_{s\text{-ref}}$) for the packed bed can be from 5 % to 19 % higher than for the loose bed (on average 12 %) if we compare two experiments of one couple during the rising limb. If τ^*_{ref} was chosen to be related to a lower $q_{s\text{-ref}}$, the difference between loose and packed would be more pronounced, but the relative trend would be the same. Once again the τ^*_{ref} is seen here as an indicator for experiment comparison. Table 8.1 recaps the different dimensionless reference bed shear stresses measured for each experiments conducted on unimodal beds.

Table 8.1: Dimensionless reference bed shear stress for each experiment conducted on unimodal beds.

Experiment	$\tau^*_{\text{ref-R}}$ [-]	$\tau^*_{\text{ref-F}}$ [-]	Experiment	$\tau^*_{\text{ref-R}}$ [-]	$\tau^*_{\text{ref-F}}$ [-]
L-G-1	0.068	0.069	P-G-1	0.072	0.072
L-G-2	0.058	0.064	P-G-2	0.070	0.068
L-G-3	0.065	0.067	P-G-3	0.073	0.073
L-G-4	/	0.070			
L-G-5	/	0.064			
L-G-6	/	0.067			
L-G-7	0.064	0.070			
$\overline{\tau^*_{\text{ref}}}$ [-]	0.064	0.067	$\overline{\tau^*_{\text{ref}}}$ [-]	0.072	0.071
$E_{\overline{\tau^*_{\text{ref}}}}$ [%]	8.4	5.8	$E_{\overline{\tau^*_{\text{ref}}}}$ [%]	2.4	3.8

$\tau^*_{\text{ref-R}}$ represents the dimensionless reference bed shear stress during the rising limb; $\tau^*_{\text{ref-F}}$ denotes the dimensionless reference bed shear stress during the falling limb; $\overline{\tau^*_{\text{ref}}}$ is the average of $\tau^*_{\text{ref-R}}$ or $\tau^*_{\text{ref-F}}$ for each type of beds; $E_{\overline{\tau^*_{\text{ref}}}}$ is the maximum deviation in percent with respect to the average $\overline{\tau^*_{\text{ref}}}$ according to our experiments conducted on same bed types ($E_{\overline{\tau^*_{\text{ref}}}} = 100 \times \max\left(|\tau^*_{\text{ref,i}} - \overline{\tau^*_{\text{ref}}}|\right) / \overline{\tau^*_{\text{ref}}}$). $\tau^*_{\text{ref,i}}$ are the different measured reference bed shear stresses for the same bed types.

We expected that all the data would collapse for one type of bed (either L-G or P-G) since the same protocol was applied. However, significant differences are observed for example between two L-G experiments (see L-G-1 and L-G-2), in particular in term of τ^*_{ref} values (see Table 8.1). These differ-

ences cannot all be explained by the measurement uncertainty and are more pronounced for experiments performed on L-G beds during the rising limb. This suggests that our experiments were not perfectly reproducible. We believe that the initial bed arrangement is the main cause for these differences. Indeed, it was very difficult to reproduce the same initial loose gravel beds in the flume. Some of them were probably looser than the others. The difference in bed arrangement was not visible by eyes but was detected using the laser-scanner data. Values from Table 8.1 show that the deviation in terms of τ^*_{ref} for packed beds during the rising limb is significantly smaller. It is thus easier to reproduce a packed bed (with the same kinds of arrangement) than a loose bed. A method to classify our experiments between very loose, loose, packed and very packed bed experiments is therefore needed in order to compare them. We used the method presented in Section 5 and its associated bed surface criteria.

Despite these differences, two main areas are distinguishable in Figure 8.2.2 during the rising limb. Data related to L-G bed experiments are grouped together in the green shaded area of the (τ^*, q^*_s) plot. Data related to P-G bed experiments are, on the other hand, grouped in the grey shaded area, which corresponds to higher τ^* values for the same q^*_s. The temporal variability detected in Figure 8.2.1 is also visible in Figure 8.2.2 where several values of q^*_s appear for the same τ^*. The scatter due to the temporal variability of bedload does not question these two distinct areas. The intersection of these areas provides a location for data related to tests on a slightly packed beds.

Differences between L-G and P-G beds are smaller during the falling limb than during the rising limb. τ^*_{ref} decreases for P-G bed experiments whereas it increases for L-G bed experimentss. This will be discussed in the Section 8.2.2. In addition, it seems that the data tend to gather in a single area: the intersection area mentioned above. This behavior characterizes hybrid beds (defined in Section 3.2). Somehow, the hydrograph seems to reset previous shear stress histories, so that both hybrid beds resulting from a loose or a packed bed present similar bedload dynamics and similar bed surface arrangements.

8.2.2 Hysteresis effect

Results show that bedload rates can vary differently on the rising and falling limbs. Different transport rates can occur for the same hydraulic conditions (or same bed shear stresses) between the rising and falling limbs. A hysteresis effect can be easily observed on the graphs $q_s = f(Q)$ or $q_s^* = f(\tau^*)$ (see Figure 8.2.3).

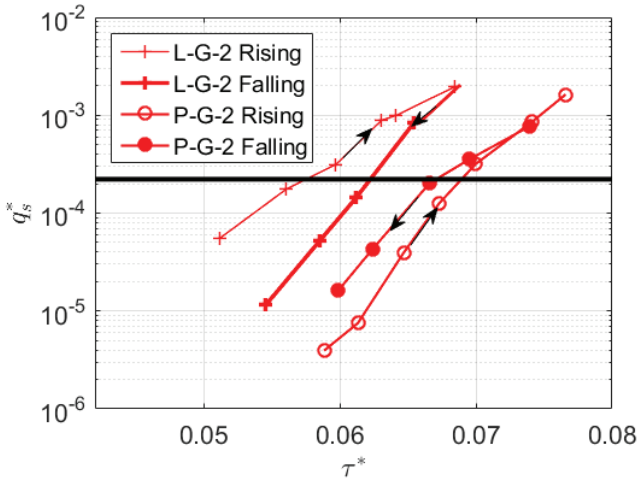

Figure 8.2.3: Bedload hysteresis patterns for L-G-2 and P-G-2. The black horizontal line corresponds to $q_{s\text{-ref}}$. Black arrows indicate the direction of the hysteresis loops. Bedload rates presented in this figure correspond to values averaged over each steady plateau.

Different types of hysteresis loops have been described previously (Williams, 1989; Waters and Curran, 2015):

- the clockwise loop, when values of bedload rates are larger during the rising limb than during the falling limb;
- the counterclockwise loop, when values of bedload rates are smaller during the rising limb than during the falling limb;
- the single-line plus loop, when values of bedload rates differ only on a part of the graph between the rising and falling limbs;
- the figure-8 loop, when values of bedload rates during the rising limb are

first larger then smaller (or smaller then larger) than the ones during the falling limb.

Only clockwise bedload hysteresis patterns were observed for L-G bed experiments. However, for P-G bed experiments, either no hysteresis or counterclockwise bedload hysteresis patterns were observed. For example, Figure 8.2.3 illustrates the two hysteresis patterns for L-G and P-G beds of the experiment couple n° 2, namely a clockwise loop for L-G-2 and a counterclockwise loop for P-G-2.

The hysteresis patterns seem to change according to the level of bed arrangement. For the L-G beds, during the rising limb, gravels are easily transported while re-arranging the bed and strengthening it. The bedload rate is then lower during the falling limb. For the P-G beds, the opposite is observed. The bed is initially packed and the gravel transport is initiated for stronger bed shear stress values. If, during the rising limb, the bed shear stress reaches sufficient values to break the grain structures and weaken the bed surface, the transport can be easier during the falling limb. If not, the gravel transport can be approximately the same during the falling limb and the rising limb. With all these observations, one can see that there is a close connexion between bedload rate and bed arrangement.

8.2.3 Impact of bed arrangement

Results of L-G and P-G bed experiments show that bedload rate depends on the bed arrangement. But how can we quantify these effects of bed arrangement? Which geometrical parameters impact the bedload rate? and how? Is there any relation existing between τ^*_{ref} and these parameters?

Bed arrangement can be characterized by geometrical parameters computed from detailed topographic surveys (see Section 5). In Table 8.2, all these parameters for each experiment performed on unimodal beds are recapped. Differences between L-G and P-G beds from one experiment couple are noticeable. The geometrical grain roughness of the bed surface (σ_{zg}) is smaller for P-G beds than for L-G beds, revealing a better bed surface particle imbrication and thus a smoother bed surface, except for the experiment couple n°2. This exception will also be seen at local scale (Section 9).

Table 8.2: Geometrical characteristics of bed surfaces computed for experiments conducted on unimodal gravel beds (see Section 5 for more details).

Exp.	σ_{zg} (mm)	S_k (-)	K_u (-)	σ_{zl} (mm)	σ_{zt} (mm)	Δ_{x0} (mm)	Δ_{y0} (mm)	H_x (-)	H_y (-)	x_0/y_0 (-)	a/b (-)	ϕ (°)
L-G-1	3.9	-0.28	3.1	4.3	4.2	7.9	7.3	0.54	0.56	1.0	1.0	18.1
P-G-1	3.3	0.00	2.9	4.6	4.3	8.3	7.3	0.51	0.54	1.3	1.2	-6.2
L-G-2	3.2	-0.34	3.1	3.5	3.2	6.8	6.6	0.54	0.54	1.0	1.1	22.4
P-G-2	3.7	0.28	2.9	5.0	4.2	12.1	10.4	0.51	0.53	1.5	1.5	-4.4
L-G-3	3.7	-0.35	2.9	4.1	4.1	6.9	6.8	0.55	0.56	0.9	1.1	-20.5
P-G-3	3.5	0.08	2.9	5.1	4.4	11.3	9.8	0.49	0.52	1.5	1.4	0.8
L-G-4	3.7	-0.49	3.4	4.2	3.9	7.1	6.8	0.55	0.56	1.0	1.1	-21.5
L-G-5	3.8	-0.48	3.2	4.4	4.0	7.3	7.2	0.54	0.54	0.9	1.1	-5.0
L-G-6	3.9	-0.41	3.1	4.3	3.8	7.7	7.1	0.54	0.55	1.0	1.1	10.1
L-G-7	3.8	-0.40	3.0	4.3	3.9	7.2	6.8	0.53	0.55	1.0	1.1	-7.4

σ_{zg} is the geometrical grain roughness of the bed surface; S_k is the skewness of the bed elevation PDF; K_u is the Kurtosis of the bed elevation PDF; σ_{zl} and σ_{zt} are the roughnesses of longitudinal and transverse bedforms, respectively; Δ_{x0} and Δ_{y0} are the longitudinal and transverse structure lengths, respectively; H_x and H_y are the Hurst coefficients in the longitudinal and transverse directions, respectively; x_0/y_0, a/b and Φ are indicators of preferential orientation of the bed surface grains.

A decrease in bed surface roughness would lead to smaller flow resistance (Smart et al., 2002; Aberle and Smart, 2003). The gravel transport should thus be reduced for the P-G bed experiments in comparison to the ones on L-G beds considering the same hydraulic conditions. This is consistent with our results (Figure 8.2.2). Regarding the experiment couple n°2, one can see that the initial geometrical roughness of longitudinal and transverse bedforms (σ_{zl} and σ_{zt}) are also particularly low for L-G-2. The L-G-2 bed is probably better compacted and particularly flat. In that case, the friction energy is not dissipated over bedforms leaving more energy to transport gravels. That is why, bedload rate is higher for the L-G-2 bed compared to the P-G-2 bed, even if the L-G-2 bed has a smaller geometrical grain roughness.

Figure 8.2.4 shows examples of bed elevation PDF measured on loose and packed beds of an experiment couple. The analysis of this figure shows that all skewness values are negative for loose beds (see Table 8.2), reflecting the presence of holes on the bed surface. On the other hand, skewness values are positive or close to zero for P-G beds, denoting an armoring process of the bed surface (see Section 5.3.1 for more details). Indeed, holes previously found in a L-G bed were filled by moving grains during the bed arrangement phase, reducing the dispersion in bed elevations below the mean bed level. P-G beds reflect a better grain imbrications. This can also be visualized on DEM figures presented in Appendix B. No strong tendency is observed concerning the Kurtosis value. All beds present a quite normal distribution (close to $K_u = 3$).

Larger σ_{zl} and σ_{zt} values in the packed beds indicates a development of bedforms that occurred probably during the arrangement phase. Bedforms were not visible by eyes but present if we refer to the bed surface indicators. Only preferential flow pathways could be visually identified.

No grain structure is present on the loose beds. Indeed, the structure lengths are close to the grain size for loose beds ($\approx D_{50}$). On the other hand, for P-G beds, structures start to appear but their lengths do not exceed $2 \times D_{50}$. If the GSD of the gravel was more scattered, the structures would have been probably longer. The Hurst exponents (H_x and H_y) represent the degree of bed surface complexity in the streamwise and cross-stream directions. The lower the value is, the more complex the bed surface is.

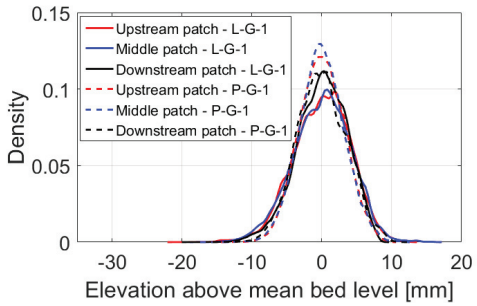

(a) experiment couple n°1

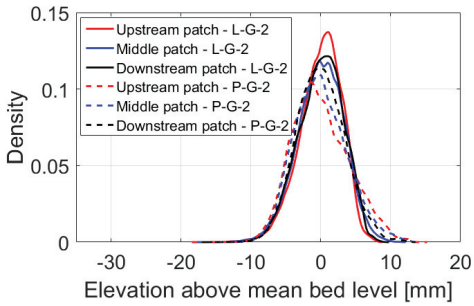

(b) experiment couple n°2

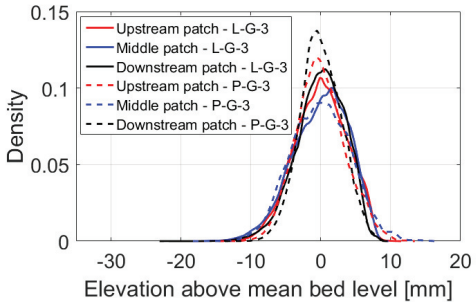

(c) experiment couple n°3

Figure 8.2.4: PDF of bed surface elevations of the three patch surveys measured on the loose and packed bed of the experiment couples n° 1, 2 and 3.

Regarding the values in Table 8.2, one can conclude that packed beds are more complex than loose beds.

The x_0/y_0, a/b and ϕ values indicates that gravels from loose beds present no significant orientation (x_0/y_0 and a/b close to 1, and ϕ larger than 0), while gravels from packed beds are clearly oriented in the flow direction (x_0/y_0 and a/b higher than 1, and ϕ approaching 0). Figure 5.3.5 illustrates these grain orientations using the variogram contour plots of experiment couple n° 2. The drag force for gravels orientated in the streamwise direction is in average smaller than the drag force for randomly orientated gravels. It could explain a part of the differences in the transport for L-G and P-G beds.

We have seen that results from loose and packed beds at the falling limb (i.e. hybrid beds, see Figure 8.2.2) form a scattered data set among which both beds cannot be distinguished. Topographic surveys of these hybrid beds were also conducted and analysed. For all hybrid beds (resulting from

an experiment performed on a loose or a packed bed), the bed surface characteristics were quite similar in terms of bed roughness, imbrication and grain orientation (see Appendix B). This confirms that it is appropriate to use the same nomenclature for all hybrid beds. However, the lengths of the bed forms showed a significant scatter. It should be recalled that the total bed shear stress τ can be broken down into a bed shear stress component due to grain resistance, τ', and a bed shear stress component due to form resistance, τ''. Sediment motion is generally attributed to the skin friction τ'. To further investigate the part of bed forms in the scatter of our data presented in Figure 8.2.2, we estimated the skin friction to analyse the sediment transport rate in our experiments.

Figure 8.2.5 shows q_s^* as a function of the dimensionless skin friction $\tau_K'^*$, computed using Manning-Strickler equation and a Strickler coefficient $K_g = 21/D_{50}^{1/6} \approx 48.2$ m$^{1/3}$/s, which represents skin roughness assumed to be identical for all experiments conducted on clean beds. The expression of τ'_K is thus deduced using the following equation :

$$\tau'_K = \rho g \left(\frac{Q}{W J K_g} \right)^{3/5} J \tag{8.5}$$

The same trend as in Figure 8.2.2 is replicated in Figure 8.2.5, namely two areas with a different behavior can be observed during the rising limb versus one area during the falling limb. The areas (green and gray shaded areas) can nevertheless be redrawn and modified. Indeed, they appear smaller and more distinguishable (see Figure 8.2.6). Assuming the same bed roughness for all the clean beds during the falling limb seems reasonable considering the analysis of the laser-scanner data. The scatter is reduced during the falling and data are closer to a single curve. The analysis of the flow resistance alone (τ' supposed equal to τ'_K) seems to be sufficient to explain the bedload dynamics during the falling limb. However, during the rising limb, differences are still present between the beds, even ignoring the bed form effect on flow resistance. Regarding the results, two points of discussion arise:

1. the flow resistance alone is not sufficient to explain the bedload behavior. That way, one should take into account the effect of bed arrange-

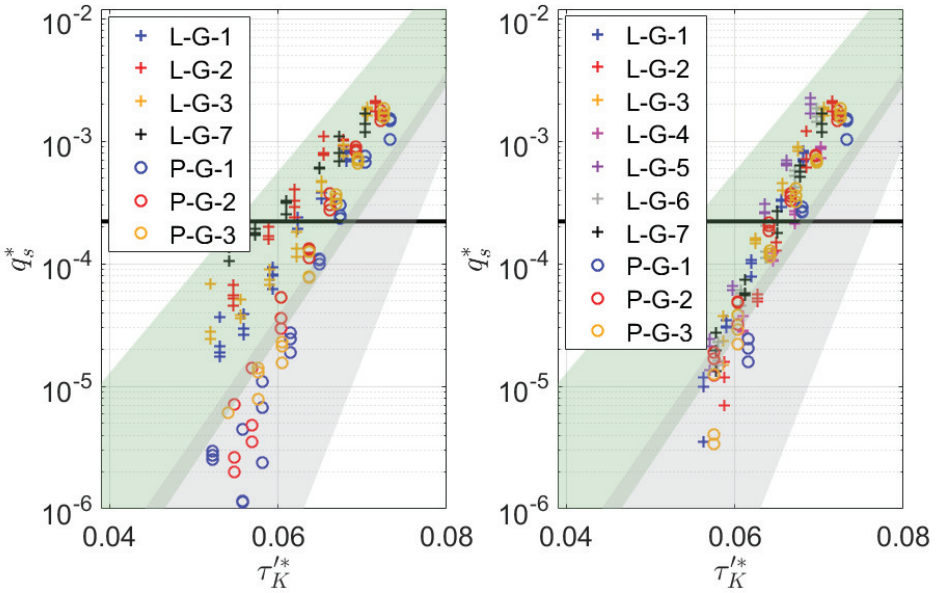

(a) Rising limb **(b)** Falling limb

Figure 8.2.5: Evolution of the dimensionless bedload rate as a function of the dimensionless skin friction $\tau_K'^*$ for experiments conducted on unimodal gravel beds with different bed arrangements: (a) at the rising limb and (b) at the falling limb. Green and grey shaded areas are the same as the one presented in Figure 8.2.2. The black horizontal line corresponds to the dimensionless reference low transport rate $q^*_{s\text{-ref}} = 2.2\times10^{-4}$.

ment on bed stability, for example by including in models a reference shear stress value τ^*_{ref} depending on flow history rather than a value of τ^*_{ref} that depends only on sediment grain size. Other parameters than τ^*_{ref} for assessing bed stability might be judicious, such as the slope of the relationship $q_s^* = f(\tau_K')$, which is clearly different according to the type of bed considered.

2. the flow resistance is the controlling parameter of the bedload dynamics but is not properly estimated. τ_K' is not a good estimate of τ'. The estimation of τ_K' is probably mistaken, partly because of the hypothesis of considering that beds have the same grain roughness (K_g) depending on the GSD of the bed material.

One can wonder if the first or second or both points are valid. The analysis of the laser scanner surveys supports the hypothesis of an incorrect estimation

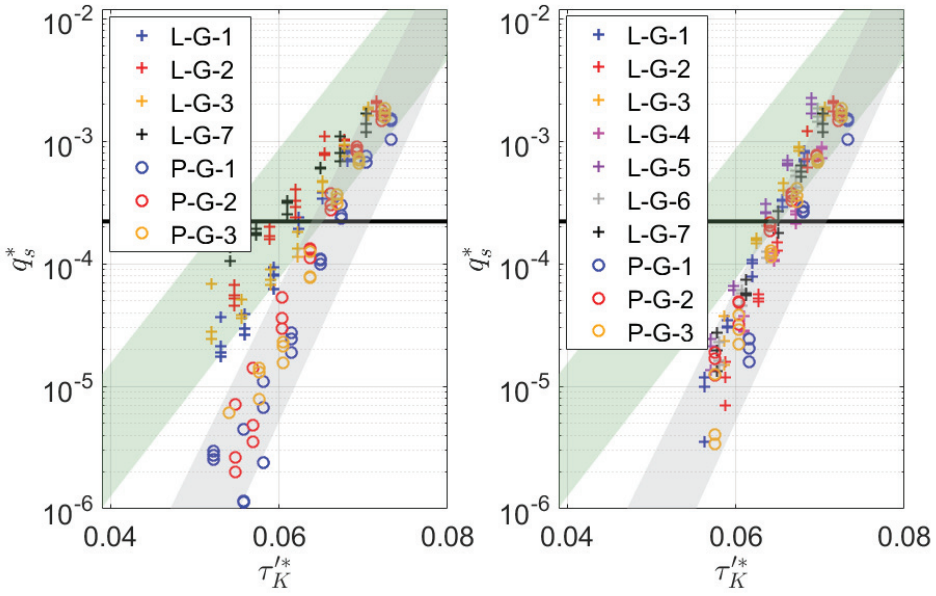

(a) Rising limb **(b)** Falling limb

Figure 8.2.6: Evolution of the dimensionless bedload rate as a function of the dimensionless skin friction $\tau_K'^*$ for experiments conducted on unimodal gravel beds with different bed arrangements: (a) at the rising limb and (b) at the falling limb. Green and grey shaded areas are redrawn in comparison to Figure 8.2.5. The black horizontal line corresponds to the dimensionless reference low transport rate $q^*_{s\text{-ref}} = 2.2{\times}10^{-4}$.

of τ'^* (point 2), but does not inform on the impact of bed arrangement on bed stability. τ'^* can be estimated using local measurements of bed shear stresses as it is presented in Section 9. In that case, τ'^* would be assumed equal to the dimensionless bed shear stress measured at the local scale.

In the absence of further analysis, it is not possible to conclude if bedload rate is impacted by bed arrangement because flow resistance or bed stability or both depend on bed arrangement. For now, improving existing bedload models requires assessing changes in both flow resistance and bed stability. We suggest that bedload rate should depend on a reference dimensionless bed shear stress τ^*_{ref} and a hydraulic roughness k_s that would be functions of a combination of several bed surface parameters, such as grain roughness (σ_{zg}), bedform roughnesses (σ_{zl} and σ_{zt}), bed armoring degree (S_K), bed structures (H_x, H_y, Δ_{x0} and Δ_{y0}), and grain preferential orientation (x_0/y_0,

a/b and ϕ):

$$\tau^*_{\text{ref}} = f\left(\sigma_{zg}, S_k, \sigma_{zl}, \sigma_{zt}, \Delta_{x0}, \Delta_{y0}, \frac{a}{b}, \Phi, k\right) \tag{8.6}$$

$$k_s = f\left(\sigma_{zg}, S_k, \sigma_{zl}, \sigma_{zt}, \Delta_{x0}, \Delta_{y0}, \frac{a}{b}, \Phi, k\right) \tag{8.7}$$

The bed compaction between a packed bed and a loose bed is a priori different but this parameter was not detectable using the scanner data. To take into account the compaction, we suggest to include the bed porosity k in the above equations but such parameter remains difficult to evaluate for a large experiment (in-bed samples are necessary).

We were not able to exhaustively explain the link between q_s and bed arrangement parameters, nor to reduce the number of controlling parameters. To achieve this, supplementary data are needed. Nevertheless, some correlations between τ^*_{ref} and bed surface indicators were highlighted (Figure 8.2.7). This could help to understand the impact of bed arrangement on bedload transport.

Figure 8.2.7 shows that :

- τ^*_{ref} increase is positively correlated with the decrease in geometrical grain roughness (see Figure 8.2.7a);

- τ^*_{ref} increase is positively correlated with the increases in bedform heights and structure lengths (see Figure 8.2.7c, d, e and f);

- τ^*_{ref} increase is positively correlated with the increase in bed armoring degree (see Figure 8.2.7b);

- τ^*_{ref} increase is positively correlated with the appearance of a preferential grain orientation (see Figure 8.2.7g).

These correlations depend probably on the value chosen for τ^*_{ref}. If τ^*_{ref} was lower, the trends might have been more detectable.

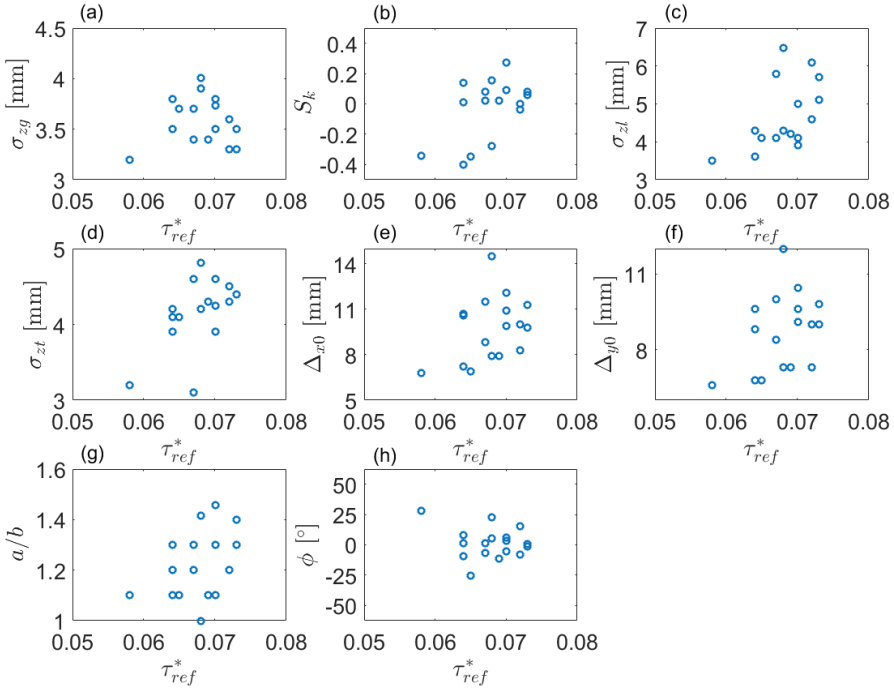

Figure 8.2.7: Relation between bed characteristic and its associated dimensionless reference bed shear stress. Bed characteristics are either the grain roughness (σ_{zg}), the PDF skewness (S_k), the longitudinal bedform roughness (σ_{zl}), the transverse bedform roughness (σ_{zt}), the longitudinal structure length (Δ_{x0}), the transverse structure length (Δ_{x0}), the parameters for grain preferential orientation (a/b and Φ).

8.3 Dynamics over an infiltrated bed

This section relates the results concerning the bimodal beds, namely the hybrid gravel beds infiltrated with sand (H-G/S), with fine sand (H-G/FS) and with medium silt (H-G/Ms).

8.3.1 General results

Figures 8.3.1 and 8.3.2 show examples of flows and sediment transport evolutions during a H-G/FS, H-G/Ms and H-G/S experiments. As for the L-G and P-G beds (Figure 8.2.1), the bedload rates for H-G/FS and H-G/Ms beds follow the water discharge with a single-peak shape. The bedload in-

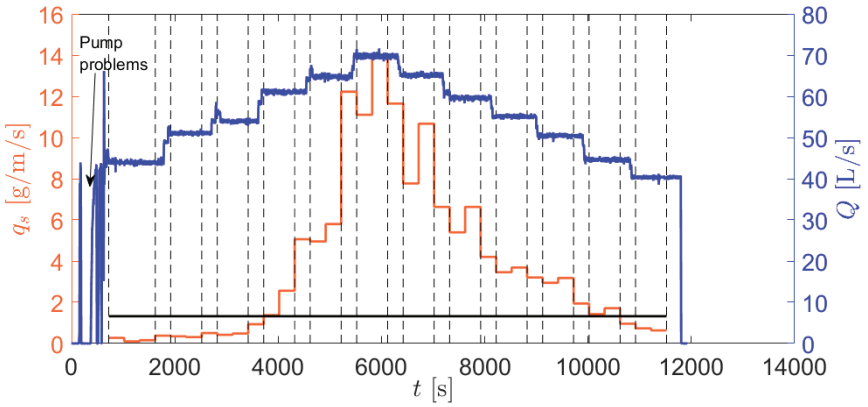

(a) H-G/FS-8

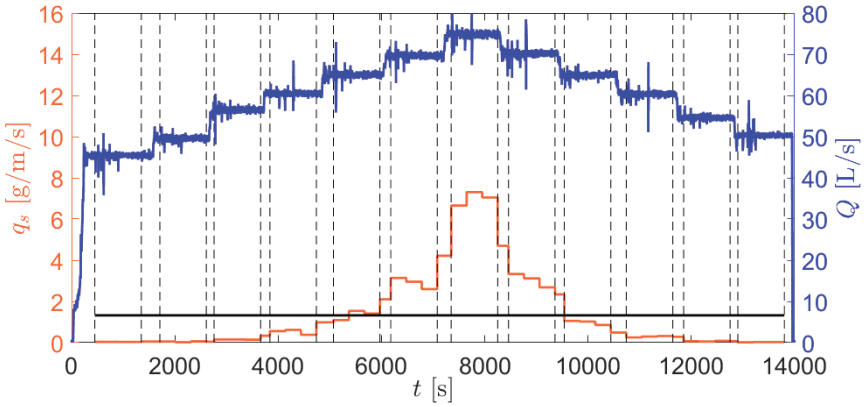

(b) H-G/Ms-5

Figure 8.3.1: Time variations of bedload (q_s) and flow (Q) rates for H-G/FS-8 and H-G/Ms-5 experiments. Grid delimits steady states from transitions zones. Black horizontal line corresponds to the reference transport rate $q_{s\text{-ref}}$. The left axis refers to the bedload rate (orange) and the right axis refers to the water discharge (blue).

tensity seems to differ between the two types of experiments and between the rising and falling limbs of the hydrograph. The shape of bedload evolution for H-G/S appears to be different than the ones of the other beds, namely a two-peak shape (Figure 8.3.2a). Considering the high transport rate during this experiment, a duration of 8 minutes was chosen for the plateaus to prevent from strong erosion. Two bedload samples of 4 minutes were collected during each plateau. The first peak of high bedload rate occurred at very low water discharge and was probably caused by the presence of a seal of sand. The second peak appeared at a water discharge of around 60 L/s, similarly to the increase in bedload observed for the L-G bed of the experiment couple n° 7 (Figure 8.3.2b). Nevertheless, the bedload rate was six-time higher in case of sand presence (Figure 8.3.2a).

Figure 8.3.3 shows all the results obtained on bimodal beds, revealing how fine sediments affect the bedload rate. As in Figure 8.2.2, the dimensionless bedload rate is represented as a function of the total dimensionless bed shear stress. Rising limbs are still separated from falling limbs for clarity. Previous areas defined for unimodal beds (Figure 8.2.2) are recalled in Figure 8.3.3 for comparison.

Experiments on hybrid beds clogged with cohesive sediments (H-G/Ms beds) gather in the area that previously corresponds to the P-G bed area during the rising limb. In our experiments, clogging with cohesive fine sediments has similar effects on bed mobility as gravel arrangement. Table 8.3 shows that τ^*_{ref} was about 12 % higher for hybrid beds infiltrated with cohesive sediments compared to non-infiltrated beds. In addition, data from H-G/Ms-6 have the same behaviour than the other data from H-G/Ms experiments, even if the bed resulted from an initial P-G bed. The lack of differences within hybrid beds is once again verified. During the falling limb, data tend to join the L-G bed area, except for H-G/Ms-5. This exception will be discussed later.

Bedload rates during the rising limb of experiment on H-G/FS bed were similar to those observed during the falling limb for L-G beds (close to the intersection area), indicating that FS has no influence on gravel dynamics. Table 8.3 shows that τ^*_{ref} for a H-G/FS is equal to the average of τ^*_{ref} values for loose beds, when looking at the rising limb. L-G and H-G/FS behave thus

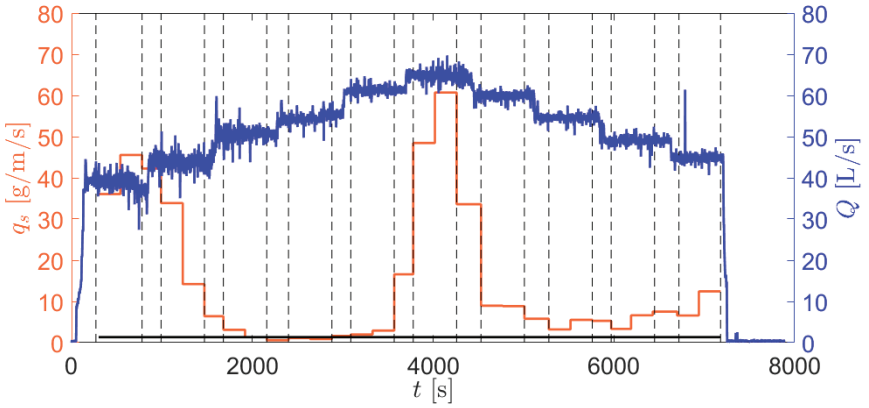

(a) H-G/S-7

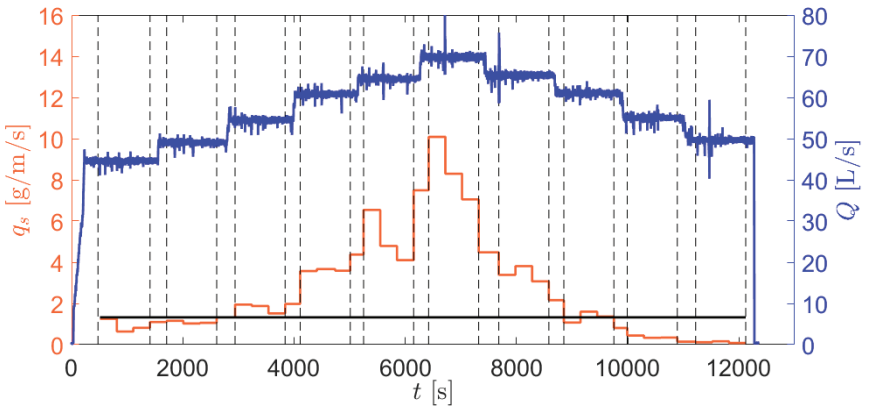

(b) H-G-7

Figure 8.3.2: Time variations of bedload (q_s) and flow (Q) rates for the experiment couple n° 7: H-G/S-7 and L-G-7. Grid delimits steady states from transitions zones. Black horizontal line corresponds to the reference transport rate $q_{s\text{-ref}}$. The left axis refers to the bedload rate (orange) and the right axis refers to the water discharge (blue).

similarly during the rising limb. However, during the falling limb, H-G/FS bed behave differently. Data remained in the same area as during the rising limb, but τ^*_{ref} is smaller, indicating an influence of FS sediments on bedload rate. The evolution of bedload follows a counter-clockwise loop, which was not the case for L-G experiments.

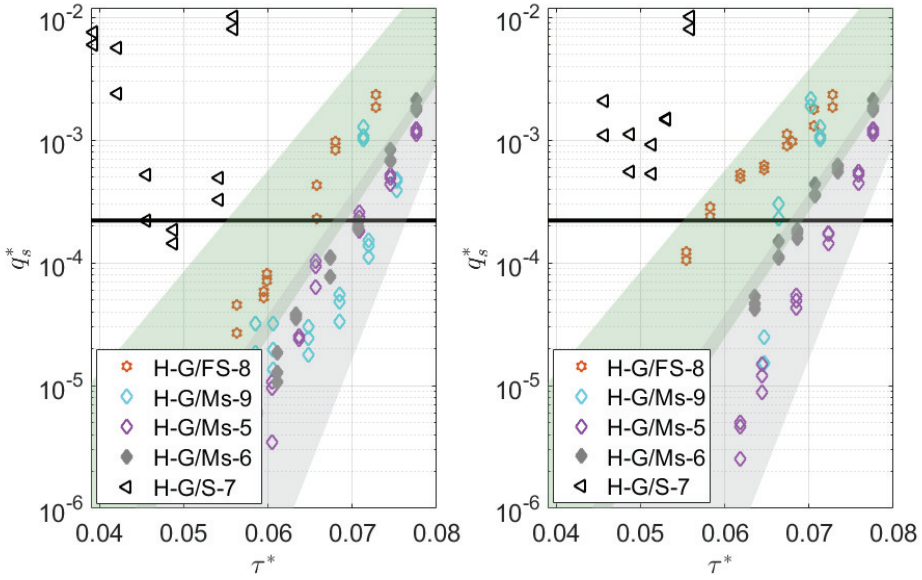

(a) Rising limb **(b)** Falling limb

Figure 8.3.3: Evolution of the dimensionless bedload rate as a function of the dimensionless bed shear stress for bimodal beds with different fine sediment infiltration: (a) at the rising limb and (b) at the falling limb. Green and grey shaded areas are the same as the one presented on Figure 8.2.2. The black horizontal line corresponds to the dimensionless reference low transport rate $q^*_{s\text{-ref}} = 2.2\times10^{-4}$.

For the gravel bed infiltrated with sand (H-G/S-7), the highly scattered bedload rates make the results difficult to interpret. Figure 8.3.3 shows a new area for the H-G/S experiment, with high bedload rates for τ^* values being much lower than those for the other experiments. The gravel transport rate is clearly enhanced in presence of a seal of sand. For this experiment, no single dimensionless reference bed shear stress could be defined during the rising and falling limbs.

Table 8.3: Dimensionless reference bed shear stress for each experiment conducted on bimodal beds, except for H-G/S-7.

Experiment	$\tau^*_{\text{ref-R}}$ [-]	$\tau^*_{\text{ref-F}}$ [-]	Experiment	$\tau^*_{\text{ref-R}}$ [-]	$\tau^*_{\text{ref-F}}$ [-]
H-G/FS-8	0.064	0.058	H-G/Ms-5	0.071	0.073
			H-G/Ms-9	0.072	0.067
			H-G/Ms-6	0.070	0.069

$\tau^*_{\text{ref-R}}$ represents the dimensionless reference bed shear stress during the rising limb; $\tau^*_{\text{ref-F}}$ denotes the dimensionless reference bed shear stress during the falling limb.

8.3.2 Hysteresis effect

Figure 8.3.4 illustrates the hysteresis patterns of the bimodal experiments. For H-G/FS bed experiment, the bedload evolution draws a counter-clockwise loop. The transport during the falling limb was thus easier than the one during the rising limb. During the rising limb, bedload rates for H-G/FS bed were similar to the ones for L-G beds suggesting that no fine sand influence was present. During the experiment, fine sediments were rapidly washed from the surface and progressively from the subsurface. The washed out sediments were still present in the flow because recirculated with the water. At the falling limb, FS reached a sufficient concentration within the water column for gravels and fine sediments to interact. The flow was more concentrated in very fine sediments, lubricating the bed.

Data from H-G/Ms tests follows counterclockwise hysteresis, meaning that the transport of gravel is enhanced during the falling limb, except in the H-G/Ms-5 test that shows a clockwise hysteresis. During the rising limb, Ms is more difficult to wash out of the bed surface than FS because of its cohesion. Gravel mobility is reduced due to the presence of cohesive Ms. During the falling limb, the infiltrated bed was partially cleaned from Ms, and then tends to behave like a clean H-G bed. The hysteresis patterns seem to change according to the fine sediment residence time (T_r). This residence time corresponds to the time during which the fines were present in the drained gravel matrix before the beginning of the sediment transport experiment (see Figure 3.2.2, the time between steps (3b) and (4)). The longer this time is, the less erodible the bed material is. When the bed was

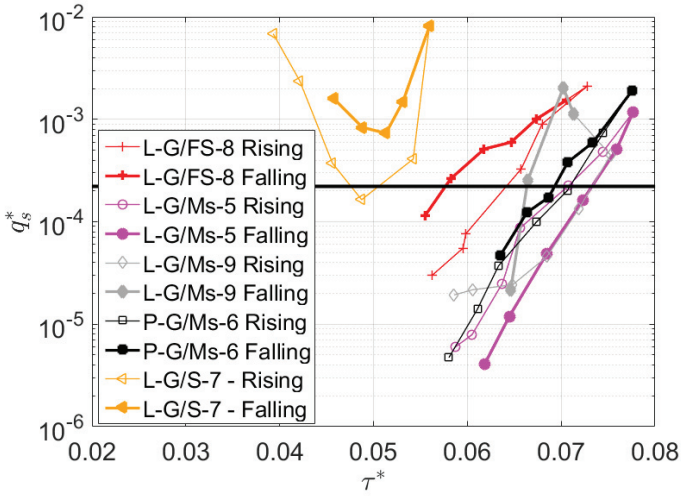

Figure 8.3.4: Bedload hysteresis patterns for the different tests performed on bimodal beds. The black horizontal line corresponds to $q_{s\text{-ref}}$. Empty and filled symbols represent bedload rates during the rising and falling limb, respectively.

drained, the water content within the bed matrix decreased and the fine sediments strongly consolidated. Clockwise hysteresis patterns was observed for the experiment having the longest fine sediment residence time (12 days for H-G/Ms-5 in comparison to 5 and 3 days for H-G/Ms-6 and H-G/Ms-9 tests, respectively). After removing fine sediments from the bed surface and transporting some gravels of the first bed layer during the rising limb, the flow in experiment H-G/Ms-5 encountered strongly consolidated fine sediments located on the subsurface during the falling limb. It was easier to de-clog the bed surface than the bed subsurface. This led to a reduction in bedload rate during the falling limb. Based on the results, T_r appeared to be an important parameter.

For H-G/S-7 experiment, no hysteresis loop was identifiable, reflecting the complexity of this case.

8.3.3 Impact of geotechnical bed properties

H-G/FS and H-G/Ms beds are both infiltrated from the bottom-up with fine sediments having similar grain sizes. However, the results show that the

presence of fine sediments affected differently the gravel mobility. FS and Ms sediments have actually opposite effects on bedload rates. In presence of Ms sediment, the transport was reduced, whereas in presence of FS sediments, the transport was enhanced. The size of the fines is therefore not the only parameter to be considered when studying infiltrated beds. The geotechnical properties of the gravel matrix can change depending on the type of infiltrated fine sediments (Table 2.2). Bed permeability, consolidation and fine sediment shape are also important parameters controlling q_s.

Bed permeability k is mainly depends on the grain size and particle shape of the coarse and fine particles. Previous studies have put forward the impact of changes in bed permeability on hydraulic roughness (Manes et al., 2009; Hamm et al., 2011). Hamm et al. (2011) measured bed shear stresses in open-channel flows over permeable beds formed by glass beads (median diameter: 1.5 mm) or cobbles (diameters: 3 - 10 cm) and found them to be 1.5 to 2 times higher than those for impermeable beds in equivalent hydraulic conditions. This effect has been attributed to the momentum balance associated with water exchange across the sediment-water interface (Manes et al., 2009). This increase in bed shear stress facilitates sediment movement for permeable beds. In permeable beds, the bed shear stress is distributed over a finite depth instead of a surface as in an impermeable bed. The observation of the in-bed water velocity profile suggests that this depth is limited to one or two grain diameters and that most of the shear stress is applied on grains of the first bed surface layer (Leonardson, 2010). In impermeable beds, the bed shear stress acts predominantly on the upper part of the surface grain, whereas in the case of permeable beds, it acts on the whole surface grain, therefore enhancing grain motion. In our study, beds infiltrated with fine sediments from the bottom-up have similar bed permeability (see the k parameter in Table 2.2), which are much smaller than in the case of L-G beds. In addition, their permeability Reynolds numbers (Re_k smaller than 1) suggests that they can be considered as impermeable beds (Breugem et al., 2006; Manes et al., 2009). On the contrary, L-G beds are considered as permeable beds (high values of Re_k). Gravel mobility should be reduced on H-G/Ms and H-G/FS beds compared to L-G beds. However, Figure 8.2.2 and Figure 8.3.3 show that this was not always the case. If L-G beds (permeable) were put into motion with

more ease than H-G/Ms beds (impermeable), the opposite behaviour was observed between L-G beds (permeable) and H-G/FS bed (impermeable). Therefore, other factors than bed permeability may also control the bedload rate.

The decreased erodibility of a H-G/Ms bed can be attributed to a change in bed stability due to the higher consolidation caused by the presence of fine sediments (see C_u in Table 2.2) rather than a change in bed shear stress profile due to bed permeability. The H-G/FS bed was not consolidated (Cu = 0) compared to beds formed with Ms. The latter consolidates the gravel matrix and prevents gravel from moving. It is important to recall that C_u, the parameters characterizing the intensity of the consolidation, varies with the water content within the bed. H-G/Ms beds with the longest fine sediment residence time are the ones with the lowest bedload rate. This observation is consistent with the assumption that the bedload rate decreases with the increase in bed material consolidation. The longer the residence time, the weakest is the water content of the bed material and thus, the more C_u becomes significant.

The bedload rate difference between H-G/Ms and H-G/FS bed experiments might also be linked to the shape of fine sediments. Several authors have investigated the effect of grain shapes of coarse sediments on bed shear stress (Li and Komar, 1986; Durafour et al., 2015). They found that particles with non-spherical shapes (flat, angular or elongated) have stronger imbrication patterns than spherical particles. Li and Komar (1986) showed that the bed shear stress required to put into motion non-spherical material might be up to six times higher than the one for moving spherical particles. Durafour et al. (2015) observed that changes in bed shear stress were controlled by changes in sediment circularity index (C_I). Transposing these findings for coarse particles to fine particles used in this study could explain why H-G/FS beds were easier to move than H-G/Ms beds. Ms sediments ($C_I = 0.75$) contributed to consolidate the bed because of their shape, reducing the sediment transport as opposed to spherical FS sediments ($C_I = 0.99$). The significant dispersion of the GSD of Ms (Table 2.1) probably also reduces the porosity and enhances the bed consolidation. In addition, the increase in erodibility of H-G/FS bed may be attributed to a decrease in bed

stability due to lubrication effect of the circular FS sediments washed out of the gravel matrix.

8.3.4 Importance of fine sediment concentration

Tests showed that gravel transport increased in presence of cohesionless fine sediments within the bed (fine sand and sand). This observation is consistent with previous studies (Jackson and Beschta, 1984; Ikeda and Iseya, 1988; Wilcock et al., 2001; Curran, 2007; Koll et al., 2010; Li et al., 2016). This enhancement is often associated with a reduction of the mean grain diameter characterizing the overall bed. This reduction depends directly on the fine sediment concentration in the bed (Jackson and Beschta, 1984; Wilcock et al., 2001; Hassan and Church, 2000).

In our case, the bedload rate was higher in the presence of sand than in the presence of fine sand. Yet, the mean grain diameter of the bed was lower for the H-G/FS bed than for the H-G/S bed. Therefore, previous indicators might not be suitable for characterizing gravel transport with infiltrated beds.

In the H-G/FS experiment, gravel transport was not influenced by the presence of fine sediments during the rising limb, whereas during the falling limb it increased (Figure 8.3.3). Yet, we expect the GSD of the overall bed surface to increase as part of the fines are washed out. The increase in sediment transport might be explained by the fact that between the rising and falling limbs, the fine sediment concentration within the flow increased due to the re-suspension of fine particles. The concentration within the transport layer was therefore higher (i.e. the concentration reached 1 g/L during the falling limb). The transport layer is a thin layer at the bed surface, where gravels are transported and where interactions between fine and coarse sediments are present.

For H-G/S bed, the concentration in sand within the transport layer was largely higher than for the H-G/FS bed entraining a higher bedload rates. This is consistent with Wilcock and Crowe (2003) observations which predict higher bedload rate when concentration of fine sediments reaches 30 %. Below this reference value, the bedload is modified but with less intensity. This could explain why gravels of H-G/FS bed were less transported than the

ones of H-G/S bed. Fine sediment concentration within the transport for H-G/FS was much lower than 30 %, but concentration was still sufficient to affect the bedload rate. In addition, in case of H-G/FS experiment, the fine sediments were circular, which enhances the lubrication of the gravel particles in the transport layer. The shape of the fine sediments within the transport layer could be also an important parameter controlling the gravel dynamics. Regarding the results, we think that what matters for bedload rate enhancement is the fine sediment content in the transport layer and not in the bed as well as the shape of the fine sediments.

The content of fine sediments will depend on their transport mode: bedload (e.g. sand) or suspension (e.g. FS). Higher concentrations within the transport layer are reached if fine sediments move as bedload (H-G/S bed experiment) in comparison to when they are transported in suspension (H-G/FS bed experiments). That is why, the gravel transport rate was higher for the H-G/S bed experiment.

The H-G/S tests was also used to put forward the importance of considering the time-variation of fine sediment concentration within the transport layer when studying gravel transport. Because gravel transport depends on the fine sediment concentration, it is important to evaluate its temporal evolution. Knowing fine sediment distribution within the bed (linked to the type of infiltration) will help the prediction of the temporal evolution of the volumetric fine sediment concentration within the transport layer ($c^*_{f\text{-TL}}(t)$). The fine sediment distribution is linked to the type of infiltration so to the ratio between coarse and fine particles (D_{15}/d_{85}). We suggest taking into account $c^*_{f\text{-TL}}(t)$ in new bedload predicting models.

8.4 Summary of the results and methodology for bedload prediction

In this thesis, we proposed original experiments that enable to visualize and understand the different mechanisms responsible for gravel movements, and to estimate the reference bed shear stress in different bed configurations. Using all the experimental results, a diagram describing the phenomenological

evolution of different beds responding to similar bed shear stresses is presented. Then, some recommendations were suggested to improve bedload predictions. The proposed methodology is discussed and validate using an in-situ experiment presented in Section 10.

8.4.1 Summary of the results

Figure 8.4.1 shows a schematic temporal evolution of different beds. Response of various beds to a similar bed shear stress time series are plotted. The diagram focuses on significant steps generating substantial changes in the bed matrix characteristics and in the sediment transport rate. These key steps are characterized by the times $T0$ to $T5$. In one line, an absence of box means that no significant change occurred between the time considered and the previous time. τ^*_{ref} are represented with horizontal bold color lines and plotted on the evolution graph (t, τ^*) for each type of bed. The latter are not quantitative values but are located on the (t, τ^*) graph in order to be compared qualitatively with each other. Each color is associated with one specific bed (see colors of the box edges). $\tau^*_{\text{ref-R}}$ corresponds to the dimensionless bed shear stress for which the initiation of motion during the rising limb was observed and $\tau^*_{\text{ref-F}}$ corresponds to the dimensionless bed shear stress for which the cessation of sediment motion was observed during the falling limb. The bed arrangement and the degree of clogging described at $T5$ refers to the final bed state T_f. These results in terms of reference bed shear stress can be transposed in terms of reference water discharge at least for L-G and P-G bed experiments (see the comparison between Figure 8.2.2 and Figure 8.2.5). The evolution is the same.

Loose and Packed beds (L-G and P-G)

Focusing on the red and black bed boxes in Figure 8.4.1, one can see that a loose bed is put into motion ($T2$) before a packed bed ($T3$). Between $T2$ and $T5$, the sediment transport rate for loose bed is higher than the reference value. During this time lapse, the L-G bed packs and organizes itself. The resulting bedload rate during the falling limb is lower than during the rising limb for the same bed shear stress (clockwise hysteresis). The

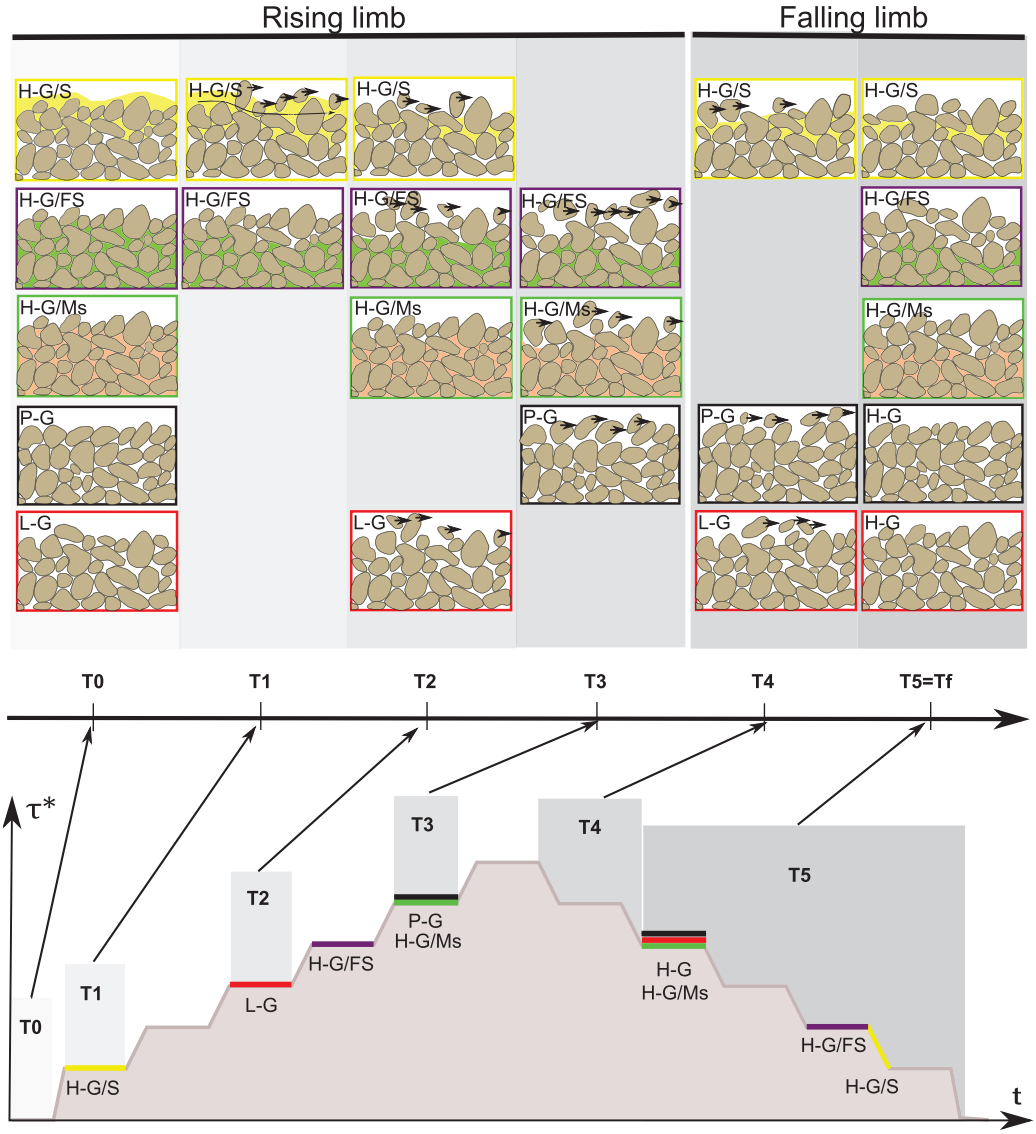

Figure 8.4.1: Description of the different bed evolutions during a hydrograph. Each line in the upper part describes how a specific bed evolves during the hydrograph schematized below. A color is attributed to each bed type (contour of the box). Key times in this evolution are denoted $T0$ to $T5$ and represented by shaded columns on both hydrograph and upper part of the diagram. A missing box in the line means that no change occurred between the time considered and the previous time. Horizontal color lines on the hydrograph correspond to $\tau^*_{\text{ref-R}}$ and $\tau^*_{\text{ref-F}}$ for each bed type. Arrows inside the boxes represent gravel transport. They are not scaled according to the sediment transport intensity.

opposite behavior is observed for the P-G bed (counterclockwise hysteresis), meaning that the flow has probably started to break some grain arrangement initially present on the bed surface ($T3$ - $T4$). The final states ($T5$) of both beds tend to become similar as well as $\tau^*_{\text{ref-F}}$. A hybrid bed H-G is obtained.

Beds infiltrated with medium silt sediments (H-G/Ms)

The following description of the H-G/Ms behaviour is suitable for both hybrid beds resulting from an initial loose bed or packed bed. At the beginning of the rising limb ($T0$ - $T1$), gravel particles forming the H-G/Ms bed (green boxes) are totally surrounded by fine consolidated sediments. The bed surface layer of the matrix is first washed of its fine sediments ($T2$). At $T3$, gravel is transported at the same $\tau^*_{\text{ref-R}}$ as the P-G bed while fine sediments are still washed of the bed. In our experiments, cementation and packed arrangement have effects of similar magnitude on gravel transport. During the falling limb, the bed behaves in the same way as a H-G bed. At $T5$, the H-G/Ms bed surface tends to become similar to the H-G bed surface, as well as the associated $\tau^*_{\text{ref-F}}$.

Beds infiltrated with fine sand sediments (H-G/FS)

The H-G/FS bed (purple boxes) evolves similarly to a H-G bed during the rising limb, because the fine sediments are quasi-instantaneously ($T1$) washed out of the bed surface. FS sediments are easily put in suspension because they are non-cohesive and have a small Rouse number ($R_o = w_s/\kappa u^* \approx 0.1$). As the dimensionless bed shear stress peak is reached, more and more FS sediments are put into suspension, causing an increase in fine sediment concentration in the flow ($T3$). It is important to keep in mind that FS was recirculated with water in our installation. This high concentration lubricates the bed surface, enhancing the gravel transport ($T3$ - $T4$). The shape of FS sediments is spherical (Figure 2.3.2), which may favor this lubrication. During the falling limb, no strong organization is observed. The significant gravel transport prevents from particle organization. If conditions of low bedload rates were longer, grain organizations might appear. The final state (T_f) of the bed surface is significantly loosen with a reference bed shear stress

$\tau^*_{\text{ref-F}}$ lower than the other cases described above.

Beds infiltrated with sand sediments (H-G/S)

The bedload evolution for the H-G/S bed (yellow boxes) is marked by two main stages. First, at low dimensionless bed shear stresses during the rising limb ($T1$), the bed surface is highly concentrated in sand, which lubricates and facilatates gravel particles rolling around their neighbours. The equal mobility phenomenon was observed, meaning that gravel particles are transported as easily as sand (Parker et al., 1982). The highly concentrated sand layer starts moving as bedload on the bed surface. The moving sand particles collide with gravel particles, destabilize them and finally entrain them. As the sand layer is washed out of the bed surface, gravel transport rate decreases. Although there was a sand feeding during this experiment, it was not sufficient to maintain a large enough concentration at the surface layer; consequently the gravel transport rate decreased. Once the bed shear stress reaches the reference value ($\tau^*_{\text{ref-R}}$) found for the L-G beds, gravels are transported significantly once again ($T2$). Even if the sand concentration infiltrated into the bed is relatively low compared to what was on the bed surface at the beginning of the experiment, it is still enough for increasing drastically the gravel transport rate ($T3$ - $T5$). The intensity of this effect may be attributed to the fact that both sediments (sand and gravel) are transported as bedload.

8.4.2 Methodology/recommendations for bedload prediction

Toward a new bedload model

The analysis of the summary of the experimental results enables to put forward the important mechanisms governing the bedload rate. It gives clues for starting to build a new sediment transport model.

Generally, two main difficulties appear when applying a bedload model. The first difficulty is linked to the estimation of the efficient bed shear stress for transporting sediment, and so of the hydraulic roughness k_s to be used

in the model. We have seen in Section 5.3 that k_s was generally estimated using a representative grain size of the bed material and that it might not be the best parameter to use (Section 8.2.3). The second difficulty is related to the choice of the reference dimensionless bed shear stress that will characterize the incipient motion (τ^*_{ref} could be taken as equal to τ^*_{cr} in some studies). Throughout this study, we have seen that τ^*_{ref} is highly subjected to uncertainties and dependent on methodological procedures and initial experimental set-up conditions.

Besides the usual consideration of the grain size and grain density, previous authors identified several factors to take into account when predicting bedload. For example, Wilcock et al. (2009) argued that bedload rate depends on several variables describing the fluid, the sediment mixture and the flow resistance. These variables are presented in Equation 8.8.

$$q_s = f(\tau, D_G, D_{\text{mix}}, \rho_s, \rho, \mu, f_G) \tag{8.8}$$

where D_G is the representative diameter of the considered size fraction (in our case the gravel fraction), D_{mix} is the representative diameter of the mixture and f_G is the proportion of the considered size fraction grains in the bed.

In this study, other impacting parameters linked to the bed topography and presence of fine sediments were put forward. Concerning the bed topography, we noticed that a change in bed surface arrangement could have strong impact on the bedload rate. We also noted that a change in bed arrangement could influence not only the flow resistance but also the bed stability. That is why, we suggest taking into account the bed topography in future sediment transport model. τ^*_{ref} and k_s depend thus on several indicators assessing for bed surface organization as explained in Section 8.2.3.

We also focused on the presence of fine sediments, which impacts directly the entire composition of the bed matrix. We showed that fine sediment presence affects the geotechnical properties of the bed, and so may affect τ^*_{ref} and k_s. For example, we observed that changes in bed permeability might impact the flow resistance whereas changes in bed cohesion modify the bed stability. That is why, we recommend including the bed permeability k and the cohesion parameter C_u depending on the fine sediment residence time

in future models. In our experiments, bed cohesion has a stronger influence on bedload than differences in bed permeability. Each parameter must be weighted differently in future models. We also propose to take into account the particle shapes of the bed material which inform about the degree of bed consolidation. The circularity index of fine ($C_{I-\mathrm{f}}$) and coarse ($C_{I-\mathrm{c}}$) sediment composing the bed material can be retained as an indicator of bed consolidation.

In addition, we saw that depending on the fine sediment concentration within the transport layer, the gravel transport was modified. We suggest adding $c^*_{f\text{-TL}}$ in future models, which refers to the volumetric concentration in fine sediments in the transport layer varying in time. To evaluate this parameter, we pointed out that knowing the ratio between fine and coarse sediments (D_{15}/d_{85}) was important. It helps to predict the type of infiltration (bottom-up or sealing) and consequently to predict the fine sediment distribution within the matrix. During an episode of sediment transport, the bed will erode and will face diverse fine sediment concentrations. The bedload will be thus affected. We highlighted that fine sediments moving as bedload are more efficient to lubricate gravels in comparison to those in suspension. That is why, we also recommend to take into account the Rouse number in models which informs about the capacity of a sediment to be put in suspension. It defines the limit between bedload and suspension.

Using our results, a new dimensionless analysis is presented in Equation 8.9, q_s should at least depend on the following variables:

$$q^*_s = f(\tau^*, \tau^*_{\mathrm{ref}}) \tag{8.9}$$

where τ^* depends on the flow velocity and k_s and τ^*_{ref} depends on bed arrangement and fine sediment presence:

$$k_s = f(\frac{\sigma_{zg}}{D_{50}}, S_k, \frac{\sigma_{zl}}{\sigma_{zg}}, \frac{\sigma_{zt}}{\sigma_{zg}}, \frac{\Delta_{x0}}{\Delta_{y0}}, \frac{\Delta_{y0}}{W}, \frac{a}{b}, \Phi_{rad}, k, 1+C^*_u, c^*_{f\text{-TL}}, C_{I-\mathrm{c}}, C_{I-\mathrm{f}}) \tag{8.10}$$

$$\tau^*_{\mathrm{ref}} = g(\frac{\sigma_{zg}}{D_{50}}, S_k, \frac{\sigma_{zl}}{\sigma_{zg}}, \frac{\sigma_{zt}}{\sigma_{zg}}, \frac{\Delta_{x0}}{\Delta_{y0}}, \frac{\Delta_{y0}}{W}, \frac{a}{b}, \Phi_{rad}, k, 1+C^*_u, c^*_{f\text{-TL}}, C_{I-\mathrm{c}}, C_{I-\mathrm{f}}) \tag{8.11}$$

where Φ_{rad} is the rotation angle of the chosen 2D structure function contour

line in radian and C_u^* is the dimensionless bed cohesion:

$$C_u^* = \frac{C_u(T_r)}{(\rho_s - \rho) g d_{50}} \tag{8.12}$$

Dimensionless analysis constitutes generally the preliminary step before developing a model. Further step would be to collect more data in different conditions to actually be able to develop a new model and reduce the number of determining variables.

In Equations 8.10 and 8.11, $c^*_{f\text{-TL}}$ depends mostly on the coarse/fine diameter ratio (D_{15}/d_{85}) and on the Rouse number (R_o). To ensure the validity of the dimensional analysis even when there is no cohesion within the bed, $1 + C_u^*$ was preferred instead of C_u^*. Based on our results, we assume that k_s, informing about the flow resistance and τ^*_{ref}, informing about the bed stability, depend on the same parameters. Our dataset was not sufficient to reduce the list of determining variables. Nevertheless, based on our observations, some parameters seem to impact more the bed stability than the bed mobility (flow resistance) and inversely. We think that the cohesion/consolidation is more determining for the estimation of τ^*_{ref} as well as the fine and coarse particle shapes. For the calculation of k_s, the impact of the coarse particle shape might have been considered within the geometrical roughness parameter σ_{zg}. k influences probably more the flow resistance than the bed stability. In Equations 8.10 and 8.11, some variables might be redundant as for instance bed arrangement parameters. Unfortunately, we are missing data for confirming these assumptions and doing correlation analyses between parameters.

Methodology to improve bedload prediction

As said before, we were not able to build an explicit bedload prediction model using our experimental results. However, based on our experiments and on previous studies (Wilcock and Crowe, 2003; Hassan et al., 2006; Jain and Kothyari, 2009; Recking, 2009) we were able to develop a methodology for improving bedload prediction in gravel-bed rivers.

The methodology is based on the adjustment of τ^*_{ref}, which is a key parameter in bedload models, according to the bed arrangement and gravel

matrix composition. It is described in the following and recapped in the Figure 8.4.2. It is important to note that this methodology typically depends on the bedload model used for the prediction of bedload and more specifically on the definition of τ^*_{ref} in the model.

The methodology can be summarised as follows:

1. Estimate $\tau^*_{\text{ref}} = \tau^*_{\text{ref1}}$ as a function of the chosen bedload formula (e.g. Meyer-Peter and Müller, 1948) and assume that it refers to the τ^*_{ref} for loose gravel beds. For example, if τ^*_{ref} is assumed equal to the critical dimensionless bed shear stress τ^*_{cr} (Shields, 1936) in the formula, the gravel GSD and existing diagrams or equations can be used to calculate its value (Yalin and Karahan, 1979; Soulsby and Whitehouse, 1997).

2. Determine the characteristics of the studied gravel-bed: the level of bed arrangement, the degree of clogging and the type of bed infiltration.

3. Adjust τ^*_{ref1} according to bed configuration:

   - from 0 to +12 % according to the level of arrangement,
   - from 0 to +12 % according to the level of consolidation,
   - and from -40 to 0 % according to the concentration of non-cohesive fine sediments in the transport layer.

   These percentage values are given as an indication and are deduced using our laboratory results (Table 8.1 and Table 8.3). They were calculated using the percentage of difference of τ^*_{ref} between experiments from the same couple of experiments. An average is made for each type of couples (loose versus packed and non infiltrated versus infiltrated (with Ms, with FS or with S). The percentage of difference could slightly increase if the arbitrary value for $q_{s\text{-ref}}$ was chosen smaller. However, the trends (i.e. increasing or decreasing τ^*_{ref}) remain the same.

4. Compute q^*_s using the new τ^*_{ref} and the chosen bedload formula.

We do not claim that the above methodology provides quantitative values for τ^*_{ref}. Even if the first estimate of τ^*_{ref} is mistaken, the recommended relative adjustment should still be valid and coherent. Further studies with

different sediments (e.g. with a GSD more scattered, with more cohesive fine sediments) and hydraulic conditions should be tested to validate the given qualitative ranges of adjustments. The final bedload trends are in coherence with those found in previous studies, namely a decrease in q_s with strong bed arrangement (Hassan et al., 2006; Guney et al., 2013) and in presence of cohesive fine sediments (Jain and Kothyari, 2009; Barzilai et al., 2013) and an increase in q_s in presence of non-cohesive fine sediments (Wilcock and Crowe, 2003; Curran and Wilcock, 2005). For now, the methodology can be used to predict qualitatively the bedload behaviour, in case of arranged beds and infiltrated beds (bottom-up, bridging, cohesive and non-cohesive fine sediments). In Section 10 this methodology will be tested and verified.

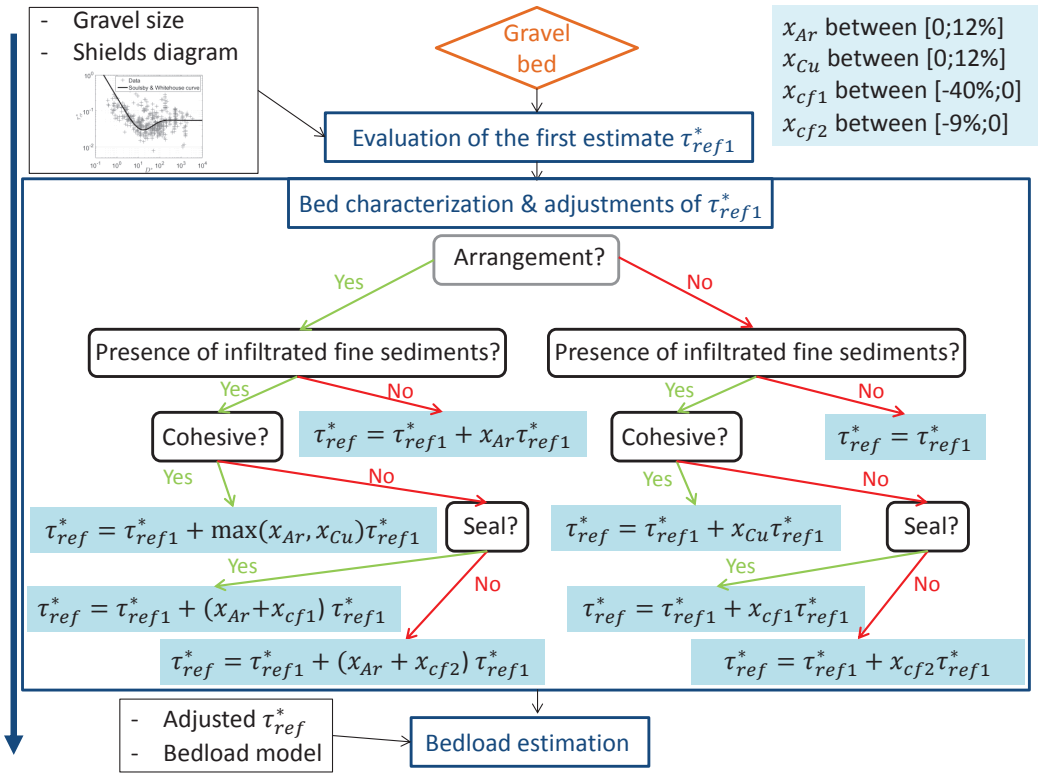

Figure 8.4.2: Methodology proposed to improve bedload prediction based on the adjustments of τ^*_{ref}. x_{Ar}, x_{Cu}, x_{cf1} and x_{cf2} are the adjustments applied on τ^*_{ref} according to the bed charaterization.

8.5 Bedload rate estimation using existing models

In this section, we evaluate some existing models for predicting bedload rate in gravel-bed rivers. Results from these models are compared to our experimental data in order to expose their limits and advantages.

8.5.1 One-state formulations

One-state formulations refer to models that characterize both the high and low transport rates with a single relationship. Two different one-state formulations were tested and compared to our experimental data:

- the Meyer-Peter and Müller (1948) formula (Equation 1.5), which is one of the most used model in engineering,
- and the Camenen and Larson (2005) formula (Equation 1.7).

The Meyer-Peter and Müller (1948) formula is based on the excess of shear stress needed to move grain. The Camenen and Larson (2005) formula is based on the ratio between dimensionless bed shear stress and dimensionless critical bed shear stress τ^*_{cr}. For the two formulations, τ^*_{cr} has to be determined. This parameter is difficult to estimate and highly uncertain. This uncertainty can lead to over or under-estimation of bedload rates.

Figure 8.5.1a and Figure 8.5.1b show the bedload rates estimated using the Meyer-Peter and Müller (1948) model and the Camenen and Larson (2005) model for different τ^*_{cr}, respectively. Our experimental data are superimposed for comparison. The Meyer-Peter and Müller (1948) formulation was not able to predict low bedload rates close to the incipient motion of gravel (defined by τ^*_{cr}). The Camenen and Larson (2005) formulation, that was initially created to overcome this problem, largely over-estimated the bedload rates. This over-estimation was observed for all the tested τ^*_{cr} values. The model was able to reproduce some of our experimental results when τ^*_{cr} =0.09. This value of τ^*_{cr} was nevertheless too high to be considered in this study. Indeed, it was larger than the dimensionless bed shear stresses generated by the flow during our laboratory experiments. In addition, only

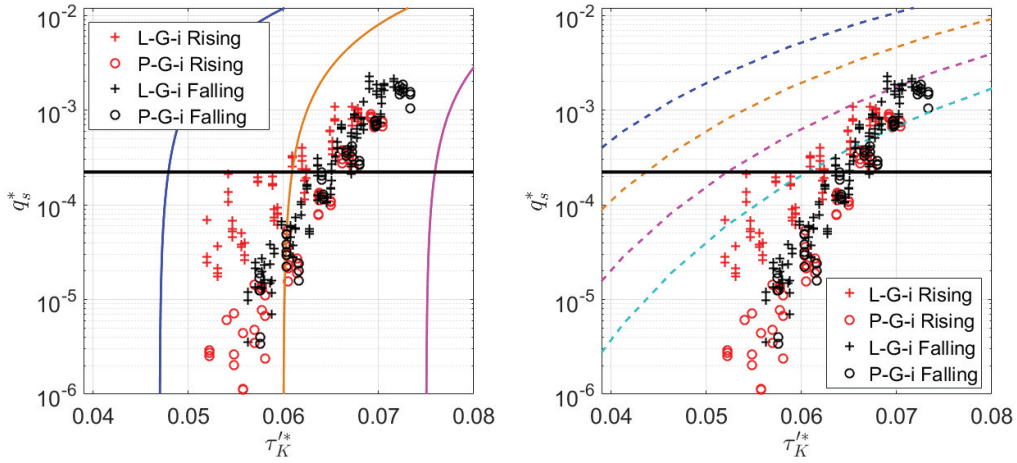

(a) Meyer-Peter and Müller (1948) **(b)** Camenen and Larson (2005)

Figure 8.5.1: Dimensionless bedload rate as a function of the dimensionless bed shear stress $\tau_K'^*$; results for loose and packed bed experiments. Red and black colors represent data during the rising and falling limb, respectively. + symbols show data related to experiments performed on loose beds. *o* symbols show data related to experiments performed on packed beds. The black horizontal line corresponds to $q^*_{s\text{-ref}} = 2.2\times10^{-4}$. The color solid lines represent the model results (a) Meyer-Peter and Müller (1948) and b) Camenen and Larson (2005)) according to the chosen τ^*_{cr} (τ^*_{cr} =0.047 for the blue line, τ^*_{cr} =0.06 for the orange line, τ^*_{cr} =0.075 for the magenta line, and τ^*_{cr} =0.09 for the cyan line.

the results over loose beds were approached with this parametrization. The loose bed case is not representative of natural rivers. These formulations are thus not adapted for complex gravel-bed rivers, in particular with bed arrangements.

Looking at Figure 8.5.1a and Figure 8.5.1b, one can see that the variation of τ^*_{cr} does not improve the bedload rate predictions. This suggests that the estimation of τ^*_{cr} is not the only point to focus on and that formulations need to be reviewed and improved as a whole. One-state formulations as those presented in this part cannot well predict both the high and low bedload rates. In this case, high bedload rates were efficiently predict at the expense of low bedload rates. Thus, the use of one-state formulas appears not adapted for such study and the methodology proposed in Section 8.4.2 did not seem

to be appropriate in that case.

8.5.2 Two-state formulations

To be able to predict both the high and low bedload rate, two-state formulations have been developed (Wilcock and Crowe, 2003; Recking, 2010). These formulations differentiate a state, which describes the high bedload rates, from another state, which characterizes the beginning of motion and low transport. These two states are governed by two different physics. For example, low bedload rates are highly influenced by a change in geometrical bed roughness, a change in bed porosity or a change in bed surface grain imbrication in contrast to high bedload rates.

The formulation of Recking (2010) was tested and compared to our experimental results:

For $\tau^*/\tau^*_{cr} < 2.3I_b^{0.08}$:

$$q^*_s = 0.00005\left(\frac{\tau^*}{\tau^*_{cr}}\right)^{12.9} \tag{8.13}$$

For $\tau^*/\tau^*_{cr} > 2.3I_b^{0.08}$:

$$q^*_s = 14\tau^{*2.45} \tag{8.14}$$

Figure 8.5.2 shows q^*_s as function of τ^* and the results obtained with the Recking (2010) model. In our experiments, the condition $\tau^*/\tau^*_{cr} < 2.3I_b^{0.08}$ was always fulfilled; so Equation 8.13 was used. As for the previous equations, τ^*_{cr} needs to be estimated. The same values as in Section 8.5.1 were used as well as τ^*_{cr} =0.055, which gives more accurate results. The predictions of bedload rates were better when using the Recking (2010) model than when using the previous one-state formulations. The τ^*_{cr} value that gave the best results was in the range of dimensionless bed shear stresses used during our experiments. The model properly approached the results obtained on the loose beds. However, the relationship $q^*_s = f(\tau'^*_K)$ for the results obtained on packed beds was still not well reproduced.

As for one-state formulations, the adjustment of τ^*_{cr} according to the bed arrangement level (loose or packed) is not sufficient for improving the bed-

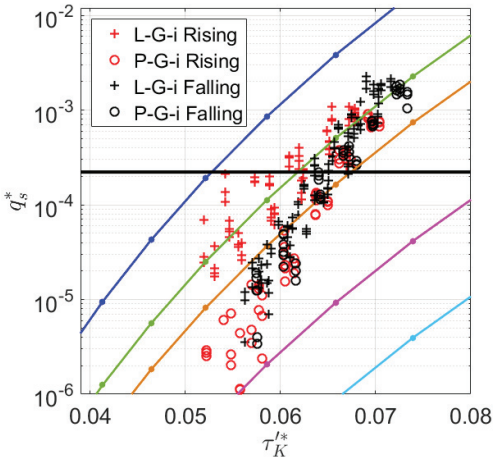

Figure 8.5.2: Dimensionless bedload rate as a function of the dimensionless bed shear stress $\tau_K'^*$; results for loose and packed bed experiments. Red and black colors represent data during the rising and falling limb, respectively. + symbols show data related to experiments performed on loose beds. *o* symbols show data related to experiments performed on packed beds. The black horizontal line corresponds to $q^*_{s\text{-ref}} = 2.2{\times}10^{-4}$. The color solid lines represent the model results (Recking, 2010) according to the chosen τ^*_{cr} (τ^*_{cr} =0.047 for the blue line, τ^*_{cr} =0.055 for the green line, τ^*_{cr} =0.06 for the orange line, τ^*_{cr} =0.075 for the magenta line, and τ^*_{cr} =0.09 for the cyan line.

load prediction. Indeed, the slopes of the $q^*_s = f(\tau'^*_K)$ relationships for loose and packed bed results are different and this difference cannot be overridden with only a variation of τ^*_{cr}. Once again, the methodology presented in Section 8.4.2 is questioned for these cases. For the results obtained during experiments performed on infiltrated hybrid beds, it seems that the adjustment of τ^*_{cr} is more relevant. Indeed, in that case, the curves do not merge at high bed shear stresses. The slopes of the $q^*_s = f(\tau'^*_K)$ relationships for non infiltrated and infiltrated hybrid beds are similar. The method is thus still of interest for such cases.

Two-state formulation improves the bedload rate prediction for loose beds at low bed shear stresses. However, such formulations still need to be reviewed by adding another parameter than τ^* and τ^*_{cr} that will take into account the effect of bed arrangement and presence of fine sediments on bedload rate. Indeed, the unique adjustment of τ^*_{cr} was found to be insufficient in case of arranged beds.

Chapter 9

Hydrodynamics at the local scale

The bed dynamics in our experiments was presented at the global scale in the previous chapter. We will now focus on the characterization of the local hydrodynamics of the different studied beds. The water-sediment interface is investigated here because it corresponds to the zone where solid transport is controlled and where turbulence is generated. Most of the momentum and mass exchanges (nutriment, sediment and pollutant) take place around this zone. In this chapter, the relation between flow and bed characteristics will be studied, with a focus on the impact of bed configuration on flow structures. The changes in hydrodynamics according to the initial bed configuration will be analysed by comparing flow resistance indicators such as the friction velocity and then examining the changes in flow structure and turbulence in the water column.

9.1 Identification of the spatial variability

A measurement at the local scale is very complex and difficult to interpret because of the spatial variability of the hydrodynamics on rough beds. Generally, a double-averaging of velocity measurements is made to overcome this variability (Nikora et al., 2001). A specific experiment was performed in order to highlight and quantify it. A loose bed was installed manually in

the flume. The slope was set at 0.3 %. The bed was then subjected to a small constant water discharge ($Q \approx 40\,\mathrm{L/s}$) during several hours. No gravel motion was detected. Twenty-five velocity measurements were conducted on a specific small zone using the Vectrino II device. Measurement points were distributed along a mesh of 5×5 cm. Before the beginning of the experiment, this zone was surveyed in order to obtain a detailed topography. Figure 9.1.1 shows the measurement locations as well as the nearby topography. The velocity measurements were realized upstream from a bump located between $x = 8.5$ and $x = 8.7\,\mathrm{m}$.

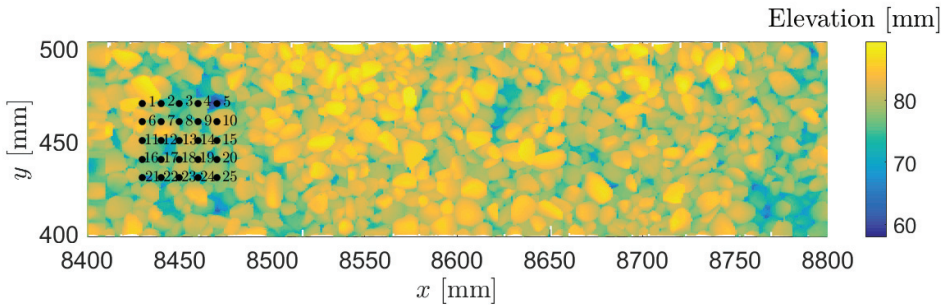

Figure 9.1.1: Locations of the 25 velocity measurements and nearby initial topography.

9.1.1 Impact of the bed spatial variability on friction velocity

Using the measured velocity profiles, friction velocities were calculated at each point (Figure 9.1.2). Three methods were tested (see Section 7.1): the log-method (u^*_{Log}), the Reynold stress method (u^*_{Re}), and the TKE method (u^*_{TKE}). The corresponding results are presented in 3 different plots (a, b and c, respectively) on which the topography was added on the background. Colored dots represent the intensity of the friction velocities.

We can first note that the variability depends on the method that we consider. This observation is confirmed when looking at Figure 9.1.3 which is in fact another representation of the spatial variability of the friction velocity according to the three different local methods. The strongest variability is

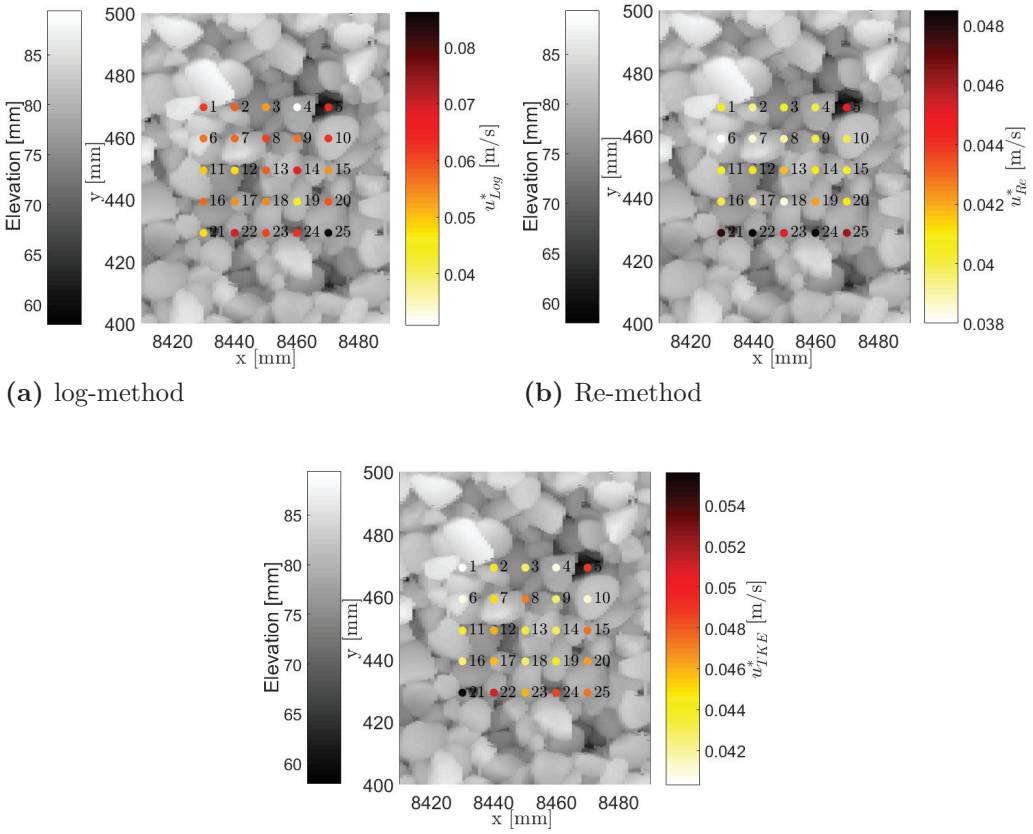

(a) log-method

(b) Re-method

(c) TKE-method

Figure 9.1.2: Friction velocity (colored dots) computed with three different methods ((a) log-method, (b) Re-method and (c) TKE-method) according to their spatial positions. The bed topography around the velocity measurement area is represented in grey scale.

observed for the friction velocities computed with the log-method (Figure 9.1.3). This variability is probably not due to topographical variations but linked to the difficulty of friction velocity estimation using the log-method. Indeed, the variability is of the order of the log-method uncertainty. In that case, u^*_{Log} can vary up to $\pm 0.01\,\mathrm{m/s}$ relative to the average value.

Friction velocities calculated with the Re-method as well as the one calculated with the TKE-method seem to be more homogeneous over the measurement area (Figure 9.1.2b and Figure 9.1.2c). As we saw in Section 7, these two methods and particularly the Re-method are less subjected to un-

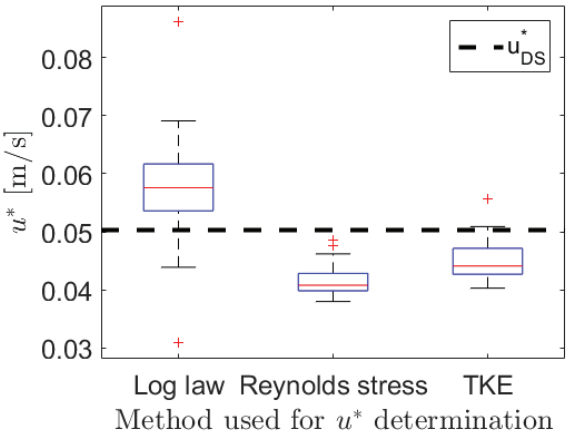

Figure 9.1.3: Box plots illustrating the spatial variations of the friction velocity computed according to the three different local methods. Values are compared with the global friction velocity calculated using the depth-slope method.

certainties. u^*_{Re} and u^*_{TKE} values vary up to $\pm 0.003\,\mathrm{m/s}$ and $\pm 0.004\,\mathrm{m/s}$ relative to their average value, respectively (Figure 9.1.3). The Re-method is less impacted by the spatial variability. In the rest of the study, the u^*_{Re} will be retained as a reference flow resistance indicator for local analysis (see Section 7.3), although these values seem to differ strongly from the global reference values obtained with the depth-slope equation, u^*_{DS} (around 15 % smaller, see Figure 9.1.3).

Despite the differences between the 3 methods, we can notice that friction velocity is more intense in line 5 (measurement points from 21 to 25) and in the upper right corner (measurement point: 5). All these points are located on a trough. This observation makes us think that the nearby topography impacts the velocity profiles and so the friction velocity. In our experiment, the changes in bed topography were small. Nevertheless, we tried to relate the friction velocity intensity with local topographical parameters, such as the nearby roughness (standard deviation of the PDF of bed elevations), the nearby degree of armoring (skewness of the PDF of bed elevations) and the nearby mean bed level. These parameters were computed on different area sizes that could potentially influence the measurement. Areas were either centered around a single measurement point, or located just upstream or

downstream (Figure 9.1.4). In that way, we expected to determine which of the upstream or the downstream topography influence the most the hydrodynamics. Lengths (L_A) and widths (l_A) of the areas were defined according to the median grain size, D_{50}. The sizes of the explored areas varied from 1 to 12×D_{50}.

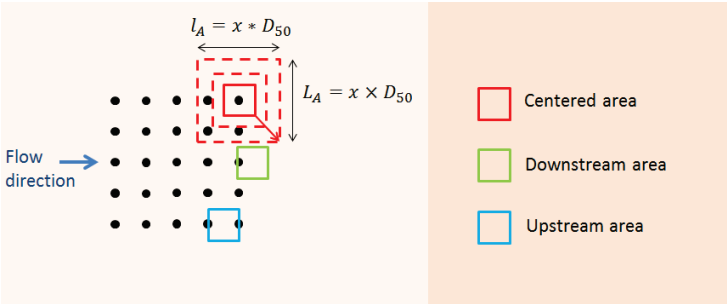

Figure 9.1.4: Definition of the areas that could influence the measurements of the hydrodynamics (centered around the measurement point or placed at the upstream or the downstream of the point).

For each area size (L_A, l_A), topographical parameters were calculated and plotted against the associated friction velocity. The relationship between topographical parameters and friction velocity was assumed linear and was evaluated by calculating the coefficient of determination R^2 of the fit. R^2 close to 1 means that a linear relationship might exist between the two variables, whereas R^2 close to 0 indicates no correlation exists. Figure 9.1.5 shows an example of a comparison between local friction velocities and their associated topographical parameters (here, the armoring degree) computed over an area of (8×D_{50}, 2×D_{50}). The area of (8×D_{50}, 2×D_{50}) is not particular but presented here as an example. Regarding this figure, a relationship between these parameters seems to be present and is confirmed by the linear fit (R^2 ≈0.5). In that case, the R^2 is not really significant, but we will see that is one of the highest value we obtained (Figure 9.1.6)

Figure 9.1.6 shows R^2 obtained for different area sizes and by fitting a linear law between friction velocity and topographical parameters. In that case, areas were centered around the measurement point. Only the results with the Reynold stress method are presented here. No relationship was detected between u^*_{Re} and the bed surface parameters. Same conclusions were made

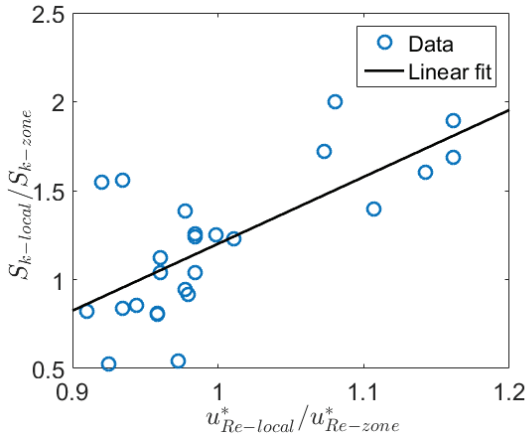

Figure 9.1.5: Local friction velocities, $u^*_{Re-\text{local}}$, in function of the armoring degree computed using the topography around each measurement points, $S_{k-\text{local}}$. The armoring degrees were calculated using bed elevations of areas of $2\times D_{50}$ long and $8\times D_{50}$ wide centered around each velocity measurements. $u^*_{Re-\text{zone}}$ and $S_{k-\text{zone}}$ are average values computed over the entire measurement zone.

when comparing bed surface parameters with u^*_{Log} or u^*_{TKE}. In addition, if we considered areas located upstream or downstream the measurement point, the trend remains the same. We were not able to find the area that influences the most the measurements. The chosen bed surface parameters might not be the most appropriate for this analysis or maybe, the linear hypothesis of a relationship was too strict. However, the absence of relationship is coherent with global results exposed in Section 8.2.3, where it was presented that no relationship exists between a single bed surface parameter and the bed shear stress. It was shown that the bed shear stress (or the friction velocity) depends on a combination of several bed surface indicators.

9.1.2 Impact of the bed spatial variability on velocity and turbulent profiles

The impact of local changes in bed surface topography on local flow structures will now be evaluated. The different longitudinal velocity profiles and the Reynold stress profile ($-\overline{u'w'_1}$) measured on column 4 (i.e. points 4, 9, 14, 19 and 24 in Figure 9.1.1) are presented in Figure 9.1.7. The bed levels measured

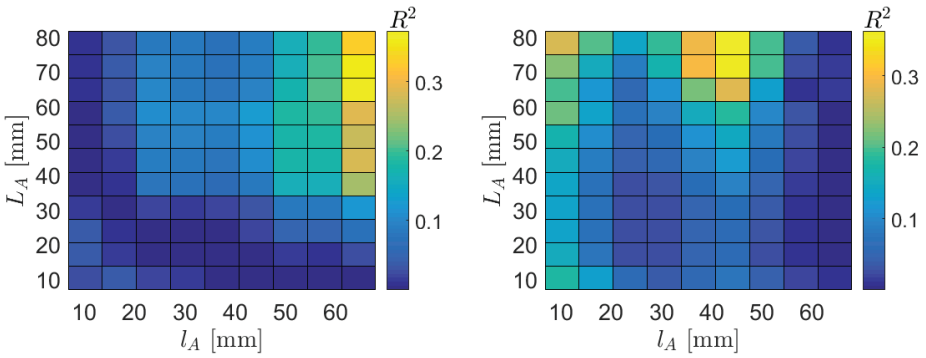

(a) relation u^*_{Re}/roughness

(b) relation u^*_{Re}/mean bed elevation

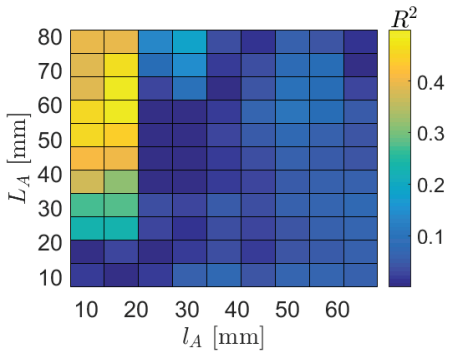

(c) relation u^*_{Re}/armoring degree

Figure 9.1.6: Relationship between friction velocity and bed surface parameters of the influencing area (roughness, mean bed elevation and degree of armoring).

with the scanner around the measurement points are added on these figures to better apprehend the impact of the bed topography on the flow structure. The spatial variability of the profiles is also presented in Figure 9.1.8, which presents local velocity profiles (Figure 9.1.8a) and Reynolds stress profiles (Figure 9.1.8b) for the 25 locations in comparison to the spatially average velocity and turbulent profiles, respectively. The spatially average velocity and turbulent profiles were added on Figure 9.1.7 for comparison with local profiles (black profiles).

According to the locations of the measurement, the velocity and turbulence profile shapes vary significantly, particularly close to abrupt variations in bed elevations (see, yellow and cyan profiles). This is more visible for the

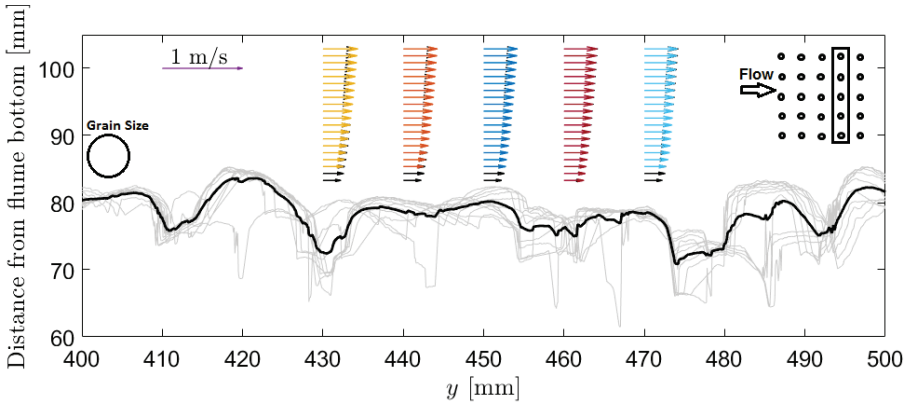

(a) Longitudinal velocity profiles

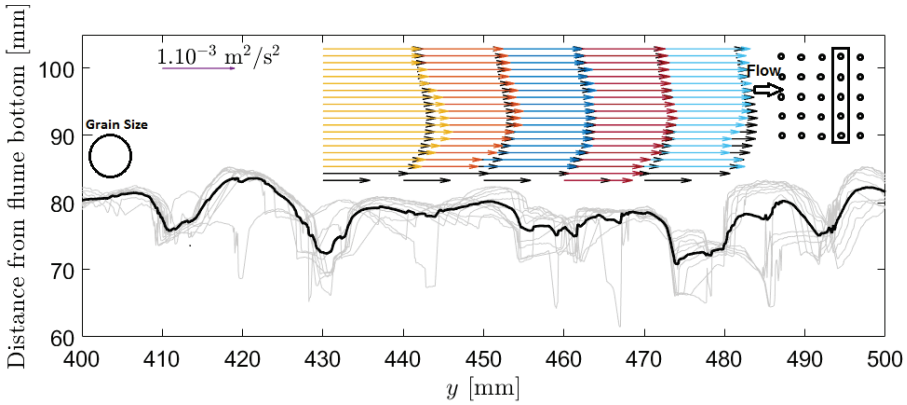

(b) Reynolds stress profiles

Figure 9.1.7: Longitudinal velocity profiles and Reynolds stress profiles of measurement points located in column 4. Gray solid lines represent the bed level profiles measured using the scanner at ±3 mm around the measurements points. This zone of ±3 mm is close to the sampling volume of the ADV device. Black solid line corresponds to the average bed level profiles which is the average of all gray solid lines. Black arrows represent the spatially average profile. Colored arrows refer to local profiles.

Reynolds stress profiles (9.1.7b).

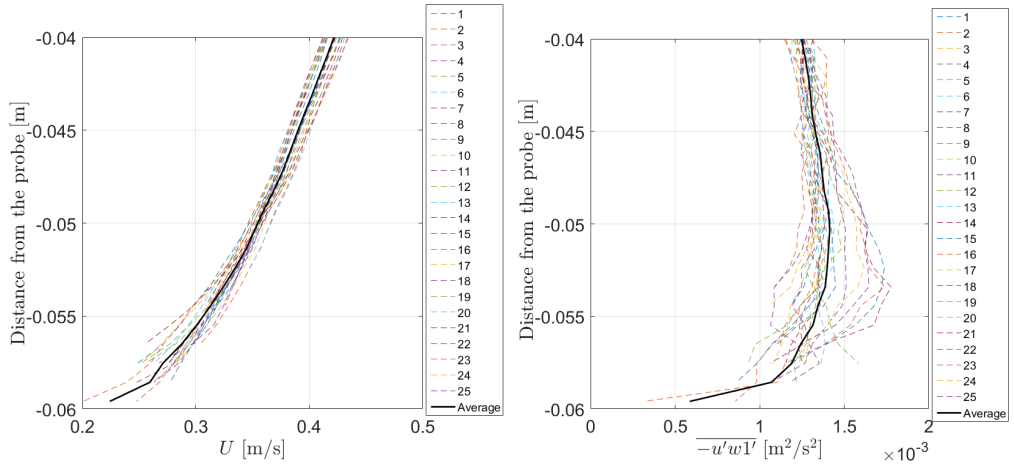

(a) Longitudinal velocities profiles **(b)** Reynold stress profiles

Figure 9.1.8: Variation of the longitudinal velocity profiles and Reynolds stress profiles relative to their spatially averaged profiles.

Figure 9.1.9 presents the friction velocity values calculated using the local profiles as a function of the friction velocity values calculated using the spatially average profile. To obtain the local friction velocity values, the upper part of the local Reynolds stress profiles were fitted up to their associated local bed levels (i.e. bed levels where the local measurements were made). The other friction velocity values were calculated using the spatially average Reynolds stress profile instead of the local profiles. The average Reynolds stress profile was fitted up to each bed elevations where the local measurements were made. That way, several friction velocities from spatially average profile were obtained. Then, the friction velocity obtained with local profiles is compared with the one obtained with the spatially averaged profile. This way, we show that the variation of u^* is mainly linked to a change in flow structure (shape of the profile) and depends little on the bed elevation. The results show that the profile shapes can change strongly from the spatially averaged profile to the point where local values of u^* can vary up to $\pm$ 10 % in comparison to u^* values obtained from the spatially average profile.

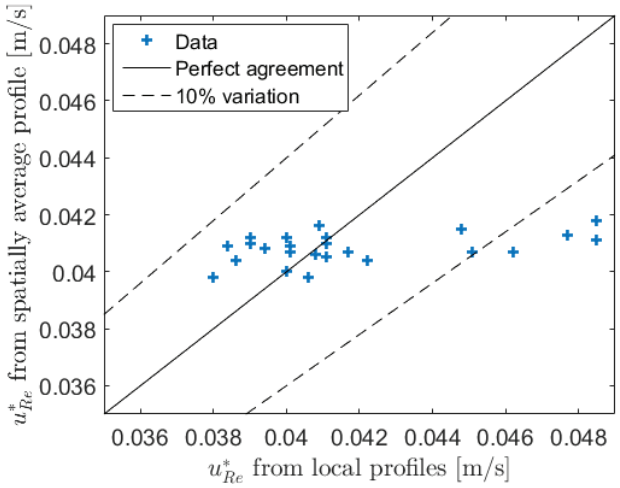

Figure 9.1.9: Friction velocities calculated with the local Reynolds stress profiles as a function of friction velocities calculated at the same point but with the spatially averaged Reynolds stress profile.

9.1.3 Impact of the bed spatial variability on sediment transport experiments

During our sediment transport experiments performed on unimodal and bimodal beds, only two velocity measurements per steady hydrograph plateaus were possible. No accurate spatial average can be made with only two points. In that case, we need to have in mind that bed spatial variability can affect the flow structure when analysing our results.

Figure 9.1.10 shows a comparison between the friction velocity values obtained using the global method (depth-slope method), u^*_{DS}, and the ones obtained using the three local methods for all our sediment transport experiments (L-G, P-G and H-G/Ms experiments). Most of the time, the local friction velocity differs from the global friction velocity. These differences inform about the spatial variability of the bed and probably about the intrinsic uncertainty of the methods.

The values of u^*_{Re} and u^*_{TKE} are underestimated in comparison to the global values. u^*_{Log} is sometimes overestimated or underestimated in comparison to the global value. Because u^*_{Log} are highly dependent on the measurement method and subjected to large uncertainties, we will not consider

these when analysing local processes responsible to sediment motion. We will focus on u^*_{Re} values which are the less impacted in terms of measurement method uncertainty and of spatial variability. The difference between u^*_{Re} and u^*_{DS} is not more than $-20\,\%$ whereas the difference between u^*_{TKE} and u^*_{DS} is of around $-35\,\%$. We assume that u^*_{DS} values take into account all the spatial variability (structure, bedforms, grain orientation, etc.), because were calculated using longitudinally averaged values. u^*_{DS} can be assimilated to the total friction velocities. In our case, the local measurements do not take into account the friction induced by structures or bedforms, but just the local grain friction or the friction induced by the nearby bed arrangement. That is why the friction velocities calculated with Re-method are lower than the global friction velocities.

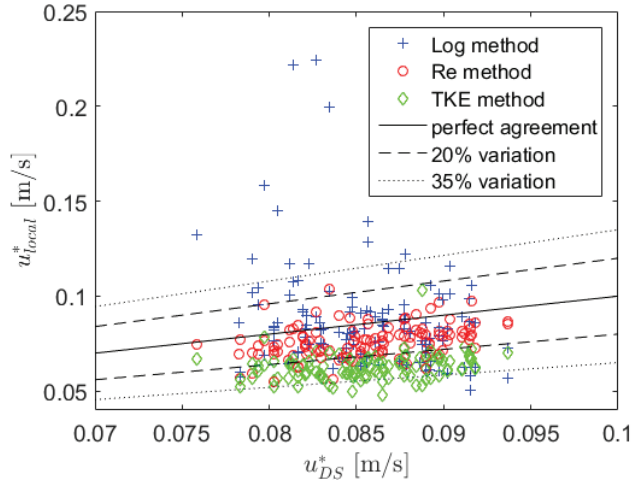

Figure 9.1.10: Comparison between local and global friction velocities calculated during all our sediment transport experiments. (Solid line represents the perfect agreement between local and global measurements. Dashed and dotted line represent a variation of $\pm 20\,\%$ or $\pm 35\,\%$ from the perfect agreement, respectively.)

9.2 Local dynamics of unimodal beds

9.2.1 Impact of bed arrangement on friction velocity

Figure 9.2.1 compares the global and local friction velocities for the entire sediment transport experiments performed on unimodal beds. Data presented here are the ones collected during the rising limbs of the hydrographs in order to focus on the impact of bed arrangement on the friction velocity. The ratio between local and global values seems to be generally lower for the packed beds than for the loose beds. In average, u^*_{Re}/u^*_{DS} is equal to 0.89±0.10 and 0.92±0.10 for packed and loose beds, respectively.

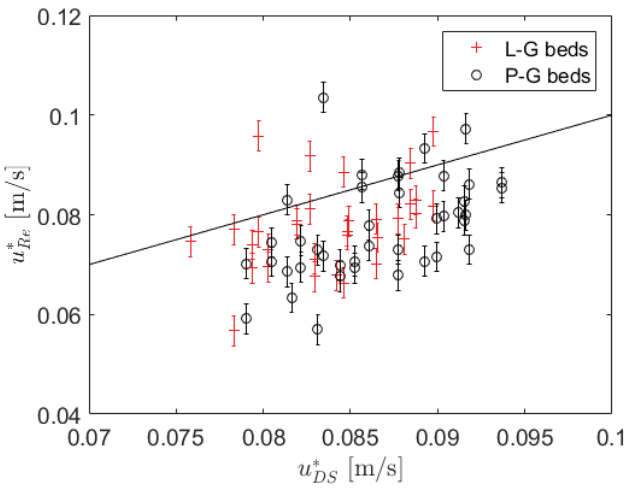

Figure 9.2.1: Comparison between local (u^*_{Re}) and global calculated friction velocities (u^*_{DS}) for all sediment transport experiments conducted on unimodal bed. Distinction between experiments performed on loose (L-G beds) and packed (P-G-beds) is made. Solid line represents the perfect agreement between local and global measurements. Error bars represent the uncertainty linked to the spatial variability discussed in Section 9.1.1.

This ratio might be assimilated to an efficiency coefficient quantifying the friction force repartition. In other words, this ratio quantifies the part of the friction force due to the grains and the one due to the bedforms or bed irregularities. In the experiments conducted on packed bed, the part associated to the bedform friction seems higher. If we consider that the grain friction is the one responsible for sediment transport, one can conclude that the trans-

port should be reduced in experiments on packed bed in comparison to loose bed experiments conducted for a same global friction force. Indeed, a part of the global friction force is dissipated through the bedforms, leaving less force to move the grains. This is coherent with results presented at global scale in Figure 8.2.2. Values of u^*_{local} that are higher than u^*_{DS} might correspond to measurements made on an area where the flow is locally accelerated due to the presence of preferential pathways (Francalanci et al., 2012). Some values of u^*_{local} are also probably mistaken due to the uncertainty of the local measurements.

Observations made in Section 8.2 questionned about the impact of the flow itself and bed stability on the sediment transport. Either the bedload transport rate is controlled by the local flow friction only, as it is commonly assumed, or the bed arrangement directly controls the bedload rate by changing the bed stability. Do two beds having two different bed arrangements and subjected to two different flows ($Q_1 \neq Q_2$) in order to obtain the same local friction velocity ($u^*_1 = u^*_2$) produce the same bedload rate? If they do ($q_{s1} = q_{s2}$), it would mean that only the flow (through friction velocity) controls bedload rate. In that case, bed arrangement has just an influence on the flow resistance and not directly on the transport rate. If $q_{s1} \neq q_{s2}$, it would mean that bed stability has a direct influence on sediment transport rate.

Figure 9.2.2 shows the local dimensionless bed shear stress (τ'^*_l) as a function of the dimensionless sediment transport for all experiments conducted on unimodal beds (L-G and P-G beds). τ'^*_l is deduced from the determination of the Reynold stress shear velocity. To build this Figure, the three measurements of transport rates per hydrograph plateaus were averaged as well as the two local friction velocity measurements. τ'^*_l is assumed to be equal of the dimensionless skin friction that is responsible for the gravel transport. We believe that the skin friction approximation made using local measurements is better than the one estimated with the classical Strickler friction coefficient K_g presented in Section 8.2.3 (τ'^*_K). Despite the large scatter in the graph, it seems that the same bed shear stress is needed to produce similar transport rate whether we are on a packed or a loose bed. The relationship $q^*_s = f(\tau'^*_l)$ is similar. This suggests that the gravel dynamic is controlled

by the skin friction only (flow resistance) and that the bed stability plays a minor role. Based on the results at local scale, it is advised to improve the determination of the flow resistance to improve the bedload prediction rather than the estimation of the bed stability. Bed arrangement has only an influence on the flow structure. The decrease in local friction velocity may be linked to a smoothing of the bed surface due to a better grain imbrication in case of experiments on P-G beds.

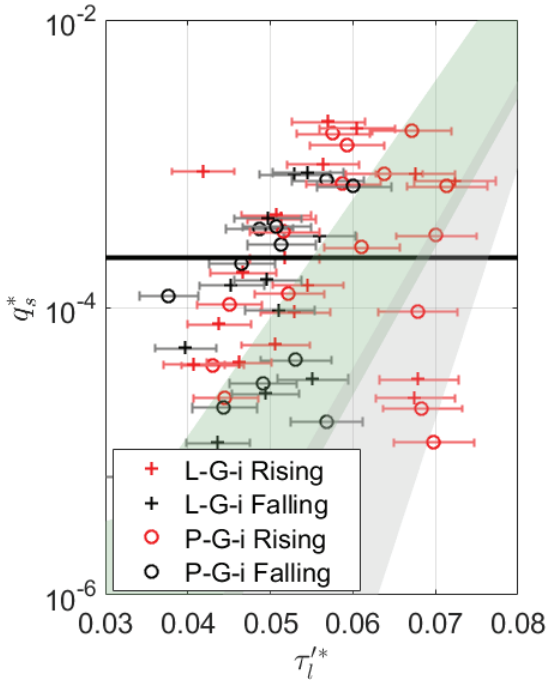

Figure 9.2.2: Comparison between dimensionless transport rate and dimensionless local friction velocities ($\tau_l'^*$) obtained for all sediment transport experiments conducted on unimodal beds. Red and black colors represent data during the rising and falling limb, respectively. + symbols show data related to experiments performed on loose beds. *o* symbols show data related to experiments performed on packed beds. Previous areas defined in Figure 8.2.2 are added for comparison. Error bars represent the uncertainty linked to the spatial variability discussed in Section 9.1.1.

9.2.2 Impact of the bed arrangement on velocity and turbulent profiles

In this part, we explore the changes in flow structure and turbulence at the vertical profile scale due to bed arrangement (loose and packed beds). Again, it is important to note that only two velocity measurements were conducted per hydrograph plateau and that it is certainly not enough to take into account the spatial variability. When looking at the results, it is crucial to have in mind the effect of spatial variability as emphasized in Section 9.1.2. Trends observed might be of same order than the spatial variability.

In Figure 9.2.3 and Figure 9.2.4, only velocity profiles measured when there is no transport are presented. It enables to focus on the impact of changes in initial bed arrangements on local velocity profiles without taking into account sediment transport. Others study investigated the impact of sediment transport on the flow structure (Carbonneau and Bergeron, 2000; Campbell et al., 2005; Dey et al., 2011). The lack of velocity data in our experiments do not provide more information about the impact of gravel transport on the flow structure.

Looking at the experiment couple n°1 and n°3 (Figure 9.2.3), one can see some trends appearing. The near bed gradient for the Reynolds stress profile is higher for a loose bed than for a packed bed. This implies a higher friction velocity for the loose bed case. Turbulence intensities in the vertical and longitudinal directions seem to be higher for a packed bed than for a loose bed. The diminution for the loose bed case is linked to its larger roughness which breaks large eddies into smaller eddies having smaller intensity. On a packed (smoother) bed, the eddies are larger and contain more energy. That is why, the turbulent kinetic energy should be higher for a packed bed than for a loose bed. This statement is assessed for experiment couple n°3 but not for experiment couple n°1 where the TKE seems to be of the same magnitude order for the two kinds of beds. No strong trend is noticed for the longitudinal velocity profile, except that the velocity seems to accelerate close to the bottom in case of packed beds. The acceleration is certainly the consequence of a smoother surface.

Experiment couple n°2 seems to differ from the other experiment couples

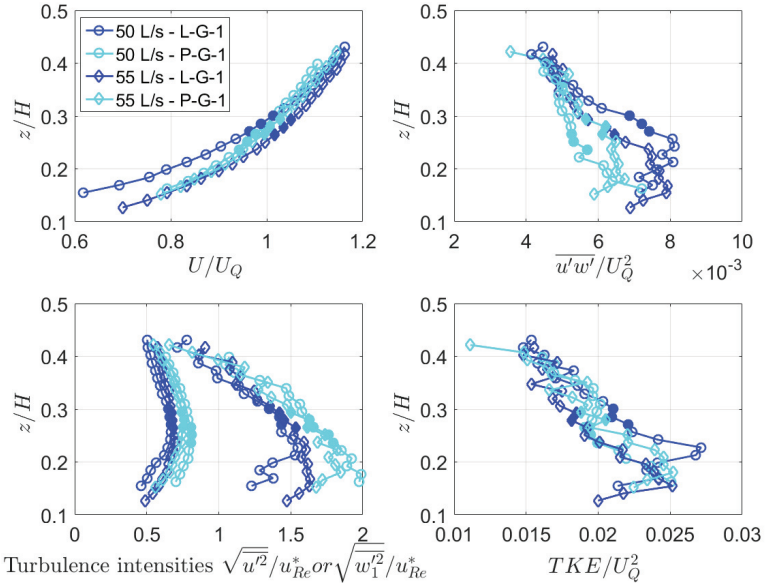

(a) Experiment couple n°1

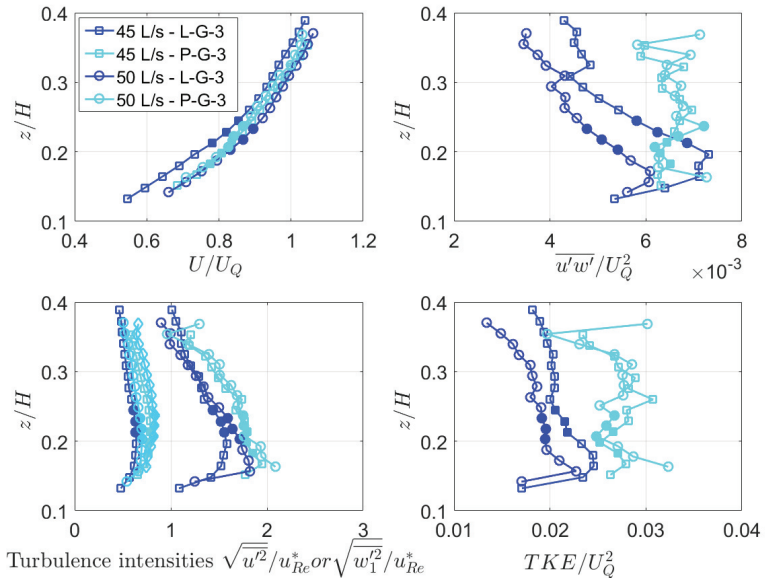

(b) Experiment couple n°3

Figure 9.2.3: Velocity and turbulent profiles for experiment couple n°1 and n°3. Smaller values of turbulent intensity correspond to turbulent intensity in the vertical direction. Filled symbols indicate the zone around the sweet spot.

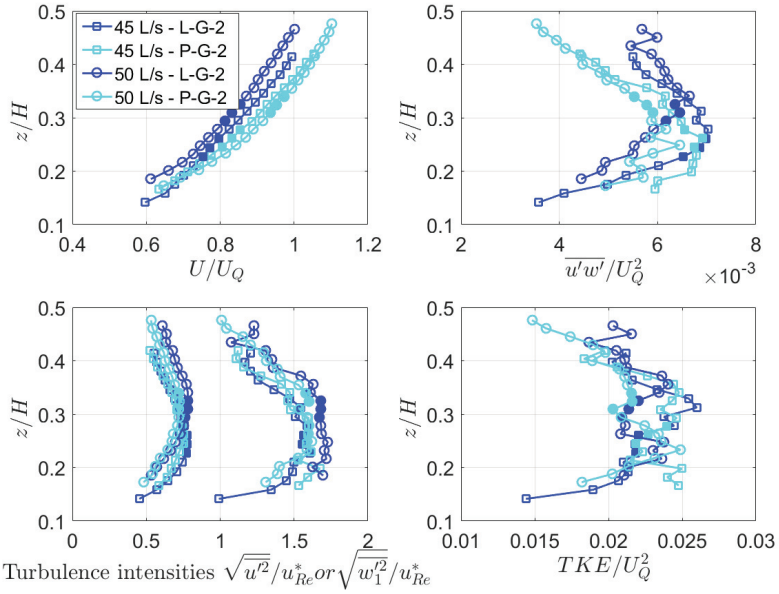

Figure 9.2.4: Velocity and turbulent profiles for experiment couple n°2. Smaller values of turbulent intensity correspond to turbulent intensity in the vertical direction. Filled symbols indicate the zone around the sweet spot.

(Figure 9.2.4). Indeed, in that case, the packed bed has a stronger Reynold stress bottom gradient in comparison to the loose bed. The turbulent intensity and the TKE are larger for the loose bed than for the packed bed. This gives the impression that trends differ from the ones found for experiment couples n°1 and 3. Looking at Table 8.2, one can see that in terms of bed surface criteria, experiment couple n°2 already differed from the others. In particular, the roughness was higher for the packed bed than for the loose bed. With this observation, one can think that it is the roughness that controls the local flow structure. In our case, the local flow was not impacted by structure at larger scales but only by the nearby roughness. Unfortunately, we lack some data to confidently conclude about the impact of bed arrangement on flow structure (e.g. double-average velocity and turbulent profiles).

9.3 Local dynamics of infiltrated beds with Ms sediments

Velocity measurements were only performed on bimodal beds composed of gravels and Ms sediments, because of technical problems. The local dynamics over H-G/FS and H-G/S beds are not investigated in this section.

9.3.1 Impact of the fine sediment presence on friction velocity

As for the experiments performed on packed beds, the ratio between local and global friction velocities seems to be generally lower for the infiltrated beds than for the non infiltrated hybrid beds (Figure 9.3.1). In average, u^*_{Re}/u^*_{DS} is equal to 0.86±0.11 and 0.92±0.10 for infiltrated and associated non infiltrated beds, respectively. This means that in the case of experiments on infiltrated beds, the local grain friction decreases with respect to the total bed friction. We can wonder how the supplementary energy is dissipated as there should not be more bedforms or irregularities than in the loose or hybrid bed case. Less friction force is thus dedicated to gravel transport. For a same global friction force, the transport should be lower for experiments conducted on H-G/Ms beds than for experiments performed on H-G beds. This is coherent with the global results presented in Figure 8.3.3.

Figure 9.3.2 shows the local dimensionless bed shear stress ($\tau_l'^*$) as a function of the dimensionless sediment transport for unimodal and bimodal loose bed experiments (L-G and H-G/Ms beds). The method to build the figure is the same as for Figure 9.2.2. Again, the relation between $\tau_l'^*$ and q_s^* is the same for both types of beds (infiltrated or not). The skin friction seems thus responsible for grain motion. Bed stability has limited influence on gravel dynamics, which was counter-intuitive in comparison to the results obtained at the global scale, where both bed stability and flow resistance were found to play a significant role in bedload transport. It is once again advised to improve flow resistance determination to improve bedload prediction rather than the estimation of bed stability. Presence of fine sediments infiltrated in the bed has only an influence on the flow structure. The decrease in local

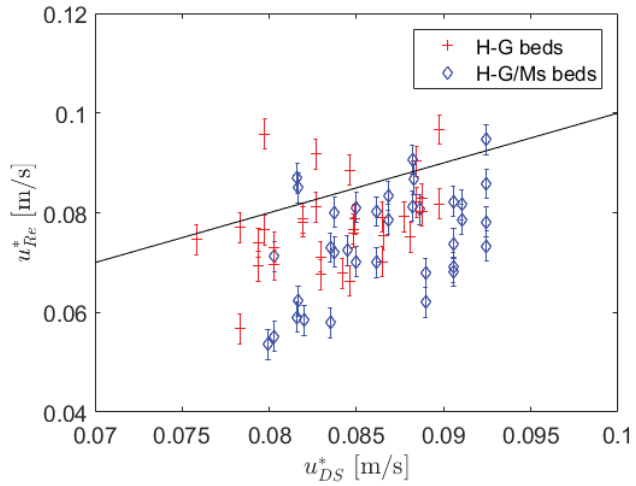

Figure 9.3.1: Comparison between local (u^*_{Re}) and global friction velocities (u^*_{DS}) calculated during sediment transport experiments conducted on hybrid beds and infiltrated with Ms sediment beds (H-G/Ms). Solid line represents the perfect agreement between local and global measurements. Error bars represent the uncertainty linked to the spatial variability discussed in Section 9.1.1.

friction velocity for the H-G/Ms beds might be a consequence of a smoothing of the bed surface or of a change in bed permeability due to the presence of fine sediments.

We have seen in Section 8.3.3 that friction velocity can be modified when fine sediments infiltrate the bed (Manes et al., 2009; Hamm et al., 2011). Thus, mixtures having similar bed permeability should impact similarly the local friction velocity. In addition, if it is only the local friction velocity that controls gravel transport, these kinds of mixtures should behave in a similar way. However, we noticed that this assumption was not verified when comparing results from experiments performed on H-G/FS beds and H-G/Ms beds. These beds had same bed permeability so potentially the same local friction velocities, but gravel transport rates were not similar (see, Figure 8.3.3).

The trend in Figure 9.3.2 showing that it is only the local friction velocity that controls the bedload rate should be examined with caution regarding the uncertainties associated to the results. Two assumptions might explain

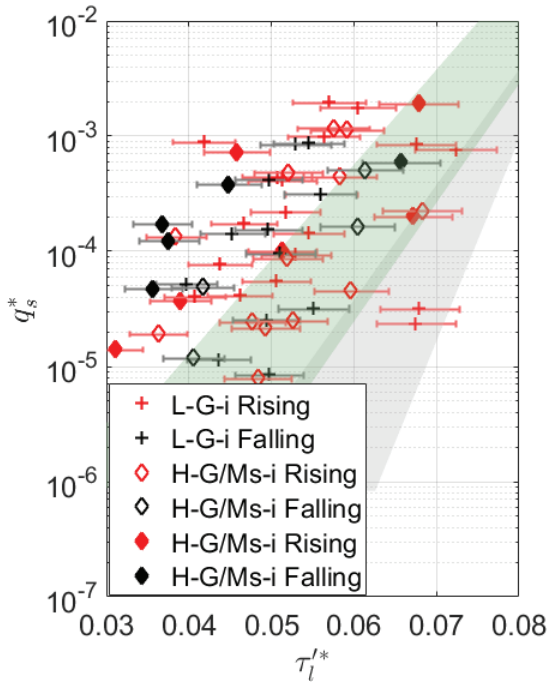

Figure 9.3.2: Comparison between dimensionless transport rate and dimensionless local friction velocities ($\tau_l'^*$) obtained for all sediment transport experiments conducted on L-G beds and H-G/Ms beds. Red and black colors represent data during the rising and falling limb, respectively. + symbols show data related to experiments performed on non infiltrated beds. symbols show data related to experiments performed on hybrid infiltrated beds. Filled ♢ correspond to hybrid beds resulting from packed beds. Previous areas defined in Figure 8.2.2 are added for comparison. Error bars represent the uncertainty linked to the spatial variability discussed in Section 9.1.1.

the difference between H-G/FS and H-G/Ms:

1. in case of H-G/FS, the non-cohesive fine sediments were probably rapidly re-suspended in the water column and washed from the bed deeper than if we were in presence of cohesive fine sediments. The surface and subsurface was thus assimilated to the one encountered in a hybrid bed without fine sediments. The fine sediments, still present deeper in the bed, have probably no influence on the flow structure. The local friction velocities for H-G/FS beds are certainly very similar to those for L-G or H-G beds. That is why, their transport rates are

alike during the rising limb of the hydrograph (Figure 8.3.3).

2. the bed stability would have a direct controls on the gravel transport rate and not only an impact on the local flow structure. H-G/Ms beds would be more resistant to the flow because they are more consolidated than H-G/FS beds due to the presence of cohesive fine sediment within their matrix. The range of local friction velocity explored is probably too small preventing trends from emerging. The bed stability impact is not detectable regarding our results.

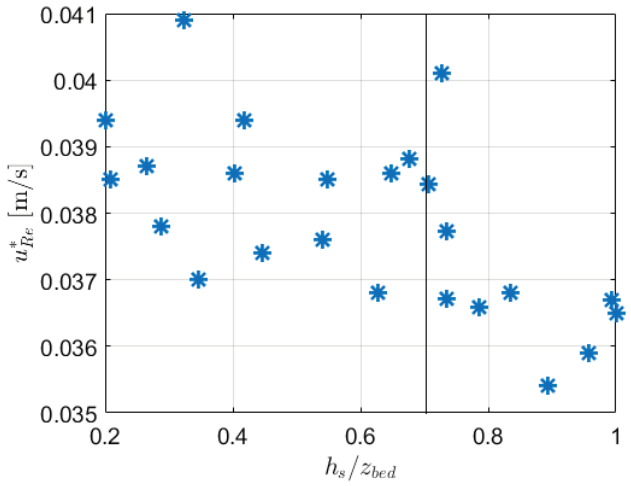

Figure 9.3.3: Evolution of the local friction velocity according to the height of the infiltrated fine sediments relative to the bed level (gravel level).

To verify the first assumption, we study the influence of the infiltration height within the bed on the flow structure. During the infiltration phase (step (3b) in Figure 3.2.2) at constant low discharge (Q =30 L/s), velocity measurements were carried out regularly. Figure 9.3.3 shows the friction velocities calculated according to the relative height of the fine sediment infiltrated (h_s) within the bed. The infiltration heights and the bed level (z_b) were measured by analysing side view photographs taken at the velocity measurement location. The velocity measurement was performed at the same location during the entire infiltration phase and no gravels were transported. The potential variations observed in terms of friction velocity values

are thus only due to the presence of fine sediments infiltrated within the bed. Regarding the results, no strong trend can be noticed, except maybe when the fine sediment height reaches a threshold value, namely 75 % of the total bed height. Beyond the threshold value, the friction velocity seems to decrease with the infiltration height. The difference between H-G/FS and H-G/Ms beds may be explained by this threshold value. The first 25 % of the subsurface (namely $2 \times D_{50}$) were probably washed in the case of H-G/FS bed experiment deleting the potential infiltration effect.

However, the observed trend are not so obvious. The hypothesis that the bed stability impact the transport rate should not be dismissed.

9.3.2 Impact of the fine sediment presence on velocity and turbulent profiles

The caution that needs to be taken when interpreting the results at the vertical profile scale is the same as the one exposed in Section 9.2.2. In this part, the focus is set on the impact of fine sediments infiltrated into the matrix on the flow structure. To prevent from observing the effect of change in bed arrangement, we chose to compare profiles obtained during the falling limb of the hydrograph for the loose bed (hybrid bed) and obtained during the rising limb of the hydrograph for the infiltrated bed. These profiles were measured when there was no gravel transport. That way, the bed arrangements were the same since the infiltration phase occurs at very low constant discharge (no gravel motion).

Figure 9.3.4 shows vertical profiles as well as TKE profiles for both infiltrated and loose beds. Two experiment couples are presented including one involving a hybrid bed resulting from a packed bed (n°6). The longitudinal velocity is lower for non-infiltrated beds which can be assimilated to permeable beds. In case of infiltrated beds, the flow energy cannot be dissipated into the bed matrix. As a consequence, we have a higher gradient velocity close to the bottom. The Reynolds stresses are higher for unimodal beds than for infiltrated beds. Permeable and rough surfaces generate more drag. The turbulent intensity in the longitudinal and vertical directions are lower for non-infiltrated beds. Indeed, in case of infiltrated bed, destruction of eddies

in smaller ones is not as intense as in permeable beds. The TKE trend seems to indicate that the turbulent energy is higher for non infiltrated beds, which is in contradiction with the trend observed for turbulent intensities. Nevertheless, the difference in terms of TKE profiles are less pronounced than the one observed for turbulent intensities.

Most of our results are coherent with the ones found by Wren et al. (2011), namely a higher Reynold stress for non-infiltrated bed and a higher turbulence intensity for infiltrated beds. Wren et al. (2014) noticed that the trends were accentuated with flow strength. They also found that the TKE was higher for infiltrated beds which is, unlike our results, coherent with the turbulent intensity.

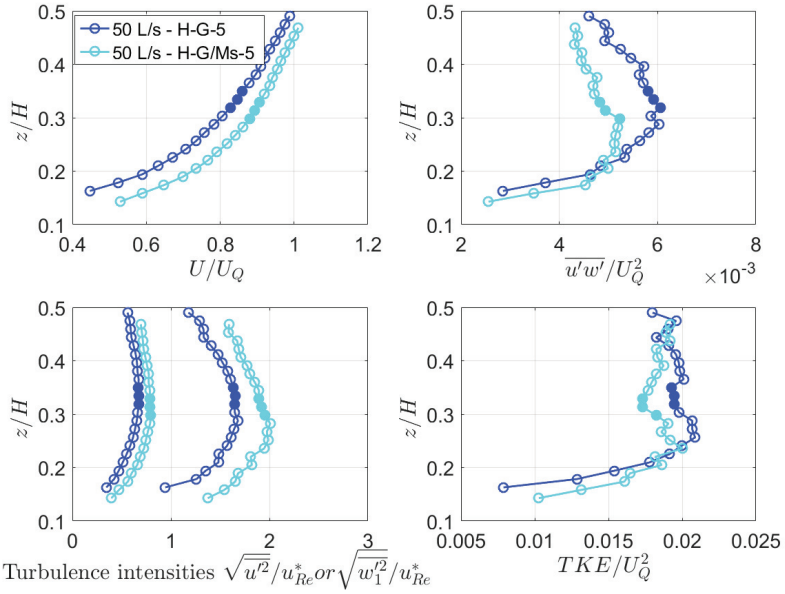

(a) Experiment couple n°5

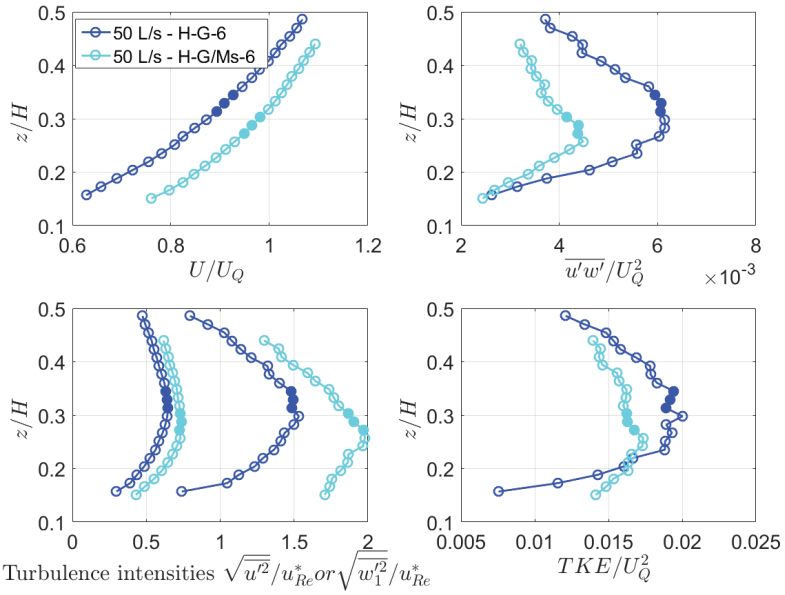

(b) Experiment couple n°6

Figure 9.3.4: Velocity and turbulent profile for experiment couple n°5 and n°6. Smaller values of turbulent intensity correspond to turbulent intensity in the vertical direction. Filled symbols indicate the zone around the sweet spot.

Chapter 10

In situ Application - Arc River

10.1 Introduction

In situ experiments were performed on a gravel-bed river to study gravel dynamic in real conditions and according to diverse initial stage of clogging. The objective is to compare field observations with results obtained in the laboratory (Section 8.4) and to test the methodology proposed in Section 8.4.2.

Field campaigns were carried out on a gravel bar located in the Arc River (France). This river was chosen because of its large grain size distribution and variability (gravel, sand, silt, clay) that could lead to various grain arrangement and degree of bed clogging. In addition, the site is interesting because regular flushing events from the upstream dams are scheduled by EDF every years in June, with the exception of years for which a large flood occurred. These flushing events are controlled operations enabling to simulate flood on the gravel bar and the hydrograph is known in advance.

The studied site had been the subject of numerous investigations since 2005 (Jodeau, 2007; Jaballah, 2013). In particular, the use of the PIT-tag technique since 2008 has brought a good knowledge about the bedload dynamics over gravel bars (Camenen et al., 2010). Sediment transport experiments were conducted during the flushing events of 2015 and 2016. A similar experiment was conducted in June 2017 but will not be presented in this thesis.

10.2 Site presentation and field experimental set-up

10.2.1 Location of field measurements

Field measurements were conducted on a gravel bar in the Arc River, located in the French Alps in the Maurienne narrow valley (Figure 10.2.1). The catchment area is about 2000 km^2. The Arc-en-Maurienne River is characterized by a nival hydrologic regime with mean water discharges from 6 - 8 $m^3.s^{-1}$ during winter to 15 - 25 $m^3.s^{-1}$ during summer (Jodeau, 2007). The Arc River is laterally constrained by dikes and regulated by many dams impacting significantly the natural river discharges and sediment transport. In particular, a flow diversion exists after the St-Martin-la-Porte reservoir (up to 70 $m^3.s^{-1}$). The Arc river bed is mostly composed of gravels but also of fine sediments (cohesive and non-cohesive) provided by its tributaries (Arvan and Glandon streams).

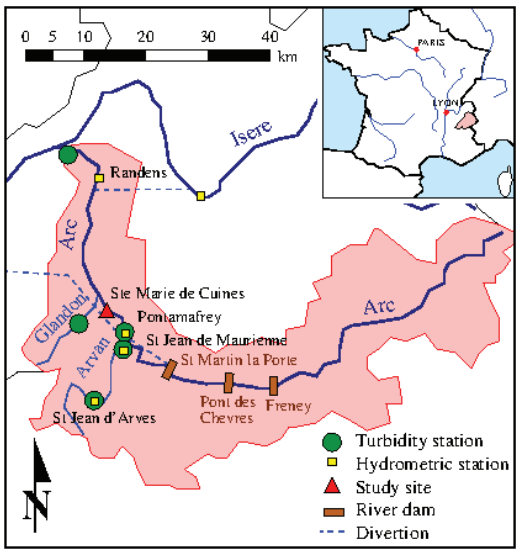

Figure 10.2.1: Overview of the patch installation in 2016.

The study site is located 15 km downstream of Saint-Jean-de-Maurienne. The gravel bar is part of a system of alternate bars (Jaballah et al., 2015), separating the channel into a main and a secondary channels (Figure 10.2.2a). The gravel bar is easily accessible most of the year during low flow periods.

During the year, the gravel bar is generally emerged, so no particle motion exists. It is only during floods that the bar is underwater and that coarse particles may be put into motion; we approximate that the bar should be underwater for flow discharges around $100\,\mathrm{m}^3.\mathrm{s}^{-1}$.

(a) **(b)**

Figure 10.2.2: Overview of the studied site: (a) the gravel bar, the secondary channel in the foreground and (b) the camera on a mast positioned on the bank for LSPIV measurements.

10.2.2 Field experimental set-up

PIT-tag technique

Bedload transport is difficult to monitor in real rivers. Recently, PIT-tag technique was developed and tested with success in mountain rivers (Lamarre et al., 2005; Liébault et al., 2009; Rollet et al., 2008; Camenen et al., 2010). It consists in measuring the travel distance of individual gravels previously tagged with Passive Integrated Transponders (PIT).

In our study, PIT-tag technique was used to monitor the transport of tagged gravels initially located on different patches on the bar. The PIT

are developed by TIRIS Technology and distributed by Texas Instruments. They are small enough (4×23 mm) to be inserted into natural gravel particles, robust, battery-less and inexpensive (3 € per PIT). In our case, PIT were carefully inserted into gravels having a size similar to the median grain size of the bar (≈6 cm). Each PIT, and thus each tagged sediment, has its own identifier. The tagged particle movements can be evaluated using a specific antenna able to detect the PIT, associated with a DGPS in order to note their locations. The overall uncertainty on the tagged particles position is about 50 cm.

Patch preparation

Six patches of about one square meter were installed on the bar close to the secondary channel (Figures 10.2.3 and 10.2.4). On the side of the secondary channel, during the flushing event, bed shear stresses should be sufficiently high to induce gravel motion and sufficiently low to limit their movement onto the bar area. In that way, the probability to recover a tagged particles should be high. Each patch contained 25 tagged gravel sediments, so in total 150 tagged particles on the bar. The tagged particles were properly distributed within the patch-surface: 5 rows and 5 columns, with a spacing of 20 - 25 cm between each tagged particles.

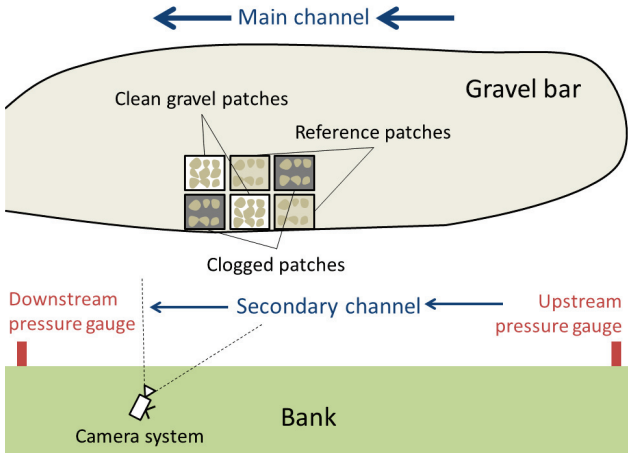

Figure 10.2.3: Schematic view of the experimental set-up. The configuration of the patches presented here is the one of 2015.

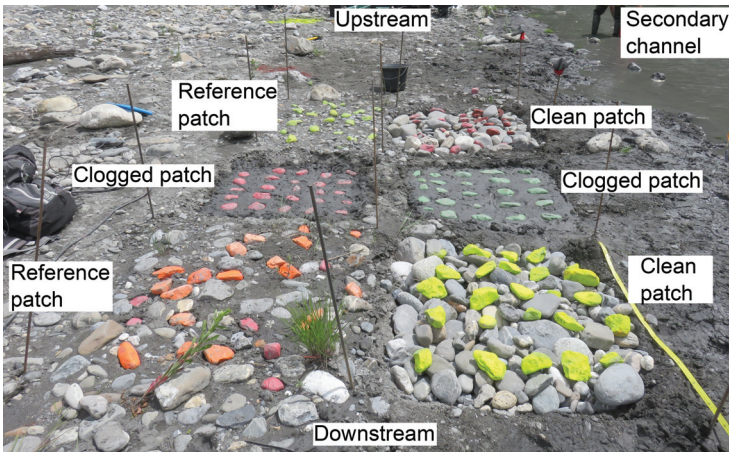

Figure 10.2.4: Photograph of the patch installation in 2016. The six patches (i.e. 2 clogged, 2 reference and 2 clean gravel patches) are marked with metal sticks. Particles are pit tagged and colored differently according to the patches.

Three types of patches having different degrees of bed clogging were realized (Figure 10.2.4):

- 2 clean gravel patches, composed of gravel particles only. No clogging was present in that case.
- 2 clogged patches, composed of few tagged gravel particles in a very fine sediments matrix (silt, clay). Gravel sediments were scattered in a fine sediment matrix which was not the case in our laboratory experiments (gravel matrix was clogged with fine sediments).
- 2 reference unmodified patches, composed of a mixture of gravels, sand, silt and clay particles. The gravel bed was naturally clogged by fine gravel, sand, silt and clay.

Reference patches were carefully chosen to be representative of the gravel bar configuration. They correspond to unmodified patches where natural gravels were substituted by tagged gravel sediments. With these patches, the bedload transport over the bar can be evaluated in an undisturbed state.

The preparation of the clean gravel patches was as follows. First, a surface of approximately one square meter was excavated to a depth of approximately

15 cm. Secondly, the excavation was filled with gravels initially present on the bar. Their sizes were chosen to be close to the median grain size of the gravel bar surface. These gravels were preliminary washed from any fine sediments and randomly packed. Then, 25 tagged gravels were installed on the patch-surface. This patch configuration is close to the loose bed configuration (L-G) created in our laboratory experiments. With these patches, the gravel motion on a bed free from fine sediments can be evaluated.

For the preparation of the clogged patches, the same excavations as the ones for clean gravel patches were performed and then filled with fine sediments only. Fine sediments were directly collected on the gravel bar or in the secondary channel. Then, the 25 tagged gravels were partially buried in the fine sediments in such a way that they still have a significant surface contact with the flow during the flushing event. No contact between tagged gravels existed. Thus, this patch configuration cannot be associated directly to our laboratory configurations (e.g.: H-G/Ms and H-G/FS). In that case, a clogged patch corresponds to tagged gravels embedded in a very fine sediments matrix (silt and clay).

Before the flushing event, the exact position of the patches were measured using a DGPS device. The initial position of each tagged gravel were then deduced. After the flushing event, tagged particles were recovered using the antenna and their position were recorded using a DGPS. Travel distances were then calculated.

Hydrodynamic measurements

To understand the gravel transport, it is important to have a description of the hydrodynamics over the gravel bar, and particularly over the patches. That is why, velocity measurements, estimations of water levels, water slopes and fine sediment concentration were performed during the flushing event. The gravel bar topography including the secondary channel was also measured before and after the flushing event.

Water levels and water slopes were estimated using two pressure gauges installed at the upstream and downstream ends of the gravel bar within the secondary channel.

During the flushing event, LSPIV (Large Scale Particle Image Velocimetry) technique was used to measure the surface velocity over the gravel bar. The LSPIV system was composed of a video camera fixed at the top of a telescopic mast installed on the side embankment (Figure 10.2.2b). Movies of about 30 s were regularly taken (in average every 30 - 40 min). Recorded images were then processed using the software Fudda-LSPIV (Le Coz et al., 2014). An ortho-rectification of the frames was made using Ground Reference Points (GRPs) positioned in the view field of the video camera (gravel bar and side embankment, see Figure 10.2.2a).

The water discharge was also measured at the hydrometric station of Pontamafrey, located at 9 km upstream the studied site (Figure 10.2.1). The time for the wave to travel from Pontamafrey to Sainte-Marie-De-Cuine (gravel bar) was estimated to be around 45 min (Camenen et al., 2015).

Fine sediment concentration was measured using water samples collected manually every 30 minutes at the upstream and downstream ends of the gravel bar and using a turbidimeter as well as an automatic sampler located at the Pontamafrey station. Water samples were also carried out at a brigde located at 2 km downstream from the bar.

10.3 General hydro-dynamical results

10.3.1 Flushing event hydrographs

Figure 10.3.1 shows the water discharges measured during the flushing events of 2015 and 2016, along with the fine sediment concentration measurements. These hydrographs are particularly different from the precedent years (Antoine et al., 2013). Generally for this site, the flushing event follows a designed hydrograph composed of two plateaus lasting both approximately 4 hours: the first at 80 - 100 $m^3.s^{-1}$ and the second at 120 - 130 $m^3.s^{-1}$.

In 2015, the second plateau was not reached due to unexpected circumstances. The hydrograph of the 2015 flushing event was composed of a unique plateau at around 100 - 110 $m^3.s^{-1}$ lasting approximately 6h30, between 10h30 and 17h00 (Figure 10.3.1a). The gravel bar was barely underwater, and bed shear stress over the patches were very low. The concentration

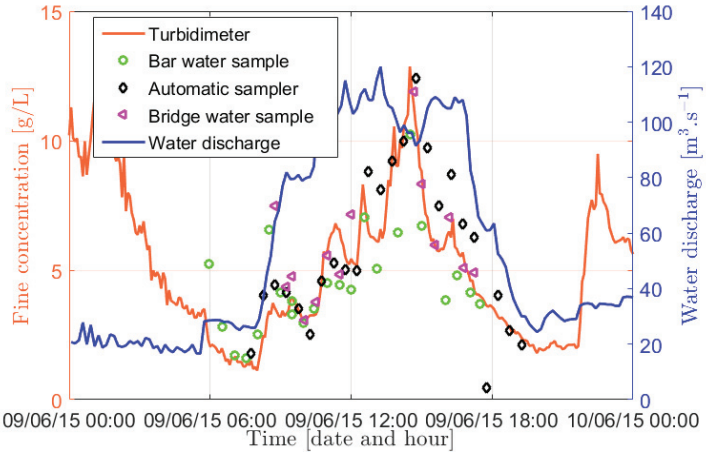

(a) 2015 flushing event

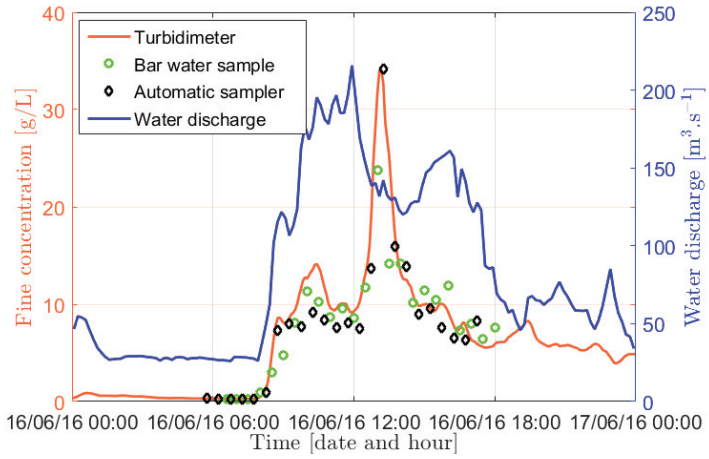

(b) 2016 flushing event

Figure 10.3.1: Water discharges and fine sediment concentrations during the flushing event of 2015 (a) and 2016 (b). Water discharge was measured at Pontamafrey station and resynchronized to represent water discharge at the gravel bar. The entire measurements of fine sediment concentration are reported on the graphs: concentrations from the Pontamafrey turbidimeter, bar and brigde water samples, and from the Pontamafrey automatic sampler.

peak was also relatively low (around 13 g/L) compared to previous events (Antoine et al., 2013).

In 2016, the design of the hydrograph was totally different from the previous years: the flushing event lasted longer (16 hours instead of 13 hours) and the peak discharge was much higher (200 $m^3.s^{-1}$ instead of 130 $m^3.s^{-1}$) (Figure 10.3.1b). The rising limb of the hydrograph was very rapid, namely two and a half hour to reach the hydrograph peak. The hydrograph falling limb was very long and composed of three plateaus: one around 190 $m^3.s^{-1}$ during 2 hours between 10h00 and 12h00, one around 160 $m^3.s^{-1}$ during 1h30 between 15h00 and 16h30 and one around 70 $m^3.s^{-1}$ during 3h30 between 19h30 and 23h00. It is important to note that on June 15th (the day before the flushing event), the water discharges reached unexpected high values (peak at around 90 $m^3.s^{-1}$) due to large natural discharges. Our patches were already installed on the gravel bar and during this event, they were underwater. This small flood might have disturbed the gravel bar by feeding fine sediments into our clean gravel patches, or by eroding a part of the fine sediments present on the clogged patches. Examining photographs taken after the June 15th flood, no movement of tagged particles nor strong difference in terms of patch configurations were perceived. In addition, during the flushing event, a flood of the Arvan River (tributary of the Arc, see Figure 10.2.1) occurred between 11h00 and 24h00 with a peak at 21h00 and may be the cause of the third plateau.

Because 2015 and 2016 flushing events were strongly different in terms of hydro-dynamic, one can expect to find different coarse sediment dynamics.

10.3.2 Water levels and depths

Pressure gauges measured the evolution of the water levels during the two flushing events. From these measurements, water depths and slopes can be deduced. Calibrations of the pressure gauges were made using topographic and water depths measurements made at the gauge levels before the beginning of the events. For the two years, the two measured signals were in concordance. There was however a small deficiency of the downstream pressure gauge at the end of the 2015 flushing event (from 16h00 after the

beginning of the flushing event to the end). The deficiency might be due to fine sediments obstructing the membrane of the pressure gauge.

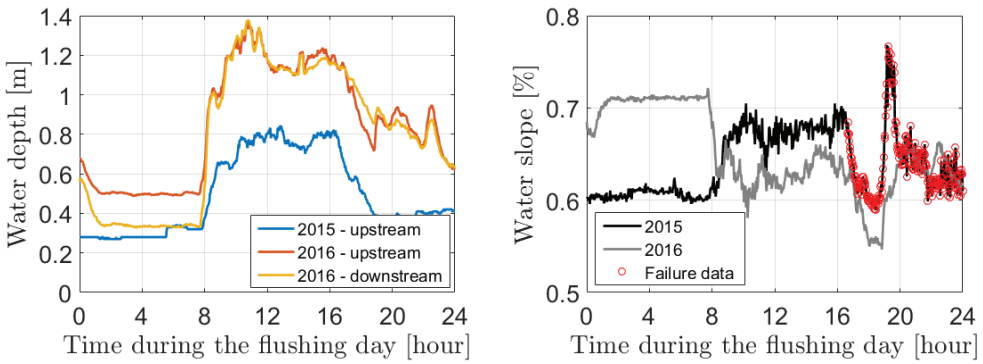

(a) Water depth **(b)** Water slope

Figure 10.3.2: Temporal evolution of water depth and water slope in the secondary channel for 2015 and 2016 flushing events. (Water depths and slopes were estimated using the pressure gauges. Red circle symbols correspond to data computed with a deficient pressure gauge.)

Figure 10.3.2a shows the water depth evolutions for the two flushing events. In case of the 2015 event, only the water depth computed using the upstream pressure gauges measurements is presented. The water depth at the downstream was not plotted because of the deficiency of the downstream pressure gauge. In case of 2016 event, a difference of around 15 cm was observed at the beginning of the event between the two calculated water depth. This difference was rapidly erased and could be explained by the existence of an hydraulic control of the downstream on the secondary channel at low flows.

Figure 10.3.2b shows the temporal evolution of the water slope within the secondary channel. Water slopes were estimated using the water levels deduced from the pressure gauges. Because the system was probably influenced by the main channel and controlled by the downstream part, the water slope was difficult to define. One can notice that it does not vary linearly with the water discharge. Water slopes were estimated of around 0.67 % at high flows ($Q \approx 100\,\mathrm{m^3.s{-}1}$) during the flushing event of 2015, and of around 0.60 % at low water discharge. The change in water slope present at the end

of the flushing event should not be taken into account because it corresponds to the period of the downstream gauge deficiency (red symbols). For 2016 event, the water slope reached 0.70 % at the beginning. When flow starts to increase, it oscillated around 0.63 %, with a brief decreasing period at 0.55 %. The slopes were quite similar between the two events. It is important to note that the water slopes were calculated using only two pressure gauges located at 140 m or 185 m from each other for 2015 and 2016 events, respectively. These values obtained with only two fixed points are probably subjected to large uncertainty, especially at low flows. This was confirmed when observing the longitudinal water profile measurement made in 2015 before the event (Figure 10.3.3). The water line was not uniform between the two pressure gauge locations. Two riffles were clearly visible. The water slope at the studied site was roughly evaluated of around 0.1 % instead of 0.6 %. These water slope uncertainties will be problematic for bed shear stress computation.

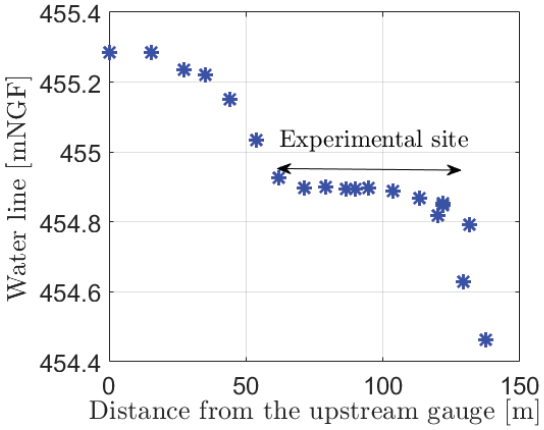

Figure 10.3.3: Water line measured before the flushing event of 2015. The unit NGF corresponds to the general levelling of France.

10.3.3 Surface velocities over the gravel bar

Surface velocities over the gravel bar and within the secondary channel were estimated using the LSPIV technique. Examples of surface velocity field are given in Figure 10.3.4 for 2015 and for 2016 flushing events at two different times.

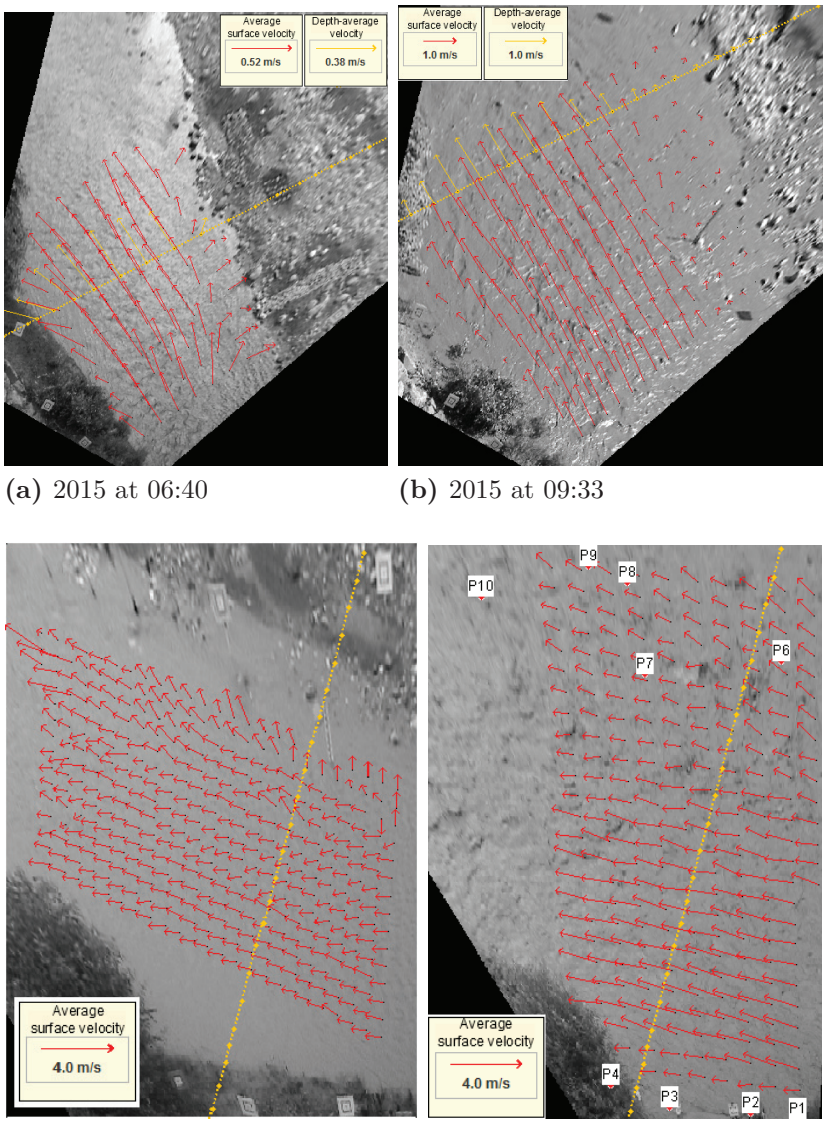

(a) 2015 at 06:40 **(b)** 2015 at 09:33

(c) 2016 at 07:00 **(d)** 2016 at 12:00

Figure 10.3.4: Velocity fields over the gravel bar and within the secondary channel estimated using the LSPIV system at 06:40 and 09:33 during the flushing event of 2015 and at 07:00 and 12:00 during the flushing event of 2016. The yellow lines represent the transect where the depth-average velocities were calculated. P1 to P10 refer to the location of the Ground Reference Points when they were not visible by eyes on the image. For 2015, the images were orthorectified and for 2016 the images were orthorectified and rotated relative to the targets on the bank.

The LSPIV results combined with the transect topography enables the estimation of the water discharge flowing over the gravel bar and within the secondary channel. Detailed topographical surveys of 3 transects located within the video camera field are available for the flushing event of 2015 whereas one is available in 2016. Figure 10.3.5 presents these transects for the two years. They were located closed to the patches. That is why, we assume that the dynamics over the patches was the same than the one over the transects. Regarding Figure 10.3.5, one can notice that the distance between the secondary channel bottom and the top of the gravel bar has reduced between 2015 and 2016. In 2016, the top of the gravel bar was still at the same elevation than in 2015 but depositions in the secondary channel have occurred. A different dynamics between these two years was then expected.

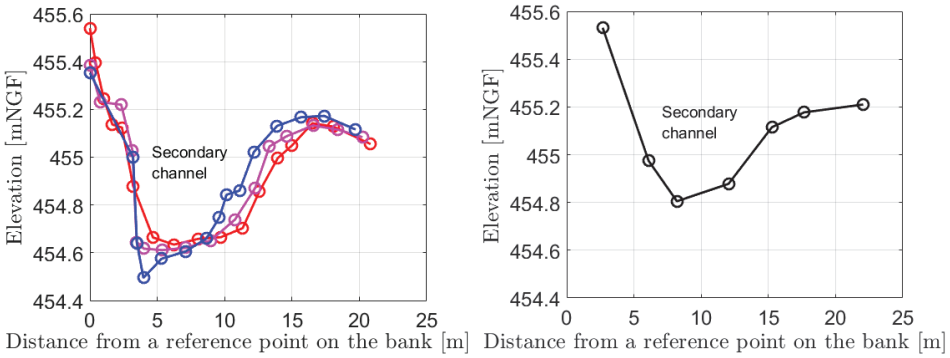

(a) 2015 **(b)** 2016

Figure 10.3.5: Topographies of transects located on the studied site, near the patches. Three transects are represented for the flushing of 2015 and only one for the flushing event of 2016.

Table 10.1 recaps the flow characteristics in the secondary channel deduced from the LSPIV measurements for the flushing events of 2015 and 2016. Total water discharges in the Arc river during the flushing events were added for information. Looking at Table 10.1 and Figure 10.3.6a which presents the water discharges within the secondary channel as a function of the section-average velocities for the two years, one can notice that in 2016, the water discharges in the secondary channel were obviously higher than the ones in 2015 but that the section-average velocities were similar. This is

Table 10.1: Flow characteristics in the secondary channel around the patch zone at different time of the flushing events (2015 and 2016) deduced from LSPIV video analysis and total water discharge of the Arc river.

Movie time [hh:mm]	Water level [mNGF]	Wetted surface [m^2]	Section average velocity [$m.s^{-1}$]	Water discharge [$m^3.s^{-1}$]	Arc water discharge [$m^3.s^{-1}$]
2015					
06:40	454.91	2.12	0.20	0.43	28
08:15	455.01	3.09	0.43	1.33	36
08:30	455.07	3.74	0.61	2.27	48
08:50	455.13	4.53	0.80	3.63	66
09:33	455.12	4.41	1.73	3.2	79
10:09	455.17	5.22	0.91	4.76	80
10:56	455.23	6.34	0.84	5.35	105
11:53	455.26	6.91	1.02	7.02	108
13:08	455.25	6.72	0.90	6.1	115
14:00	455.20	5.78	0.86	5.03	99
16:00	455.26	6.91	0.98	6.79	106
17:04	455.15	4.87	0.60	2.95	83
17:46	455.12	4.41	0.53	2.35	61
2016					
06:40	454.85	0.26	0.36	0.1	26
07:00	454.86	0.35	0.38	0.13	28
08:30	455.46	9.48	1.01	9.57	82
09:30	455.64	12.97	1.11	14.41	118
10:30	455.73	14.89	1.27	18.84	193
11:30	455.77	15.64	1.41	22.11	185
12:00	455.61	12.53	1.16	14.47	205
12:30	455.56	11.53	1.1	12.67	152
13:00	455.58	11.83	1.11	13.09	136
14:00	455.56	11.47	1.12	12.84	122
16:00	455.60	12.27	1.1	13.47	159
17:30	455.49	10.05	0.8	8.04	105
18:00	455.37	7.71	0.72	5.53	77

explained by the local changes in bed morphology at the patch locations between the two years (Figure 10.3.5). Indeed, in 2015, the secondary channel was deeper and narrower than in 2016 reducing its wetted surface and consequently increasing its section-average velocity. On the contrary, in 2016, the wetted surface was larger entraining smaller section-average velocities at same discharges.

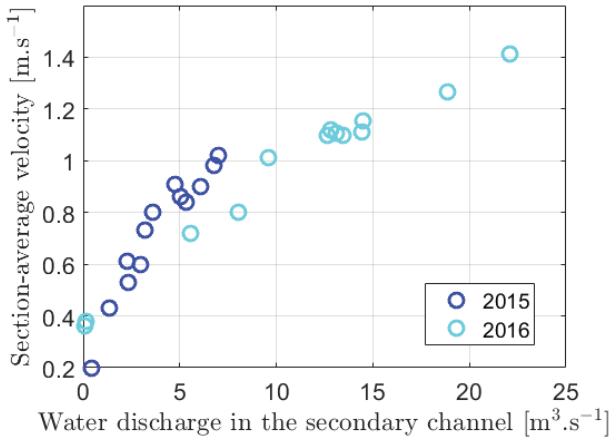

(a)

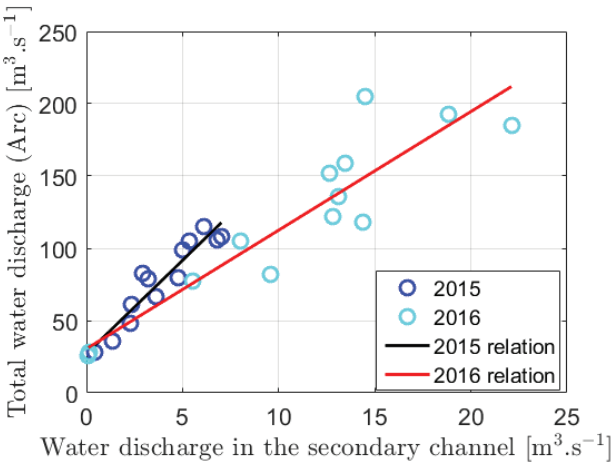

(b)

Figure 10.3.6: (a) Water discharges within the secondary channel in function of the section-average velocities estimated using the LSPIV technique over the patch zone. (b) Water discharges within the secondary channel in function of the total water discharges of the Arc river.

Figure 10.3.6b shows the relationship between the water discharge within the secondary channel and the total water discharge of the Arc river. For 2015 and 2016, two distinct relations can be observed. This indicates that the upstream hydraulic controls were different between the two years. This is probably the consequence of a change in bed morphology around the entrance of the secondary channel. These changes impact the flow along the secondary channel.

Particular attention was paid to the description of the surface velocity over the patches. Figure 10.3.7 shows the temporal evolution of the local depth-averaged velocities estimated along the transects passing through the patch zone for the two flushing events. In 2015, the local velocities over the gravel bar were very low even during the peak hydrograph of the flushing event (around 12h00). On the contrary, in 2016, the local velocities increased rapidly on the gravel bar reaching a maximum at around 11h30 which corresponds to the hydrograph peak of the flushing event.

As the hydrodynamic was very different over the patch zone between 2015 and 2016 event, it was expected that the sediment dynamic would be different too.

10.3.4 Bed shear stresses over the gravel bar

As for the laboratory experiments, bed shear stresses were calculated for the field experiments at global (slope) and local (velocity) scales.

Global bed shear stresses over the gravel bar were calculated using the depth-slope method (Equation 7.1). The water depth were deduced from the pressure gauge measurements. As explained in Section 10.3.2, the estimation of the water slope J was uncertain, impacting the bed shear stress value. In addition, the flow was not uniform in the secondary channel, making questionable the use of the depth-slope equation, at least for low flows.

Local bed shear stresses (τ_l) were estimated using the LSPIV measurements over the gravel bar at different moments of the flushing events. The method used for the computation was based on the log-law (7.2):

$$\tau_l = \rho C_D U^2 = \rho \left(\frac{\kappa}{1 + \ln(h/Z_0)} \right)^2 U^2 \tag{10.1}$$

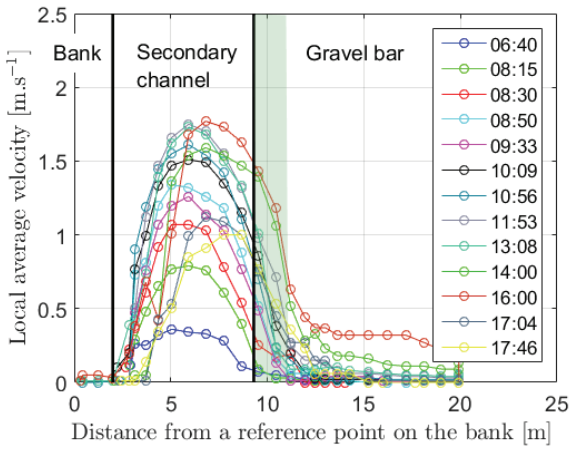

(a) 2015

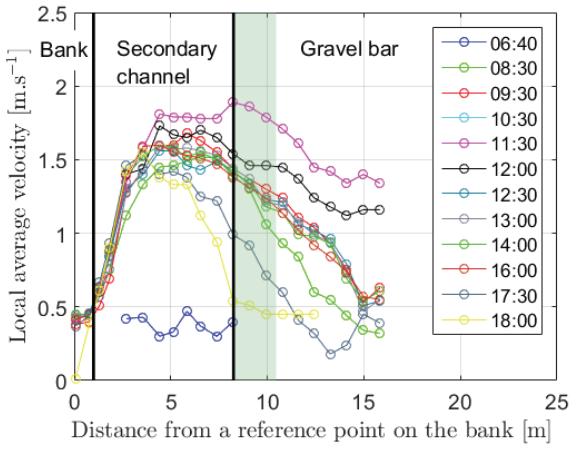

(b) 2016

Figure 10.3.7: Temporal evolution of the local deth-averaged velocities along the transects passing through the patch zone for 2015 and 2016 flushing events. Black vertical lines represent the delimitation between the bank, the secondary channel and the gravel bar. Hours indicated in the legend correspond to times at which videos for LSPIV process were taken. Shaded areas represent the locations of the patches within the gravel bar.

where C_D is a friction coefficient, h is the local water depth, U is the local depth-averaged velocity estimated with the local surface velocity U_s ($U = 0.85U_s$), the coefficient 0.85 is a parameter taking into account the vertical velocity profile shape (Moramarco et al., 2017), Z_0 represents the roughness height and is estimated here as $Z_0 = 30k_s$ (Nikuradse, 1933), and k_s is the equivalent grain roughness assumed to be equal to $2D_{90}$ (Yalin, 1977; Camenen et al., 2006), namely 0.16 m.

Figure 10.3.8 shows global bed shear stress calculated with the water slope estimated from the pressure gauges in comparison to global bed shear stress calculated with a constant water slope estimated to fit the LSPIV values. Bed shear stress values from the LSPIV technique were obtained by averaging the local bed shear stresses obtained using Equation 10.1 along the transverse. To approach the LSPIV transverse-averaged values, a water slope of 0.085 % and 0.14 % was estimated for 2015 and 2016 event, respectively.

Large difference between global bed shear stress values can be observed in Figure 10.3.8. According to the calculations, the maximum bed shear stress was either of around 80 Pa or 10 Pa for 2015 or of around 80 Pa or 18 Pa for 2016. Because the estimation of the water slope was highly uncertain, one can think that the global bed shear stress values obtained with the LSPIV process are the more accurate. However, the estimation of the bed roughness in Equation 10.1 is practically as much uncertain. As we see in our laboratory experiments, the roughness height is difficult to estimate. The mean value $k_s = 2D_{90}$ is probably not correct for this field study, where sediments are poorly sorted and bedforms are present. A k_s based on parameters taking into account the gravel bar arrangement might give a better estimation.

Looking at Figure 10.3.8, one can predict two opposite bedload behaviors. Referring to the Shields diagram (presented in Section 1.2), the bed shear stress necessary for moving gravels of around 6 cm is estimated at around 53 Pa. If we consider global bed shear stresses obtained with the pressure gauges, gravel movement should be possible. However, if we consider τ estimated using the LSPIV process, no gravel should be in motion. One should be careful when using the Shields diagram value as reference value for describing the gravel movement. Indeed, sometimes, the value refers to a general movement. It is then not excluded to have partial movement over the gravel

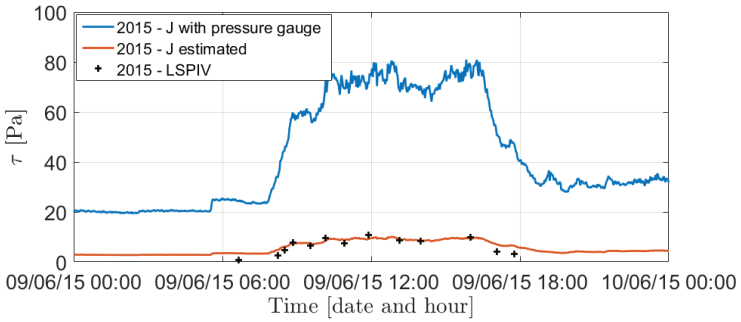

(a) 2015

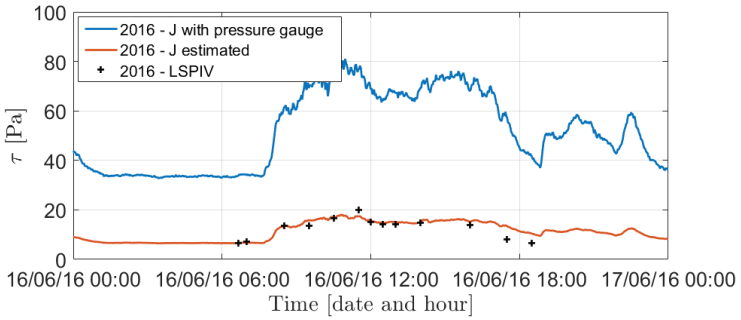

(b) 2016

Figure 10.3.8: Global bed shear stresses within the secondary channel during the 2015 and 2016 flushing events. Blue lines represent global bed shear stresses obtained using the depth-slope equation and the instantaneous measured water slope deduced from the pressure gauges. Cross symbols represent transverse-averaged values of bed shear stress deduced from the analysis of LSPIV data. Orange lines represent global bed shear stresses obtained using the depth-slope equation and an estimation of the water slope chosen to fit the LSPIV values.

bar at lower bed shear stresses.

Figure 10.3.9 shows the local bed shear stresses estimated over the patch zone and in the secondary channel for 2015 and 2016 flushing event. During the 2015 flushing events, local bed shear stresses over the gravel bar (patch zone) barely exceeded 20 Pa. However, within the secondary channel, they varied strongly until reaching a maximum of 35 Pa. For 2016, the behaviour on the gravel bar was different. Local bed shear stresses were much larger than in 2015 and varied rapidly, reaching a maximum of 33 Pa at the hydrograph peak (11:30). Within the secondary channel, the maximum values

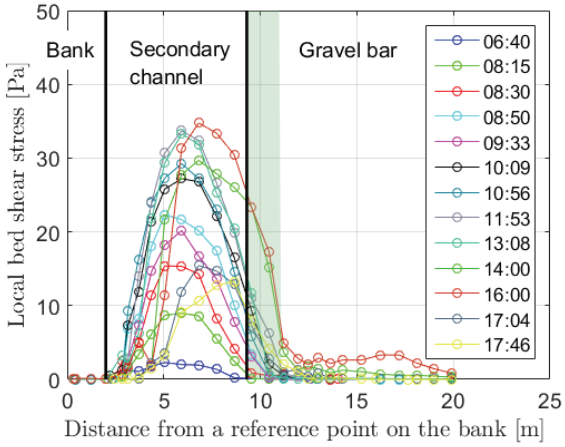

(a) 2015

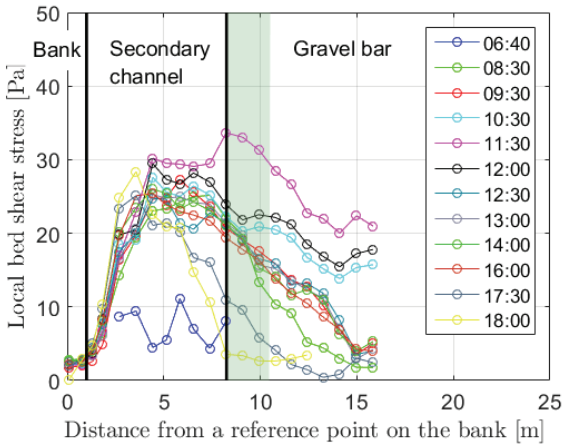

(b) 2016

Figure 10.3.9: Temporal evolution of the local bed shear stresses along the transects passing through the patch zone for 2015 and 2016 flushing events. Black vertical lines represent the delimitation between the bank, the secondary channel and the gravel bar. The hours indicated in the legend correspond to times at which the videos were taken. Shaded areas represent the locations of the patches within the gravel bar.

were similar to the one of 2015. For large discharges, local bed shear stresses tend to homogenize along the secondary channel and on the gravel bar.

Figure 10.3.10 presents the temporal evolution of the local bed shear stresses measured on the patch areas. It shows that in 2016 the values were effectively higher than in 2015. Patches located close to the secondary channel (left) were differentiated from the others (right). The bed shear stresses differed according to their position on the gravel bar. The patches close to the secondary channel were exposed to higher bed shear stress, especially in 2015. More gravel movements were thus expected. In 2016, the difference between the two areas was not strong. Similar bedload behaviors were thus expected.

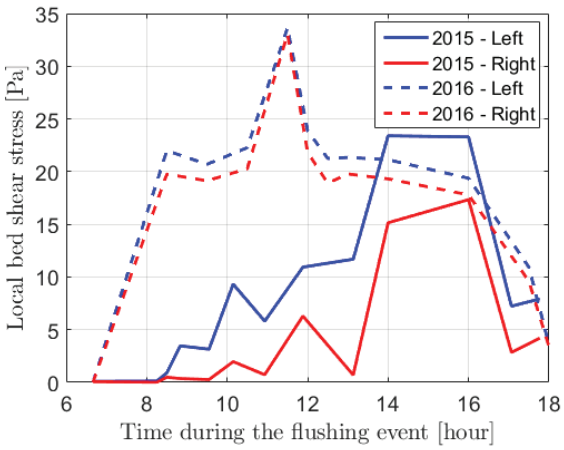

Figure 10.3.10: Temporal evolution of the local bed shear stresses on the patches for 2015 and 2016 flushing events. *Left* denotes patches located close to the secondary channel. *Right* refers to the other patches located more on the gravel bar.

Regarding the local bed shear stress results and based on Shields diagram, no movement of gravel sediments was expected on the gravel bar during the two events (i.e. $\tau \leq 53\,\mathrm{Pa}$). Local estimations might have been underestimated because partial movements were observed in 2016. As for global bed shear stress values, the underestimation might be caused by a wrong estimation of the roughness height.

10.4 Gravel dynamics

10.4.1 Observed movements

Figure 10.4.1 and Figure 10.4.2 present the studied site topography (from the bank to the gravel bar via the secondary channel) before and after the flushing event of 2015 and 2016, respectively. Initial locations of the patches as well as final locations of the individual tagged particles (for 2016 only) were reported on the figures. The black line corresponds to the transect where the estimations of local velocities and bed shear stresses were made. The tagged particles were differentiated following their initial position and patch.

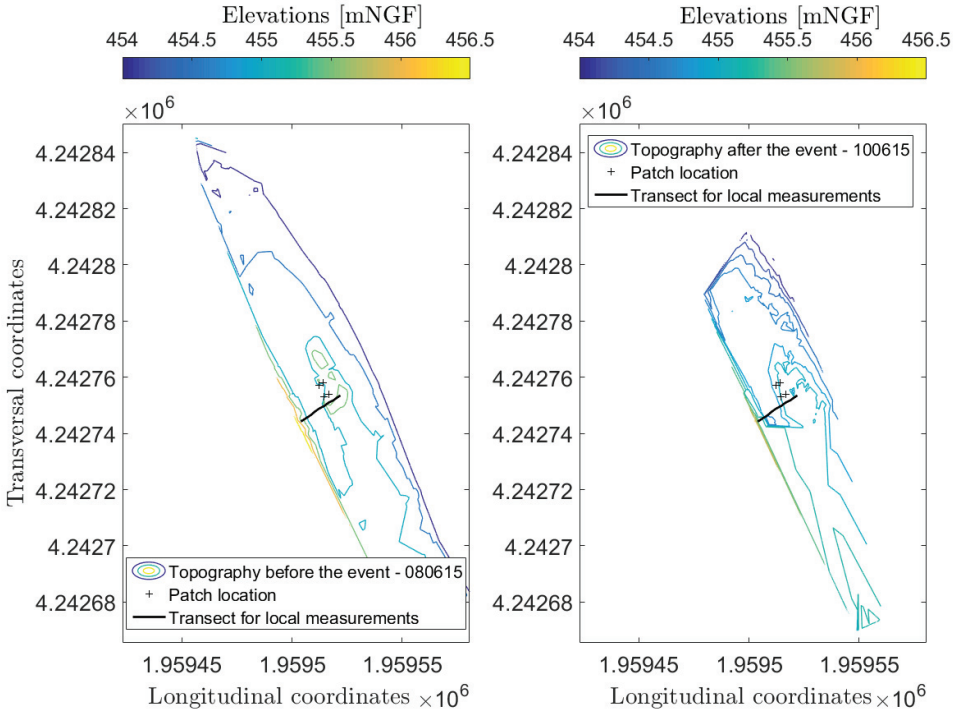

Figure 10.4.1: Topography of the gravel bar before and after the flushing event of 2015. Location of the patches is reported on the graphs. (Coordinates are in Lambert 93 and elevations are in mNGF.)

For the two campaigns, the gravel bar did not evolve significantly. However, a large quantity of fine sediment was deposited over the gravel bar after

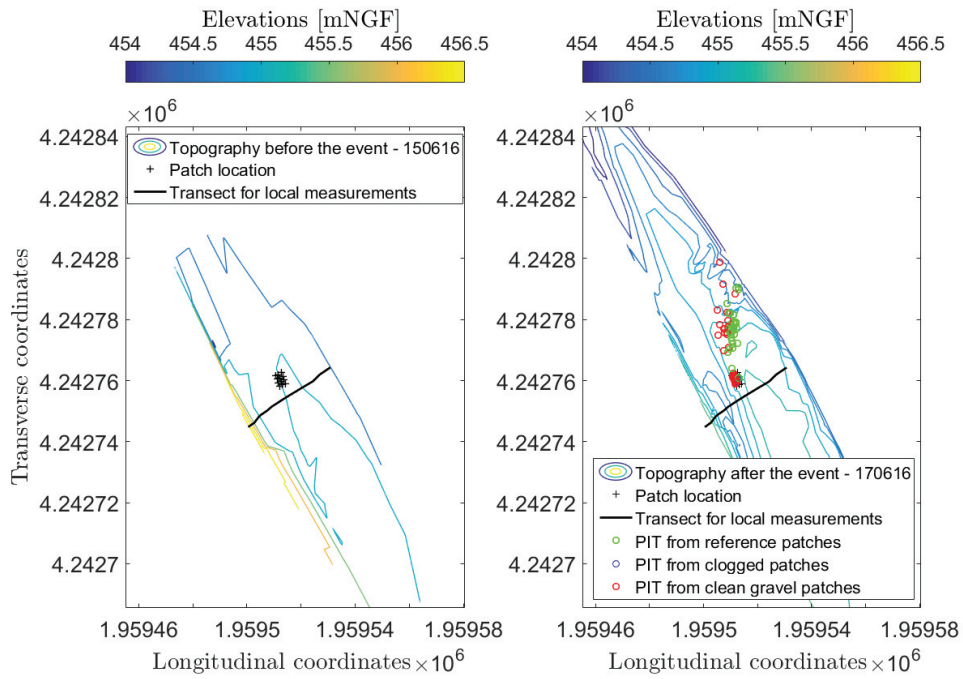

Figure 10.4.2: Topography of the gravel bar before and after the flushing event of 2016. Locations of the patches and of tagged particles are reported on the graphs. (Coordinates are in Lambert 93 CC45 and elevations are in mNGF.)

the event of 2015. In one case, no gravel transport was detectable (2015). In the other case, it was clearly present (2016). In the following, we describe the gravel transport over the bar for the two years. Then, a comparison with our laboratory results will help to validate our proposed methodology.

Flushing event of 2015

During the flushing event of 2015, almost no gravel movement was detected. This was coherent with the prediction made using the local bed shear stress values estimated using the LSPIV measurements. Bed shear stresses were though sufficient to move fine sediments. Figure 10.4.3 shows photographs of patches taken before and after the flushing event of 2015. After the flushing event, a large amount of fine sediments (mixture of fine sand, silt and clay) were deposited on the patches. This deposition might have contributed to limit the gravel movement, if fine sediments were cohesive and infiltrated

(a) Before - reference patch

(b) After - reference patch

(c) Before - clean gravel patch

(d) After - clean gravel patch

(e) Before - clogged patch

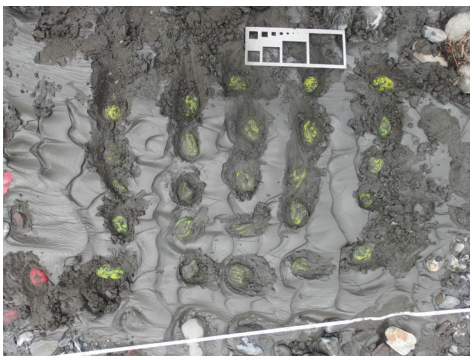

(f) After - clogged patch

Figure 10.4.3: Examples of photographs taken before and after the flushing event in 2015. The three kinds of patches, namely reference, clean gravel, and clogged patches are shown.

within the coarse matrix (see diagram in Section 8.4). Limited gravel movements were detected on one reference patch and one clean gravel patch. These patches were the closest to the secondary channel, so were subjected to larger bed shear stresses than the other patches (see Figure 10.3.10).

Gravel travel distance were evaluated after analysing the photographs with the Matlab toolbox "Image Processing". The procedure is detailled in the following. First, contour of each tagged particles were manually detected. The automatic detection was excluded in that case, because of the large amount of fine sediments polluting the particle edges. Then, images before and after the flushing event were superimposed (see Figure 10.4.4). A step of orthorectification using fixed points was necessary to compare the two images. Finally, thank to the Wolmann scale placed on the photograph, real gravel travel distances were calculated.

Figure 10.4.4 shows two examples of post-treated photographs. Only patches where movements were detected are presented here, namely the reference patch and clean gravel patch close to the secondary channel. The transparent image corresponds to the photograph taken after the flushing event.

The reference patch was the most mobile. Two tagged gravels moved of around 20 - 30 cm which corresponds to the longest travel distance recorded after the 2015 event. The reference patch can be assimilated to the case L-G/S in our laboratory experiments. In other words, the tagged gravels lied on a bed infiltrated with a large amount of fine sediments having a wide grain size distribution (fine gravel, sand, silt, clay). Fine gravels and sand could be observed in both subsurface and surface layers. Their presence enhanced the gravel transport, as the sand enhance the bedload in our laboratory experiments.

Small movements of around 10 cm were detected on the clean gravel patch. In reality, these movements were assimilated to a re-arrangement of the bed surface (i.e. imbrication occurring at low bed shear stress). This behaviour can be compared to the one found in our laboratory experiments during the arrangement phase. In addition, the large amount of infiltrated fine sediment might have clogged the bed, and reduce the bedload. This patch can eventually be assimilated to the P-G/Ms bed of our laboratory experiments.

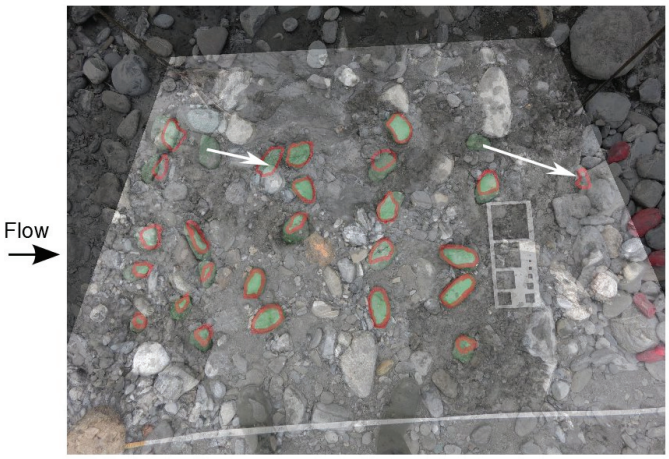

(a) Reference patch

(b) Clean gravel patch

Figure 10.4.4: Detection of the gravel travel distance using image analysis. Contours represent the location of the tagged particles after the flushing event. White arrows point tagged particles in motion. The water flowed from left to right.

Following our experimental results and methodology, we predict that the movement over this patch should be more difficult than if the patch was loose and free from fine sediments.

Clogged patches, even the one close to the secondary channel, were immobile. The bed shear stress applied on the bed was probably not sufficient to move gravels. It is important to remember that these kinds of patches cannot be assimilated to the H-G/Ms beds presented in our laboratory experiments. That is why, in that case, the clogging is probably not the phenomenon preventing the gravels to move. Using the 2016 observations, we will better understand what really happened with these patches.

Flushing event of 2016

During the 2016 flushing event, movements of tagged particles were observed. 150 PIT were installed before the flushing event. 121 were recovered, namely around 80 % of the particles. Several causes might explain the loss of tagged particles in 2016:

- 1: tagged particles were transported to the main channel;
- 2: tagged particles were too close to each other preventing their detection by the antenna (Chapuis et al., 2014);
- 3: tagged particles were too buried because of the strong deposition that occurred during the flushing event, making their detection impossible by the antenna. Several particles were recovered at around 25 cm deep.

Figure 10.4.5 shows that movements were different according to the considered patches. Tagged particles initially placed on a clogged patches did not moved and 92 % of these particles were recovered. Causes 2 and 3 might explain the 8 % lost. Tagged particles from reference and clean patches were transported. 78 % of tagged particles from reference patches and 70 % of tagged particles from clean patches were recovered at distances up to 40 m (close to the main channel). Causes 1 and 3 are probably the main causes for particles loss in that case. Particles from clean and reference patches

have followed two different trajectories based on their initial position on the gravel bar. The two clean patches were both installed close to the secondary channel (Figure 10.2.4) whereas the two reference patches were on the bar side. They clearly followed different preferential flow paths (Figure 10.3.4). In Section 10.3.4, we highlighted that local bed shear stress tends to homogenize at high flows over the gravel bar. This might explain the similar travel distances (between 10 to 25 m mostly) observed for the two kinds of patches (Figure 10.4.7).

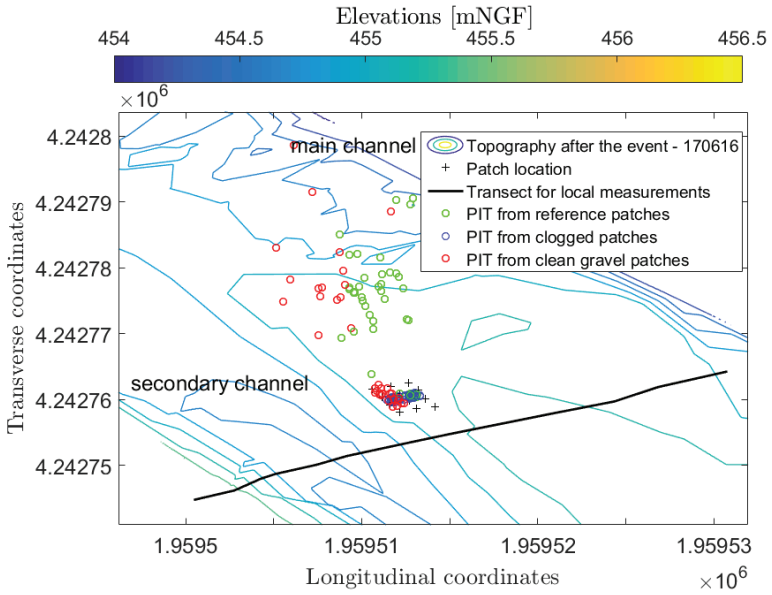

Figure 10.4.5: Topography of the patch zone after the flushing event of 2016. Locations of the patches and of tagged particles are reported on the graphs. Coordinates are in Lambert 93 CC45 and elevations are in mNGF.

Figure 10.4.6 shows that the travel distance was not associated with the tagged particle mass (nor the tagged particle diameter). Particle diameter measurements were not as precise as the one of the mass; that is why we choose to present only the results in terms of mass. No correlation between particle mass and travel distance was observed as well as no correlation between particle mass and immobile gravels or lost gravels. Grain diameter is thus not the controlling parameter for bedload transport in this study. The type of bed configuration is probably more important. The non-dependency of the travel distance on grain diameter is coherent with previous bedload

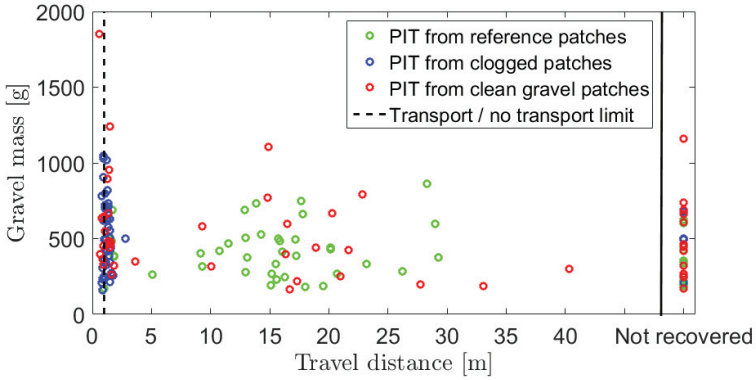

Figure 10.4.6: Grain travel distance in function of the grain mass. The transport/no transport limit was fixed at 1 m to consider the measurement uncertainty. Tagged particles were identified according to their patch configurations.

models, such as Meyer-Peter and Müller (1948) model (Equation 1.5) which predict that the transport q_s is not sensitive to the grain size once the bed shear stress reaches values largely higher than the one required to put gravels in motion.

Indeed, assuming $\tau^* >> \tau^*_{cr}$, Meyer-Peter and Müller (1948) formula becomes:

$$q_s(t) \approx \frac{1}{(s-1)g}\tau^{3/2} \tag{10.2}$$

In our case, the assumption $\tau^* >> \tau^*_{cr}$ is not valid. Indeed, only a partial transport was observed and bed shear stresses did not exceed the critical bed shear stress for incipient motion estimated by the Shields diagram. Most of τ^*_{cr} values in Figure 1.2.2 were estimated for general transport (i.e. when the mobilised sediments are representative of all the bed material GSD). If we use another definition for incipient motion which does not correspond to a general transport of gravels, as for instance the one used in our laboratory studies, one can assume that $\tau^* >> \tau^*_{\text{ref}}$. This means that $\tau^*_{\text{ref}} < \tau^*_{cr}$, if τ^*_{cr} is defined as in Shields (1936). With this assumption, the bedload rate is still independent of the grain size.

Using the Meyer-Peter and Müller (1948) model (Equation 1.5) and the temporal variation of the bed shear stress calculated in Figure 10.3.10, the

travel distance, D_t, can be computed (Camenen et al., 2010):

$$D_t = \int_0^T \frac{q_s(t)}{\delta_s} dt \tag{10.3}$$

where δ_s is the bedload thickness generally assumed equal to $2 \times D_{90}$ (Camenen et al., 2006). In this study, the bedload thickness was small and not larger than one grain size. That is why, we chose to take δ_s equal to D_{90}. The average travel distance measured in 2016 (Figure 10.4.6) as well as Equation 10.3 can be used to find the dimensionless reference bed shear stress of the gravel bar. τ^*_{ref} was estimated of around 0.018 for reference patches using the values of $\tau(t)$ presented in Figure 10.3.10. Applying this value on results from 2015 flushing event, a travel distance of around 80 cm was found which is consistent with experimental observations. To recall, few movements of 20 - 30 cm were observed in 2015 flushing event.

Figure 10.4.7 shows that the travel distance distribution are quite similar for tagged particles coming from the clean gravel patches and the ones coming from the reference patches during 2016 flushing event. Bed shear stresses were thus sufficient to move gravels present on these two types of patches and for their respective positions to the secondary channel. Because the gravel travel distance are similar for the two distributions, one can think that τ^*_{ref} for tagged particles on clean gravel patches and on reference patches were quite close. However, in the case of the 2016 flushing event, the rising limb of the hydrograph was very rapid and high bed shear stresses were rapidly reached. It is thus possible that τ^*_{ref} for tagged particles on the clean gravel patches were effectively different from τ^*_{ref} for tagged particles on the reference patches. Due to the rapidity of the rising limb, times of transport were approximately the same for the particles of the two bed configurations, explaining why there is no strong differences in terms of gravel travel distance. With this kind of experiment, we were not able to know which patches were transported at first. Based on our experimental observations in the laboratory, we can hypothesize that the particles from the reference patches were transported before the one of the clean patches. In 2016, the clean gravel patches could be assimilated to the loose gravel bed case (L-G) studied in our laboratory. Indeed, because of the quick rising limb of the hydrograph,

we assumed that these patches were not able to re-arrange them-selves in comparison to 2015 flushing event.

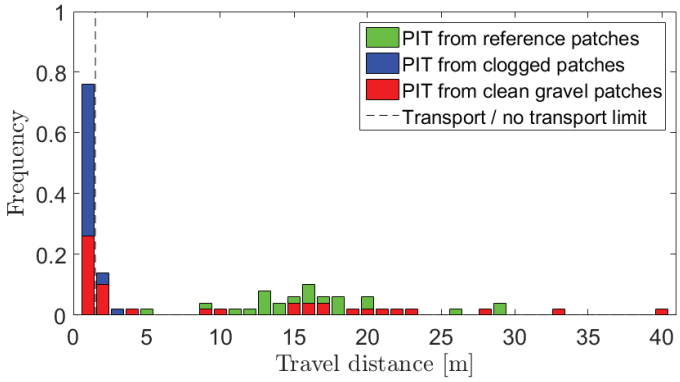

Figure 10.4.7: Distribution of the travel distances of the tagged gravels in function of their initial patch configurations during 2016 flushing event. The transport/no transport limit was fixed at 1 m to consider the measurement uncertainty.

The non-mobility of the gravels belonging to the clogged patches cannot be explained by the same reasons as in the H-G/Ms experiments performed on the laboratory. Indeed, in this field experiment, no contact were present between the tagged grains forming the bed matrix. We think that during the beginning of the flushing event, a large part of the fine sediments clogging the patches were transported whereas the gravels were immobile. Due to the re-suspension of the fine sediment and because no strengthened coarse matrix were present on these patches, their general levels decreased creating holes at the place of the patches containing the tagged particles. These holes can be assimilated to bed irregularities, where bed shear stress intensities were probably lower. So, the gravels could not be transported. In addition, the particles transported from upstream the holes might have been trapped by these irregularities. Then, these upstream grains might have covered the tagged particles, making even more difficult the motion of the latter. This might explain why several tagged particles from the upstream clean gravel patch were located on the clogged patches at the end of the flushing event (Figure 10.4.5).

10.4.2 Comparisons with laboratory results

Regarding the results of the two flushing events, one can conclude that the methodology proposed in Section 8.4.2 provides a good insight into field data interpretation. The different transport behaviours observed on the gravel bar are coherent with those observed in our experiments, namely:

- Tagged particles placed on the reference patches were the easiest to move in comparison to particles from loose, packed or clogged beds (conclusion from the 2015 flushing event);

- Packed or arranged beds were more difficult to move in comparison to loose bed (conclusion from the comparison between 2015 event, where the clean patch was assimilated to a packed patch, and 2016 event, where the clean patch was assimilated to a loose patch because of the rapidity of the hydrograph rising limb during this event);

- Tagged particles placed on clogged patches may be the harder to transport (conclusion from 2016 event). The conclusion is similar to the one found for the flume experiments, although it may be related to different reasons, such as the absence of gravel matrix (i.e. no contact between gravel particles);

- Grain size is not the only parameter controlling the transport: the initial bed surface configuration play an important role (conclusion from 2016 event).

It will be judicious to use the recommendations made in Section 8.4.2 as a complement of the Shields diagram (Figure 1.2.2). The Shields diagram gives only an estimation of the bed shear stress necessary to move gravel particles in function of the particle diameter (τ^*_{cr} =0.055 for coarse particles in our case). In the field case, the simple use of Shields diagram predicted no gravel motion for all patches. On the contrary, if we use the methodology and adjust the critical bed shear stress estimated with the Shields diagram according to the different configurations of the patches (arrangement, clogging), bedload transport is predicted.

The reference dimensionless bed shear stress has been predicted in the previous section equal to τ^*_{ref} =0.018 for the reference patches, so a decrease of 67 % in comparison to the initial estimated Shields values. In the reference patches, small bed arrangement are observed and fine sediments infiltrated in the bed are present. Most of the fine sediments are non-cohesive sand particle. If we refer to the methodology and Figure 8.4.2, the reference bed shear stress should be adjusted up to -40 %. This estimation is lower than the -67 % predicted. We believe that it is because τ^*_{cr} estimated from the Shields diagram refer to a general gravel transport. On the contrary, in our methodology, the initial τ^*_{ref1} corresponds to the first low bedload rate measurable with accuracy on a loose bed. τ^*_{cr} is then over-estimated in comparison to τ^*_{ref1}. Our recommended adjustments are thus under-estimated in that case because the initial reference dimensionless bed shear stress was not the same.

Even if the estimated value proposed by the methodology is not quantitatively correct, the relative and qualitative adjustments are still valid and consistent.

Part IV

Conclusions and prospects

Chapter 11

Conclusions and prospects

11.1 General conclusion

The purpose of this study was to investigate the gravel dynamics at low bed shear stress in case of moderately or poorly sorted bed materials (pebble, gravel, sand, silt and clay) using laboratory experiments.

First challenge was to reproduce, in an 18 m long laboratory flume, bed configurations approaching those found in mountain rivers (i.e. beds with different arrangements and degrees of clogging). A reproducible protocol and a method to create different types of beds were established. A total of 15 experiments were performed:

- 7 experiments on a loose bed (grains were randomly organized);
- 3 experiments on a packed bed (grains were arranged by the flow);
- 1 experiment on a bed infiltrated with fine sand (FS);
- 3 experiments on a bed infiltrated with medium silt (Ms);
- 1 experiment on a bed infiltrated with sand (S).

Second challenge was to determine a dimensionless reference bed shear stress for the incipient motion of gravels, τ^*_{ref}, which is often the key parameter used in previous bedload models. We made the assumption that τ^*_{ref} is a value corresponding to a minimum measurable bedload rate (i.e. $q_s =$

1.325 g/m/s). The study of sediment transport close to the onset of motion showed that it is largely subjected to uncertainties (linked to methodological procedures and experimental conditions). Yet, incipient motion condition needs to be investigated because are the more frequent in rivers. Indeed, bed shear stresses are often close to τ_{ref} value in gravel bed rivers (Camenen et al., 2012). Applying the same definition for incipient motion, we were able to compare one experiment to another and assess how τ^*_{ref} can vary according to the diverse bed configurations.

Third challenge was to understand and characterize the physical processes controlling the bedload rate at different scales (global and local). A large amount of data was collected during sediment transport experiments that enables to distinguish key processes influencing the bedload rate and to develop a phenomenological model synthesizing all the experimental observations. Bed arrangement and fine sediment presence within the transport layer were described as the determining factors for gravel transport. A methodology and recommendations were then given for improving the bedload prediction based on the experimental results and the phenomenological description of the gravel dynamics over different bed configurations. The method was applied to a field case made on the Arc River. It can help to interpret the bedload rate in natural rivers. It also provides clues for adjusting variables of bedload models (such as hydraulic roughness and reference bed shear stress) in numerical simulations.

All these results were encouraging and helped to better understand the gravel transport over moderately or poorly sorted sediments. Further investigations are needed to clarify some points and assumptions in order to develop a new bedload predicting model.

11.1.1 Approach at the global scale

The analysis of the gravel dynamics at the global scale showed that bedload is controlled by flow resistance and bed mobility. The study showed that bed arrangement and the presence of fine sediments within the bed matrix (cohesive or not) highly impact the reference bed shear stress and the hydraulic roughness. The latter are the key variables for bedload models. The

hydraulic roughness informs about the flow resistance and the reference bed shear stress informs about the bed mobility.

To succeed in understanding the impact of bed arrangement on bedload rates, a bed surface characterization method was developed to compare the topography of diverse beds. The bed surface characterization enabled to classify our beds according to their bed arrangement degrees. Bedload rate was found to decrease with decreasing bed roughness, with increasing lengths of structures or bedforms, with increasing grain imbrication and when the grains were aligned with the flow direction. Our study highlighted that even small differences in topography can lead to significant differences in bedload rates.

The impact of the presence of cohesive and non-cohesive sediments on bedload rate were also investigated. Their presence impacts the bed matrix composition and changes the properties of the bed. Comparison between beds infiltrated with fine sediments having similar grain sizes (H-G/FS and H-G/Ms) have suggested that the grain size was not the only determining parameter for understanding bedload rate. Bed permeability, bed cohesion and sediment shapes were found to be significant too. An increase in bed cohesion, which is directly related to the fine sediment residence time, makes the transport more difficult. Similarly, angular fine sediments strengthen the bed reducing the gravel transport. On the contrary, circular fine grains tend to lubricate the bed. Comparison between beds infiltrated with cohesionless sediments having different grain sizes (H-G/FS and H-G/S) have highlighted that the fine sediment concentration within the transport layer influence the bedload rate. When the concentration is sufficient, bedload rate is highly enhanced (the number of contacts between coarse and fine sediments increases). This was previously observed with sand and gravel mixtures (Wilcock et al., 2001).

11.1.2 Approach at the local scale

Analysis of the dynamics at the local scale enabled to identify the impact of bed spatial variability on the local flow structure and friction velocity. The friction velocity obtained using the Reynolds stress method were found to

be the less impacted by spatial variability and uncertainties linked to the computation method. The results showed that only the nearby roughness controls the local flow structure and not the structures or bedforms present on the bed surface. The local analysis was only performed under three kinds of beds: loose, packed and infiltrated with Ms sediments beds.

The part of the friction force used to transport gravel was found to be reduced in case of experiments conducted on packed and infiltrated beds. If we consider that grain friction is responsible for the transport, its reduction leads to a decrease in bedload rates, that was indeed observed. In case of packed beds, a part of the total friction force was dissipated through the bedforms. In case of infiltrated beds, we wonder where this energy were dissipated since no bedforms were present.

Local results show that q_s is mainly controlled by the flow resistance and not by the bed stability. Indeed, same local bed shear stress is needed to produce similar q_s. This assessment should be taken with caution because large uncertainties were associated to local results. Regarding local observations, bed arrangement and infiltration only influence the flow structure that will consequently modify the bedload rate.

A complementary study on the influence of the infiltration height within the bed on the flow structure proved that it is only when the distance between bed surface and height of infiltrated fine sediments becomes lower than $2\times D_{50}$ that the local flow structure are affected. This result probably explains why gravels from H-G/FS and H-G/Ms beds behaved differently. In case of H-G/FS, the fine sediment were rapidly washed from the bed surface and subsurface. They were almost not present below the surface in the two first gravel layers. The flow structure was not affected by the infiltration of fine sediments, and the bed behaved like a H-G bed.

Bed arrangement and the presence of infiltrated fine sediments impact the flow structure and turbulence. Accelerations of the flow close to the bottom were seen for packed and infiltrated beds. For the packed bed, this acceleration was due to a smoothing of the bed surface and for the infiltrated bed it was due to a reduction of the bed porosity. Reynold stress profiles were steeper in case of loose beds leading to a higher friction velocity. Turbulence intensities were smaller for loose beds. Indeed, L-G bed have higher

bed roughness which enhances the destruction of large turbulent eddies and transforms them into smaller ones with less intensity.

11.1.3 Toward a general understanding of gravel transport

Figure 11.1.1 shows the relationship between flow resistance and dimensionless bedload rate for beds having different surface arrangements. Flow resistance is quantified either using the dimensionless total bed shear stress, or using the dimensionless skin friction estimated using the Manning-Strickler equation ($\tau_K'^*$), or using the dimensionless skin friction estimated using local measurements ($\tau_l'^*$). Figure 11.1.2 shows the same relationship but for infiltrated beds in comparison to non infiltrated beds. Analysing these Figures, we can discuss the main mechanisms influencing the bedload dynamics.

The analysis of the results at the global scale shows that there is a large scatter in the relation $q_s^* = f(\tau^*)$ with distinct behaviors for loose and packed beds (see Figure 11.1.2a). Taking into account the fact that we should consider skin friction rather than the total bed shear stress in sediment transport prediction (Figure 11.1.1b), the scatter is reduced but there is still a clear difference between loose (L-G-i Rising) and packed or hybrid beds (L-G-i Falling or P-G-i Rising and Falling). With these observations, one can conclude that both the estimations of flow resistance and bed stability are necessary to predict the sediment transport q_s. In other words, if we want to predict q_s with classical formula, both the reference (or critical) bed shear stress value τ_{ref}^* and the parameter describing the flow resistance (often k_s, which represents the relation between discharge (or flow velocity) and bed shear stress) has to be modified in case of packed bed instead of loose bed. We did not compute skin friction for infiltrated bed but results with total bed shear stress (Figure 11.1.2a) suggest also the importance of flow resistance and bed stability in the bedload rate prediction.

If we now look at the results at the local scales, one can note that the relation $q_s^* = f(\tau_l'^*)$ is the same for all type of beds. No significant difference in the relation $q_s^* = f(\tau_l'^*)$ is observed between loose and packed beds and between non-infiltrated and infiltrated beds (see Figures11.1.1c and 11.1.2b).

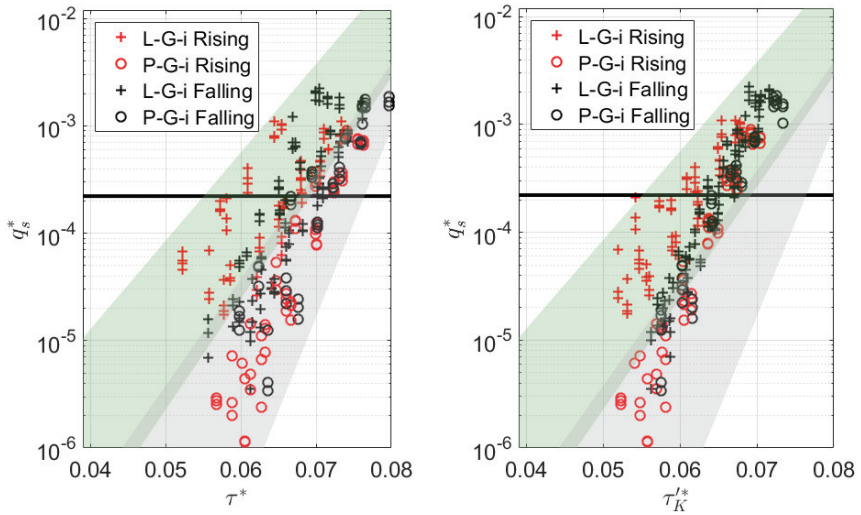

(a) $q_s^* = f(\tau^*)$ **(b)** $q_s^* = f(\tau_K'^*)$

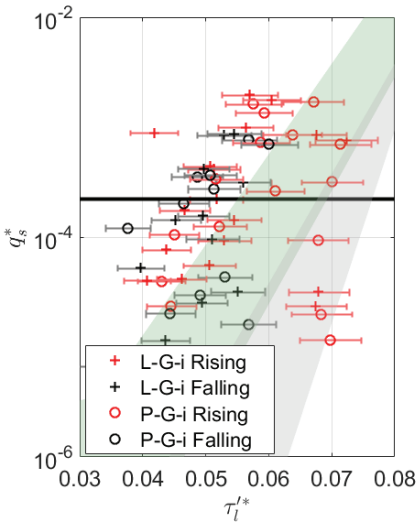

(c) $q_s^* = f(\tau_l'^*)$

Figure 11.1.1: The q_s^* as a function of a) the total dimensionless bed shear stress τ^*, b) the dimensionless skin friction $\tau_K'^*$ and c) the dimensionless skin friction $\tau_l'^*$; results for all sediment transport experiments conducted on unimodal beds. Red and black colors represent data during the rising and falling limb, respectively. + and *o* symbols show data related to experiments performed on loose and packed beds, respectively. The black horizontal line corresponds to the dimensionless reference low transport rate.

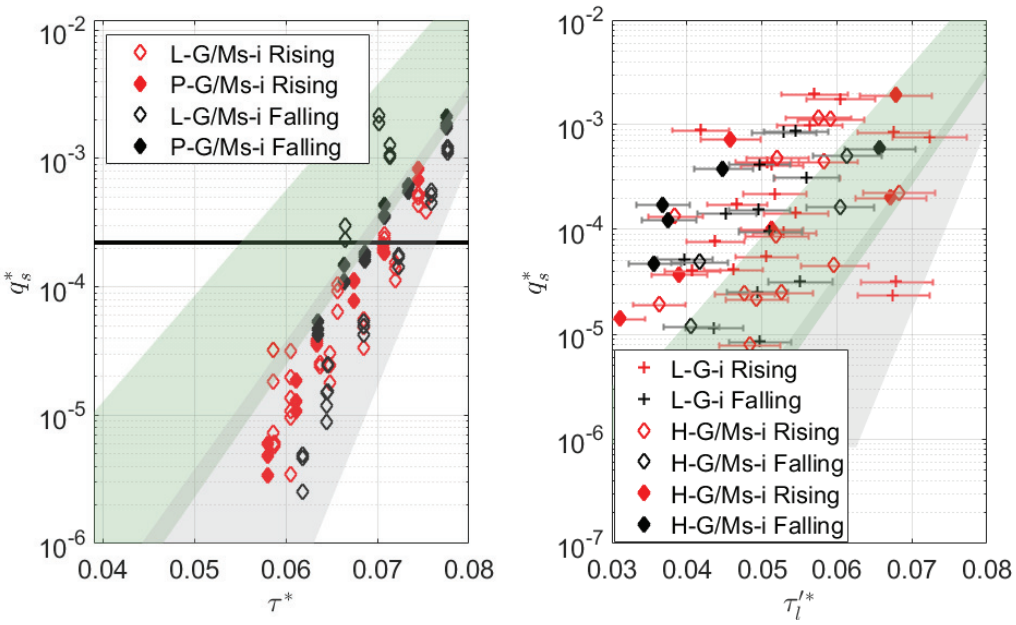

(a) $q_s^* = f(\tau^*)$ **(b)** $q_s^* = f(\tau_l'^*)$

Figure 11.1.2: The dimensionless bedload rate as a function of a) the total dimensionless bed shear stress τ^* and b) the dimensionless skin friction $\tau_l'^*$; results for all sediment transport experiments conducted on non infiltrated and associated infiltrated with Ms beds. Red and black colors represent data during the rising and falling limb, respectively. + and ♢ symbols show data related to experiments performed on non infiltrated and infiltrated with Ms beds, respectively. The black horizontal line corresponds to the dimensionless reference low transport rate.

Considering that $\tau_l'^*$ characterizes flow resistance, it could mean that q_s depends on flow resistance only and not on bed stability. This suggests that bedload rate is impacted by changes in bed arrangement and by fine sediment presence because flow resistance is impacted. One should have in mind that large uncertainties were associated to these local results, which makes difficult to conclude about the validity of the previous assessment.

11.1.4 Summary of the controlling parameters

The main mechanisms influencing the bedload rate were identified and partly understood in this study. This part summarizes how bedload rate is impacted

by changes in bed arrangement and fine sediment presence. The relative importance between flow resistance and bed stability in the estimation of q_s^* is also examined.

Figure 11.1.3 schematizes the effect of bed arrangement and fine sediment presence on flow resistance and on bed stability, so on transport rate. Let's consider a gravel-bed with no particular bed surface arrangements. A flow is imposed on this bed, which generates a water-worked bed surface. In that case, the gravel matrix becomes more compact and the bed porosity decreases. The bed surface geometrical roughness also decreases. In addition, more bedforms are observed on the water-worked bed. All the previous changes due to bed arrangement impact directly the flow resistance by decreasing it. This leads to a reduction in bedload rate. The process of arrangement also have an impact on structures and grain imbrications within the bed. The latter increase, which conducts in a stronger bed stability and reduces the bedload rate. To conclude, bed arrangement leads to a decrease in bedload rate. The effect of bed arrangement on sediment transport due to flow resistance changes prevails on the effect due to bed stability changes, according to the local measurement results.

In comparison to a non infiltrated bed, an infiltrated bed has a smaller bed porosity. Consequently, its flow resistance should be reduced and so its bedload rate. Let's consider a flow running over an infiltrated bed. The flow would have some difficulties to remove fine sediments from the gravel bed matrix in case of cohesive fine sediments. That is why, the porosity remains low, so does the flow resistance and the bedload rate. On the contrary, non cohesive fine sediments are easy to wash from the bed surface. The bed porosity therefore increases until reaching the value corresponding to a non infiltrated bed. That way, the flow resistance and the bedload rate are the same as those of a non infiltrated bed. If the bed is infiltrated with cohesive fine sediments, the bed stability increases because of the strong consolidation induced by fine particles. This leads to a decrease in bedload rate. The consolidation is probably related to the concentration of cohesive fine sediments in the gravel matrix. If the bed is infiltrated with non cohesive fine sediments, the bed stability decreases due to the lubrication effect generated by the fines. This conducts to an increase in bedload rates. The lubrication

effect is proportional to the concentration of non cohesive fine sediments in the transport layer as well as their shape. To conclude, in presence of non cohesive fine sediments, the bedload rate is enhanced whereas in presence of cohesive fine sediments, the bedload rate is reduced. In our studied cases, the presence of fine sediments seems to impact in an equivalent manner flow resistance and bed stability.

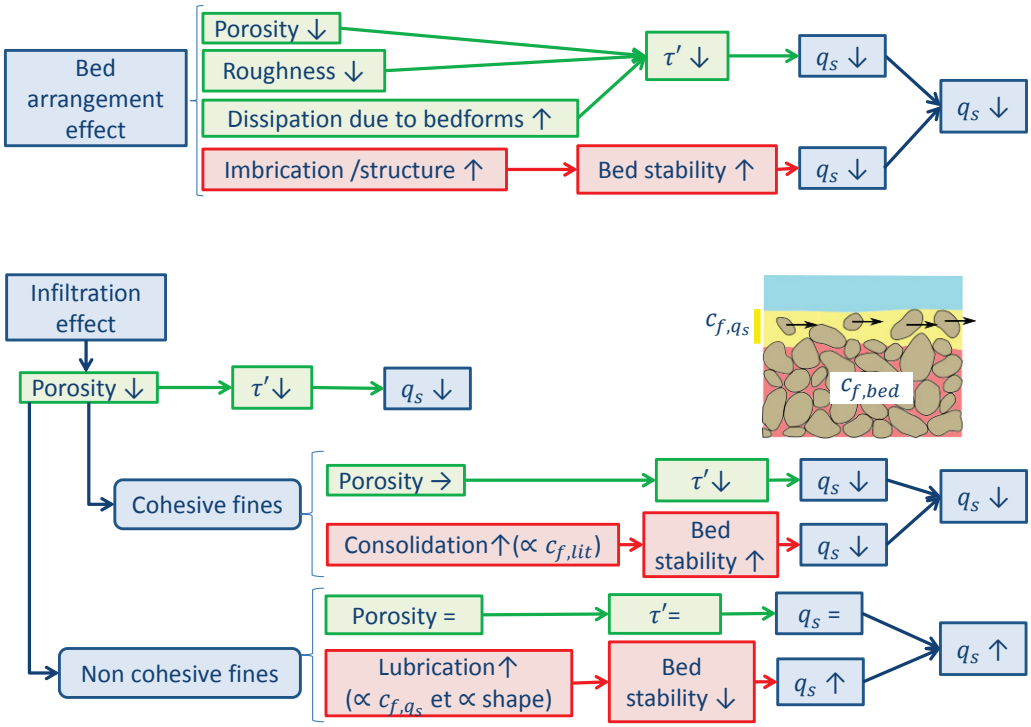

Figure 11.1.3: Summary of the effect of bed arrangement and presence of fine sediment on bedload rate.

11.2 Prospects

During this study, an important data set was collected providing the means to better understand the gravel transport over moderately or poorly sorted bed material. However, several questions remain unanswered. This part present different suggestions for further works with the aim of improving the

bedload transport knowledge and associated morphodynamics using a similar experimental set-up (as the one present in Irstea Lyon-Villeurbanne) or using other means.

11.2.1 Improvement of the flow and sediment transport descriptions at local scale

Experiments using our installations

We saw that the gravel dynamics analysis at the local scale was difficult to interpret because of a relative lack of data. It would be interesting to perform experiments over the same bed configurations and for the same hydraulic conditions, but spending more time on local measurements to better understand the dynamics at this scale. Several Vectrino II devices could be installed on the mobile platform to measure at several locations at the same time in order to double-average our data (average in time and space). In that way, the effect of spatial variability could be avoided and only effect of bed arrangement and infiltration on flow and turbulence structures could be highlighted. The relationship between the hydraulic roughness k_s and bed arrangement parameters could be clarified. In addition, the turbulence and its associated events (sweep and ejection) could be studied. Eventually, it would give new clues for characterizing the incipient motion of gravels.

The measurements at the local scale could be made using the Particle Image Velocimetry (PIV) technique when the fine sediment concentration is not too high in the water column. Loose and packed beds could be studied with this technique. However, it might be more difficult for infiltrated beds. It could be possible with sand/gravel mixture if sand particles are mainly transported as bedload.

Experiments in collaboration with an institute in Québec

During my thesis, I have helped B. Camenen to perform flume experiments in the INRS laboratory in Quebec (Canada) in order to study the dynamics of a fine and coarse sediment mixture using a medical CT-scan (Camenen et al., 2017). The propagation of sand (ripples or dunes) was monitored over

the coarse bed using the CT-scan. This device enables to have a detailed description of the inside bed and its surface. Using these results, we hope to be able to evaluate the evolution of bed properties (e.g. bed porosity) and to characterize more precisely the process of infiltration (sealing). In addition, during these experiments a PIV system was available. Using the PIV measurements associated with precise bed surface measurements (as well as bed properties), we expect to understand the impact of the infiltration on the local flow structure and consequently on the bedload rate which was measured at the downstream end on a the flume. All the data of these experiments are not analysed, yet.

11.2.2 Improvement of the methodology for improving bedload prediction

First of all, another validation of the phenomenological model and of the methodology should be done using other experiments performed under the same conditions and using the same sediments as those chosen for this study. Multiplying the experiments takes a lot of time knowing that the duration for carrying out an experiment couple is about one month. That is why, this kind of validation was not done. At least three times the same test should be done. It could help making the difference between general trends and individual cases. In this phD thesis, we chosen to perform a wide range of tests in different conditions, in order to cover a sufficiently wide range of cases to build our phenomenological model as general as possible. Others tests are nevertheless needed to improve the developed model and precise our recommendations.

Case of multimodal bed material

The experiments were only performed on unimodal or bimodal beds. Yet, in natural rivers, multimodal beds can be encountered. The methodology needs to be expanded to multimodal cases. Using our actual sediments, one can think of conducting experiments on gravel beds infiltrated with sand and fine sand (H-G/S/FS) or with sand and medium silt (H-G/S/Ms). Two types of infiltration would be present: sealing for the sand sediments and

bottom-up infiltration for the Ms and FS sediments. The bed behaviour could be modified because of the inhomogeneity of the fine sediment distribution within the bed matrix.

Case of water-worked beds

To complete the dataset, sediment transport experiments on water-worked bed (Cooper and Tait, 2009) need to be carried out. In our laboratory, the sediment feeding system can be used to built such a bed. Then, sediment transport experiments with the same hydraulic conditions (hydrograph) than the others can be performed. The sediment feeding was installed during the last year of my PhD thesis, that is why the water-worked method was not used since the beginning of the study. Water-worked beds can be formed by gravels only but also with multimodal bed material. In that latter case, phenomena of grain sorting can be investigated. These new experiments might enable to detect new areas in (q_s^*, τ^*) plot and explore larger range of incipient motion thresholds. A first test of experiment on a water-worked bed is presented in the following.

One sediment transport experiment was conducted on a water-worked bed composed of gravels only. The preparation of this bed was not easy and reveals that the protocol needs to be improved. Some interesting observations were nevertheless put forward.

We tried to create a water-worked bed which has approximately the same thickness as the loose or packed beds (around 8 - 9 cm) to facilitate the comparison between experiments. Approximately 2.3 tons of gravels are needed to realize such a bed. The construction of a water-worked bed is a long process. We estimated specific hydraulic conditions and feeding rates in order to create it in a limited time (2 days). We set the channel slope at 1.8 % and the flow discharge at 45 L/s. It corresponds to a transport capacity of the flow of about 25 g/s according to observations from sediment transport experiment performed on a loose bed under these conditions. To ensure the gravel deposition in the channel, the feed rate was adjusted to at least twice the flow transport capacity. During the creation of the water-worked bed, the flume was fed with a constant gravel rate of 70 g/s. In the middle of the

construction, the channel slope was reset at 1.3 % because there was no more deposition in the flume at 1.8 %.

Figure 11.2.1a present a DEM of the final state of the water-worked bed. Bed elevations varies from 5 cm to 10 cm along the flume. The morphology of the water-worked bed differs strongly from the one of loose or packed beds, which were very flat. Here, the morphology is clearly more complex with presence of bedforms and preferential flow pathways. It seems that gravel bars start to appear. This change in morphology will probably influence the transport rate.

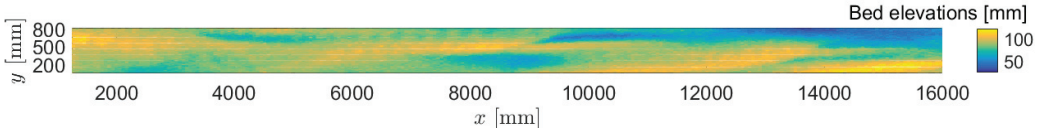

(a) Water-worked bed before gravel transport experiment

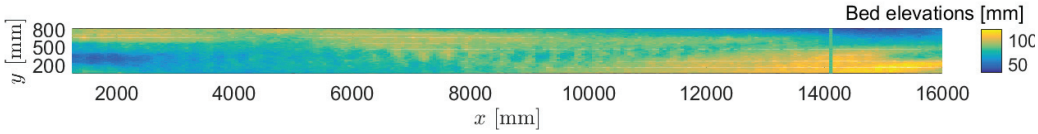

(b) Water-worked bed after gravel transport experiment

Figure 11.2.1: Topography of the water-worked bed: (a) after its construction in the flume of Irstea Lyon-Villeurbanne and (b) after the gravel transport experiment.

Gravel transport experiment was performed on the water-worked bed presented in Figure 11.2.1a. Same experimental protocol as the one for experiments conducted on loose or packed beds was used. The channel slope was set at 1 % and the bed was subjected to a symmetrical hydrograph (rising and falling limbs). No gravel feeding was present during this experiment. Figure 11.2.2 shows the flow and gravel rate variations during the experiment. At the peak of the hydrograph, the gravel rates reach values up to 20 $g.m^{-1}.s^{-1}$ which are higher than the one obtained for the loose or packed gravel beds (of around 10 g/m/s). The shape of the bedload evolution follows a single-peak shape. Bedload intensity seems different during the rising limb compared to the falling limb. Bedload rate is probably enhanced due to the presence of bedforms. During the falling limb, bedforms are slightly smoothed reduc-

ing progressively the bedload rate. Figure 11.2.1b shows topography of the water-worked bed after the gravel transport experiment. Bars and forms are less clear. The bed has changed its state of equilibrium.

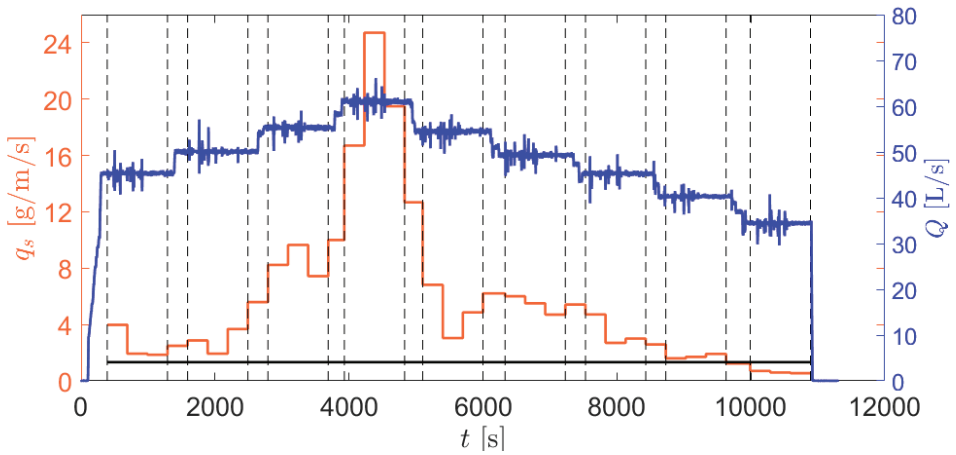

Figure 11.2.2: Time variations of bedload (q_s) and flow (Q) rates for an experiment performed on a water-worked bed. (Grid delimits steady states from transitions zones. Black horizontal line corresponds to the reference transport rate $q_{s\text{-ref}}$. The left axis refers to the bedload rate (orange) and the right axis refers to the water discharge (blue).)

Figure 11.2.3 presents all the results obtained for unimodal beds as well as the ones obtained during the experiment on the water-worked bed. It shows the dimensionless bedload rate, q_s, as a function of the dimensionless bed shear stress, τ^*. Regarding the data at the hydrograph rising and falling limb, a counterclokwise hysteresis for the water-worked experiment was observed. For this case, sediment transport is far from what we obtained at similar bed shear stress for loose or packed beds. Data points are located in a new area with high bedload rates for τ^* values being smaller. With these differences between the diverse experiments performed on unimodal gravel beds, we highlight the impact of a change in bed arrangement and/or the presence of bedforms.

Case of rivers with alternate bars

Because rivers in the Alps are often constraint (e.g. the Arc river), it could be interesting to analyse the morphological evolution of such rivers. The

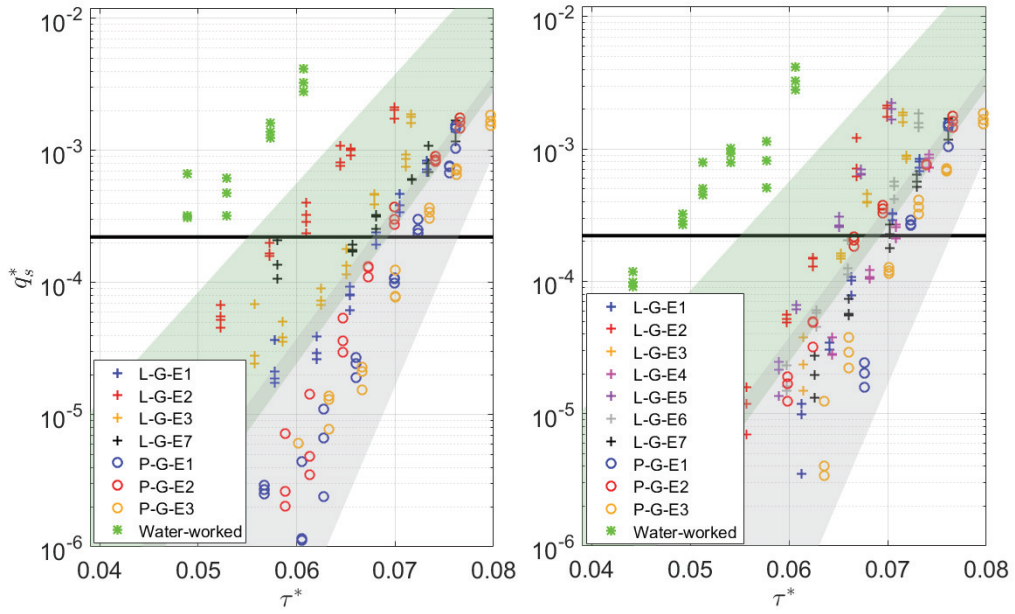

(a) Rising limb **(b)** Falling limb

Figure 11.2.3: Evolution of the dimensionless bedload rate according to the dimensionless bed shear stress for experiments performed on unimodal gravel beds (loose, packed and water-worked): (a) at the rising limb and (b) at the falling limb. (Green and grey shaded areas delimit data from experiments conducted on loose beds to data from experiments conducted on packed beds during the rising limb. These areas are reported on data at the falling limb. The black horizontal line corresponds to the dimensionless reference low transport rate $q^*_{s\text{-ref}} = 2.2\times10^{-4}$.)

beds of these kinds of rivers are often composed of alternate bars. These bars have probably an influence on the bedload rate evolution and on the sediment incipient motion. To understand the morphological evolution of these mountain rivers, it is important to try to reproduce such beds in a flume experiment (Lisle et al., 1991). Our channel side will represent dikes for example. Using the proper setting, our actual installations could be sufficient to create a bed with alternate bars. Indeed, the experiment on the water-worked bed presented above was encouraging. Bars were almost created. The global impact of the presence of alternate bars (unimodal or multimodal) on the transport rate could be studied. Bars could be composed of gravels only but also of a large range of sediments which is more representative of natural river bars.

11.2.3 Impact of bedload rate on fine sediment transport

The study focuses on the bedload transport. The impact of fine sediment transport on bedload was investigated. No tests were performed to understand the impact of bedload on the fine sediment transport. Yet, fine and coarse particles are continuously in interaction. It could be thus interesting to complete this study with another point of view by focusing on the fine sediments and the impact of the gravel presence on their transport.

11.2.4 Improvement of restoration operations

The experiments on bimodal beds monitored the evolution of the fine sediment height within the bed during an hydrograph. These observations could be used to help some restoration operations in natural river which consists in declogging the bed from its fine sediments infiltrated within the bed matrix. The declogging process needs to be operated without transporting too much the coarse matrix which constitutes the fish habitat. Other experiments should be performed to quantify the efficiency of the declogging during such operations (i.e. evaluate the declogging depth). Different hydraulic conditions than a symmetrical hydrograph should be tested. An ongoing project supervised by Irstea is dealing with these questions.

11.2.5 Use of different material

The gravels available for my PhD study were probably too sorted. Different bed arrangements were difficult to obtain. We think that performing this study with gravels having more scattered grain size distribution could reveal stronger bed arrangements. Structures and bedforms would be clearer and easier to detect. The difference between the bed surface criteria obtained on the different bed configurations would probably be more identifiable. The determining bed surface criteria influencing the calculation of k_s and the determination of τ^*_{ref} could be clarified.

Experiments using more cohesive and natural fine sediments are needed to investigate the cementation phenomena. These phenomena may strongly

affects sediment transport in natural rivers. We have seen that the cementation depends on the fine sediment residence time. Several experiments could be done to relate the degree of bed consolidation or cohesion (C_u) to the bedload rate in order to specify the relation between τ^*_{ref} and C_u. Core samples of the clogged beds and laboratory analyses might be needed to quantify C_u as a function of the fine sediment residence time. C_u will also depends on the type of fine sediments (organics presence, percentage of clay, etc.)

Bibliography

Aberle, J. and Nikora, V. (2006). Statistical properties of armored gravel bed surfaces. *Water Resources Research*, 42(W11414):1–11.

Aberle, J. and Smart, G. M. (2003). The influence of roughness-structure on flow resistance on steep slopes. *Journal of Hydraulic Research*, 41(3):259–269.

Ancey, C., Bohorquez, P., and Heyman, J. (2015). Stochastic interpretation of the advection-diffusion equation and its relevance to bed load transport. *Journal of Geophysical Research: Earth Surface*, 120(12):2529–2551.

Ancey, C., Davison, A. C., Böhm, T., Jodeau, M., and Frey, P. (2008). Entrainment and motion of coarse particles in a shallow water stream down a steep slope. *Journal of Fluid Mechanics*, 595(011302):83–114.

Antoine, G., Jodeau, M., Camenen, B., Esteves, M., Némery, J., and Lauters, F. (2013). Estimation des flux de matières en suspension lors des chasses hydrauliques de l'Arc de 2006 à 2011. *La Houille Blanche*, 4:43–49. (in French).

Armanini, A. and Gregoretti, C. (2005). Incipient sediment motion at high slopes in uniform flow condition. *Water Resources Research*, 41(W12431):1–8.

Ashida, K. and Michiue, M. (1972). Study on hydraulic resistance and bed-load transport rate in alluvial streams. *Transaction, Japan Society of Civil Engineering*, 206:59–69.

Barzilai, R., Laronne, J. B., and Reid, I. (2013). Effect of changes in fine-grained matrix on bedload sediment transport in a gravel-bed river. *Earth Surface Processes and Landforms*, 38:441–448.

Bathurst, J. C. (1985). Flow resistance estimation in mountain rivers. *Journal of Hydraulic Engineering*, 111:625–643.

Beheshti, A. and Ataie-Ashtiani, B. (2008). Analysis of threshold and incipient conditions for sediment movement. *Coastal Engineering*, 55(5):423–430.

Bergeron, N. (1996). Scale-space analysis of stream-bed roughness in coarse gravel-bed streams. *Mathematical Geology*, 28(5):537–564.

Bertin, S. and Friedrich, H. (2014). Measurement of gravel-bed topography: Evaluation study applying statistical roughness analysis. *Journal of Hydraulic Engineering*, 140(3):269–279.

Beschta, R. L. and Jackson, W. L. (1979). The intrusion of fine sediments into a stable gravel bed. *Journal of the Fisheries Research Board of Canada*, 36(2):204–210.

Biron, P., Robson, C., Lapointe, M., and Gaskin, S. J. (2004). Comparing different methods of bed shear stress estimates in simple and complex flow fields. *Earth Surface Processes and Landforms*, 29:1403–1415.

Blott, S. J. and Pye, K. (2008). Particle shape: a review and new methods of characterization and classification. *Sedimentology*, 55(1):31–63.

Booth, D. (1991). Urbanization and the natural drainage system - impacts, solutions, and prognoses. *Northwest Environmental Journal*, 7:93–118.

Brand, A., Noss, C., Dinkel, C., and Holzner, M. (2016). High-resolution measurements of turbulent flow close to the sediment-water interface using a bistatic acoustic profiler. *Journal of Atmospheric and Oceanic Technology*, 33(4):769–788.

Brayshaw, A. C., Frostick, L. E., and Reid, I. (1983). The hydrodynamics of particle clusters and sediment entrainment in coarse alluvial channels. *Sedimentology*, 30:137–143.

Breugem, W., Boersma, B., and Uittenbogaard, R. (2006). The influence of wall permeability on turbulent channel flow. *Journal of Fluid Mechanics*, 562:35–72.

Brooker, M. (1985). The ecological effects of channelization. *The Geographical Journal*, 151(1):63–69.

Buffington, J. M. and Montgomery, D. R. (1997). A systematic analysis of eight decades of incipient motion studies, with special reference to gravel-bedded rivers. *Water Resources Research*, 33(8):1993–2029.

Buscombe, D. and Conley, D. (2012). Effective shear stress of graded sediments. *Water Resources Research*, 48(W05506):1–13.

Camenen, B. (2012). Discussion of understanding the influence of slope on the threshold of coarse grain motion: Revisiting critical stream power by C. Parker, N.J. Clifford, and C.R. Thorne. *Geomorphology*, 139-140:34–38.

Camenen, B., Bayram, A., and Larson, M. (2006). Equivalent roughness height for plane bed under steady flow. *Journal of Hydraulic Engineering*, 132(11):1146–1158.

Camenen, B., Herrero, A., Dramais, G., Thollet, F., Le Bescond, C., Perret, E., and Berni, C. (2015). Field experiment on the dynamics of fine and coarse sediments over a gravel bar in an alpine river. In *Proceedings of the 36th IAHR Congress*, The Hague, The Netherlands.

Camenen, B., Holubová, K., Lukač, M., Le Coz, J., and Paquier, A. (2011). Assessment of methods used in 1D models for computing bedload transport in a large river: the Danube River in Slovakia. *Journal of Hydraulic Engineering*, 137(10):1190–1199.

Camenen, B., Jaballah, M., Geay, T., Belleudy, P., Laronne, J. B., and Laskowski, J. P. (2012). Tentative measurements of bedload transport in

an energetic alpine gravel bed river. In Murillo Mũnoz, R. E., editor, *River Flow, Proceedings of 6th International Conference on Fluvial Hydraulics*, pages 379–386, San Jose, Costa Rica.

Camenen, B. and Larson, M. (2005). A bedload sediment transport formula for the nearshore. *Estuarine, Coastal and Shelf Science*, 63:249–260.

Camenen, B. and Larson, M. (2005). A general formula for non-cohesive bed load transport. *Estuarine, Coastal and Shelf Science*, 63:246–260.

Camenen, B., Le Coz, J., Paquier, A., and Lagouy, M. (2010). An estimation of gravel mobility over an alpine river gravel bar (Arc en Maurienne, France) using PIT-tag tracers. In Dittrich, A., Koll, K., Aberle, J., and Geisenhainer, P., editors, *River Flow, Proceeding of the 5th International Conference on Fluvial Hydraulics*, pages 953–960, Braunschweig, Germany.

Camenen, B., Perret, E., Brunelle, C., Francus, P., Des Roches, M., and Daigle, L.-F. (2017). Dynamics of a fine and coarse sediment mixture using a medical ct-scan. *10th IAHR symposium on River, Coastal and Estuarine Morphodynamics*.

Campbell, L., McEwan, I., Nikora, V., Pokrajac, D., Gallagher, M., and Manes, C. (2005). Bed-load effects on hydrodynamics of rough-bed open-channel flows. *Journal of Hydraulic Engineering*, 131(7):576–585.

Carbonneau, P. E. and Bergeron, N. (2000). The effect of bedload transport on mean and turbulent flow properties. *Geomorphology*, 35:267–278.

Chapuis, M., Bright, C., J., H., and MacVicar, B. (2014). Detection range and uncertainty of passive radio frequency identification (RFID) transponders for sediment tracking in gravel rivers and coastal environments. *Earth Surface Processes and Landforms*.

Chiew, Y.-M. and Parker, G. (1994). Incipient sediment motion on non-horizontal slopes. *Journal of Hydraulic Research*, 32:649–660.

Church, M., Hassan, M. A., and Wolcott, J. F. (1998). Stabilizing self-organized structures in gravel-bed stream channels: Field and experimental observations. *Water Resources Research*, 34(11):3169–3179.

Cooper, J. R. and Tait, S. J. (2009). Water-worked gravel beds in laboratory flumes - a natural analogue? *Earth Surface Processes and Landforms*, 34(3):384–397.

Craig, R., Loadman, C., Rusellon, P., and Siegel, E. (2011). Characterization and testing of a new bistatic porfiling acoustic doppler velocimeter: The vectrino II. In *Proceedings of 10th IEEE/OES/CWTM Working Conference on Current Measurement Technology*, Monterey, USA.

Curran, J. and Wilcock, P. R. (2005). Effect of sand supply on transport rates in a gravel-bed channel. *Journal of Hydraulic Engineering*, 131(11):961–967.

Curran, J. C. (2007). The decrease in shear stress and increase in transport rates subsequent to an increase in sand supply to a gravel-bed channel. *Sedimentary Geology*, 202(3):572–580. Special issue: From Particle Size to Sediment Dynamics.

Curran, J. C. (2010). An investigation of bed armoring process and the formation of microclusters. In *Proceedings of the 2nd Joint Federal Interagency Conference*, Las Vegas, NV.

Dany, A. (2016). *Accompagner la politique de restauration physique des cours d'eau*. Agence de l'eau Rhône Méditerranée Corse. (in French).

Dey, S. (1999). Sediment threshold. *Applied Mathematical Modelling*, 23(5):399 – 417.

Dey, S., Sarkar, A., and Solari, L. (2011). Near-bed turbulence characteristics at the entrainment threshold of sediment beds. *Journal of Hydraulic Engineering*, 137(9):945–958.

Durafour, M., Jarno, A., Le Bot, S., Lafite, R., and Marin, F. (2015). Bedload transport for heterogeneous sediments. *Environmental Fluid Mechanics*, 15(4):731–751.

Egiazaroff, I. V. (1955). Calculation of nonuniform sediment concentrations. *Journal of Hydraulic Division*, 91(HY4):225–253.

Einstein, H. A. (1937). The bed load transport as probability problem [Der geschiebetrieb als wahrscheinlichkeitsproblem]. Technical report, Mitteilungen der Versuchsanstalt für Wasserbau, Hydrologie und Glaziologie an der Eidgenössischen Technischen Hochschule Zürich, Rascher, Zürich, Switzerland. (in German).

Einstein, H. A. (1942). Formulas for bed-load transportation. *Transactions of the American Society of Civil Engineers*, 107:575–577.

Fehr, R. (1987). Geschiebeanalysen in gebirgsflüssen. *Mitteilungen der Versuchsanstalt für Wasserbau, Hydrologie und Glaziologie*, 92:1–137. (in German).

Fenton, J. D. and Abbott, J. E. (1977). Initial movement of grains on a stream bed: The effect of relative protrusion. *Proceedings of the Royal Society of London*, 352:523–537.

Fernandez - Luque, R. and van Beek, R. (1976). Erosion and transport of bed-load sediment. *Journal of Hydraulic Research*, 14:127–144.

Francalanci, S., Solari, L., Toffolon, M., and Parker, G. (2012). Do alternate bars affect sediment transport and flow resistance in gravel-bed rivers? *Earth Surface Processes and Landforms*, 37:866–875.

Fries, J. and Taghon, G. (2010). Particle fluxes into permaeable sediments: comparison of mechanisms mediating deposition. *Journal of Hydraulic Engineering*, 136(4).

Galay, V. (1983). Causes of river bed degradation. *Water Resources Research*, 19:1057–1090.

Garcia, M. H. (2008). Sediment transport and morphodynamics. In Garcia, M. H., editor, *Sedimentation Engineering: Processes, Measurements, Modeling, and Practice*, volume 110, pages 21–163, Reston, VA, USA. American Society of Civil Engineers.

Gibson, S., Abraham, D., Heath, R., and Schoellhamer, D. (2009). Vertical gradational variability of fines deposited in a gravel framework. *Sedimentology*, 56:661–676.

Goring, D. G. and Nikora, V. I. (2002). Despiking acoustic doppler velocimeter data. *Journal of Hydraulic Engineering*, 128(1):117–126.

Guney, M. S., Bombar, G., and Aksoy, A. (2013). Experimental study of the coarse surface development effect on the bimodal bed-load transport under unsteady flow conditions. *Journal of Hydraulic Engineering*, 139(1):12–21.

Hamm, N., Dade, W., and Renshaw, C. (2011). Fine particle deposition to porous beds. *Water Resources Research*, 47(W11508):1–13.

Hassan, M. A. and Church, M. (2000). Experiments on surface structure and partial sediment transport on a gravel bed. *Water Resources Research*, 36(7):1885–1895.

Hassan, M. A., Egozi, R., and Parker, G. (2006). Experiments on the effect of hydrograph characteristics on vertical grain sorting in gravel bed rivers. *Water Resources Research*, 42(W09408):1–15.

Herrero, A. and Berni, C. (2016). Sand infiltration into a gravel bed: A mathematical model. *Water Resources Research*, 52(11):8956–8969.

Hill, K., Gaffney, J., Baumgardner, S., Wilcock, P., and Paola, C. (2017). Experimental study of the effect of grain sizes in bimodal mixture on bed slope, bed texture, and the transition to washload. *Water Resources Research*, 53:923–941.

Houssais, M., Ortiz, C., Durian, D., and Jerolmack, D. (2015). Onset of sediment transport is a continuous transition driven by fluid shear and granular creep. *Nature Communications*, 6(6527):1–8.

Huet, M. and Timmersmans, J. (1976). *Influence sur les populations de poissons des aménagement hydrauliques de petits cours d'eau assez rapide*. Ministère de l'agriculture. (in French).

Hurther, D. and Lemmin, U. (2001). A correction method for turbulence measurements with a 3d acoustic doppler velocity profiler. *Journal of Atmospheric and Oceanic Technology*, 18:446–458.

Ikeda, H. and Iseya, F. (1988). Experimental study of heterogeneous sediment transport. Technical Report 12, Environmental Reserch Center, University of Tsukuba.

Irwin, R. and Whiteley, H. (1983). Effects of land drainage on stream flow. *Canadian Water Resources Journal*, 8(2):88–103.

Jaballah, M. (2013). *Alternate bar morphodynamics in an engineered mountainous river.* PhD thesis, Claude Bernard University, Lyon 1.

Jaballah, M., Camenen, B., Penard, L., and Paquier, A. (2015). Alternate bar development in an alpine river following engineering works. *Advances in Water Resources*, 81:103–113.

Jackson, W. L. and Beschta, R. L. (1984). Influences of increased sand delivery on the morphology of sand and gravel channel. *Journal of the American Water Resources Association*, 20(4):527–533.

Jain, R. K. and Kothyari, U. C. (2009). Cohesion influences on erosion and bed load transport. *Water Resources Research*, 45(W06410):1–17.

Jesson, M., Sterling, M., and Bridgeman, J. (2013). Despiking velocity time-series - optimisation through the combination of spike detection and replacement methods. *Flow Measurement and Instrumentation*, 30:45 – 51.

Jodeau, M. (2007). *Morphodynamique d'un banc de galets en rivière aménagée lors de crues [Gravel bar morphodynamics in an engineered river during high flow events].* PhD thesis, Claude Bernard University, Lyon 1. (in French).

Katul, G., Wiberg, P., Albertson, J., and Hornberger, G. (2002). A mixing layer theory for flow resistance in shallow streams. *Water Resources Research*, 38(11):1–8.

Kim, S. C., Friedrichs, C. T., Maa, J. P. Y., and Wright, L. D. (2000). Estimating bottom stress in tidal boundary layer from acoustic Doppler velocimeter data. *Journal of Hydraulic Engineering*, 126(6):399–406.

Kirchner, J., Dietrich, W., Iseya, F., and Ikeda, H. (1990). The variability of critical shear stress, friction angle, and grain protrusion in water-worked sediments. *Sedimentology*, 37:647–672.

Koca, K., Noss, C., Anlanger, C., Brand, A., and Lorke, A. (2017). Performance of the vectrino profiler at the sediment-water interface. *Journal of Hydraulic Research*.

Koll, K., Koll, K., and Dittrich, A. (2010). Sediment transport over a static armour layer and its impact on bed stability. In Dittrich, A., Koll, K., Aberle, J., and Geisenhainer, P., editors, *River Flow, Proceeding of the 5th International Conference on Fluvial Hydraulics*, pages 929–936, Braunschweig, Germany.

Kondolf, G. (1995). Managing bedload sediments in regulated rivers: examples from california, usa. *Geophysical Monograph Series*, 89:165–176.

Kondolf, G., Gao, Y., Annandale, W., Morris, G., Jiang, E., Cao, Y., Carling, P., Fu, K., Guo, Q., Hotchkiss, R., Peteuil, C., Sumi, T., Wang, H., Wang, Z., Wei, Z., Wei, Z., Wu, B., Wu, C., and Yand, C. (2014). Sustainable sediment management in reservoirs and regulated rivers: experience from five continents. *Earth's Future*, 2:256–280.

Kothyari, U. C. and Jain, R. K. (2008). Influence of cohesion on the incipient motion condition of sediment mixtures. *Water Resources Research*, 44(W04410):1–15.

Lagasse, P. (1986). River response to dredging. *Journal of Waterway Port Coastal and Ocean Engineering*, 112:1–14.

Lamarre, H., Mac Vicar, B., and Roy, A. G. (2005). Using passive integrated transponders (PIT) tags to investigate sediment transport in gravel-bed rivers. *Journal of Sedimentary Research*, 75:736–741.

Lamb, M. P., Dietrich, W. E., and Venditti, J. G. (2008). Is the critical shields stress for incipient sediment motion dependent on channel-bed slope? *Journal of Geophysical Research*, 113(F02008):1–20.

Lane, E. W. (1955). The importance of fluvial morphology in hydraulic engineering. Technical Report 372, U.S. Department of the Interior, Bureau of Reclamation.

Laronne, J. B. and Carson, M. A. (1976). Interrelationships between bed morphology and bed-material transport for a small, gravel-bed channel. *Sedimentology*, 23(1):67–85.

Lavelle, J. W. and Mofjeld, H. O. (1987). Do critical stress for incipient motion and erosion really exist? *Journal of Hydraulic Engineering*, 113(3):370–385.

Le Coz, J., Le Boursicaud, R., Jodeau, M., Hauet, A., and Marchand, B. (2014). Image-based velocity and discharge measurements in field and laboratory river engineering studies using the free fudaa-lspiv software. In Schleiss, A. J., de Cesare, G., Franca, M. J., and Pfister, M., editors, *River Flow, Proceedings of the 7th International Conerence on Fluvial Hydraulics*, Lausanne, Switzerland.

Leonardson, R. (2010). *Exchange of fine sediments with gravel riverbeds*. Phd thesis, Berkeley University, Berkeley, California, USA.

Li, Z., Cao, Z., L., H., and Pender, G. (2016). Graded and uniform bed load sediment transport in a degrading channel. *International Journal of Sediment Research*, 31(4):376–385.

Li, Z. and Komar, P. D. (1986). Laboratory measurements of pivoting angle for applications to selective entrainment of gravel in a current. *Sedimentology*, 33(3):413–423.

Liébault, F., Chapuis, M., Bellot, H., and Deschatres, M. (2009). A radio-frequency tracing experiment of bedload transport in a small braided mountain stream. In *European Geosciences Union General Assembly*, Vienna, Autria.

Ligon, F., Dietrich, W., and Trush, W. (1995). Downstream ecological effects of dams. *BioScience*, 45(3):183–192.

Lisle, T. E., Ikeda, H., and Iseya, F. (1991). Formation of stationary alternate bars in a steep channel with mixed-size sediment: a flume experiment. *Earth Surface Processes and Landforms*, 16:463–469.

MacArthur, R., Neill, C., Hall, B., Galay, V., and Shvidchenko, A. B. (2008). *Overview of sedimentation engineering*. American Society of Civil Engineers in Sedimentation Engineering: Processes, Measurements, Modeling, and Practice [book edited by M.H. Garcia].

MacVicar, B. (2014). A quality analysis of the vectrino II instrument using a new open-source matlab tootool and 2D ARMA models to detect and replace spikes. In Schleiss, A., De Cesare, G., Franca, M., and Pfister, M., editors, *River Flow*. Taylor & Francis.

Manes, C., Pokrajac, D., McEwan, I., and Nikora, V. (2009). Turbulence structure of open channel flows over permeable and impermeable beds: A comparative study. *Physics of Fluids*, 21(125109):1–12.

Mao, L. (2012). The effect of hydrographs on bed load transport and bed sediment spatial arrangement. *Journal of Geophysical Research: Earth Surface*, 117(F03024):1–16.

Mao, L., Cooper, J. R., and Frostick, L. E. (2011). Grain size and topographic differences between static and mobile armour layers. *Earth Surface Processes and Landforms*, 36:1321–1334.

Marion, A., Tait, S. J., and McEwan, I. K. (2003). Analysis of small-scale gravel bed topography during armoring. *Water Resources Research*, 39(12):1–11.

Masteller, C. and N.J., F. (2017). Interplay between grain protrusion and sediment entrainment in an experimental flume. *Journal of Geophysical Research: Earth Surface*, 122:274–289.

Meyer-Peter, E. and Müller, R. (1948). Formulas for bed-load transport. In *Proceedings of the 2nd IAHR Congress*, pages 39–64, Stockholm, Sweden.

Miller, J. P. (1958). *High mountain streams : effects of geology on channel characteristics and bed material*. Socorro, New Mexico : State Bureau of Mines and Mineral Resources, New Mexico Institute of Mining and Technology.

Mitchener, H. and Torfs, H. (1996). Erosion of mud-sand mixtures. *Coastal Engineering*, 29:1–25.

Monteith, H. and Pender, G. (2005). Flume investifations into the influence of shear stress history on a graded sediment bed. *Water Resources Research*, 41(W12401):1–7.

Montgomery, D. R. and Buffington, J. M. (1997). Channel reach morphology in mountain drainage basins. *Geological Society of America Bulletin*, 109(5):596–611.

Moramarco, T., Barbetta, S., and Tarpanelli, A. (2017). From surface flow velocity measurements to discharge assessment by the entropy theory. *Water*, 9(120):2–12.

Morris, G. L. and Fan, J. (1998). *Reservoir Sedimentation Handbook: Design and management of dams, reservoirs, and watersheds for sustainable use*. McGraw-Hill Book Compagny, New York, USA.

Mueller, E. R., Pitlick, J., and Nelson, J. M. (2005). Variation in the reference shields stress for bed load transport in gravel-bed streams and rivers. *Water Resources Research*, 41(W04006):1–10.

NF P 94-072 (1995). Sols: reconnaissance et essais. essai scissométrique en laboratoire. Technical report, AFNOR Norm. (in French).

Nikora, V. and Goring, D. (2000). Flow turbulence over fixed and weakly mobile gravel beds. *Journal of Hydraulic Engineering*, 126(9):679–690.

Nikora, V., Goring, D., McEwan, I., and Griffiths, G. (2001). Spatially averaged open-channel flow over rough bed. *Journal of Hydraulic Engineering*, 127(2):123–133.

Nikora, V. and Goring, D. G. (1998). ADV measurements of turbulence: can we improve their interpretation? *Journal of Hydraulic Engineering*, 124(6):630–634.

Nikora, V. and Walsh, J. (2004). Water-worked gravel surfaces: High-order structure functions at the particle scale. *Water Resources Research*, 40(W12601):1–7.

Nikora, V. I., Goring, D. G., and Biggs, B. J. F. (1998). On gravel-bed roughness characterization. *Water Resources Research*, 34(3):517–527.

Nikuradse, J. (1933). Strömungsgesetz in rauhen rohren [Laws of flow in rough pipes]. *Forschung auf dem Gebiete des Ingenieurwesens*, 361. (in German).

Ockelford, A. and Haynes, H. (2013). The impact of stress history on bed structure. *Earth Surface Processes and Landforms*, 38:717–727.

Orrú, C., Blom, A., and Uijttewaal, W. S. J. (2016). Armor breakup and reformation in a dedegradation laboratory experiement. *Earth Surface Dynamics*, 4:461–470.

Paintal, A. S. (1971). A stochastic model of bedload transport. *Journal of Hydraulic Research*, 9(4):527–554.

Parker, G., Dhamotharan, S., and Stefan, H. (1982). Model experiments on mobile, paved gravel bed streams. *Water Resources Research*, 18:1395–1408.

Parker, G. and Klingeman, P. C. (1982). On why gravel bed streams are paved. *Water Resources Research*, 18(5):1409–1423.

Parker, G., Klingeman, P. C., and McLean, D. G. (1982). Bed load and size distribution in paved gravel-bed streams. *Journal of Hydraulic Division*, 108(HY4):544–571.

Peltier, Y., Rivière, N., Proust, S., Mignot, E., Paquier, A., and Shiono, K. (2013). Estimation of the error on the mean velocity and on the reynolds

stress due to a misoriented adv probe in the horizontal plane: case of experiments in a compound open-channel. *Flow Measurement and Instrumentation*, 34:34–41.

Petit, F., Houbrechts, G., Peeters, A., Hallot, E., Van Campenhout, J., and Denis, A.-C. (2015). Dimensionless critical shear stress in gravel-bed rivers. *Geomorphology*, 250:308–320.

Pizzuto, J. (2002). Effects of dam removal on river form and process. *BioScience*, 52(8):683–691.

Pope, N., Widdows, J., and Brinsley, M. (2006). Estimation of bed shear stress using the turbulent kinetic energy approach - a comparison of annular flume and field data. *Continental Shelf Research*, 26:959–970.

Prancevic, J. P. and Lamb, M. P. (2015). Unraveling bed slope from relative roughness in initial sediment motion. *Journal of Geophysical Research: Earth Surface*, 120:474–489.

Proffitt, G. and Sutherland, A. (1983). Transport of non-uniform sediments. *Journal of Hydraulic Research*, 21(1):33–43.

Qin, J. and Leung Ng, S. (2012). Estimation of effective roughness for water-worked gravel surfaces. *Journal of Hydraulic Engineering*, 138(11):923–934.

Raupach, M., Antonias, R., and Rajagopalan, S. (1991). Rough-wall turbulent boundary layer. *Applied Mechanics Reviews*, 44:1–25.

Recking, A. (2009). Theoretical development on the effects of changing flow hydraulics on incipient bedload motion. *Water Resources Research*, 45:1–16.

Recking, A. (2010). A comparison between flume and field bedload transport data and consequences for surface based bedload transport prediction. *Water Resources Research*, 46(W03518):1–16.

Recking, A., Frey, P., Paquier, A., Belleudy, P., and Champagne, J. Y. (2008). Feedback between bed load transport and flow resistance in gravel and cobble bed rivers. *Water Resources Research*, 44(W05412):1–21.

Recking, A., Liébault, F., Peteuil, C., and Jolimet, T. (2012). Testing bedload transport equations with consideration of time scales. *Earth Surface Processes and Landforms*, 37(7):774–789.

Reid, I., Frostick, L. E., and Layman, J. T. (1985). The incidence and nature of bedload transport during flood flows in coarse-grained alluvial channels. *Earth Surface Processes and Landforms*, 10:33–44.

Ridgway, K. and Tarbuck, K. (1968). Particulate mixture bulk densities. *Chemical and Process Engineering*, 49(2).

Robert, A. (1988). Statistical properties of sediment bed profiles in alluvial channels. *Mathematical Geology*, 20(3):205–225.

Robert, A. and Richards, K. S. (1988). On the modelling of sand bedforms using the semivariogram. *Earth Surface Processes and Landforms*, 13(5):459–473.

Rollet, A.-J., McVicar, B., Piégay, H., and Roy, A. (2008). L'utilisation de transpondeurs passifs pour l'estimation du transport sédimentaire : premiers retours d'expérience [A comparative study on the use of passive integrated transponders to estimate sediment transport : first results]. *La Houille Blanche*, 4:110–116. (in French).

Schmidt, J. and Wilcock, P. (2008). Metrics for assessing the downstream effects of dams. *Water Resources Research*, 44(4).

Schumm, S. A. (2005). *River variability and complexity.* Cambridge University Press.

Schumm, S. A., Harvey, M., and Watson, C. (1984). *Incised Channels. Morphologt, Dynamics and Control.* Water Resources Publications.

Shields, A. (1936). Anwendung der Ahnlichkeits-mechanik und der turbulenzforschung auf die geshiebebewegung [Application of similarity principles and turbulence research to bed-load movement]. *Preussische Versuchsanstalt fur Wasserbau und Schiffbau*, 26:1–26. Berlin, Germany (in German).

Shvidchenko, A. B. and Pender, G. (2000). Flume study of the effect of relative depth on the incipient motion of coarse uniform sediments. *Water Resources Research*, 36(2):619–628.

Sklar, L., Fadde, J., Venditti, J. G., Nelson, P., Wydzga, M., Cui, Y., and Dietrich, W. (2009). Translation and dispersion of sediment pulses in flume experiments simulating gravel augmentation below dams. *Water Resources Research*, 45(W08439):1–14.

Smart, G. M. (1999). Turbulent velocity profiles and boundary shear stress in gravel bed rivers. *Journal of Hydraulic Engineering*, 125:106–116.

Smart, G. M., Maurice, M. J., and Walsh, J. M. (2002). Relatively rough flow resistance equations. *Journal of Hydraulic Engineering*, 128(6):568–578.

Soulsby, R. (1981). Measurements of the reynolds stress components close to a marine sand bank. *Marine Geology*, 42:35–47.

Soulsby, R. L. (1997). *Dynamics of marine sands, a manual for practical applications*. Thomas Telford, London, UK. ISBN 0-7277-2584 X.

Soulsby, R. L. and Whitehouse, R. J. S. W. (1997). Threshold of sediment motion in coastal environment. In *Pacific Coasts and Ports '97: Proceedings of the 13th Australasian Coastal and Ocean Engineering Conference and the 6th Australasian Port and Harbour Conference*, volume 1, pages 149–154, Christchurch, New Zealand. University of Canterbury.

Stapleton, K. R. and Huntley, D. A. (1995). Seabed stress determinations using the inertial dissipation method and the turbulent kinetic energy method. *Earth Surface Processes and Landforms*, 20(9):807–815.

Sutter, R. D., Huygens, M., and Verhoeven, R. (2000). Transport of sediment mixtures. In M., S., editor, *IAHS Publication*, volume 263, pages 261–268, Waterloo, ON, Canada. International Association of Hydrological Sciences.

Swales, S. (1980). *Investigations into the effects of river channel works on the ecology of fish populations*. PhD thesis, Liverpool University.

Tait, S. (1993). *The physical processes of bed armouring in mixed grain sediment transport*. PhD thesis.

Tan, L. (2012). *An Investigation of Bed Armoring Process and its Implications for Channel Bed Stability*. PhD thesis, University of Virginia, the faculty of the School of Engineering and Applied Science.

Townsend, A. (1976). *The structure of turbulent shear flow*. Cambridge University Press.

Turowski, J. M., Badoux, A., and Rickenmann, D. (2011). Start and end of bedload transport in gravel-bed streams. *Geophysical Research Letters*, 38(L04401):1–5.

USWES (1935). Studies of river bed materials and their movement with special reference to the lower Mississippi River. Technical Report 17, U. S. Army Corps of Engineers, Vicksburg, Mississippi, U.S.A. page 161.

van Rijn, L. C. (1984). Sediment transport, part I : bed load transport. *Journal of Hydraulic Division*, 110(10):1431–1456.

Venditti, J. G., Dietrich, W., Nelson, P., Wydzga, M., Fadde, J., and Sklar, L. (2010). Effect of sediment pulse grain size on sediment transport rates and bed mobility in gravel bed rivers. *Journal of Geophysical Research*, 115(F03039):1–19.

Voulgaris, G. and Trowbridge, J. (1998). Evaluation of the acoustic doppler velocitmeter (ADV) for turbulence measurements. *Journal of Atmospheric and Oceanic Technology*, 15:272–289.

Wasson, J. G., Malavoi, J. R., Maridet, L., Souchon, Y., and Paulin, L. (1998). *Impact écologiques de la chenalisation des rivière*. CEMAGREF, Lyon. (In French).

Waters, K. and Curran, J. (2015). Linking bed morphology changes of two sediment mixtures to sediment transport predictions in unsteady flows. *Water Resources Research*, 51:2724–2741.

Wentworth, C. K. (1922). A scale of grade and class terms for clastic sediments. *The Journal of Geology*, 30(5):377–392.

Wiberg, P. L. and Smith, J. D. (1987). Calculations of the critical shear stress for motion of uniform and heterogeneous sediments. *Water Resources Research*, 23(8):1471–1480.

Wiberg, P. L. and Smith, J. D. (1991). Velocity distribution and bed roughness in high-gradient streams. *Water Resources Research*, 27:825–838.

Wilcock, P., Potlick, J., and Cui, Y. (2009). Sediment transport primer: estimating bed-material transport in gravel-bed rivers. Technical report, U. S. Department of Agriculture, Forest Service, Rocky Mountain Research Station.

Wilcock, P. R. (1996). Estimating local bed shear stress from velocity observations. *Water Resources Research*, 32:3361–3366.

Wilcock, P. R. and Crowe, J. C. (2003). Surface-based transport model for mixed-size sediment. *Journal of Hydraulic Engineering*, 129(2):120–128.

Wilcock, P. R. and DeTemple, B. T. (2005). Persistence of armor layers in gravel-bed streams. *Geophysical Research Letters*, 32(L08402):1–4.

Wilcock, P. R., Kenworthy, S. T., and Crowe, J. C. (2001). Experimental study of the transport of mixed sand and gravel. *Water Resources Research*, 37:3349–3358.

Wilcock, P. R. and McArdell, B. W. (1993). Surface-based fractional transport rates: Mobilization thresholds and partial transport of a sand-gravel sediment. *Water Resources Research*, 29:1297–1312.

Williams, G. (1989). Sediment concentration versus water discharge during single hydrologic events in rivers. *Journal of Hydrology*, 111:89–106.

Williams, G. and Wolman, G. M. (1984). Downstream effects of dams on alluvial rivers. Technical Report 1286, United States Government Printing Office.

Wilson, K. C. (1966). Bed-load transport at high shear stress. *Journal of Hydraulic Division*, 92(6):49–59.

Wong, M. and Parker, G. (2006). Reanalysis and correction of bed-load relation of meyer-peter and müller using their own database. *Journal of Hydraulic Engineering*, 132(11):1159–1168.

Wood, P. J. and Armitage, P. D. (1997). Biological effects of fine sediment in the lotic environment. *Environmental Management*, 21:203–217.

Wood, P. J. and Armitage, P. D. (1999). Sediment deposition in a small lowland stream - Management implications. *Regulated Rivers: Research and Management*, 15:199–210.

Wren, D., Kuhnle, R., Langendoen, E., and Rigby, J. (2014). Turbulent flow and sand transport over a cobble bed in a laboratory flume. *Journal of Hydraulic Engineering*, 140(4):167–176.

Wren, D., Ursic, M., Kuhnle, R., and Langendoen, E. (2016). Examining the gengeneral of τ_0/TKE for gravel and cobble beds with sand fill. *Journal of Hydraulic Engineering*, 143(4).

Wren, D. G., Langendoen, E. J., and Kuhnle, R. A. (2011). Effects of sand addition on turbulent flow over an immobile gravel bed. *Journal of Geophysical Research: Earth Surface*, 116(F01018):1–12.

Wu, W., Wang, S. S. Y., and Jia, Y. F. (2000). Nonuniform sediment transport in alluvial rivers. *Journal of Hydraulic Research*, 38(6):427–434.

XP CEN ISO/TS 17892-6 (2006). Reconnaissance et essais géotechniques - essais de laboratoire sur les sols - partie 6 : essai de pénétration de cône. Technical report, AFNOR norms. (in French).

Yalin, M. and Karahan, E. (1979). Inception of sediment transport. *Journal of Hydraulic Engineering*, 105:1433–1443.

Yalin, M. S. (1977). *Mechanics of Sediment Transport*. Pergamon Press, Oxford. 2nd edition.

Part V

Appendices

Appendix A

Experimental data

This appendix recaps the important data measured during each experiments.

Figure 1, Figure 2, Figure 3, Figure 4 and Figure 5 shows the temporal evolution of gravel transport rates measured during an hydrograph for all the experiments.

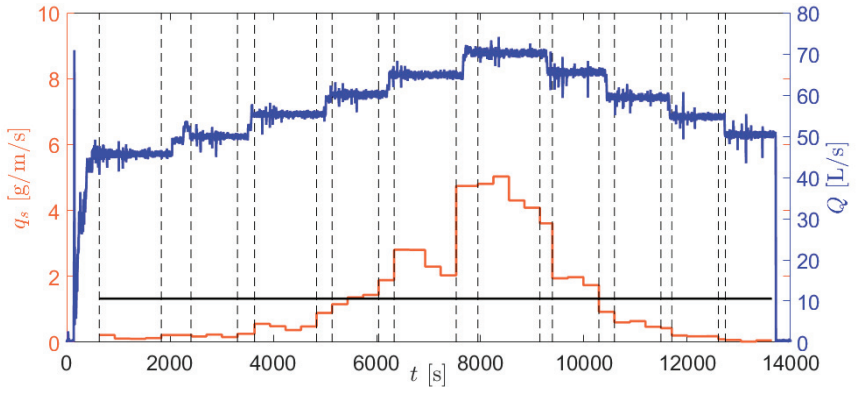

(a) L-G-1

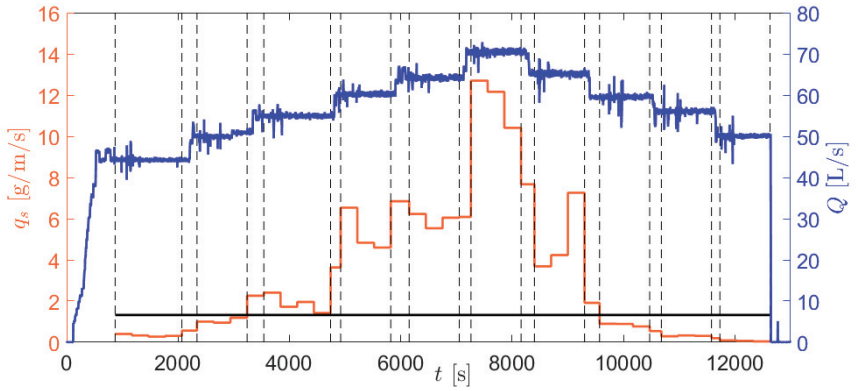

(b) L-G-2

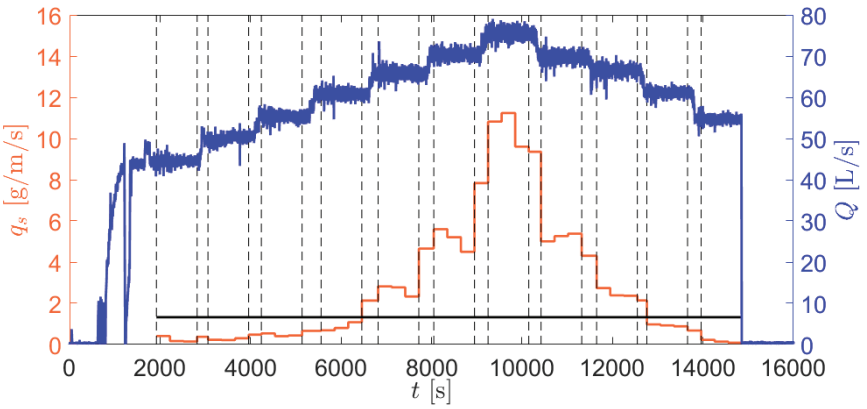

(c) L-G-3

Figure 1: Time variations of bedload (q_s) and flow (Q) rates for experiments on loose beds. (Grid delimits steady states from transitions zones. Black horizontal line corresponds to the reference transport rate $q_{s\text{-ref}}$. The left axis refers to the bedload rate (orange) and the right axis refers to the water discharge (blue).)

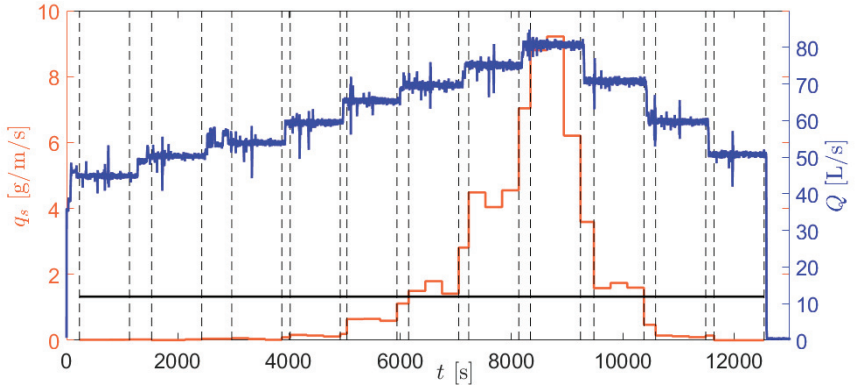

(a) P-G-1

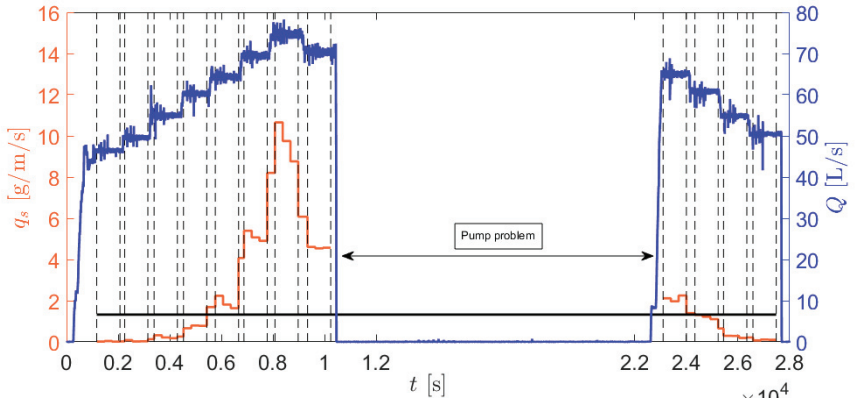

(b) P-G-2

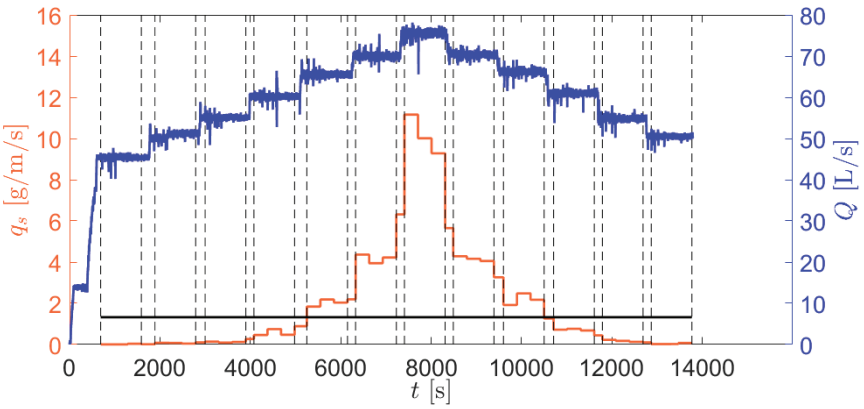

(c) P-G-3

Figure 2: Time variations of bedload (q_s) and flow (Q) rates for experiments on packed beds. (Grid delimits steady states from transitions zones. Black horizontal line corresponds to the reference transport rate $q_{s\text{-ref}}$. The left axis refers to the bedload rate (orange) and the right axis refers to the water discharge (blue).)

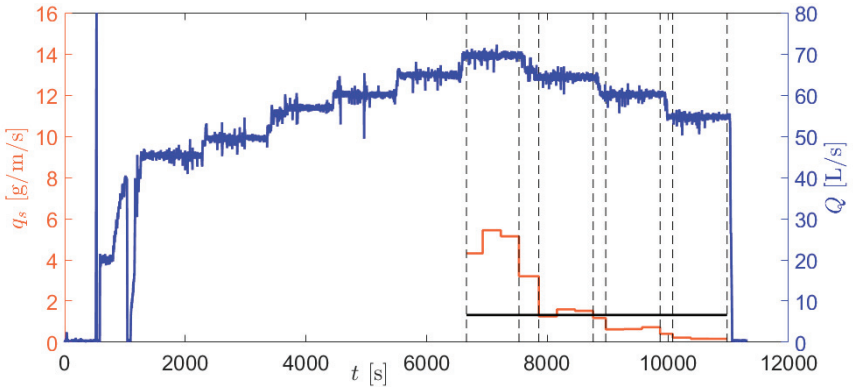

(a) L-G-4

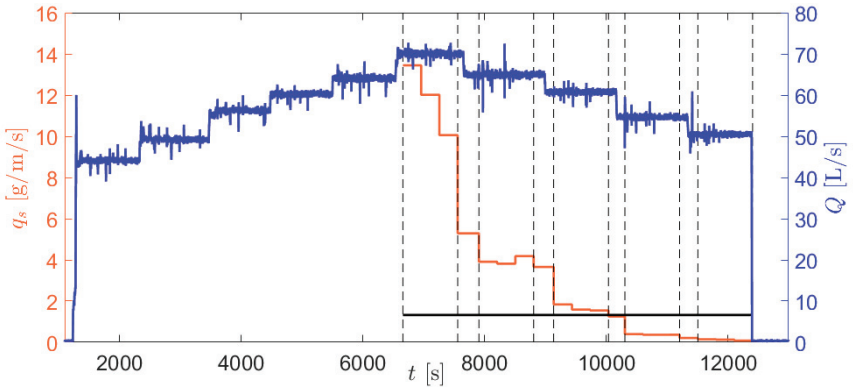

(b) L-G-5

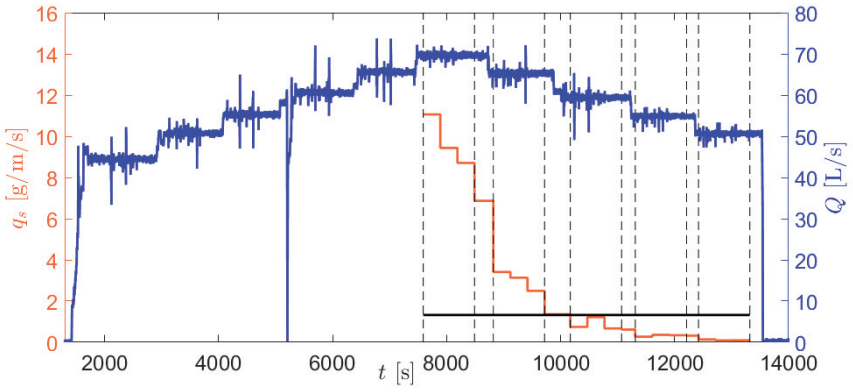

(c) L-G-6

Figure 3: Time variations of bedload rates and hydraulic conditions for experiments on loose beds. (Grid delimits steady states from transitions zones. These experiments were performed to detect Q_{ref-F}; that is why gravel transport rates were only measured at the falling limb of the hydrograph.)

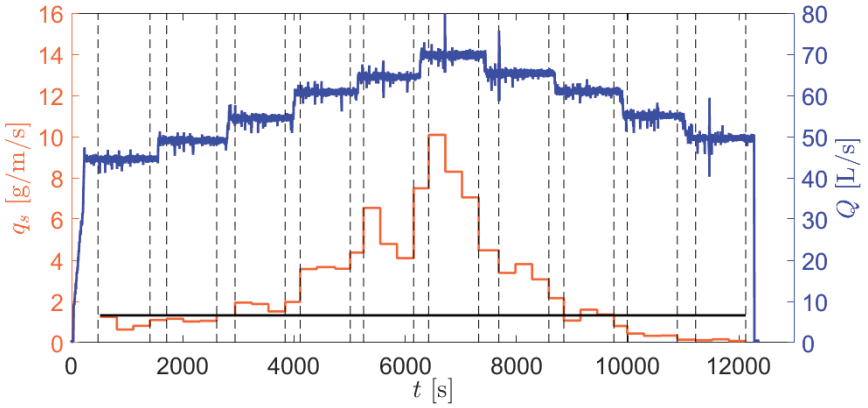

(a) L-G-7

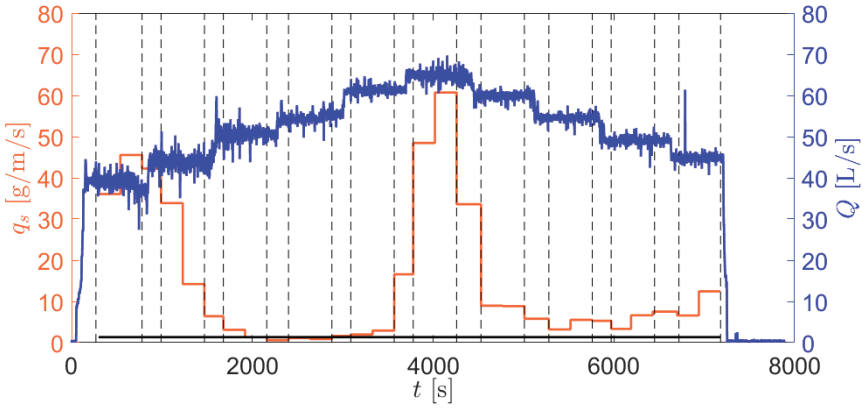

(b) H-G/S-7

Figure 4: Time variations of bedload (q_s) and flow (Q) for experiments on a loose bed and associated bed infiltrated with sand particles. (Grid delimits steady states from transitions zones. Black horizontal line corresponds to the reference transport rate $q_{s\text{-ref}}$. The left axis refers to the bedload rate (orange) and the right axis refers to the water discharge (blue).)

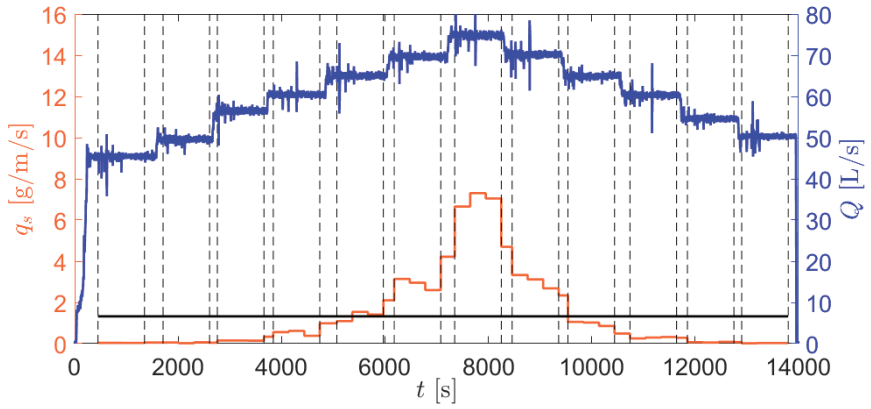

(a) H-G/Ms-5

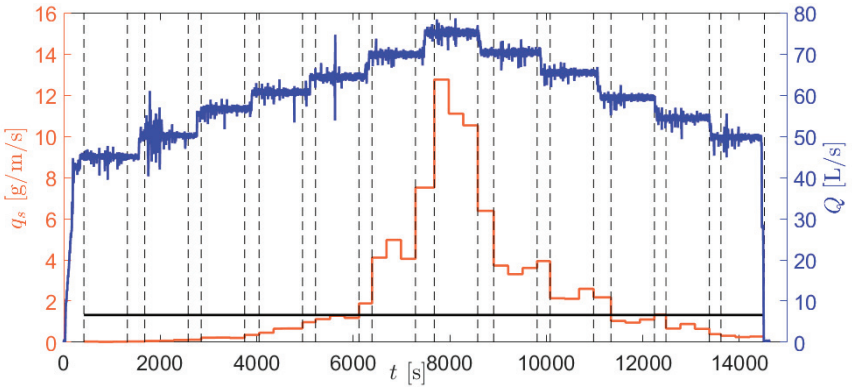

(b) H-G/Ms-6

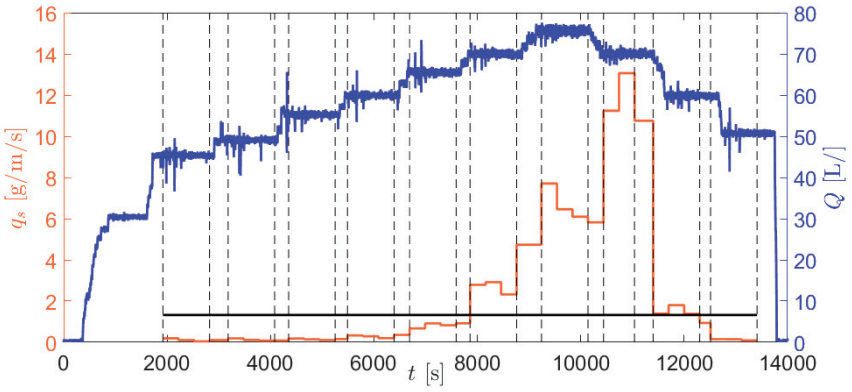

(c) H-G/Ms-9

Figure 5: Time variations of bedload (q_s) and flow (Q) for experiments on beds infiltrated with medium silt particles. (Grid delimits steady states from transitions zones. Black horizontal line corresponds to the reference transport rate $q_{s\text{-ref}}$. The left axis refers to the bedload rate (orange) and the right axis refers to the water discharge (blue).)

Appendix B

Bed surface characteristics

B.1 L-G-1 experiment

General bed surface surveys

No DEM of the entire bed surface is available. Three longitudinal bed surface surveys are presented in Figure B.1.1.

Surveys of bed surface patches

In the following, initial and final states mean before and after an experiment of sediment transport, respectively. Initial and final bed surface surveys were performed on 3 zones distributed along the channel: downstream (patch Z1), middle (patch Z2), and upstream (patch Z3). In this experiment, patches Z1, Z2 and Z3 were located at 6.6 m, 8.6 m, and 10.6 m from the downstream end of the flume, respectively.

Figure B.1.2 represents the resulting digital elevation models (DEM). Figure B.1.3 shows the probability density function of the bed surface elevations for the 3 patches. Two representations of the structure function D_b associated to the 3 patches are given: one in 3D (Figure B.1.4) and one in contour plot (Figure B.1.5).

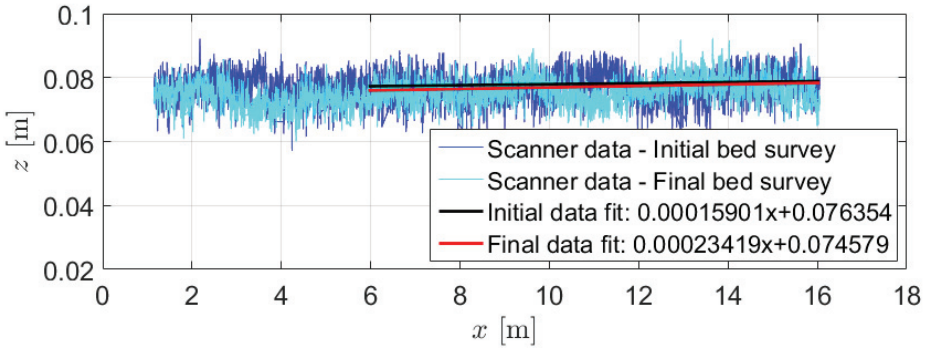

(a) Center line

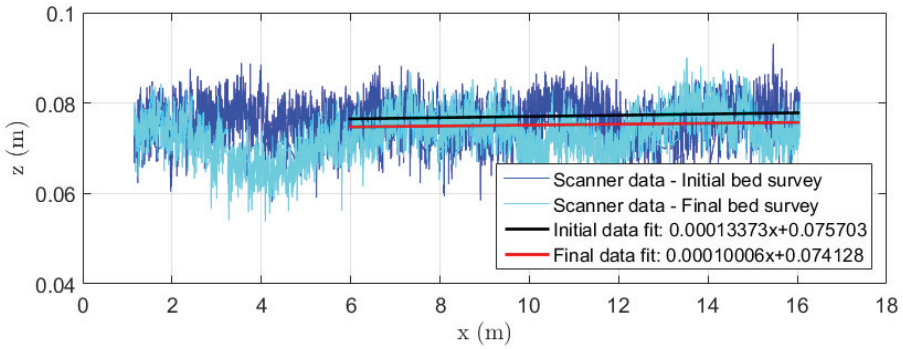

(b) Right side

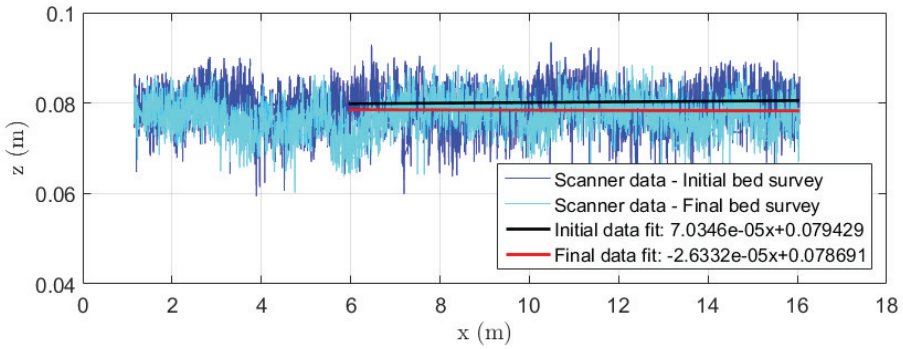

(c) Left side

Figure B.1.1: Longitudinal surveys of the bed surface before and after the experiment of sediment transport.

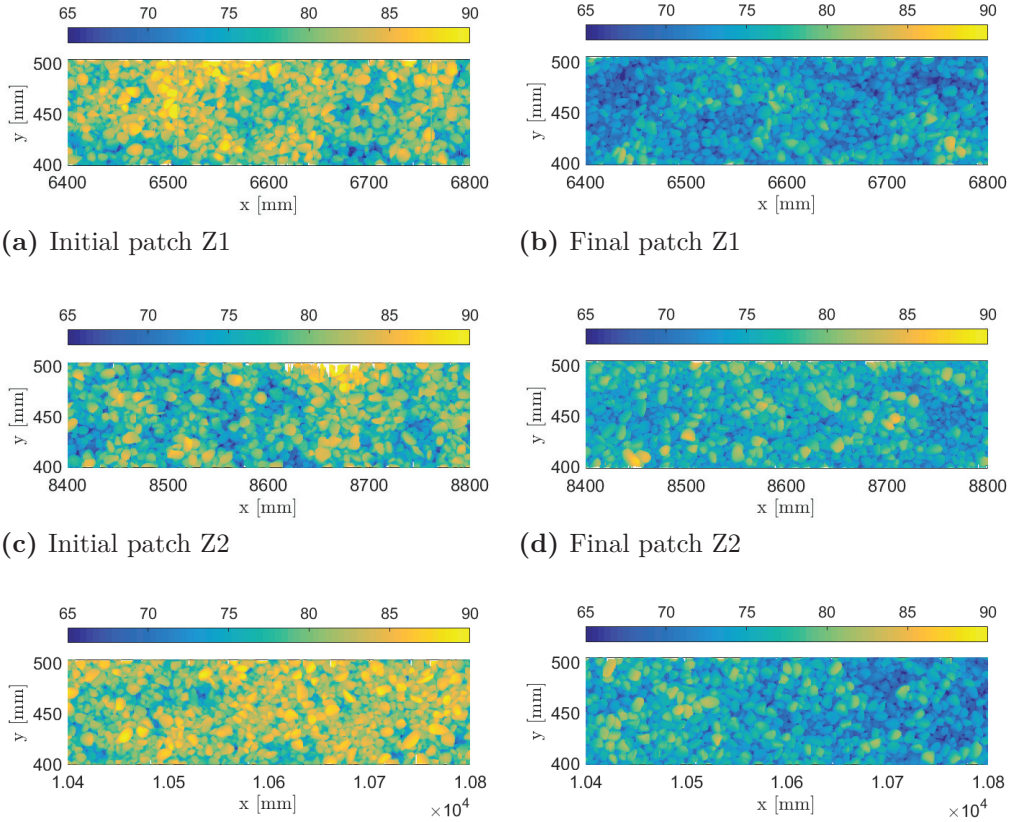

(a) Initial patch Z1 **(b)** Final patch Z1

(c) Initial patch Z2 **(d)** Final patch Z2

(e) Initial patch Z3 **(f)** Final patch Z3

Figure B.1.2: DEM of bed surface patches: left and right sides of this figure correspond to initial and final states of the bed surface, respectively.

Bed surface criteria

Table B.1a recaps all the bed surface criteria calculated for the three patches surveyed (initial and final states). Table B.1b reports the bed surface criteria computed at the scale of the entire bed surface, either by averaging data of the three patches or by using the transverse and longitudinal surveys of the bed.

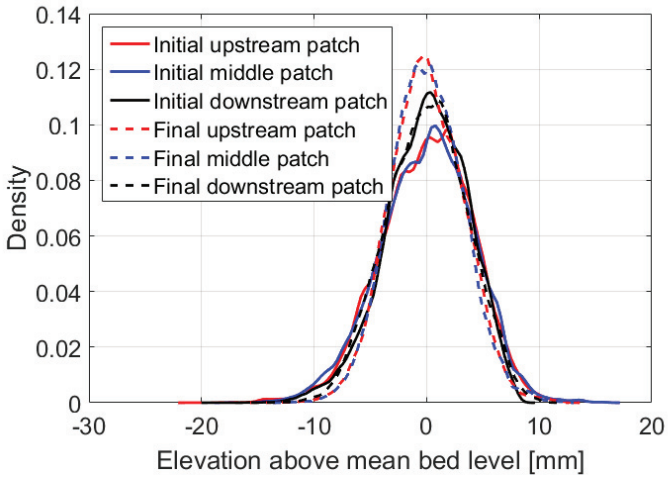

Figure B.1.3: PDF of the bed surface elevations for the 3 patches before and after the sediment transport experiment.

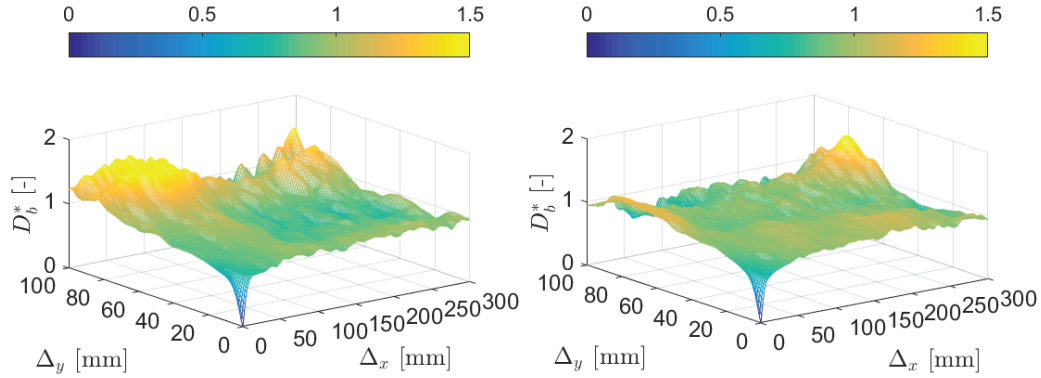

(a) Initial patch Z1

(b) Final patch Z1

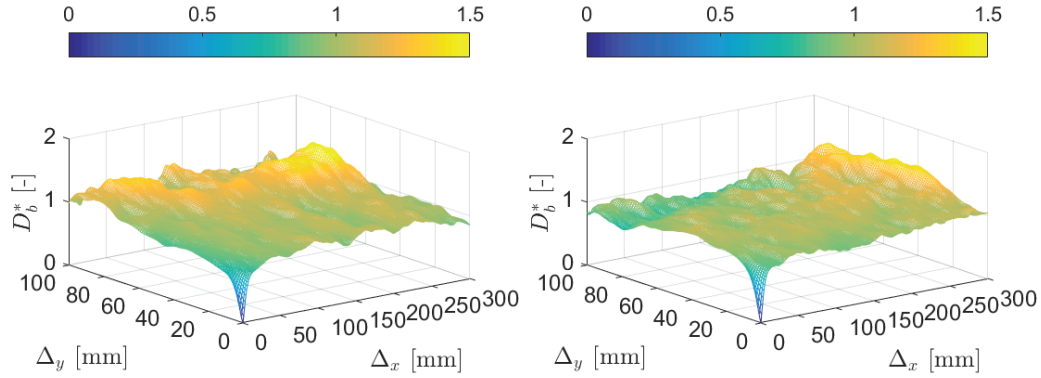

(c) Initial patch Z2

(d) Final patch Z2

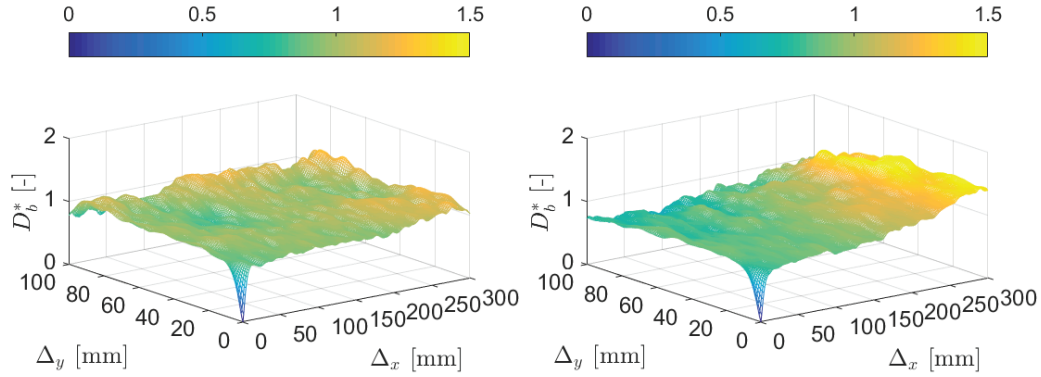

(e) Initial patch Z3

(f) Final patch Z3

Figure B.1.4: D_b^* plots for the three patches: left and right sides of this figure correspond to initial and final states of the bed surface, respectively.

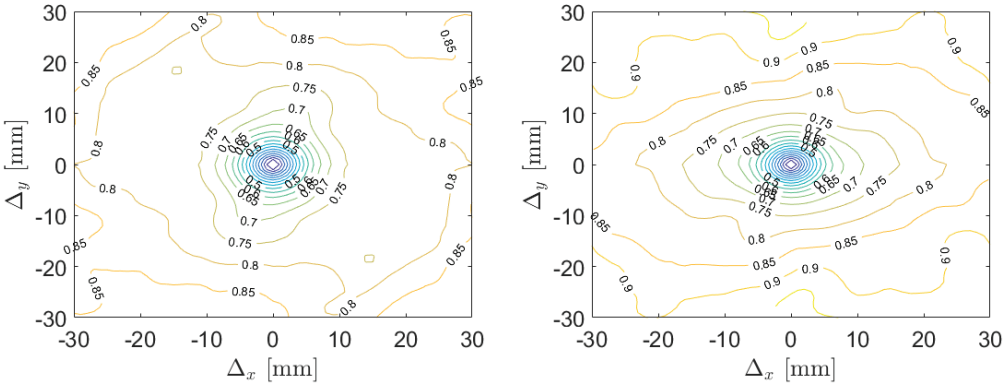

(a) Initial patch Z1

(b) Final patch Z1

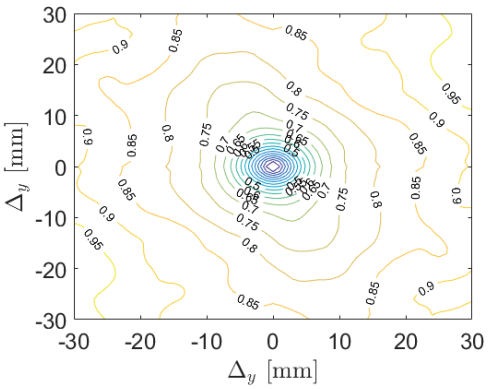

(c) Initial patch Z2

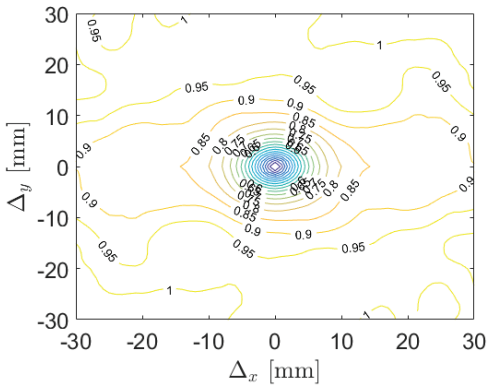

(d) Final patch Z2

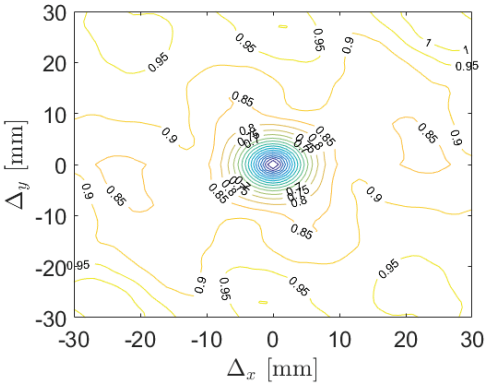

(e) Initial patch Z3

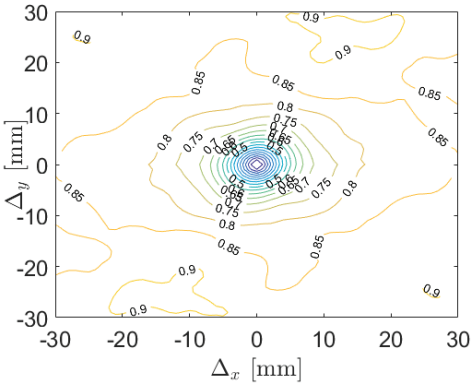

(f) Final patch Z3

Figure B.1.5: Contour plots for the three patches: left and right sides of this figure correspond to initial and final states of the bed surface, respectively.

Table B.1: Bed surface criteria of the 3 patches surveyed before and after the sediment transport experiment.

(a)

		σ_{zg} (mm)	S_k (mm^3)	K_u (mm^4)	Δ_{x0} (mm)	Δ_{y0} (mm)	H_x (-)	H_y (-)	x_0 (mm)	y_0 (mm)	a (mm)	b (mm)	$\frac{x_0}{y_0}$ (-)	$\frac{a}{b}$ (-)	ϕ (°)
Z1	Initial	4.1	-0.30	3.2	8.8	7.8	0.51	0.55	6.3	6.7	6.2	6.6	0.9	1.1	0.8
	Final	3.3	0.05	3.0	8.1	7.4	0.51	0.53	8.4	6.7	8.1	6.5	1.3	1.2	4.1
Z2	Initial	4.1	-0.16	3.1	8.2	7.6	0.55	0.56	7.0	6.9	7.1	6.7	1.0	1.1	42.7
	Final	3.2	0.09	3.1	7.5	6.9	0.50	0.54	7.2	6.7	7.2	6.8	1.1	1.1	2.5
Z3	Initial	3.6	-0.39	3.1	6.7	6.5	0.55	0.56	6.8	6.7	6.9	6.8	1.0	1.0	10.9
	Final	3.6	-0.09	2.7	8.0	7.7	0.52	0.54	7.2	6.7	7.3	6.5	1.1	1.1	-33.5

(b)

		σ_{zg} (mm)	S_k (mm^3)	K_u (mm^4)	σ_{zl} (mm)	σ_{zt} (mm)	Δ_{x0} (mm)	Δ_{y0} (mm)	H_x (-)	H_y (-)	$\frac{x_0}{y_0}$ (-)	$\frac{a}{b}$ (-)	ϕ (°)
General bed	Initial	3.3	0.00	2.9	4.6	4.3	8.3	7.3	0.51	0.54	1.3	1.2	-6.2
	Final	3.4	0.02	3.0	4.2	4.3	7.9	7.3	0.51	0.54	1.1	1.1	-9.0

B.2 P-G-1 experiment

General bed surface surveys

No DEM of the entire bed surface is available. Three longitudinal bed surface surveys are presented in B.2.1.

Surveys of bed surface patches

In the following, initial and final states mean before and after an experiment of sediment transport, respectively. Initial and final bed surface surveys were performed on 3 zones distributed along the channel: downstream (patch Z1), middle (patch Z2), and upstream (patch Z3). In this experiment, patches Z1, Z2 and Z3 were located at 6.6 m, 8.6 m, and 10.6 m from the downstream end of the flume, respectively.

Figure B.2.2 represents the resulting digital elevation models (DEM). Figure B.2.3 shows the probability density function of the bed surface elevations for the 3 patches. Two representations of the structure function D_b associated to the 3 patches are given: one in 3D (Figure B.2.4) and one in contour plot (Figure B.2.5).

Bed surface criteria

Table B.2a recaps all the bed surface criteria calculated for the three patches surveyed (initial and final states). Table B.2b reports the bed surface criteria computed at the scale of the entire bed surface, either by averaging data of the three patches or by using the transverse and longitudinal surveys of the bed.

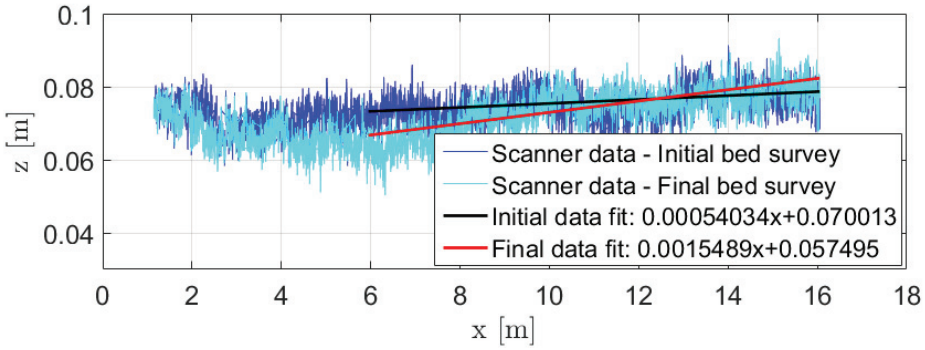

(a) Center line

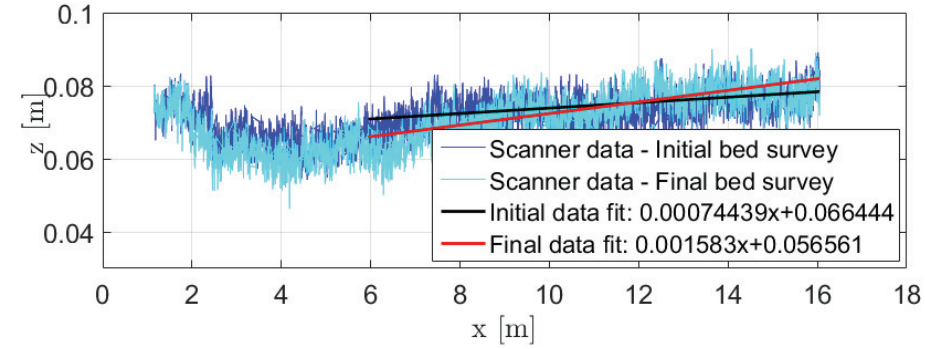

(b) Right side

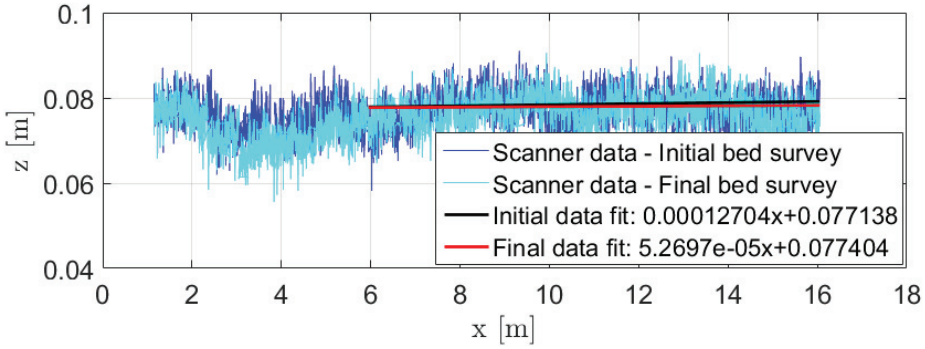

(c) Left side

Figure B.2.1: Longitudinal surveys of the bed surface before and after the experiment of sediment transport.

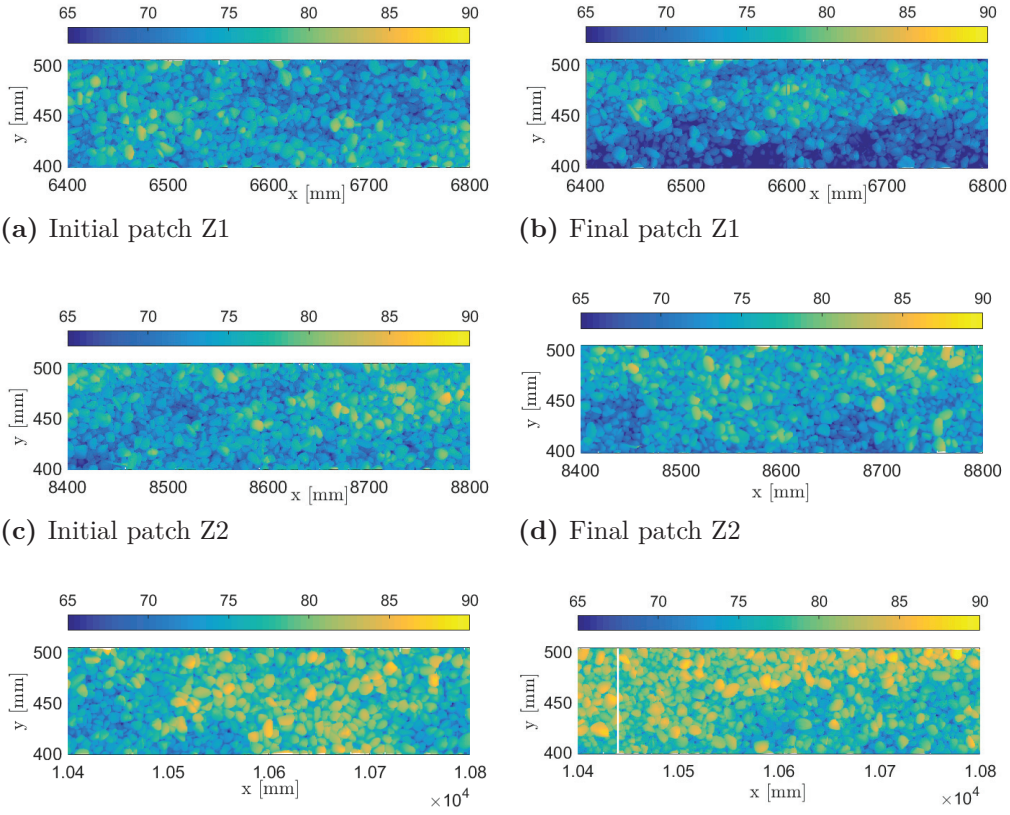

(a) Initial patch Z1

(b) Final patch Z1

(c) Initial patch Z2

(d) Final patch Z2

(e) Initial patch Z3

(f) Final patch Z3

Figure B.2.2: DEM of bed surface patches: left and right sides of this figure correspond to initial and final states of the bed surface, respectively.

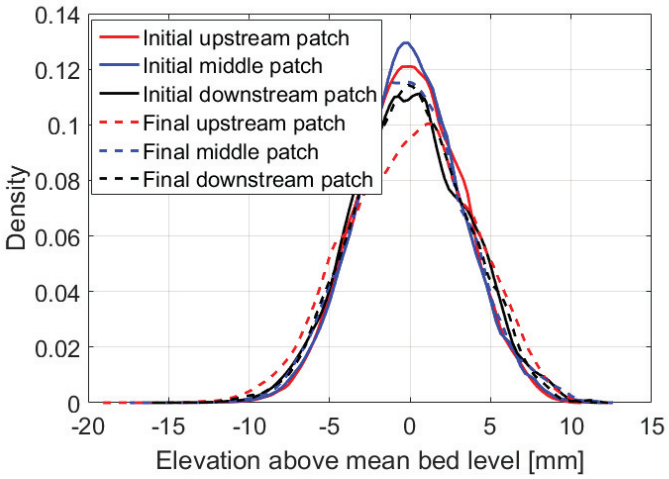

Figure B.2.3: PDF of the bed surface elevations for the 3 patches before and after the sediment transport experiment

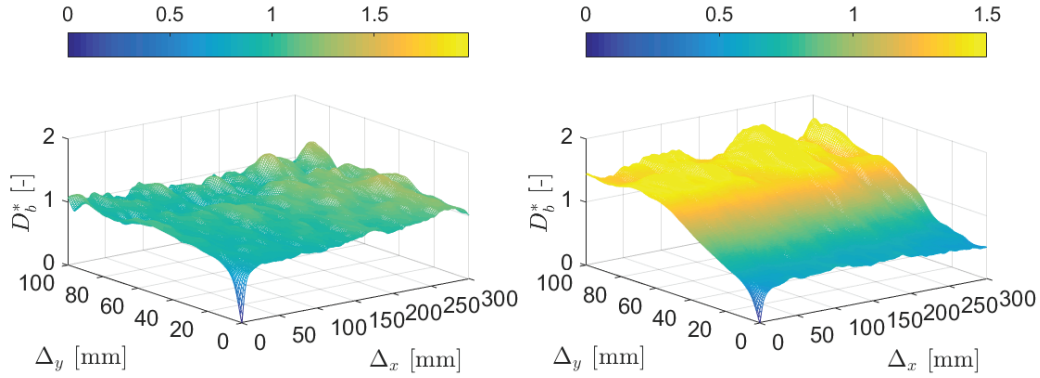

(a) Initial patch Z1

(b) Final patch Z1

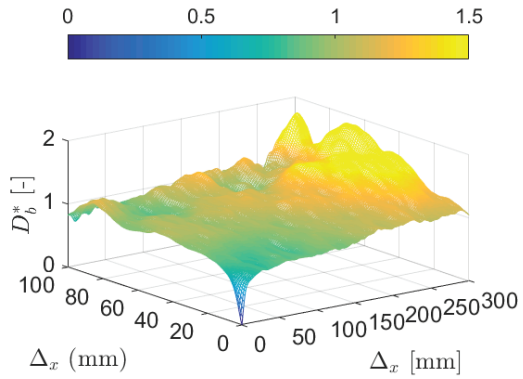

(c) Initial patch Z2

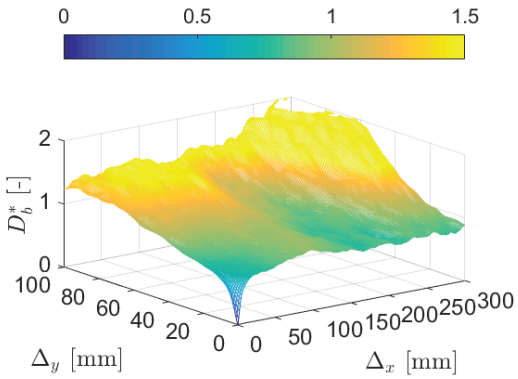

(d) Final patch Z2

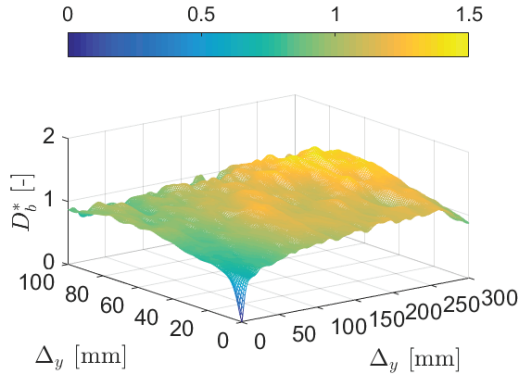

(e) Initial patch Z3

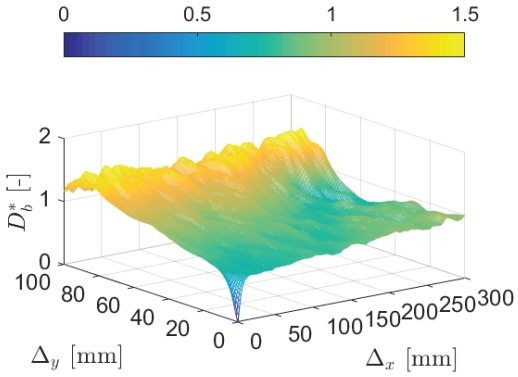

(f) Final patch Z3

Figure B.2.4: D_b^* plots for the three patches: left and right sides of this figure correspond to initial and final states of the bed surface, respectively.

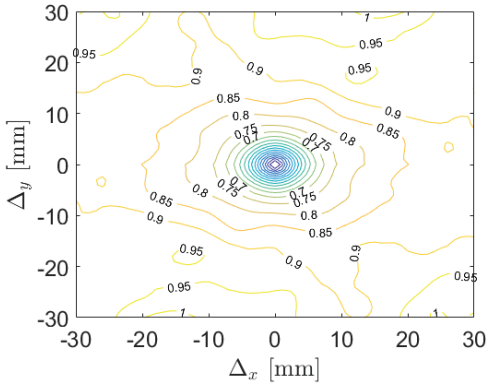

(a) Initial patch Z1

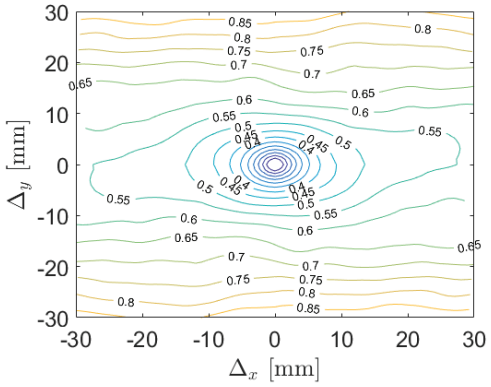

(b) Final patch Z1

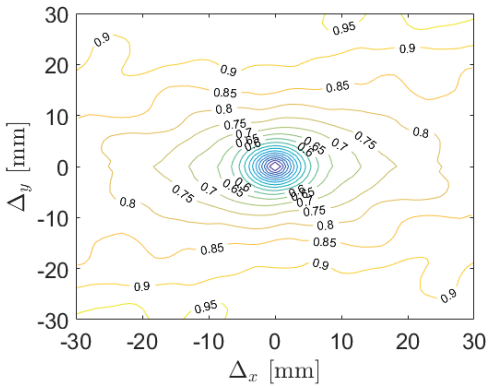

(c) Initial patch Z2

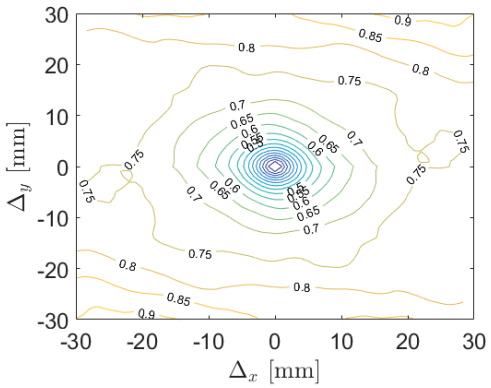

(d) Final patch Z2

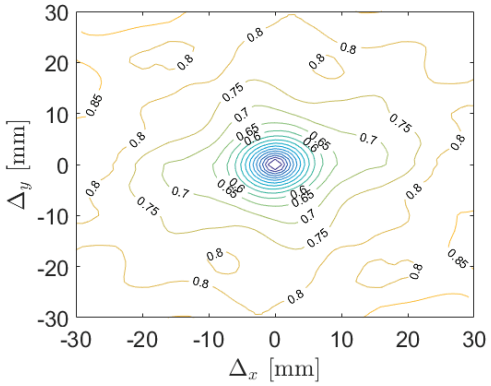

(e) Initial patch Z3

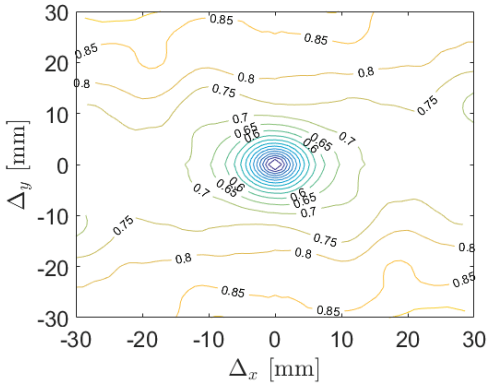

(f) Final patch Z3

Figure B.2.5: Contour plots for the three patches: left and right sides of this figure correspond to initial and final states of the bed surface, respectively.

Table B.2: Bed surface criteria of the 3 patches surveyed before and after the sediment transport experiment.

(a)

		σ_{zg} (mm)	S_k (mm^3)	K_u (mm^4)	Δ_{x0} (mm)	Δ_{y0} (mm)	H_x (-)	H_y (-)	x_0 (mm)	y_0 (mm)	a (mm)	b (mm)	$\frac{x_0}{y_0}$ (-)	$\frac{a}{b}$ (-)	ϕ (°)
Z1	Initial	3.2	-0.03	2.8	8.3	6.7	0.47	0.53	8.0	6.8	7.9	6.8	1.2	1.2	3.5
	Final	3.9	-0.14	2.7	12.4	10.7	0.51	0.53	9.9	6.9	9.8	6.8	1.4	1.4	2.2
Z2	Initial	3.2	0.02	3.2	8.1	7.2	0.51	0.53	10.2	6.8	9.8	6.7	1.5	1.5	-4.1
	Final	3.5	0.06	3.0	9.1	8.4	0.52	0.53	7.3	6.8	7.2	6.4	1.1	1.1	28.6
Z3	Initial	3.5	0.02	2.8	8.6	8.0	0.54	0.55	7.5	6.8	7.5	6.7	1.1	1.1	-18.0
	Final	3.5	-0.04	2.9	8.6	8.0	0.53	0.55	7.9	6.8	7.7	6.8	1.2	1.1	6.1

(b)

		σ_{zg} (mm)	S_k (mm^3)	K_u (mm^4)	σ_{zl} (mm)	σ_{zt} (mm)	Δ_{x0} (mm)	Δ_{y0} (mm)	H_x (-)	H_y (-)	$\frac{x_0}{y_0}$ (-)	$\frac{a}{b}$ (-)	ϕ (°)
General bed	Initial	3.3	0.00	2.9	4.6	4.3	8.3	7.3	0.51	0.54	1.3	1.2	-6.2
	Final	3.6	-0.04	2.8	6.1	4.5	10.0	9.0	0.52	0.54	1.2	1.2	12.3

B.3 L-G-2 experiment

General bed surface surveys

No DEM of the entire bed surface is available. Three longitudinal bed surface surveys are presented in B.3.1.

Surveys of bed surface patches

In the following, initial and final states mean before and after an experiment of sediment transport, respectively. Initial and final bed surface surveys were performed on 3 zones distributed along the channel: downstream (patch Z1), middle (patch Z2), and upstream (patch Z3). In this experiment, patches Z1, Z2 and Z3 were located at 6.6 m, 8.6 m, and 10.6 m from the downstream end of the flume, respectively.

Figure B.3.2 represents the resulting digital elevation models (DEM). Figure B.3.3 shows the probability density function of the bed surface elevations for the 3 patches. Two representations of the structure function D_b associated to the 3 patches are given: one in 3D (Figure B.3.4) and one in contour plot (Figure B.3.5).

Bed surface criteria

Table B.3a recaps all the bed surface criteria calculated for the three patches surveyed (initial and final states). Table B.3b reports the bed surface criteria computed at the scale of the entire bed surface, either by averaging data of the three patches or by using the transverse and longitudinal surveys of the bed.

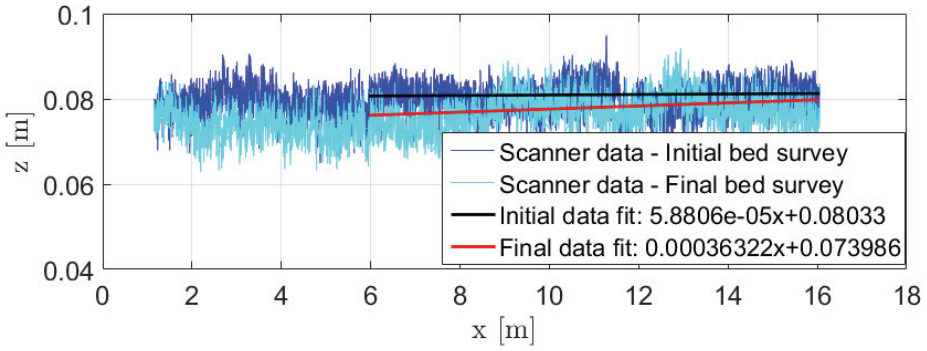

(a) Center line

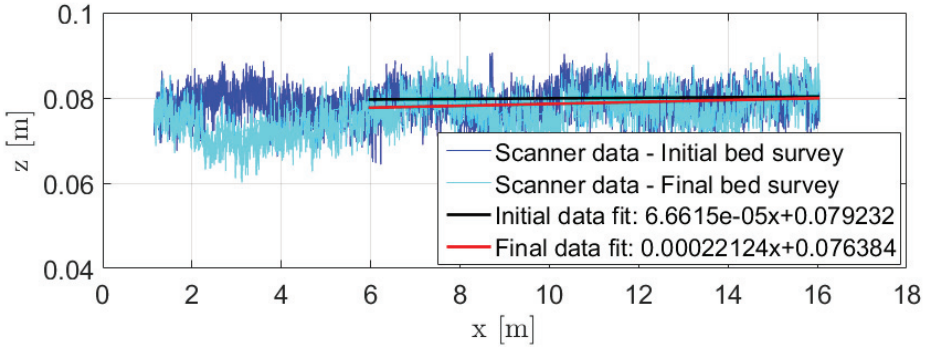

(b) Right side

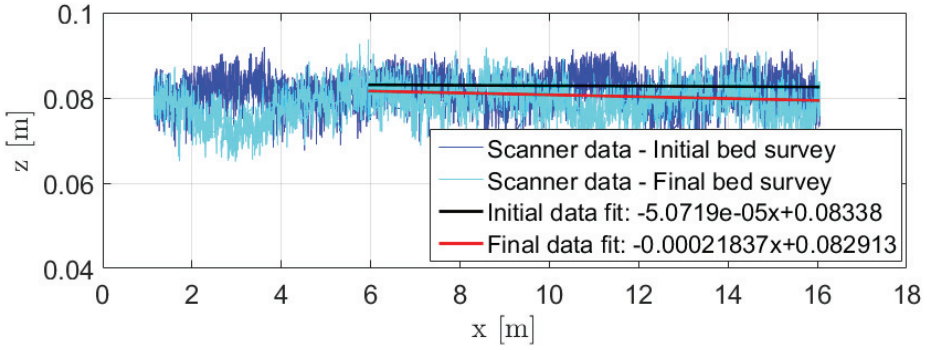

(c) Left side

Figure B.3.1: Longitudinal surveys of the bed surface before and after the experiment of sediment transport.

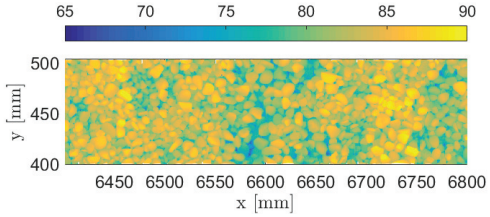

(a) Initial patch Z1

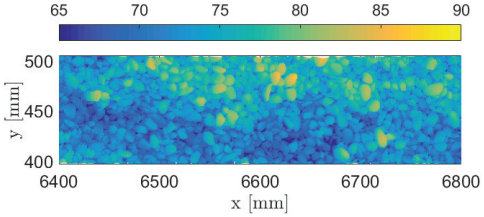

(b) Final patch Z1

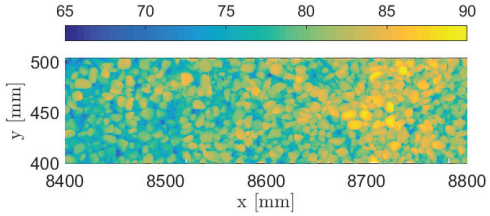

(c) Initial patch Z2

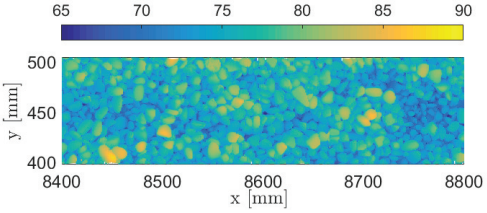

(d) Final patch Z2

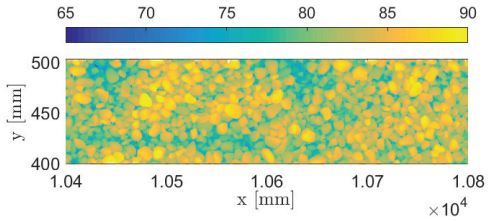

(e) Initial patch Z3

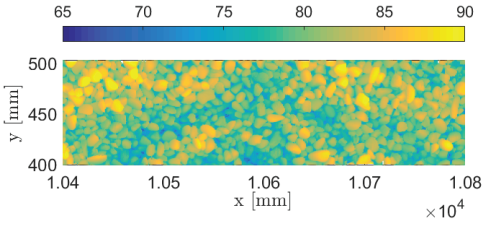

(f) Final patch Z3

Figure B.3.2: DEM of bed surface patches: left and right sides of this figure correspond to initial and final states of the bed surface, respectively.

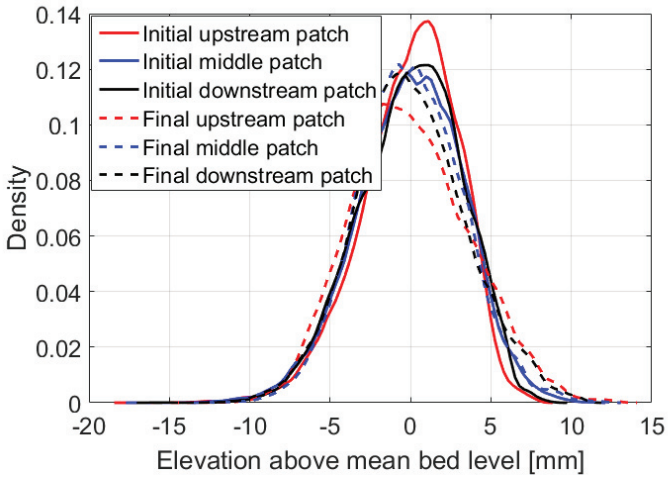

Figure B.3.3: PDF of the bed surface elevations for the 3 patches before and after the sediment transport experiment

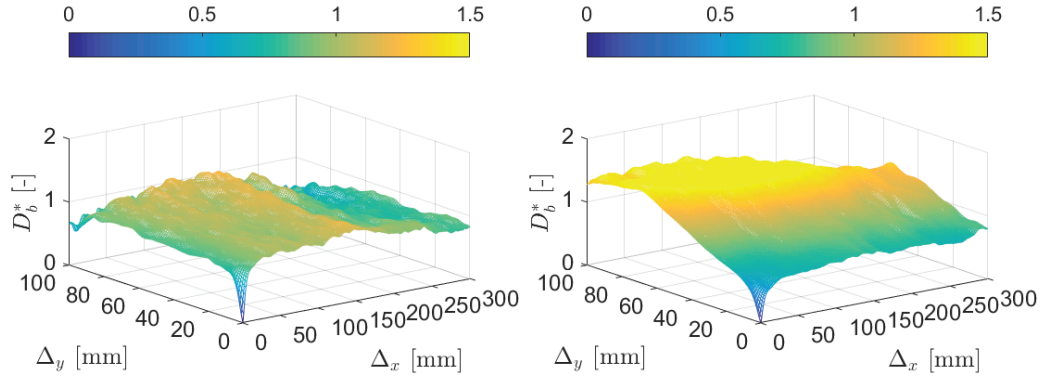

(a) Initial patch Z1

(b) Final patch Z1

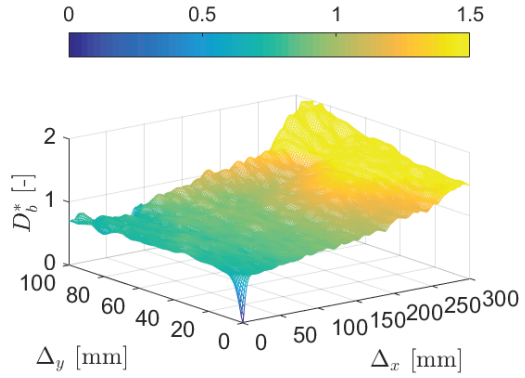

(c) Initial patch Z2

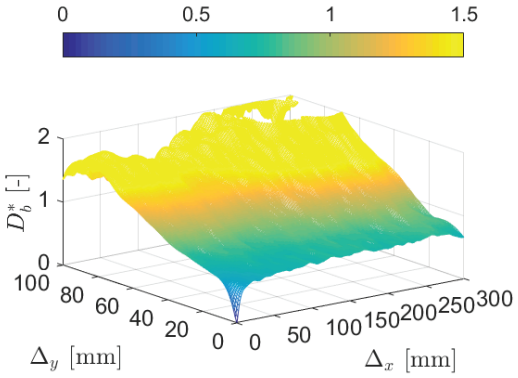

(d) Final patch Z2

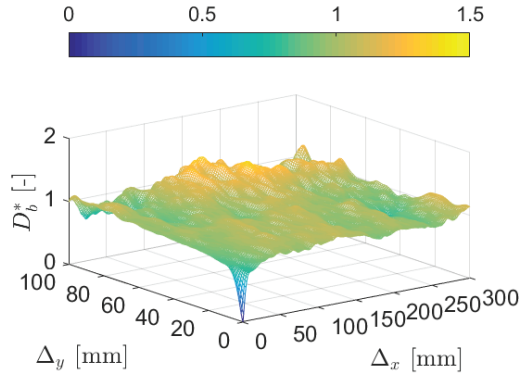

(e) Initial patch Z3

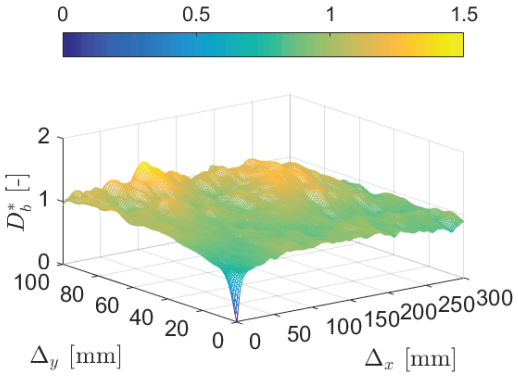

(f) Final patch Z3

Figure B.3.4: D_b^* plots for the three patches: left and right sides of this figure correspond to initial and final states of the bed surface, respectively.

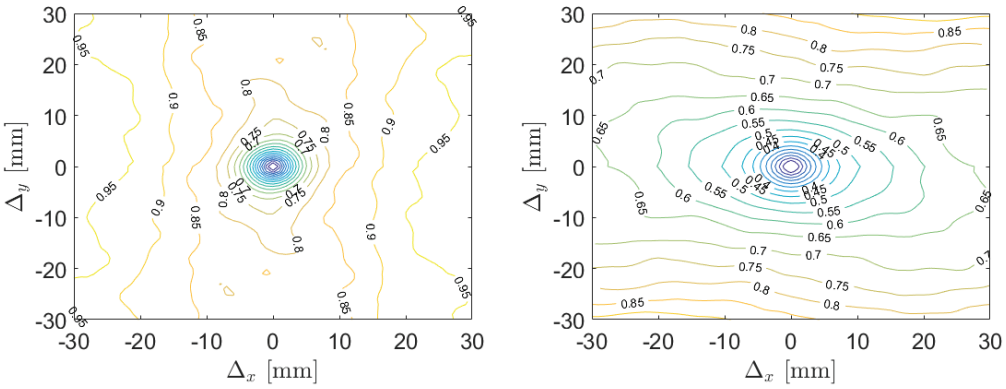

(a) Initial patch Z1

(b) Final patch Z1

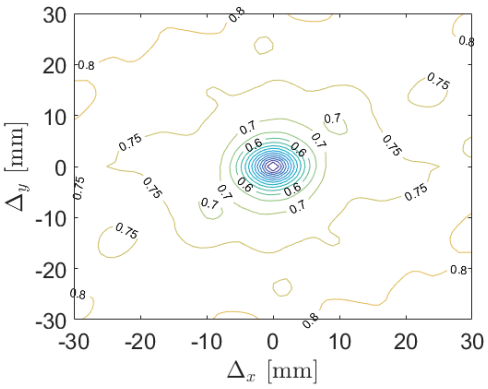

(c) Initial patch Z2

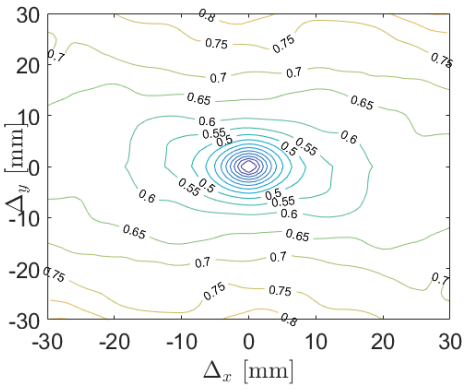

(d) Final patch Z2

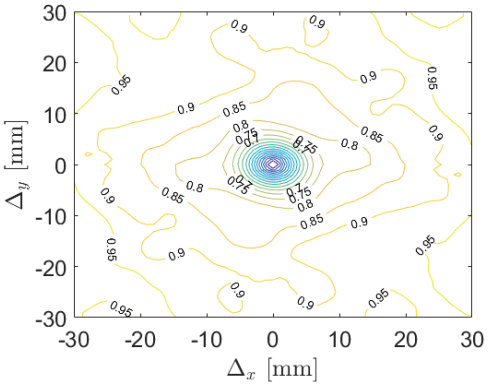

(e) Initial patch Z3

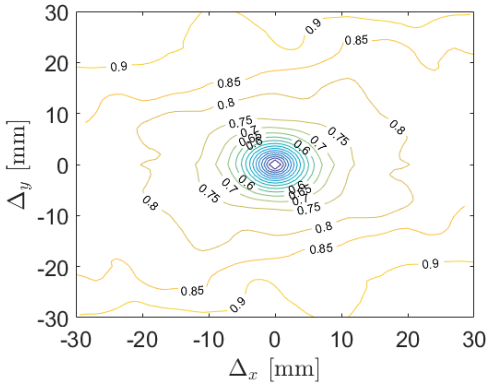

(f) Final patch Z3

Figure B.3.5: Contour plots for the three patches: left and right sides of this figure correspond to initial and final states of the bed surface, respectively.

Table B.3: Bed surface criteria of the 3 patches surveyed before and after the sediment transport experiment.

(a)

		σ_{zg} (mm)	S_k (mm^3)	K_u (mm^4)	Δ_{x0} (mm)	Δ_{y0} (mm)	H_x (-)	H_y (-)	x_0 (mm)	y_0 (mm)	a (mm)	b (mm)	$\frac{x_0}{y_0}$ (-)	$\frac{a}{b}$ (-)	ϕ (°)
Z1	Initial	3.0	-0.52	3.4	6.4	6.3	0.53	0.54	6.0	6.6	5.7	6.7	0.9	1.2	20.5
	Final	3.7	0.23	2.8	13.3	10.0	0.48	0.54	8.9	6.7	8.6	6.6	1.3	1.3	4.8
Z2	Initial	3.3	-0.22	3.1	7.3	7.1	0.54	0.54	6.5	6.7	6.4	6.8	1.0	1.1	25.2
	Final	3.2	0.09	3.1	10.7	9.3	0.51	0.54	9.8	6.7	9.5	6.6	1.5	1.5	4.1
Z3	Initial	3.2	-0.30	2.8	6.6	6.3	0.54	0.55	7.6	6.7	7.5	6.6	1.1	1.1	21.6
	Final	3.5	0.12	3.0	7.7	7.1	0.53	0.55	8.1	6.8	7.9	6.8	1.2	1.2	9.9

(b)

		σ_{zg} (mm)	S_k (mm^3)	K_u (mm^4)	σ_{zl} (mm)	σ_{zt} (mm)	Δ_{x0} (mm)	Δ_{y0} (mm)	H_x (-)	H_y (-)	$\frac{x_0}{y_0}$ (-)	$\frac{a}{b}$ (-)	ϕ (°)
General bed	Initial	3.2	-0.34	3.1	3.5	3.2	6.8	6.6	0.54	0.54	1.0	1.1	22.4
	Final	3.5	0.14	3.0	4.3	4.2	10.6	8.8	0.51	0.54	1.3	1.3	6.2

B.4 P-G-2 experiment

General bed surface surveys

No DEM of the entire bed surface is available. Three longitudinal bed surface surveys are presented in B.4.1.

Surveys of bed surface patches

In the following, initial and final states mean before and after an experiment of sediment transport, respectively. Initial and final bed surface surveys were performed on 3 zones distributed along the channel: downstream (patch Z1), middle (patch Z2), and upstream (patch Z3). In this experiment, patches Z1, Z2 and Z3 were located at 6.6 m, 8.6 m, and 10.6 m from the downstream end of the flume, respectively.

Figure B.4.2 represents the resulting digital elevation models (DEM). Figure B.4.3 shows the probability density function of the bed surface elevations for the 3 patches. Two representations of the structure function D_b associated to the 3 patches are given: one in 3D (Figure B.4.4) and one in contour plot (Figure B.4.5).

Bed surface criteria

Table B.4a recaps all the bed surface criteria calculated for the three patches surveyed (initial and final states). Table B.4b reports the bed surface criteria computed at the scale of the entire bed surface, either by averaging data of the three patches or by using the transverse and longitudinal surveys of the bed.

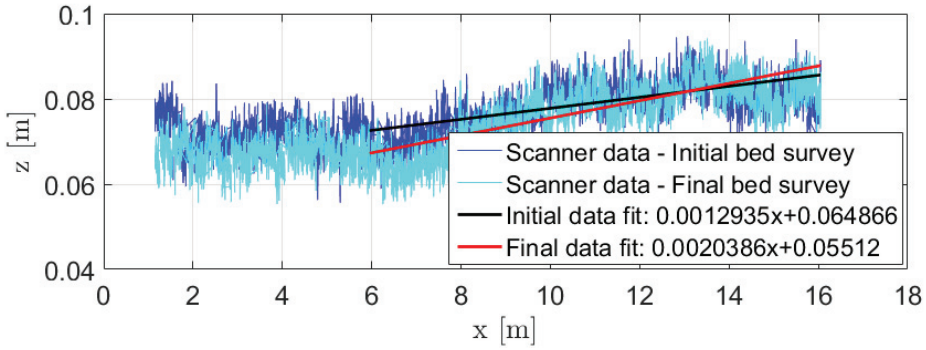

(a) Center line

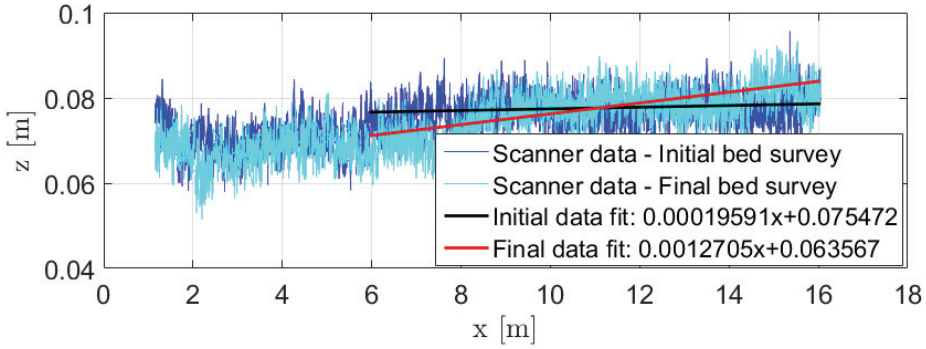

(b) Right side

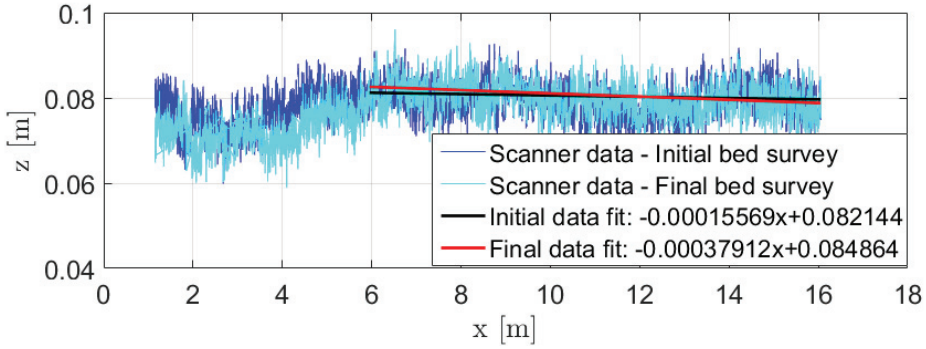

(c) Left side

Figure B.4.1: Longitudinal surveys of the bed surface before and after the experiment of sediment transport.

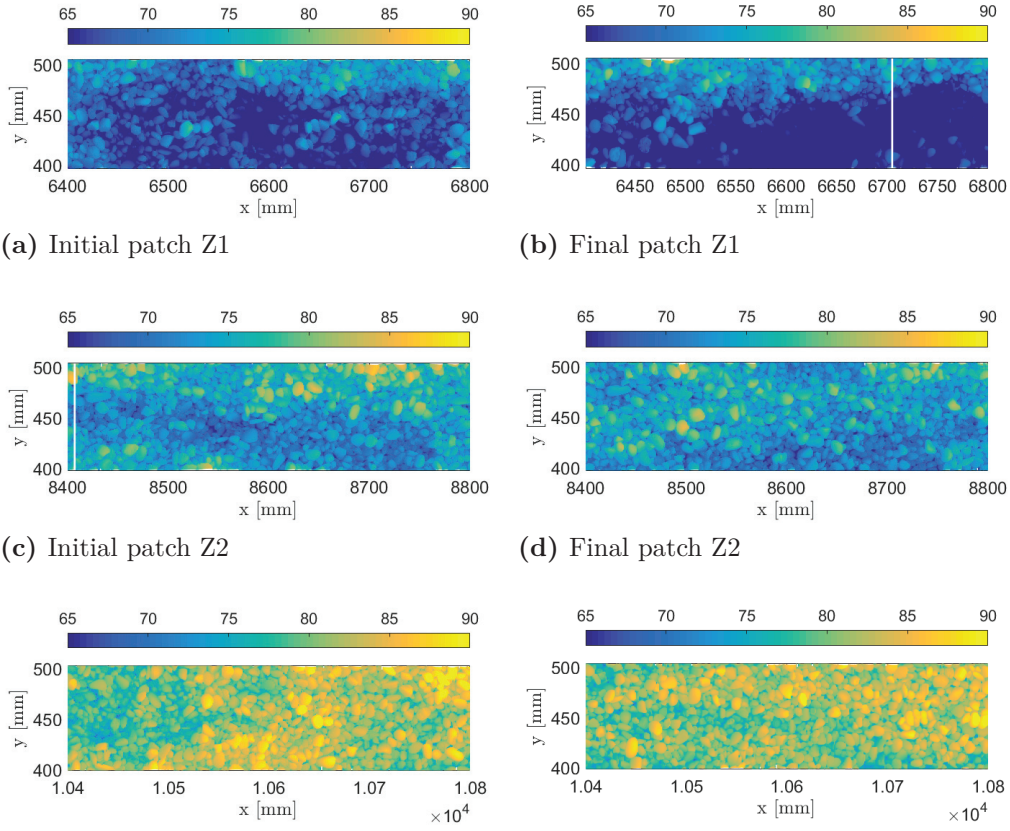

(a) Initial patch Z1 **(b)** Final patch Z1

(c) Initial patch Z2 **(d)** Final patch Z2

(e) Initial patch Z3 **(f)** Final patch Z3

Figure B.4.2: DEM of bed surface patches: left and right sides of this figure correspond to initial and final states of the bed surface, respectively.

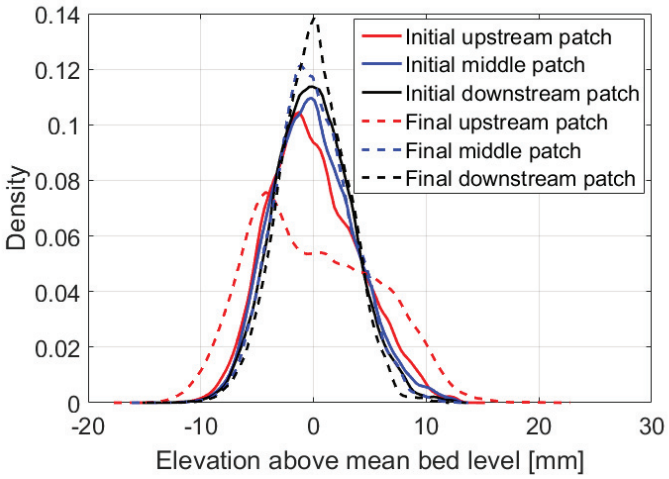

Figure B.4.3: PDF of the bed surface elevations for the 3 patches before and after the sediment transport experiment

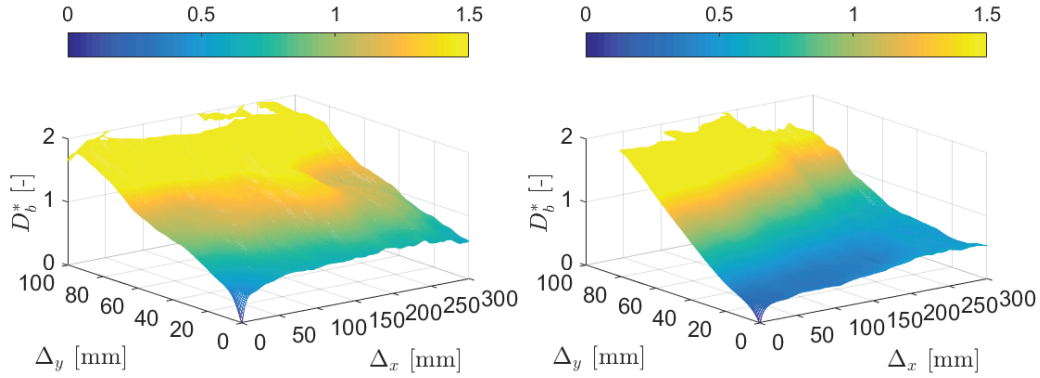

(a) Initial patch Z1

(b) Final patch Z1

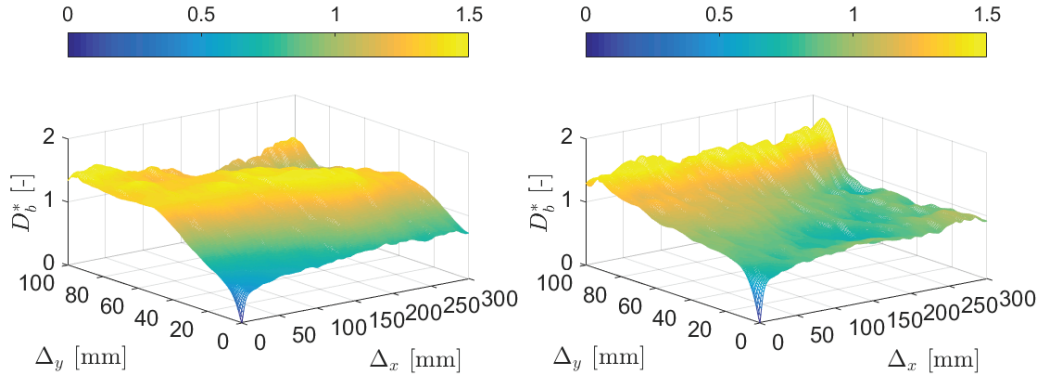

(c) Initial patch Z2

(d) Final patch Z2

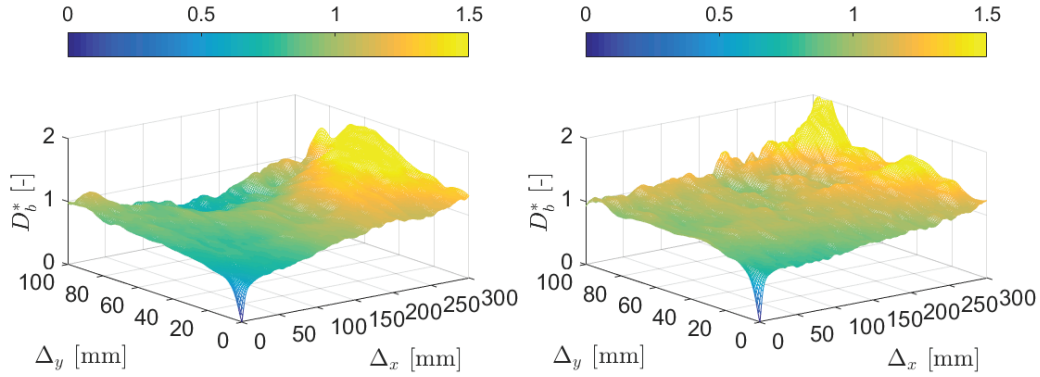

(e) Initial patch Z3

(f) Final patch Z3

Figure B.4.4: D_b^* plots for the three patches: left and right sides of this figure correspond to initial and final states of the bed surface, respectively.

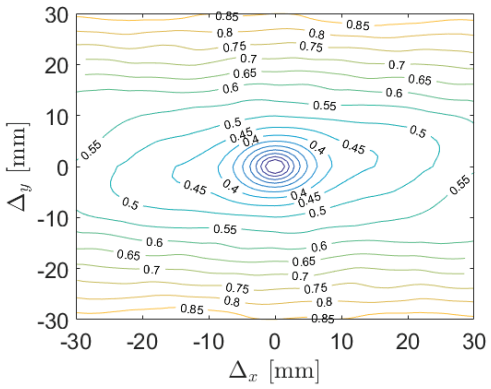

(a) Initial patch Z1

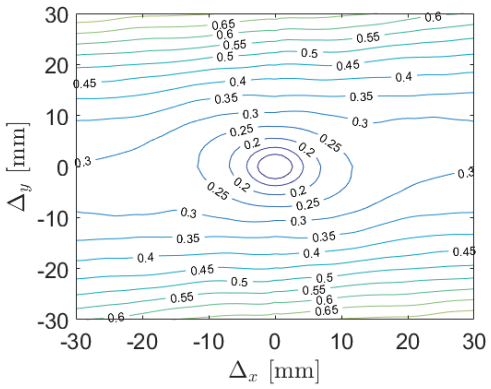

(b) Final patch Z1

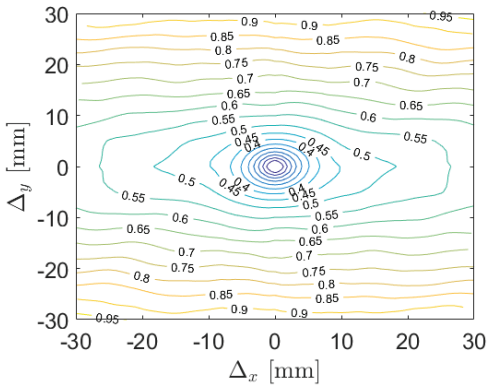

(c) Initial patch Z2

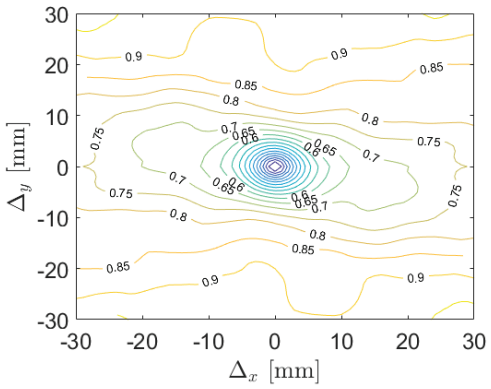

(d) Final patch Z2

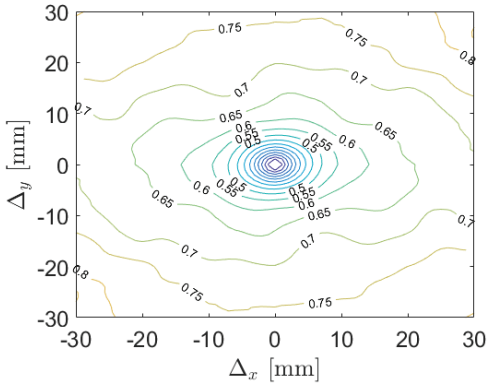

(e) Initial patch Z3

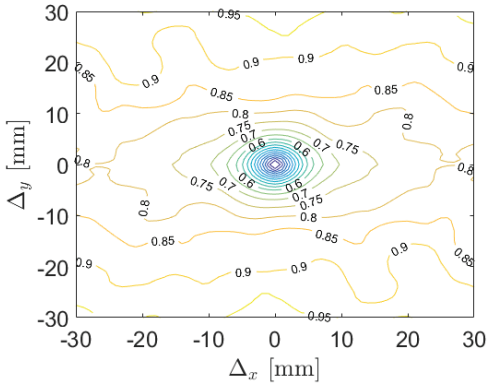

(f) Final patch Z3

Figure B.4.5: Contour plots for the three patches: left and right sides of this figure correspond to initial and final states of the bed surface, respectively.

Table B.4: Bed surface criteria of the 3 patches surveyed before and after the sediment transport experiment.

(a)

		σ_{zg} (mm)	S_k (mm^3)	K_u (mm^4)	Δ_{x0} (mm)	Δ_{y0} (mm)	H_x (-)	H_y (-)	x_0 (mm)	y_0 (mm)	a (mm)	b (mm)	$\frac{x_0}{y_0}$ (-)	$\frac{a}{b}$ (-)	ϕ (°)
Z1	Initial	4.0	0.34	2.8	13.7	11.6	0.52	0.54	10.0	6.7	9.8	6.6	1.5	1.5	-7.2
	Final	5.6	0.28	2.3	26.9	21.0	0.50	0.53	9.5	6.8	9.4	6.9	1.4	1.4	7.0
Z2	Initial	3.7	0.32	3.0	12.4	10.9	0.51	0.52	11.1	6.8	10.4	6.6	1.6	1.6	2.3
	Final	3.4	0.18	3.0	8.9	8.1	0.52	0.53	10.5	6.9	10.1	6.7	1.5	1.5	9.1
Z3	Initial	3.4	0.17	3.1	10.2	8.8	0.50	0.54	8.8	6.7	8.8	6.7	1.3	1.3	-8.3
	Final	3.0	0.01	3.0	7.7	6.9	0.50	0.53	9.7	6.9	9.0	6.7	1.4	1.4	-3.3

(b)

		σ_{zg} (mm)	S_k (mm^3)	K_u (mm^4)	σ_{zl} (mm)	σ_{zt} (mm)	Δ_{x0} (mm)	Δ_{y0} (mm)	H_x (-)	H_y (-)	$\frac{x_0}{y_0}$ (-)	$\frac{a}{b}$ (-)	ϕ (°)
General bed	Initial	3.7	0.28	2.9	5.0	4.2	12.1	10.4	0.51	0.53	1.5	1.5	-4.4
	Final	4.0	0.16	2.8	6.5	4.8	14.5	12.0	0.50	0.53	1.4	1.4	4.3

B.5 L-G-3 experiment

General bed surface surveys

No DEM of the entire bed surface is available. Three longitudinal bed surface surveys are presented in B.5.1.

Surveys of bed surface patches

In the following, initial and final states mean before and after an experiment of sediment transport, respectively. Initial and final bed surface surveys were performed on 3 zones distributed along the channel: downstream (patch Z1), middle (patch Z2), and upstream (patch Z3). In this experiment, patches Z1, Z2 and Z3 were located at 6.6 m, 8.6 m, and 10.6 m from the downstream end of the flume, respectively.

Figure B.5.2 represents the resulting digital elevation models (DEM). Figure B.5.3 shows the probability density function of the bed surface elevations for the 3 patches. Two representations of the structure functions D_b associated to the 3 patches are given: one in 3D (Figure B.5.4) and one in contour plot (Figure B.5.5).

Bed surface criteria

Table B.5a recaps all the bed surface criteria calculated for the three patches surveyed (initial and final states). Table B.5b reports the bed surface criteria computed at the scale of the entire bed surface, either by averaging data of the three patches or by using the transverse and longitudinal surveys of the bed.

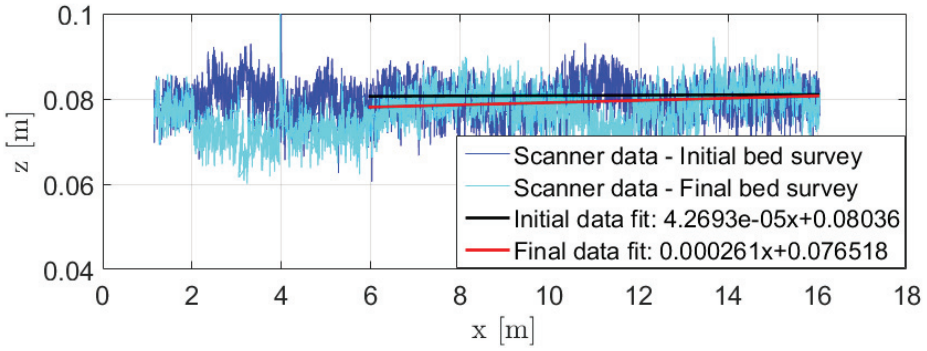

(a) Center line

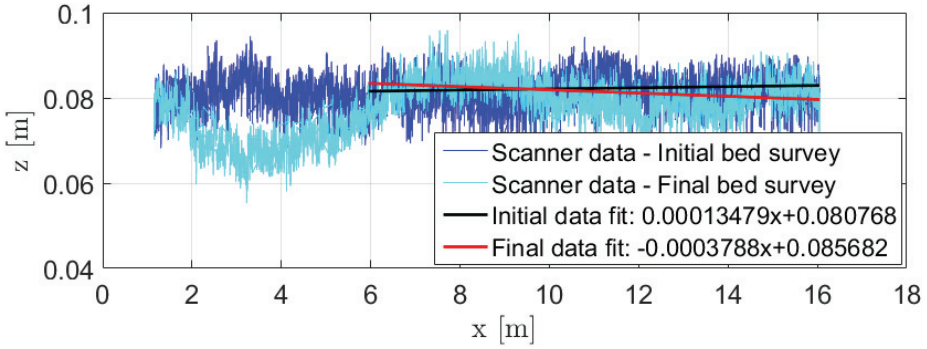

(b) Right side

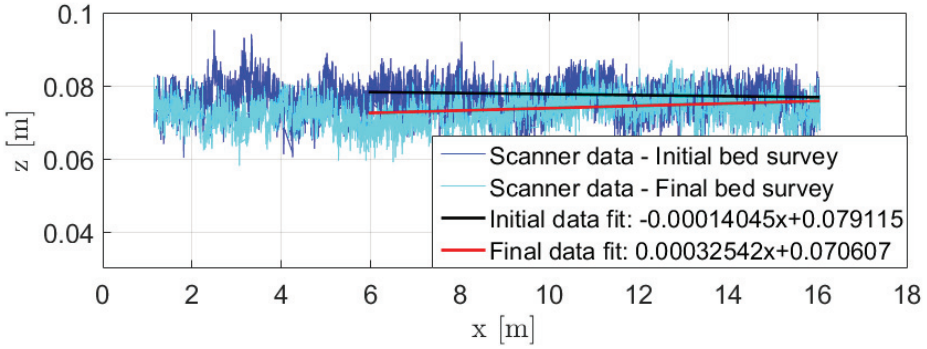

(c) Left side

Figure B.5.1: Longitudinal surveys of the bed surface before and after the experiment of sediment transport.

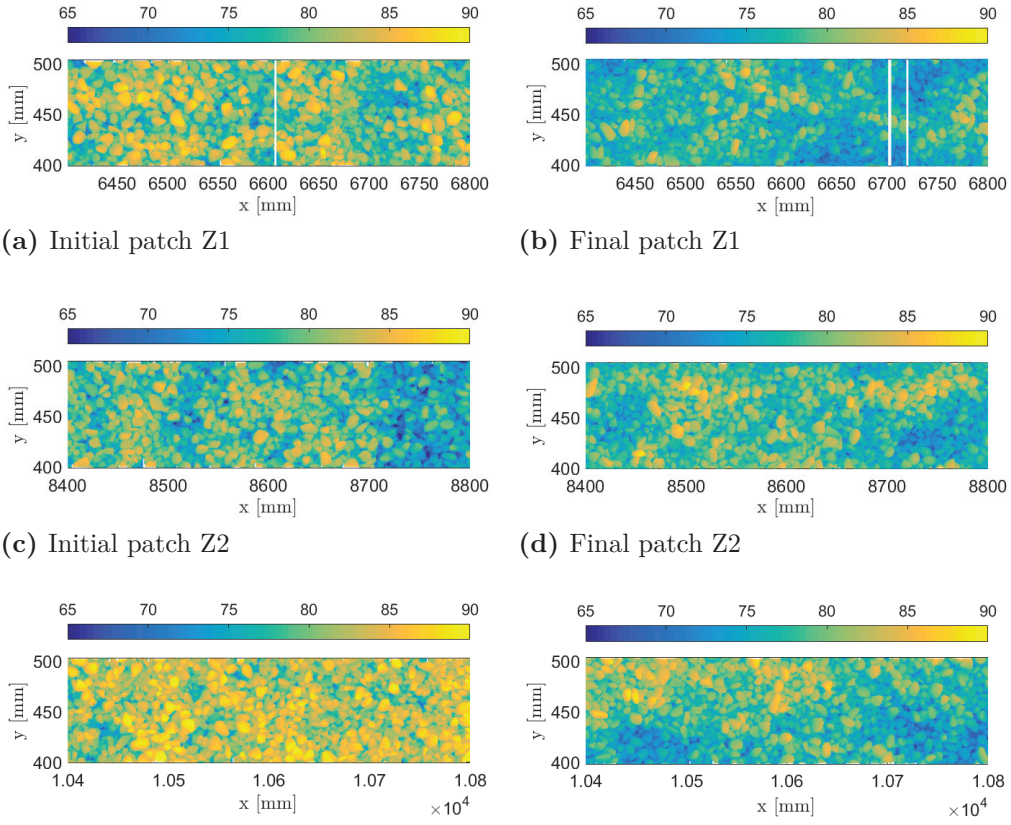

(a) Initial patch Z1

(b) Final patch Z1

(c) Initial patch Z2

(d) Final patch Z2

(e) Initial patch Z3

(f) Final patch Z3

Figure B.5.2: DEM of bed surface patches: left and right sides of this figure correspond to initial and final states of the bed surface, respectively.

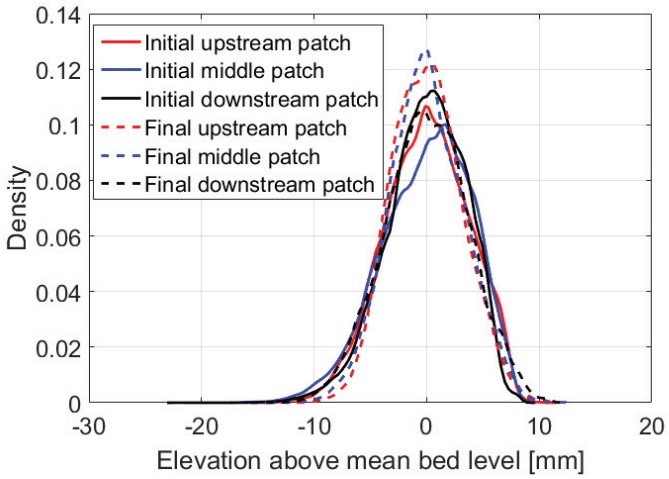

Figure B.5.3: PDF of the bed surface elevations for the 3 patches before and after the sediment transport experiment

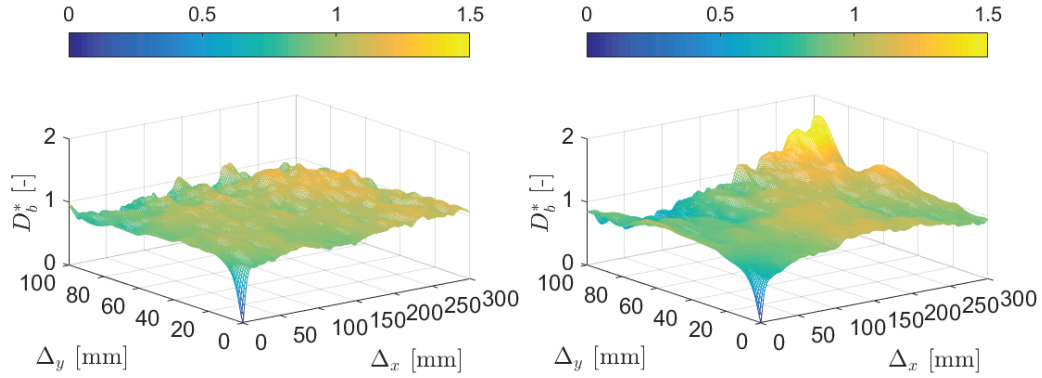

(a) Initial patch Z1

(b) Final patch Z1

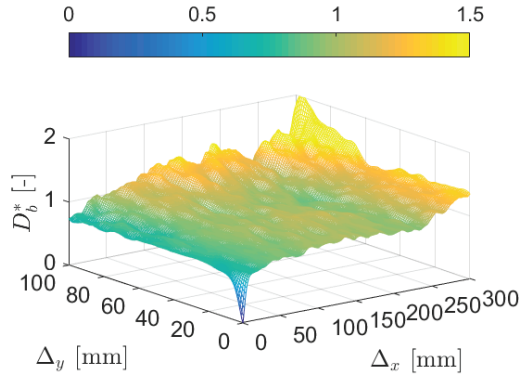

(c) Initial patch Z2

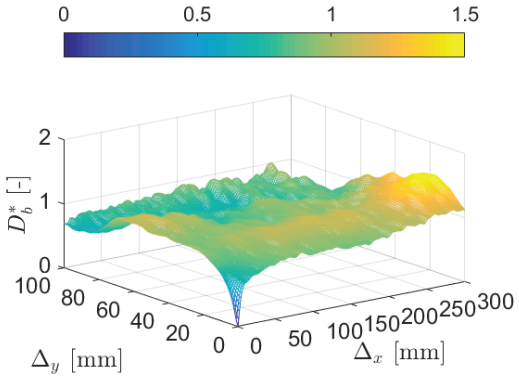

(d) Final patch Z2

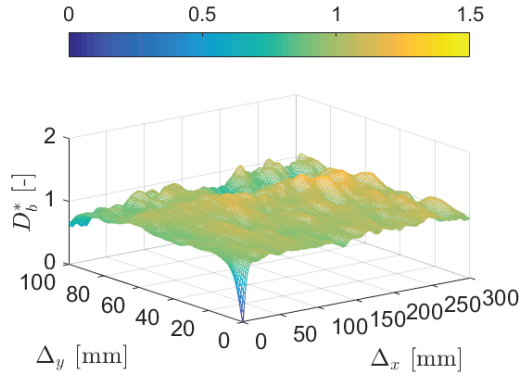

(e) Initial patch Z3

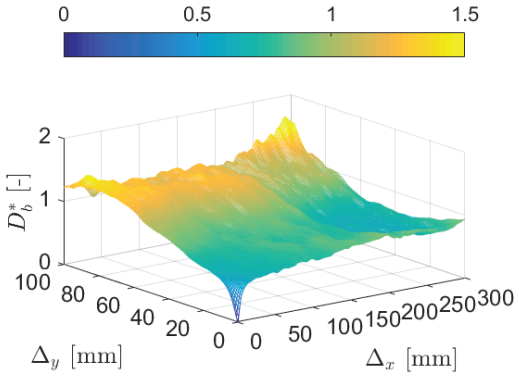

(f) Final patch Z3

Figure B.5.4: D_b^* plots for the three patches: left and right sides of this figure correspond to initial and final states of the bed surface, respectively.

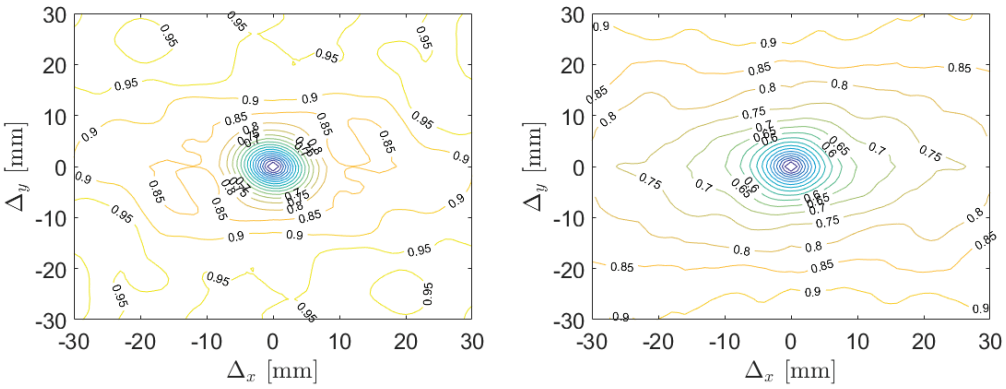

(a) Initial patch Z1

(b) Final patch Z1

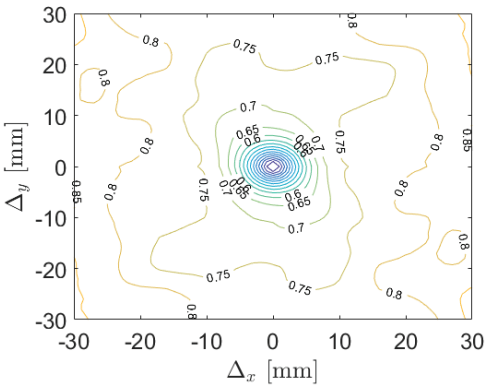

(c) Initial patch Z2

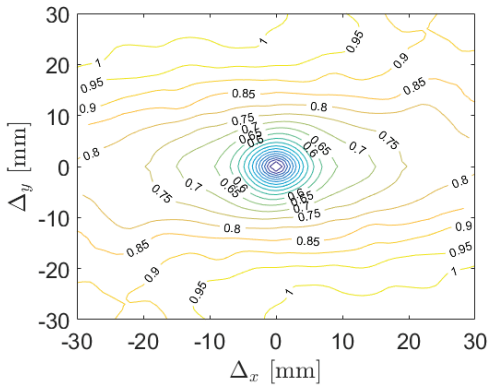

(d) Final patch Z2

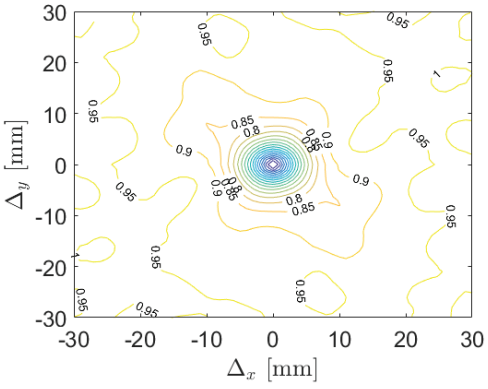

(e) Initial patch Z3

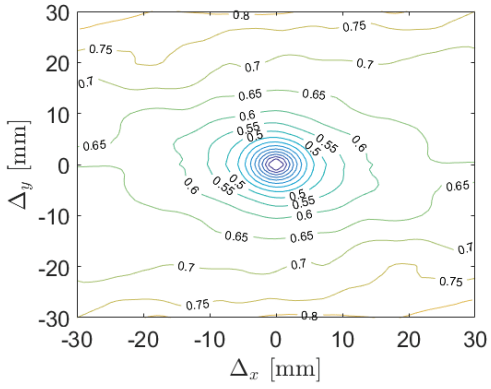

(f) Final patch Z3

Figure B.5.5: Contour plots for the three patches: left and right sides of this figure correspond to initial and final states of the bed surface, respectively.

Table B.5: Bed surface criteria of the 3 patches surveyed before and after the sediment transport experiment.

(a)

		σ_{zg} (mm)	S_k (mm^3)	K_u (mm^4)	Δ_{x0} (mm)	Δ_{y0} (mm)	H_x (-)	H_y (-)	x_0 (mm)	y_0 (mm)	a (mm)	b (mm)	$\frac{x_0}{y_0}$ (-)	$\frac{a}{b}$ (-)	ϕ (°)
Z1	Initial	3.7	-0.19	2.7	6.9	6.7	0.56	0.56	6.6	6.7	6.3	6.9	1.0	1.1	-32.9
	Final	3.1	0.12	2.8	8.5	8.1	0.51	0.52	8.0	6.8	7.8	6.7	1.2	1.2	-2.6
Z2	Initial	3.9	-0.43	2.9	7.6	7.4	0.55	0.56	6.3	6.9	6.2	7.4	0.9	1.2	-26.5
	Final	3.3	0.03	2.9	8.2	7.9	0.52	0.54	7.7	6.9	7.4	6.7	1.1	1.1	-8.7
Z3	Initial	3.5	-0.44	3.1	6.3	6.2	0.54	0.56	6.3	6.8	6.2	6.9	0.9	1.1	-2.2
	Final	3.7	-0.07	2.8	9.8	9.3	0.53	0.54	8.1	6.8	8.0	6.6	1.2	1.2	14.4

(b)

		σ_{zg} (mm)	S_k (mm^3)	K_u (mm^4)	σ_{zl} (mm)	σ_{zt} (mm)	Δ_{x0} (mm)	Δ_{y0} (mm)	H_x (-)	H_y (-)	$\frac{x_0}{y_0}$ (-)	$\frac{a}{b}$ (-)	ϕ (°)
General bed	Initial	3.7	-0.35	2.9	4.1	4.1	6.9	6.8	0.55	0.56	0.9	1.1	-20.5
	Final	3.4	0.02	2.9	5.8	4.6	8.8	8.4	0.52	0.53	1.2	1.2	1.0

B.6 P-G-3 experiment

General bed surface surveys

No DEM of the entire bed surface is available. Three longitudinal bed surface surveys are presented in B.6.1.

Surveys of bed surface patches

In the following, initial and final states mean before and after an experiment of sediment transport, respectively. Initial and final bed surface surveys were performed on 3 zones distributed along the channel: downstream (patch Z1), middle (patch Z2), and upstream (patch Z3). In this experiment, patches Z1, Z2 and Z3 were located at 6.6 m, 8.6 m, and 10.6 m from the downstream end of the flume, respectively.

Figure B.6.2 represents the resulting digital elevation models (DEM). Figure B.6.3 shows the probability density function of the bed surface elevations for the 3 patches. Two representations of the structure functions D_b associated to the 3 patches are given: one in 3D (Figure B.6.4) and one in contour plot (Figure B.6.5).

Bed surface criteria

Table B.6a recaps all the bed surface criteria calculated for the three patches surveyed (initial and final states). Table B.6b reports the bed surface criteria computed at the scale of the entire bed surface, either by averaging data of the three patches or by using the transverse and longitudinal surveys of the bed.

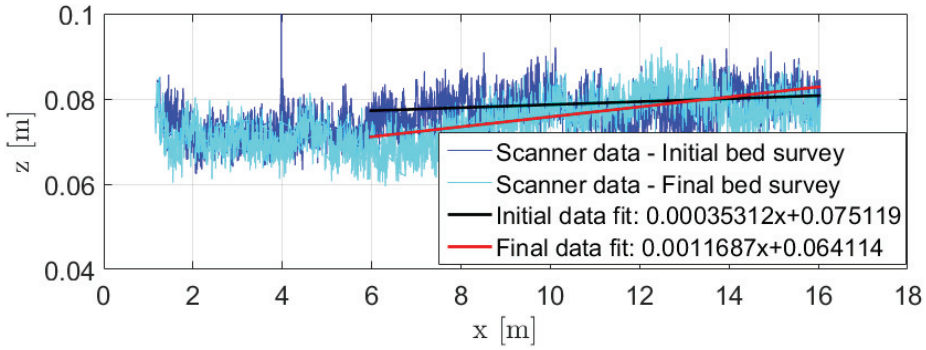

(a) Center line

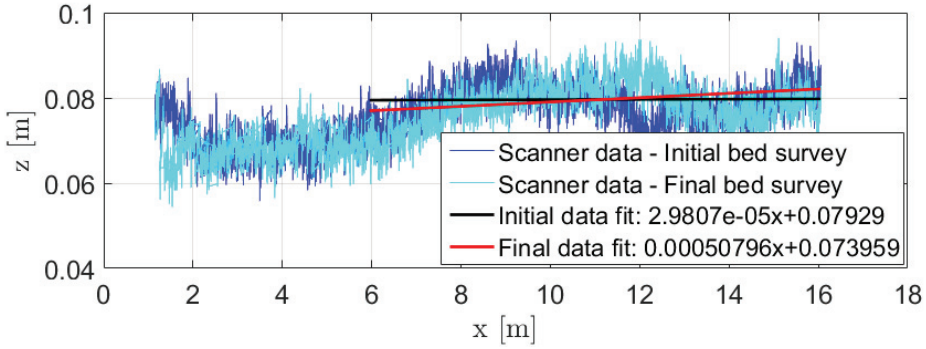

(b) Right side

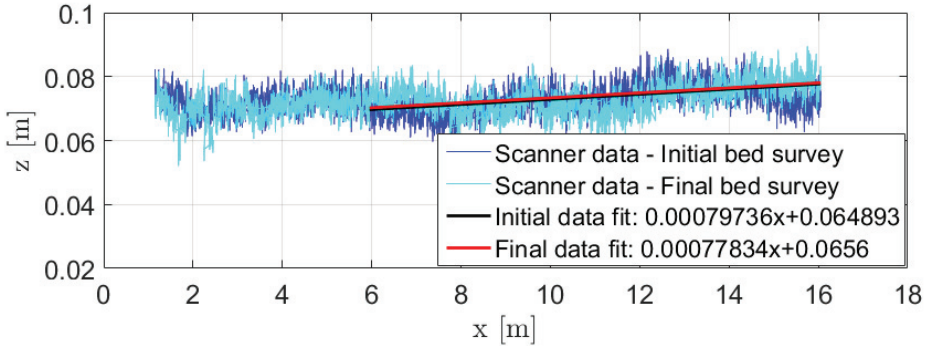

(c) Left side

Figure B.6.1: Longitudinal surveys of the bed surface before and after the experiment of sediment transport.

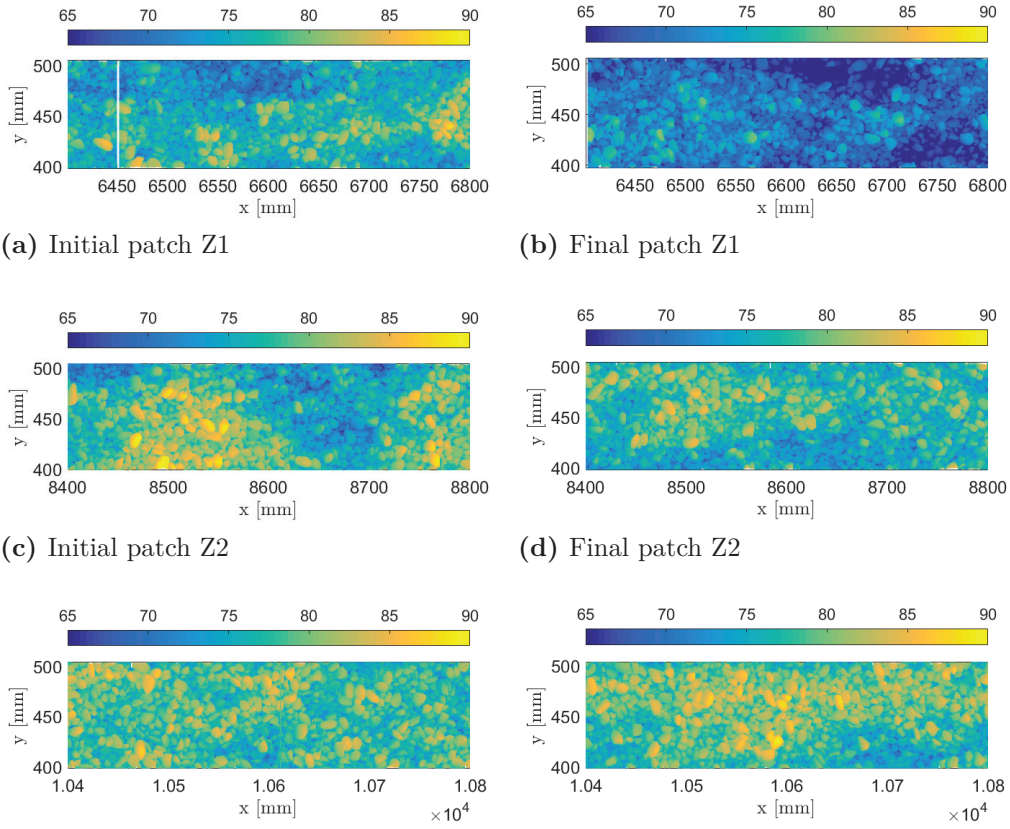

(a) Initial patch Z1

(b) Final patch Z1

(c) Initial patch Z2

(d) Final patch Z2

(e) Initial patch Z3

(f) Final patch Z3

Figure B.6.2: DEM of bed surface patches: left and right sides of this figure correspond to initial and final states of the bed surface, respectively.

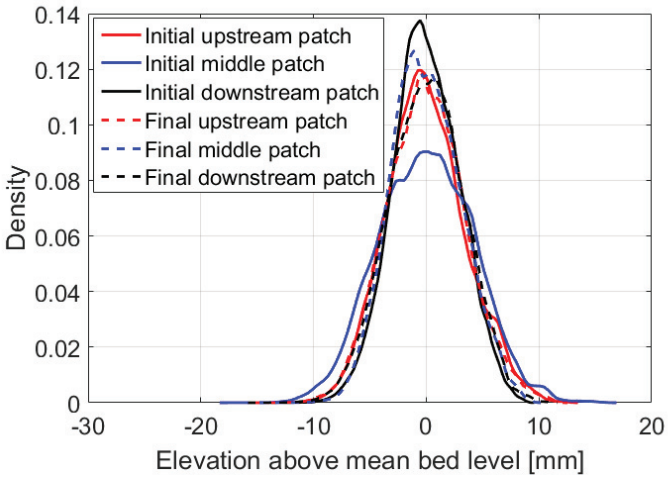

Figure B.6.3: PDF of the bed surface elevations for the 3 patches before and after the sediment transport experiment

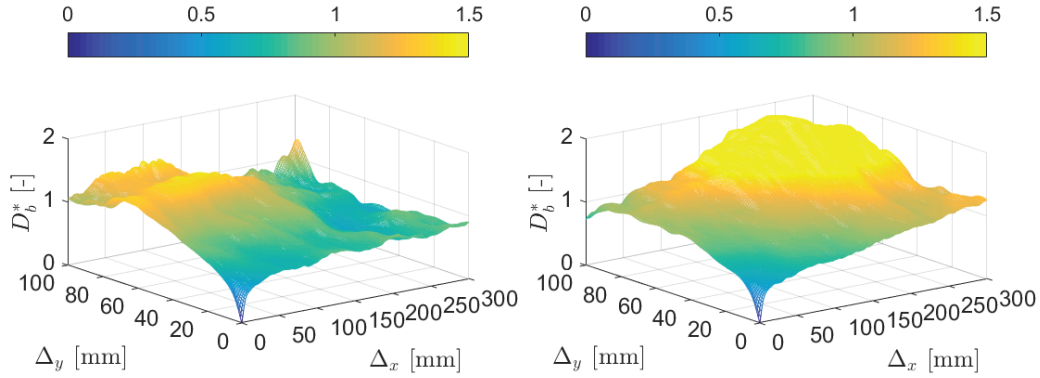

(a) Initial patch Z1 **(b)** Final patch Z1

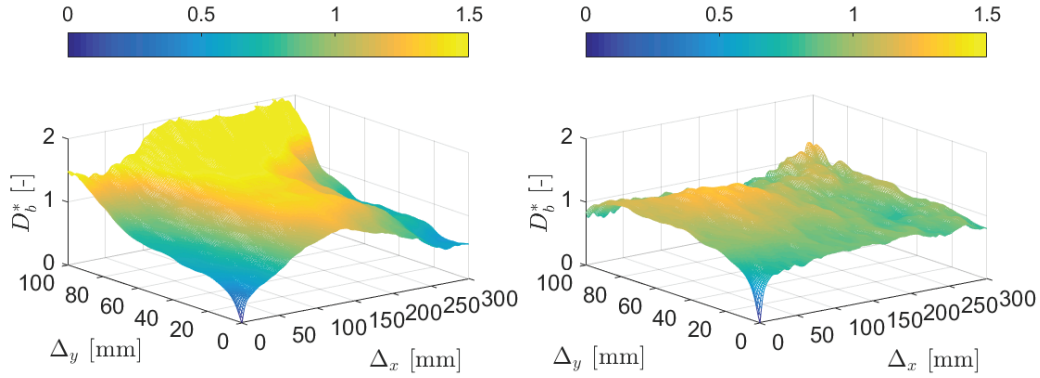

(c) Initial patch Z2 **(d)** Final patch Z2

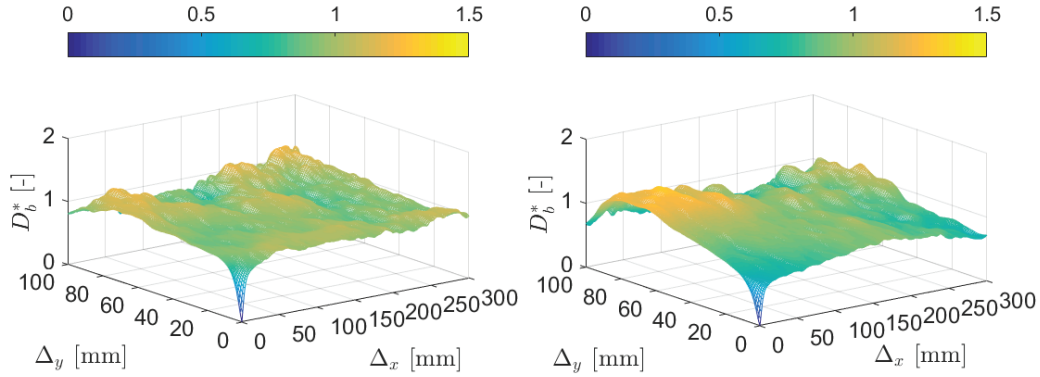

(e) Initial patch Z3 **(f)** Final patch Z3

Figure B.6.4: D_b^* plots for the three patches: left and right sides of this figure correspond to initial and final states of the bed surface, respectively.

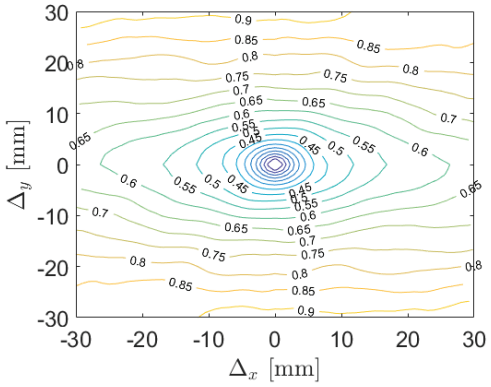

(a) Initial patch Z1

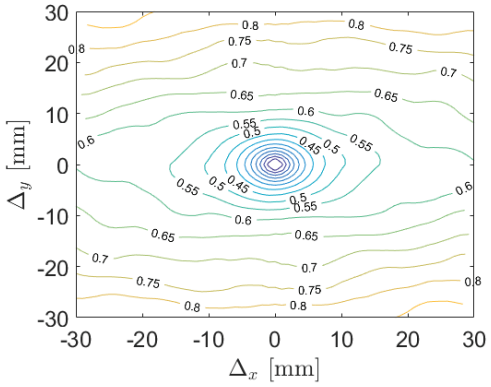

(b) Final patch Z1

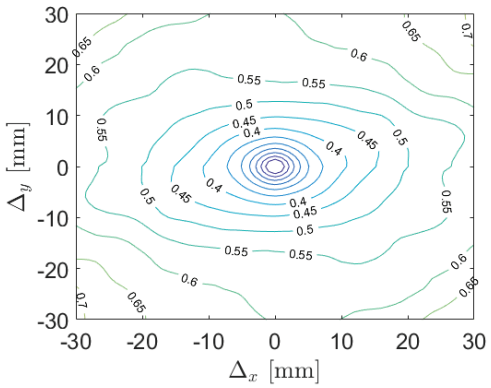

(c) Initial patch Z2

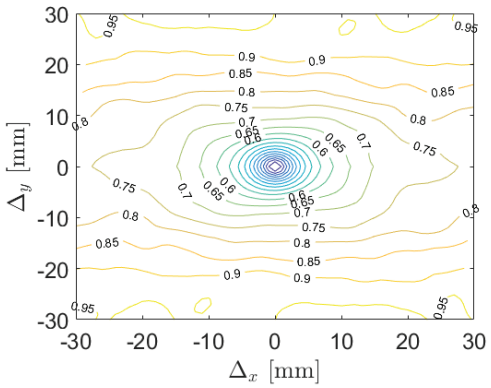

(d) Final patch Z2

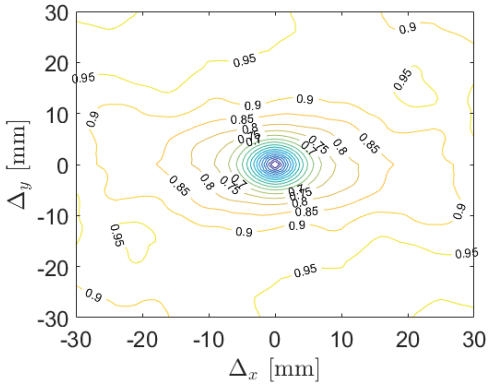

(e) Initial patch Z3

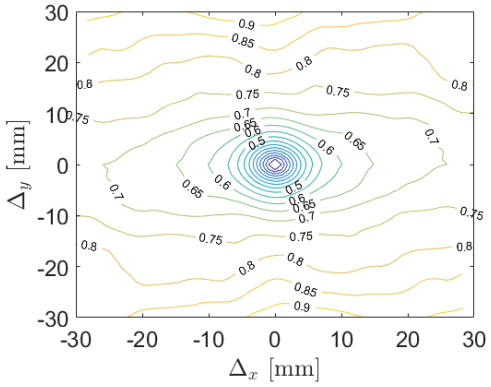

(f) Final patch Z3

Figure B.6.5: Contour plots for the three patches: left and right sides of this figure correspond to initial and final states of the bed surface, respectively.

Table B.6: Bed surface criteria of the 3 patches surveyed before and after the sediment transport experiment.

(a)

		σ_{zg} (mm)	S_k (mm^3)	K_u (mm^4)	Δ_{x0} (mm)	Δ_{y0} (mm)	H_x (-)	H_y (-)	x_0 (mm)	y_0 (mm)	a (mm)	b (mm)	$\frac{x_0}{y_0}$ (-)	$\frac{a}{b}$ (-)	ϕ (°)
Z1	Initial	3.5	0.20	3.0	12.0	10.2	0.49	0.52	10.9	6.8	10.5	6.8	1.6	1.5	-0.1
	Final	3.5	0.10	3.0	11.7	10.4	0.49	0.51	9.1	6.8	8.9	6.6	1.3	1.3	-3.1
Z2	Initial	4.2	0.05	2.8	14.7	12.7	0.49	0.53	9.2	6.7	8.9	6.6	1.4	1.3	1.1
	Final	3.1	0.13	2.8	8.8	7.9	0.51	0.53	9.7	6.9	9.7	6.9	1.4	1.4	-4.4
Z3	Initial	2.9	0.00	2.9	7.2	6.4	0.48	0.52	9.7	6.8	9.5	6.8	1.4	1.4	1.4
	Final	3.3	-0.06	2.8	9.0	8.7	0.51	0.53	7.5	6.7	7.2	6.5	1.1	1.1	4.5

(b)

		σ_{zg} (mm)	S_k (mm^3)	K_u (mm^4)	σ_{zl} (mm)	σ_{zt} (mm)	Δ_{x0} (mm)	Δ_{y0} (mm)	H_x (-)	H_y (-)	$\frac{x_0}{y_0}$ (-)	$\frac{a}{b}$ (-)	ϕ (°)
General bed	Initial	3.5	0.08	2.9	5.1	4.4	11.3	9.8	0.49	0.52	1.5	1.4	0.8
	Final	3.3	0.06	2.8	5.7	/	9.8	9.0	0.51	0.53	1.3	1.3	-1.0

B.7 L-G-4 experiment

General bed surface surveys

DEM of the entire bed surface channel is showed on figure B.7.1. Three longitudinal bed surface surveys are presented in B.7.2.

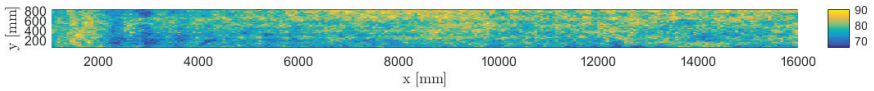

(a) Initial state

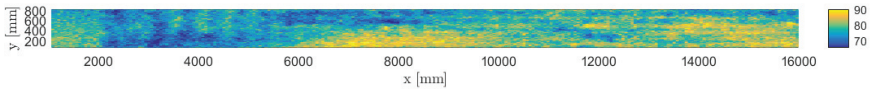

(b) Final state

Figure B.7.1: DEM of the entire bed surface channel before and after the experiment of sediment transport.

Surveys of bed surface patches

In the following, initial and final states mean before and after an experiment of sediment transport, respectively. Initial and final bed surface surveys were performed on 3 zones distributed along the channel: downstream (patch Z1), middle (patch Z2), and upstream (patch Z3). In this experiment, patches Z1, Z2 and Z3 were located at 7 m, 10.9 m, and 14.8 m from the downstream end of the flume, respectively.

Figure B.7.3 represents the resulting digital elevation models (DEM). Figure B.7.4 shows the probability density function of the bed surface elevations for the 3 patches. Two representations of the structure functions D_b associated to the 3 patches are given: one in 3D (Figure B.7.5) and one in contour plot (Figure B.7.6).

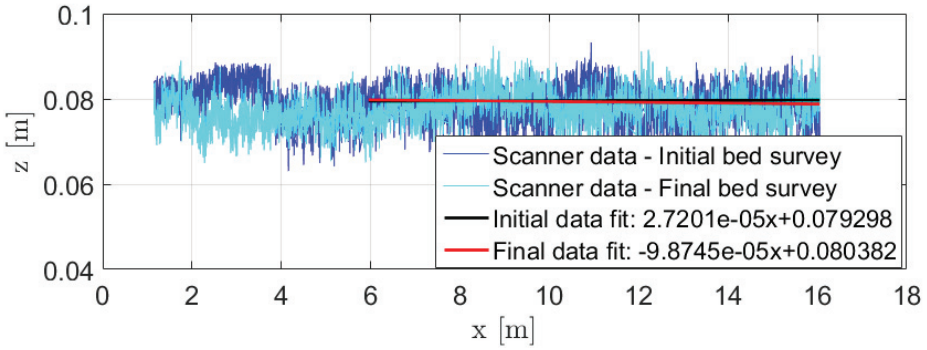

(a) Center line

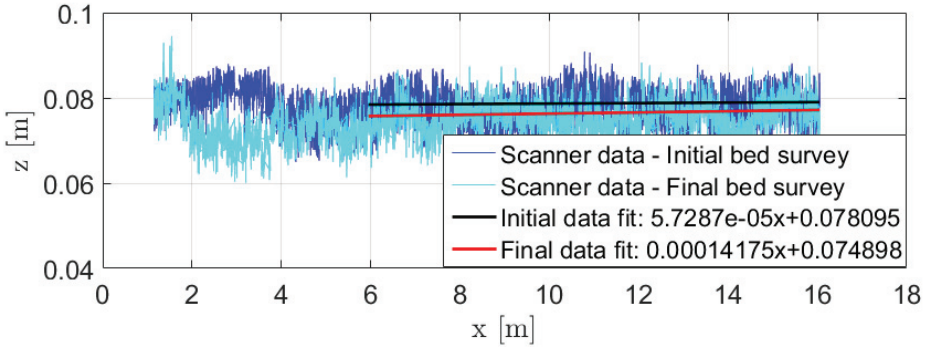

(b) Right side

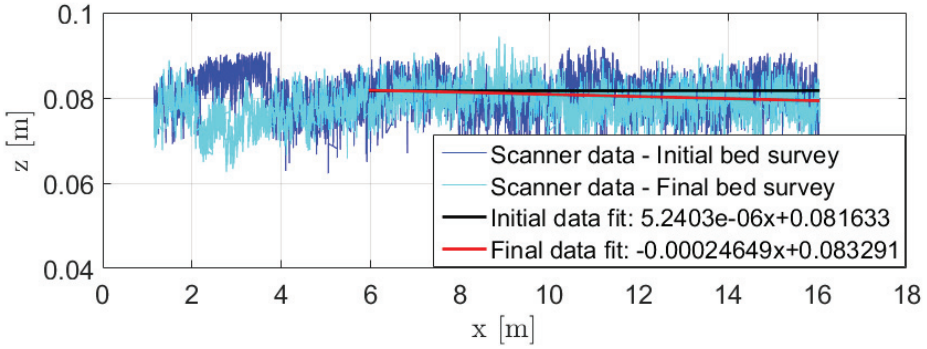

(c) Left side

Figure B.7.2: Longitudinal surveys of the bed surface before and after the experiment of sediment transport.

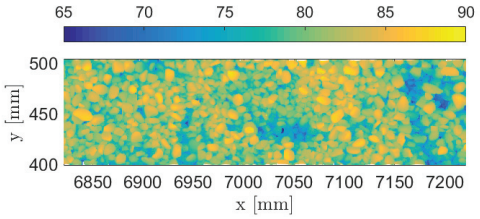

(a) Initial patch Z1

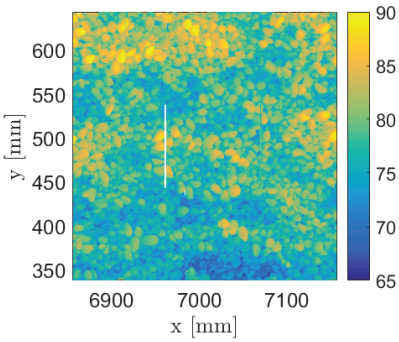

(b) Final patch Z1

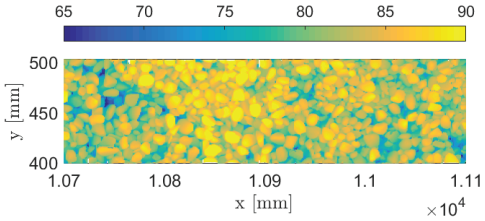

(c) Initial patch Z2

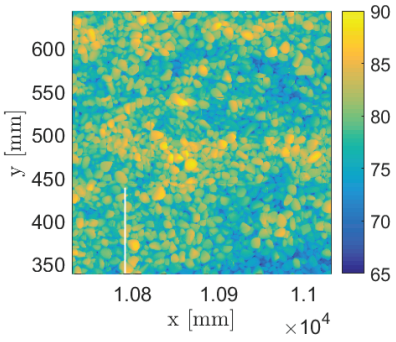

(d) Final patch Z2

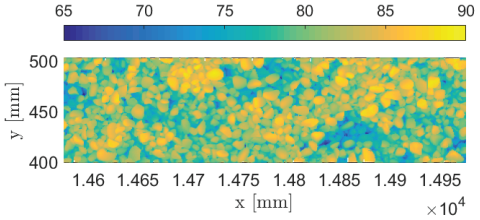

(e) Initial patch Z3

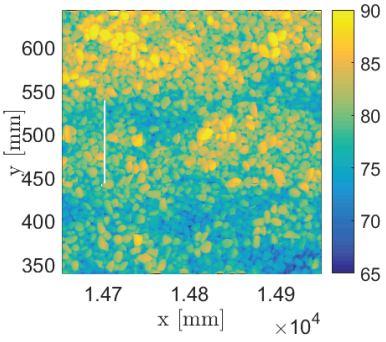

(f) Final patch Z3

Figure B.7.3: DEM of bed surface patches: left and right sides of this figure correspond to initial and final states of the bed surface, respectively.

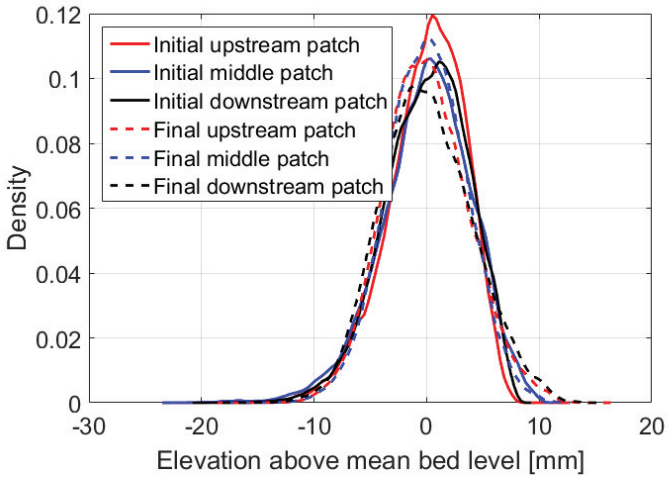

Figure B.7.4: PDF of the bed surface elevations for the 3 patches before and after the sediment transport experiment

Bed surface criteria

Table B.7a recaps all the bed surface criteria calculated for the three patches surveyed (initial and final states). Table B.7b reports the bed surface criteria computed at the scale of the entire bed surface, either by averaging data of the three patches or by using the transverse and longitudinal surveys of the bed.

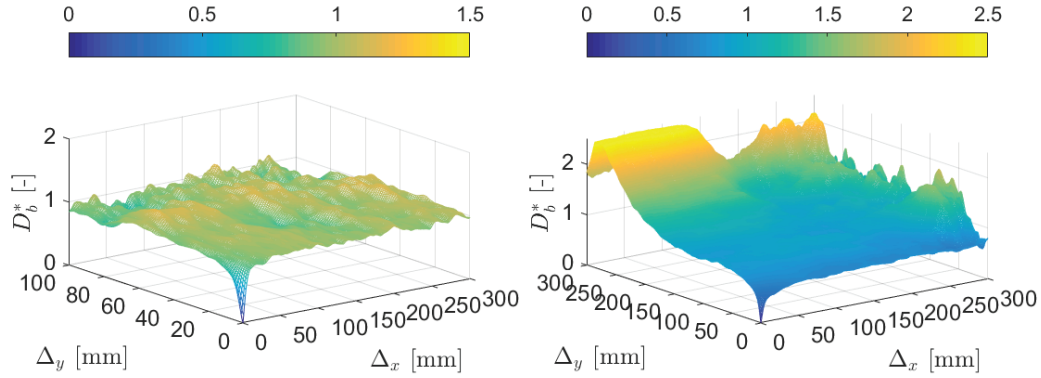

(a) Initial patch Z1

(b) Final patch Z1

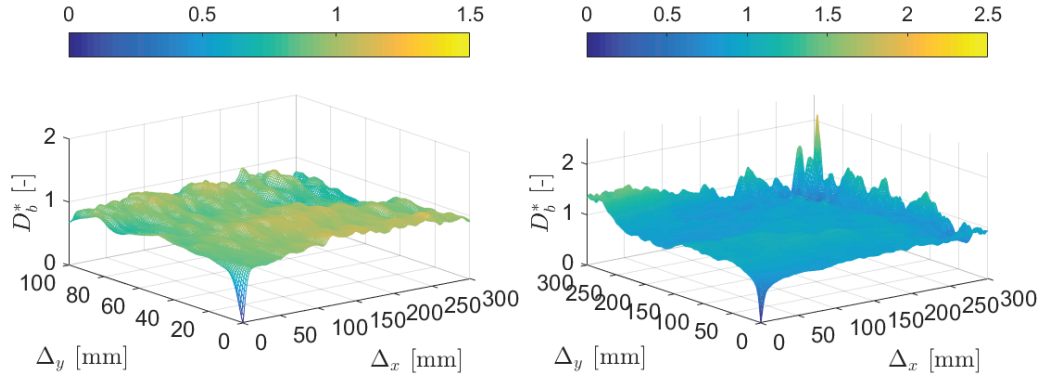

(c) Initial patch Z2

(d) Final patch Z2

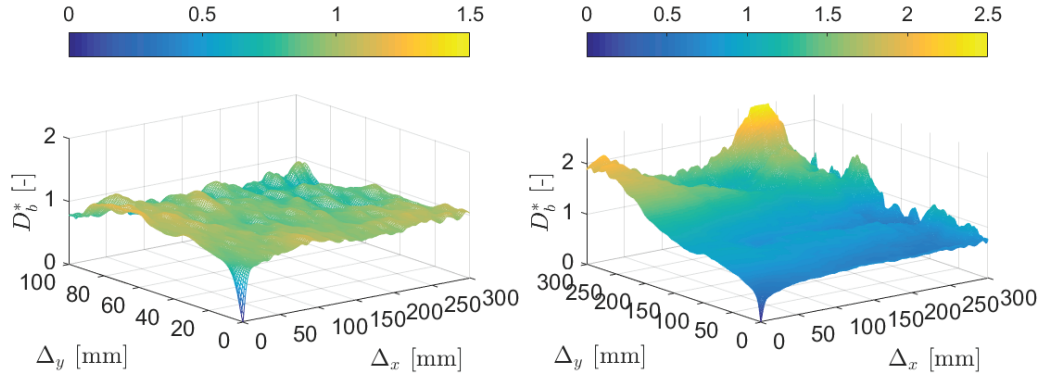

(e) Initial patch Z3

(f) Final patch Z3

Figure B.7.5: D_b^* plots for the three patches: left and right sides of this figure correspond to initial and final states of the bed surface, respectively.

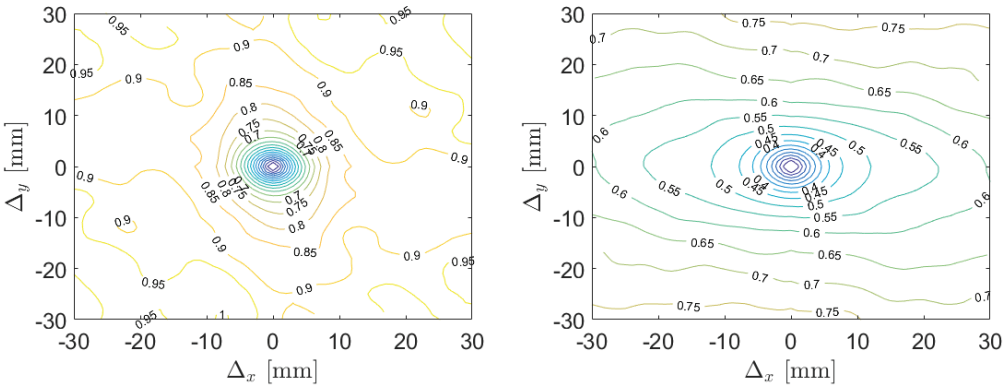

(a) Initial patch Z1

(b) Final patch Z1

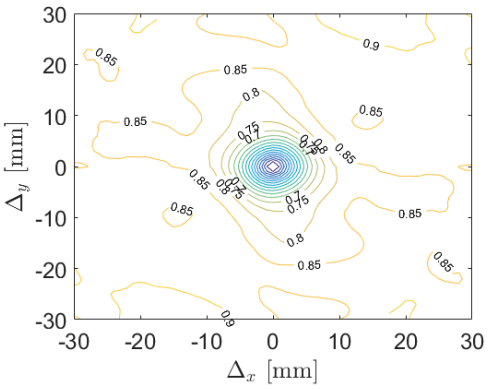

(c) Initial patch Z2

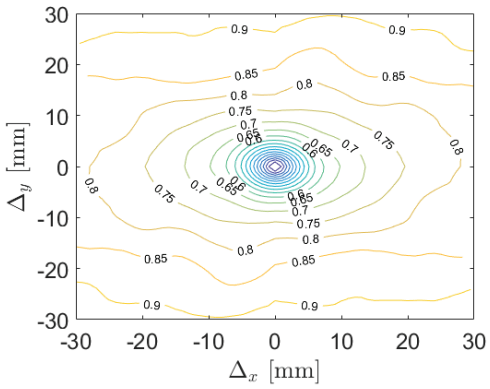

(d) Final patch Z2

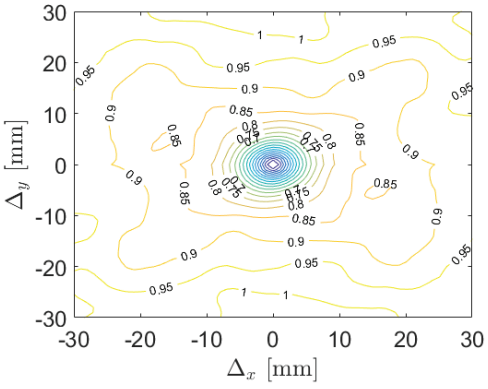

(e) Initial patch Z3

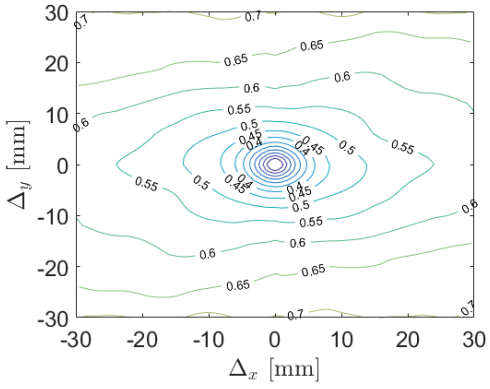

(f) Final patch Z3

Figure B.7.6: Contour plots for the three patches: left and right sides of this figure correspond to initial and final states of the bed surface, respectively.

Table B.7: Bed surface criteria of the 3 patches surveyed before and after the sediment transport experiment.

(a)

		σ_{zg} (mm)	S_k (mm^3)	K_u (mm^4)	Δ_{x0} (mm)	Δ_{y0} (mm)	H_x (-)	H_y (-)	x_0 (mm)	y_0 (mm)	a (mm)	b (mm)	$\frac{x_0}{y_0}$ (-)	$\frac{a}{b}$ (-)	ϕ (°)
Z1	Initial	3.5	-0.58	3.4	6.9	6.6	0.54	0.54	6.1	6.7	5.9	6.7	0.9	1.1	-19.0
	Final	3.8	0.16	3.0	12.0	10.6	0.49	0.52	9.1	6.8	9.0	6.8	1.3	1.3	2.8
Z2	Initial	4.0	-0.47	3.6	7.2	7.1	0.56	0.57	6.6	6.8	6.4	6.7	1.0	1.1	-11.1
	Final	3.5	-0.05	2.9	8.8	7.7	0.51	0.54	9.1	6.9	8.9	6.8	1.3	1.3	7.1
Z3	Initial	3.7	-0.42	3.1	7.1	6.7	0.54	0.55	7.2	6.8	7.4	6.7	1.1	1.1	-34.5
	Final	4.1	0.15	2.9	11.9	10.5	0.51	0.54	9.0	6.9	8.7	6.8	1.3	1.3	4.0

(b)

		σ_{zg} (mm)	S_k (mm^3)	K_u (mm^4)	σ_{zl} (mm)	σ_{zt} (mm)	Δ_{x0} (mm)	Δ_{y0} (mm)	H_x (-)	H_y (-)	$\frac{x_0}{y_0}$ (-)	$\frac{a}{b}$ (-)	ϕ (°)
General bed	Initial	3.7	-0.49	3.4	4.2	3.9	7.1	6.8	0.55	0.56	1.0	1.1	-21.5
	Final	3.8	0.09	2.9	4.1	4.6	10.9	9.6	0.50	0.53	1.3	1.3	4.7

B.8 L-G-5 experiment

General bed surface surveys

DEM of the entire bed surface channel is showed on figure B.8.1. Three longitudinal bed surface surveys are presented in B.8.2.

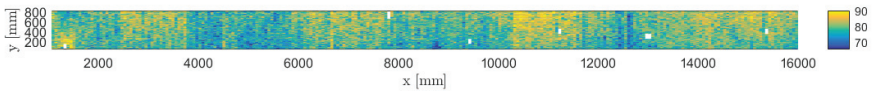

(a) Initial state

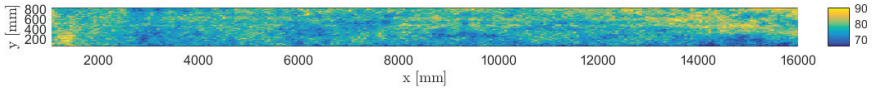

(b) Final state

Figure B.8.1: DEM of the entire bed surface channel before and after the experiment of sediment transport.

Surveys of bed surface patches

In the following, initial and final states mean before and after an experiment of sediment transport, respectively. Initial and final bed surface surveys were performed on 3 zones distributed along the channel: downstream (patch Z1), middle (patch Z2), and upstream (patch Z3). In this experiment, patches Z1, Z2 and Z3 were located at 7 m, 10.9 m, and 14.8 m from the downstream end of the flume, respectively.

Figure B.8.3 represents the resulting digital elevation models (DEM). Figure B.8.4 shows the probability density function of the bed surface elevations for the 3 patches. Two representations of the structure functions D_b associated to the 3 patches are given: one in 3D (Figure B.8.5) and one in contour plot (Figure B.8.6).

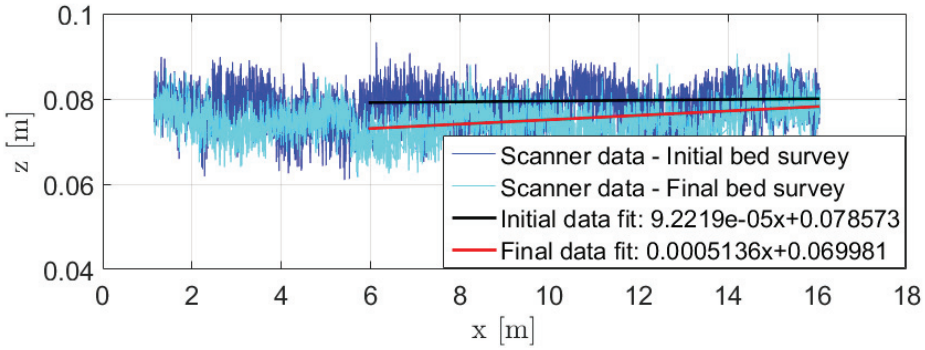

(a) Center line

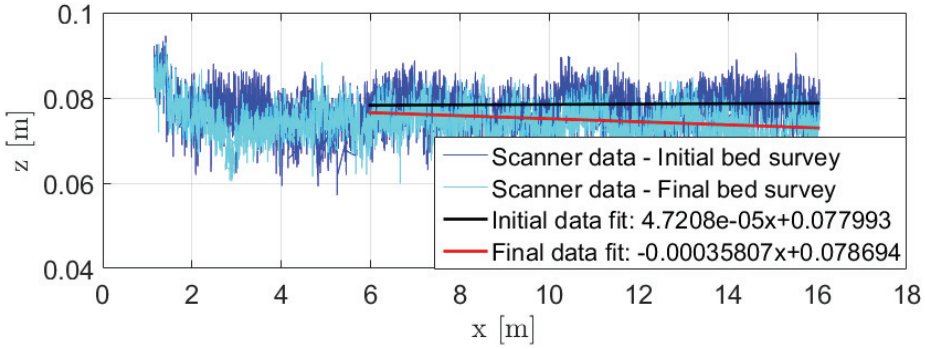

(b) Right side

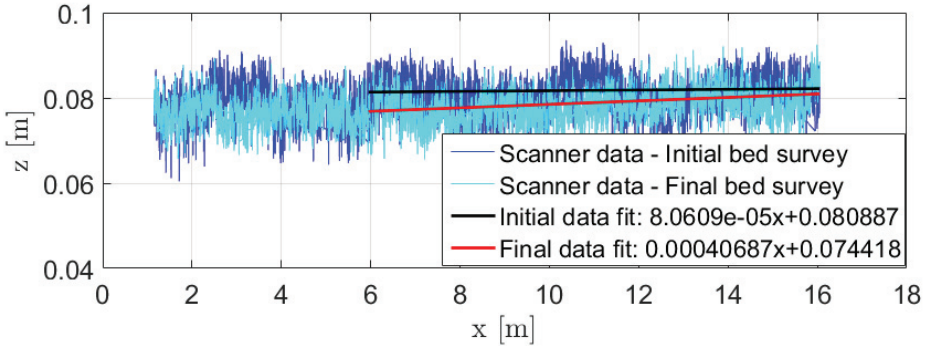

(c) Left side

Figure B.8.2: Longitudinal surveys of the bed surface before and after the experiment of sediment transport.

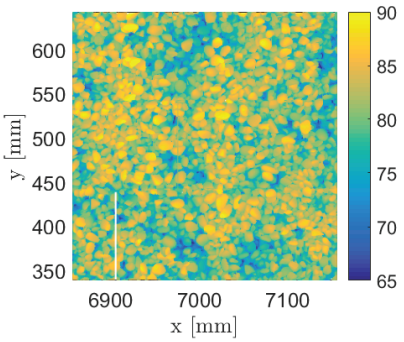

(a) Initial patch Z1

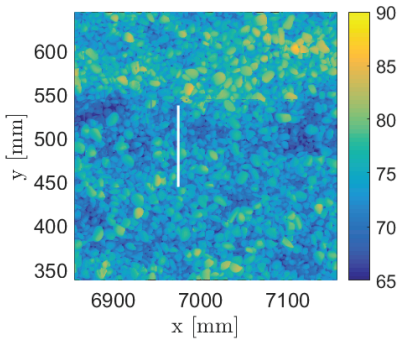

(b) Final patch Z1

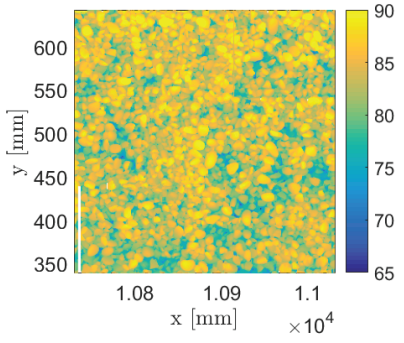

(c) Initial patch Z2

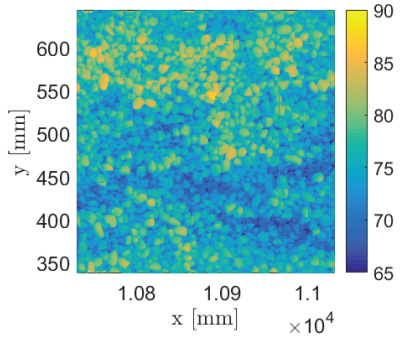

(d) Final patch Z2

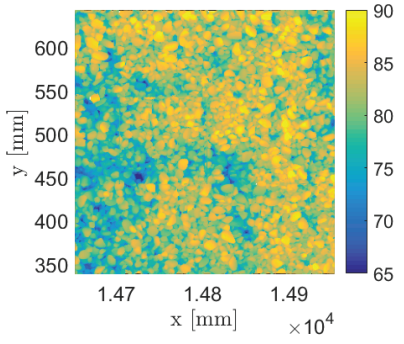

(e) Initial patch Z3

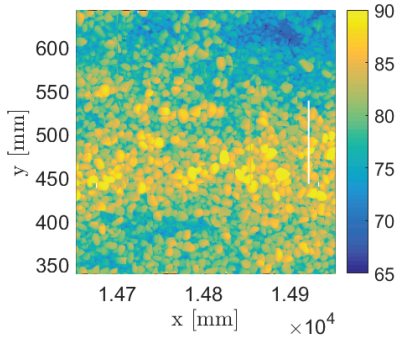

(f) Final patch Z3

Figure B.8.3: DEM of bed surface patches: left and right sides of this figure correspond to initial and final states of the bed surface, respectively.

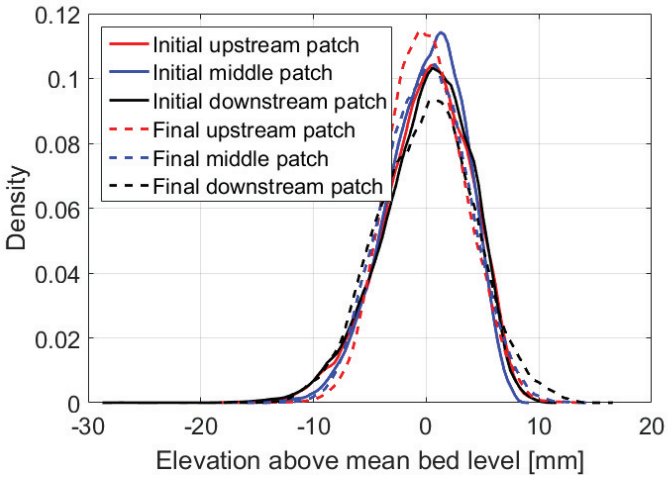

Figure B.8.4: PDF of the bed surface elevations for the 3 patches before and after the sediment transport experiment

Bed surface criteria

Table B.8a recaps all the bed surface criteria calculated for the three patches surveyed (initial and final states). Table B.8b reports the bed surface criteria computed at the scale of the entire bed surface, either by averaging data of the three patches or by using the transverse and longitudinal surveys of the bed.

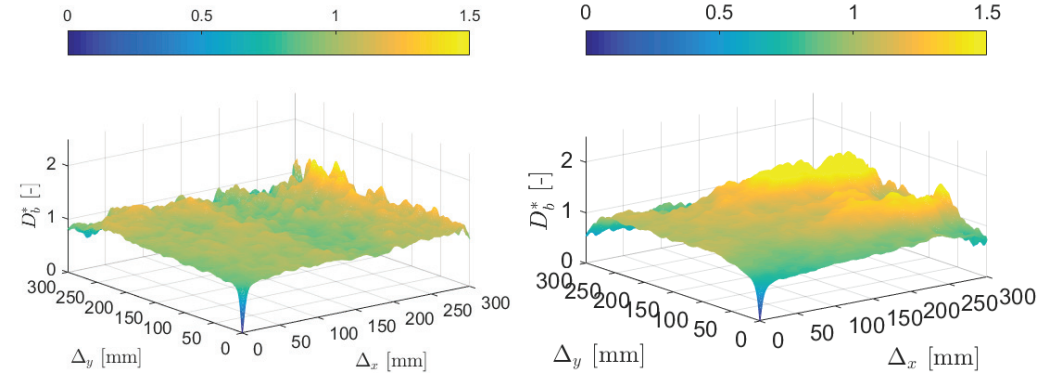

(a) Initial patch Z1 **(b)** Final patch Z1

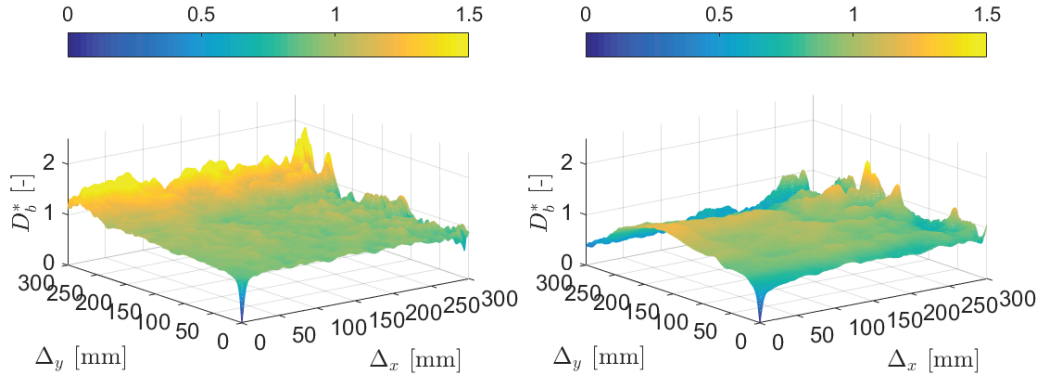

(c) Initial patch Z2 **(d)** Final patch Z2

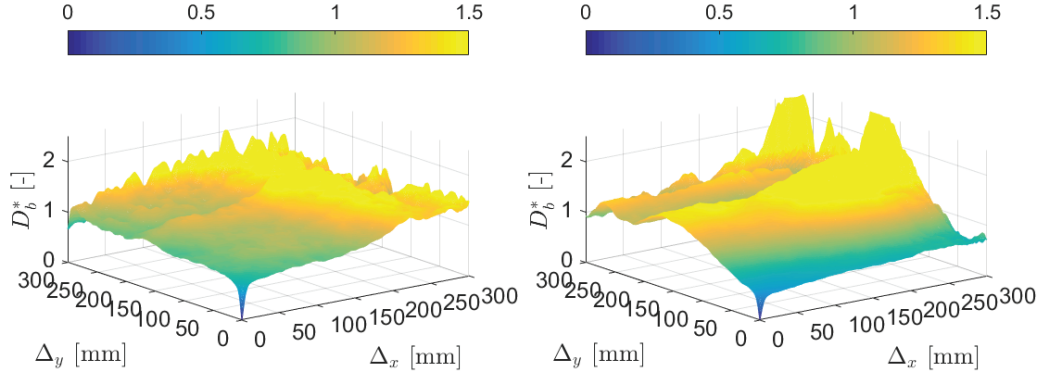

(e) Initial patch Z3 **(f)** Final patch Z3

Figure B.8.5: D_b^* plots for the three patches: left and right sides of this figure correspond to initial and final states of the bed surface, respectively.

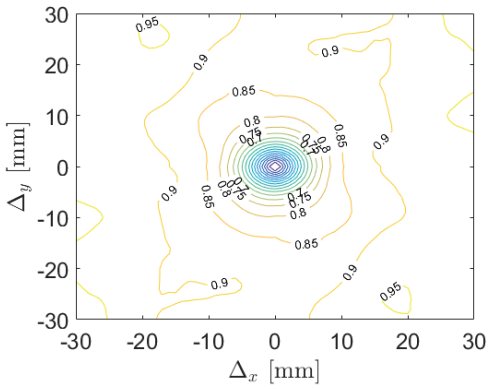

(a) Initial patch Z1

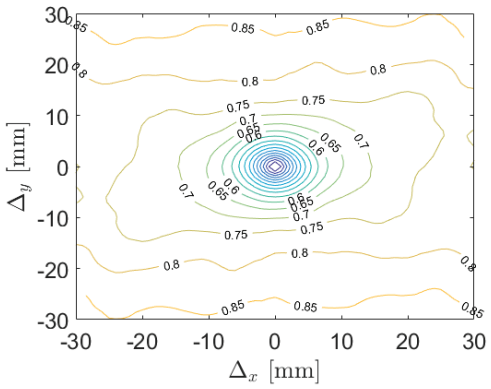

(b) Final patch Z1

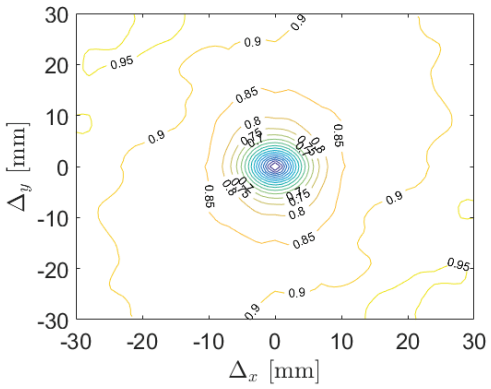

(c) Initial patch Z2

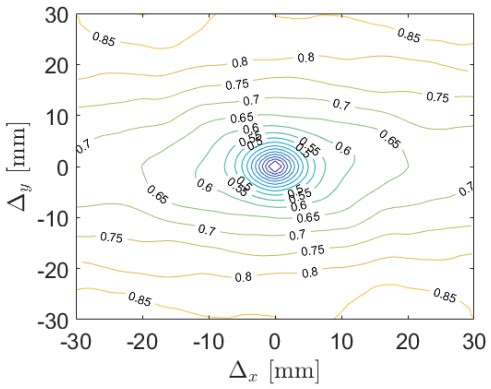

(d) Final patch Z2

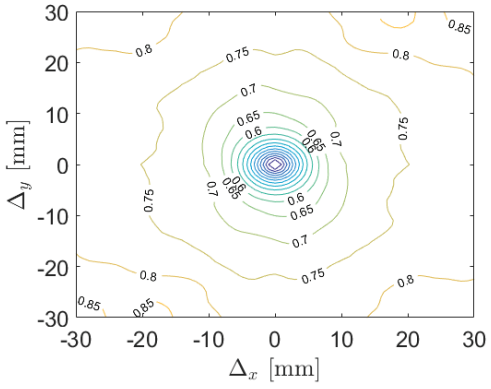

(e) Initial patch Z3

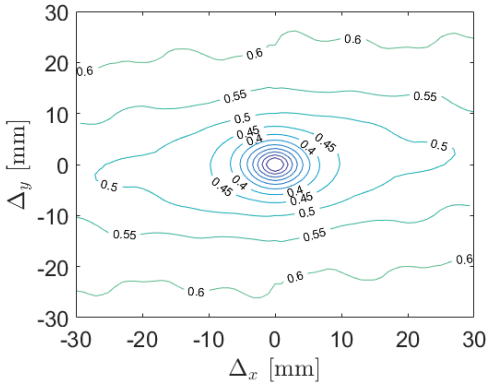

(f) Final patch Z3

Figure B.8.6: Contour plots for the three patches: left and right sides of this figure correspond to initial and final states of the bed surface, respectively.

Table B.8: Bed surface criteria of the 3 patches surveyed before and after the sediment transport experiment.

(a)

		σ_{zg} (mm)	S_k (mm^3)	K_u (mm^4)	Δ_{x0} (mm)	Δ_{y0} (mm)	H_x (-)	H_y (-)	x_0 (mm)	y_0 (mm)	a (mm)	b (mm)	$\frac{x_0}{y_0}$ (-)	$\frac{a}{b}$ (-)	ϕ (°)
Z1	Initial	3.9	-0.44	3.1	7.1	6.8	0.55	0.56	6.5	6.7	6.4	6.8	1.0	1.0	10.0
	Final	3.4	0.07	2.9	9.3	8.5	0.49	0.52	7.7	6.8	7.5	6.7	1.1	1.1	-4.9
Z2	Initial	3.5	-0.43	3.0	6.6	6.5	0.54	0.54	6.3	6.9	6.2	6.9	0.9	1.1	-11.4
	Final	3.7	0.00	2.7	9.9	9.1	0.50	0.53	8.0	6.9	8.0	6.8	1.2	1.2	8.8
Z3	Initial	4.0	-0.56	3.4	8.3	8.2	0.53	0.53	6.2	6.7	6.2	6.8	0.9	1.1	-13.8
	Final	4.3	-0.03	2.8	12.8	11.2	0.51	0.54	8.1	6.8	8.1	6.7	1.2	1.2	-0.5

(b)

		σ_{zg} (mm)	S_k (mm^3)	K_u (mm^4)	σ_{zl} (mm)	σ_{zt} (mm)	Δ_{x0} (mm)	Δ_{y0} (mm)	H_x (-)	H_y (-)	$\frac{x_0}{y_0}$ (-)	$\frac{a}{b}$ (-)	ϕ (°)
General bed	Initial	3.8	-0.48	3.2	4.4	4.0	7.3	7.2	0.54	0.54	0.9	1.1	-5.0
	Final	3.8	0.01	2.8	3.6	4.1	10.7	9.6	0.50	0.53	1.2	1.2	1.1

B.9 H-G/Ms-5 experiment

General bed surface surveys

DEM of the entire bed surface channel is showed on figure B.9.1. Three longitudinal bed surface surveys are presented in B.9.2.

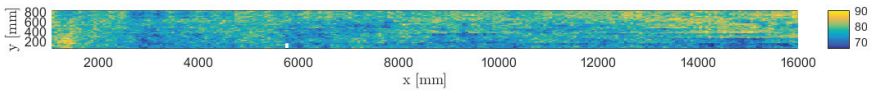

(a) Initial state

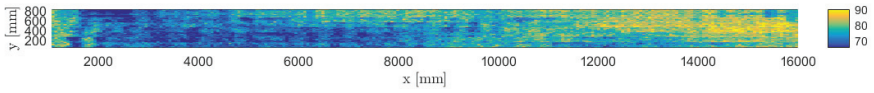

(b) Final state

Figure B.9.1: DEM of the entire bed surface channel before and after the experiment of sediment transport.

Surveys of bed surface patches

In the following, initial and final states mean before and after an experiment of sediment transport, respectively. Initial and final bed surface surveys were performed on 3 zones distributed along the channel: downstream (patch Z1), middle (patch Z2), and upstream (patch Z3). In this experiment, patches Z1, Z2 and Z3 were located at 7 m, 10.9 m, and 14.8 m from the downstream end of the flume, respectively.

Figure B.9.3 represents the resulting digital elevation models (DEM). Figure B.9.4 shows the probability density function of the bed surface elevations for the 3 patches. Two representations of the structure functions D_b associated to the 3 patches are given: one in 3D (Figure B.9.5) and one in contour plot (Figure B.9.6).

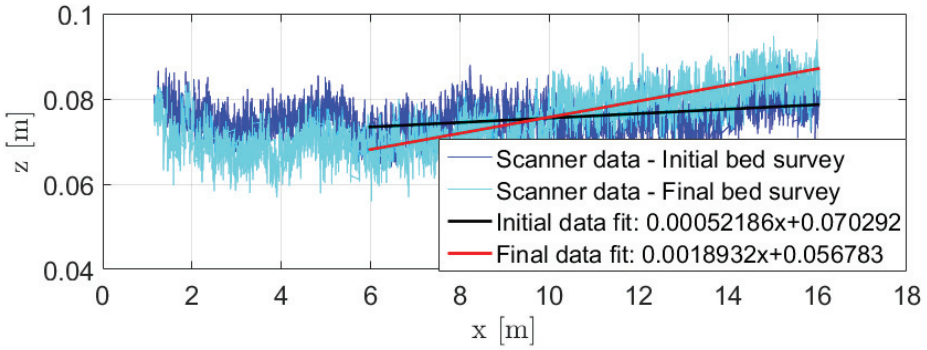

(a) Center line

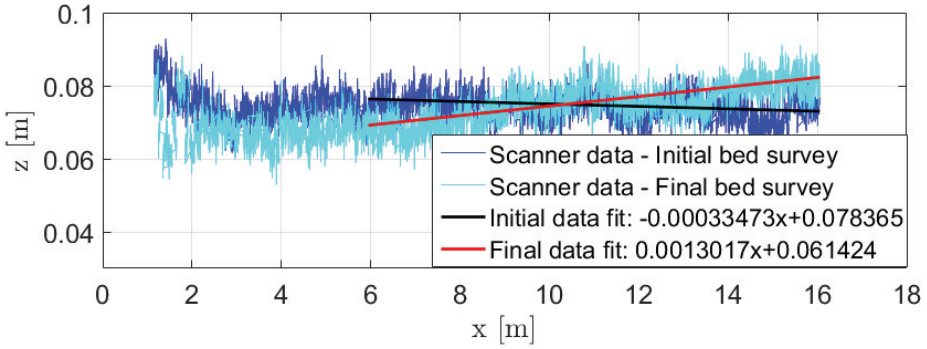

(b) Right side

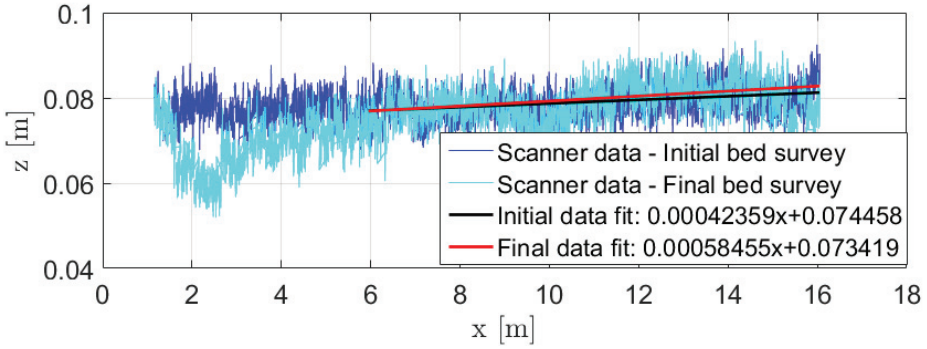

(c) Left side

Figure B.9.2: Longitudinal surveys of the bed surface before and after the experiment of sediment transport.

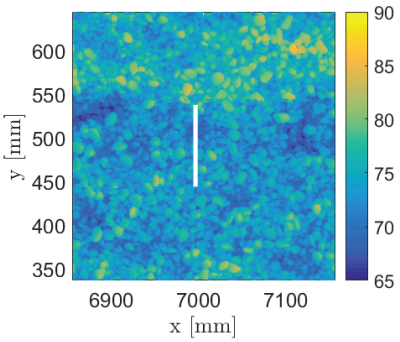

(a) Initial patch Z1

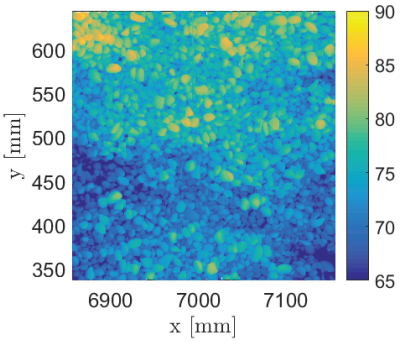

(b) Final patch Z1

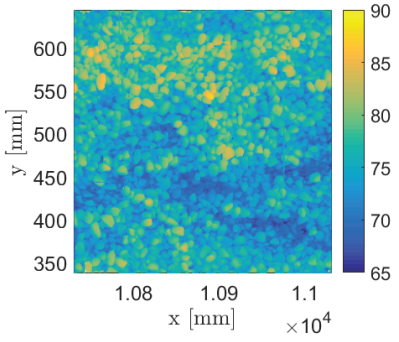

(c) Initial patch Z2

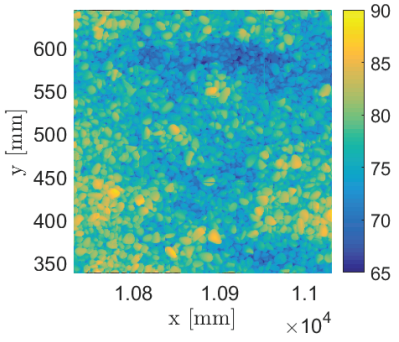

(d) Final patch Z2

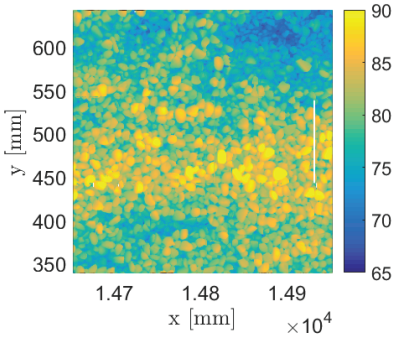

(e) Initial patch Z3

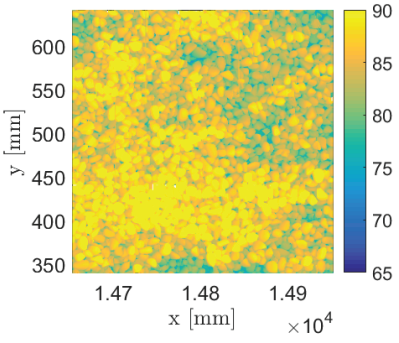

(f) Final patch Z3

Figure B.9.3: DEM of bed surface patches: left and right sides of this figure correspond to initial and final states of the bed surface, respectively.

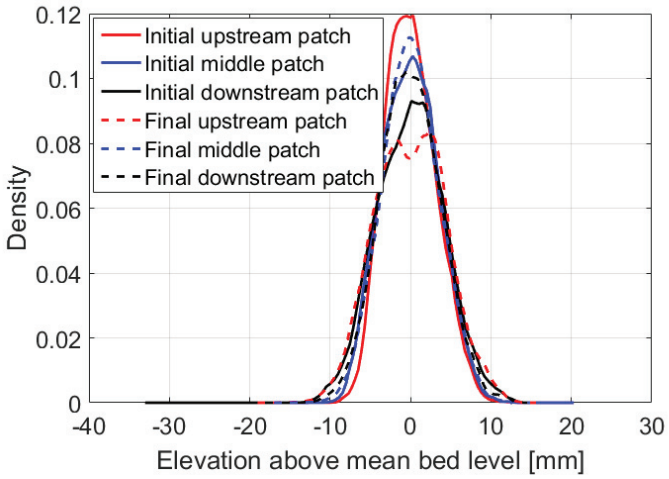

Figure B.9.4: PDF of the bed surface elevations for the 3 patches before and after the sediment transport experiment

Bed surface criteria

Table B.9a recaps all the bed surface criteria calculated for the three patches surveyed (initial and final states). Table B.9b reports the bed surface criteria computed at the scale of the entire bed surface, either by averaging data of the three patches or by using the transverse and longitudinal surveys of the bed.

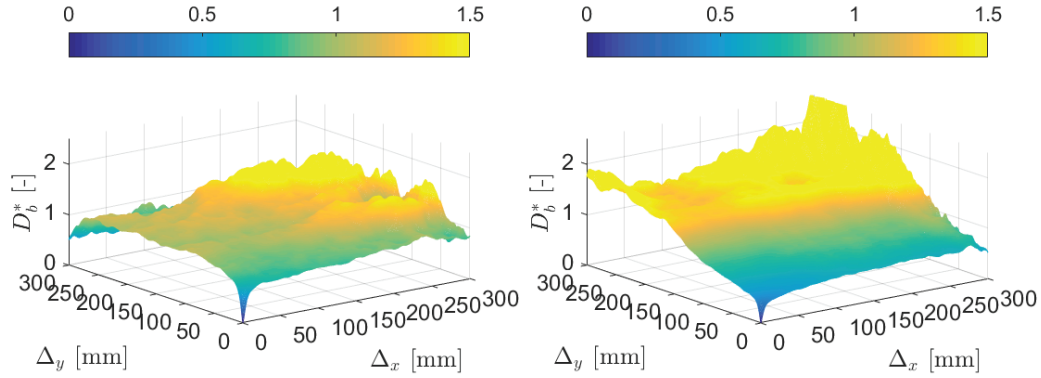

(a) Initial patch Z1

(b) Final patch Z1

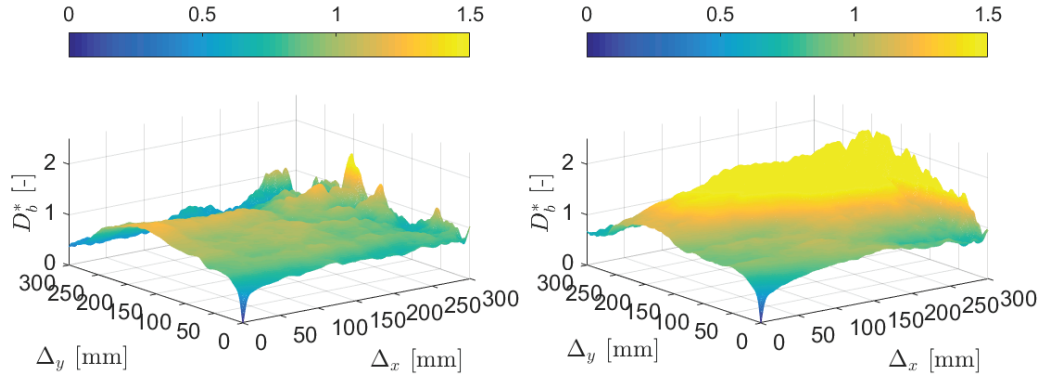

(c) Initial patch Z2

(d) Final patch Z2

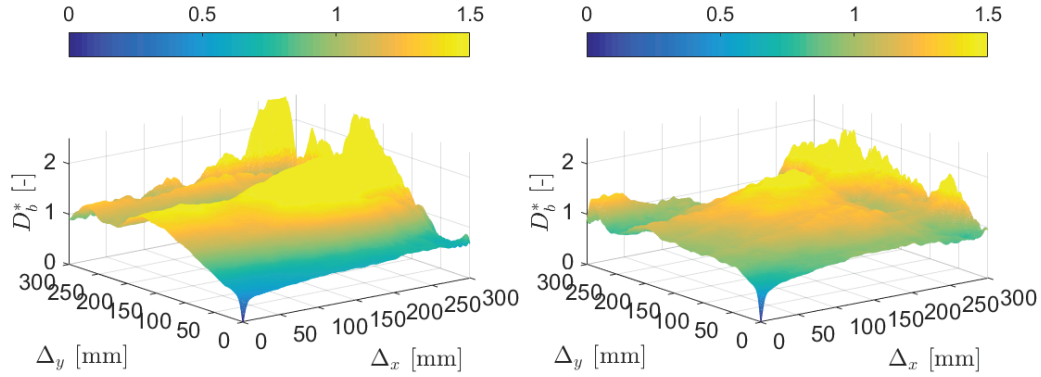

(e) Initial patch Z3

(f) Final patch Z3

Figure B.9.5: D_b^* plots for the three patches: left and right sides of this figure correspond to initial and final states of the bed surface, respectively.

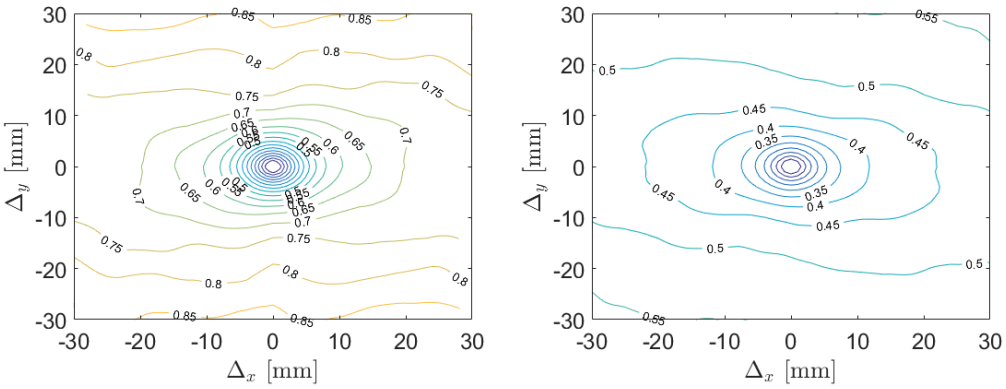

(a) Initial patch Z1

(b) Final patch Z1

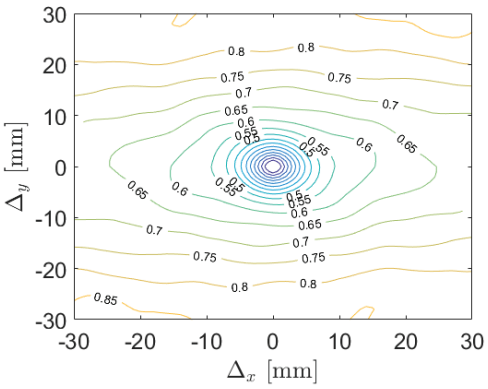

(c) Initial patch Z2

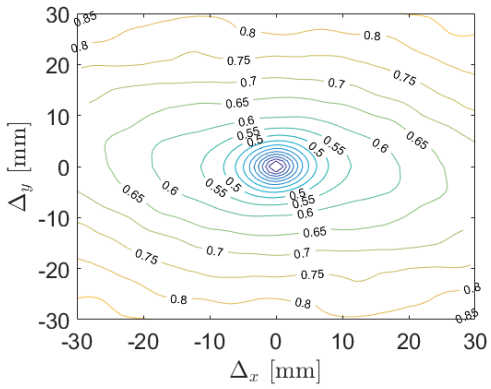

(d) Final patch Z2

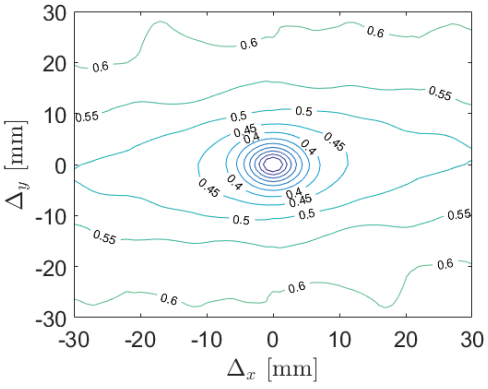

(e) Initial patch Z3

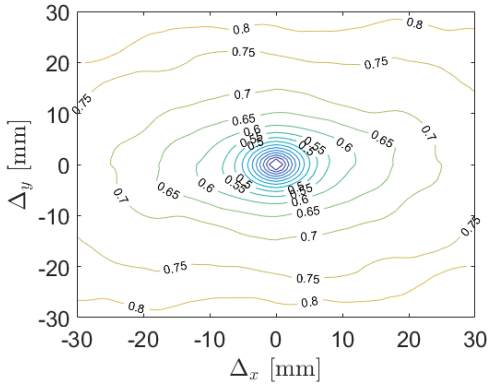

(f) Final patch Z3

Figure B.9.6: Contour plots for the three patches: left and right sides of this figure correspond to initial and final states of the bed surface, respectively.

Table B.9: Bed surface criteria of the 3 patches surveyed before and after the sediment transport experiment.

(a)

		σ_{zg} (mm)	S_k (mm^3)	K_u (mm^4)	Δ_{x0} (mm)	Δ_{y0} (mm)	H_x (-)	H_y (-)	x_0 (mm)	y_0 (mm)	a (mm)	b (mm)	$\frac{x_0}{y_0}$ (-)	$\frac{a}{b}$ (-)	ϕ (°)
Z1	Initial	3.2	0.27	2.8	9.5	8.6	0.56	0.58	8.4	6.9	8.3	6.8	1.2	1.2	-4.5
	Final	4.4	0.01	2.7	15.4	12.9	0.50	0.53	8.8	6.7	8.8	6.6	1.3	1.3	5.6
Z2	Initial	3.5	0.11	2.6	8.8	9.2	0.56	0.58	7.8	6.7	7.8	6.6	1.2	1.2	14.2
	Final	3.5	0.04	2.9	11.0	9.3	0.49	0.52	9.0	6.6	8.8	6.6	1.4	1.3	-4.4
Z3	Initial	4.2	0.01	2.8	12.1	11.3	0.55	0.56	8.2	6.9	8.1	6.8	1.2	1.2	-2.3
	Final	3.8	0.08	3.0	9.8	8.5	0.50	0.54	9.2	6.8	9.2	6.6	1.4	1.4	-5.9

(b)

		σ_{zg} (mm)	S_k (mm^3)	K_u (mm^4)	σ_{zl} (mm)	σ_{zt} (mm)	Δ_{x0} (mm)	Δ_{y0} (mm)	H_x (-)	H_y (-)	$\frac{x_0}{y_0}$ (-)	$\frac{a}{b}$ (-)	ϕ (°)
General bed	Initial	3.6	0.13	2.8	4.9	4.6	10.1	9.7	0.55	0.57	1.2	1.2	2.5
	Final	3.9	0.05	2.8	6.6	4.1	12.0	10.2	0.50	0.53	1.3	1.4	-1.6

B.10 L-G-6 experiment

General bed surface surveys

DEM of the entire bed surface channel is showed on figure B.10.1 where data are missing due to a dysfunction of the laser-scanner device. Three longitudinal bed surface surveys are presented in B.10.2.

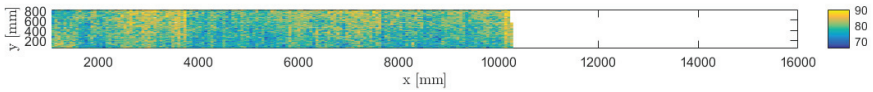

(a) Initial state

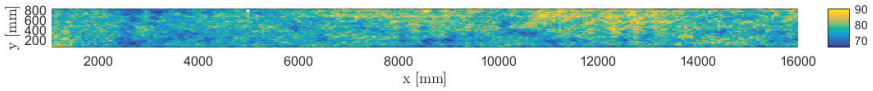

(b) Final state

Figure B.10.1: DEM of the entire bed surface channel before and after the experiment of sediment transport.

Surveys of bed surface patches

In the following, initial and final states mean before and after an experiment of sediment transport, respectively. Initial and final bed surface surveys were performed on 3 zones distributed along the channel: downstream (patch Z1), middle (patch Z2), and upstream (patch Z3). In this experiment, patches Z1, Z2 and Z3 were located at 7 m, 10.9 m, and 14.8 m from the downstream end of the flume, respectively.

Figure B.10.3 represents the resulting digital elevation models (DEM). Figure B.10.4 shows the probability density function of the bed surface elevations for the 3 patches. Two representations of the structure functions D_b associated to the 3 patches are given: one in 3D (Figure B.10.5) and one in contour plot (Figure B.10.6).

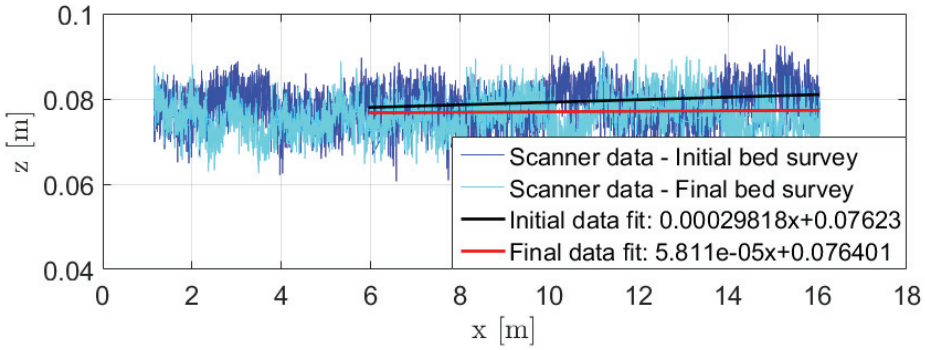

(a) Center line

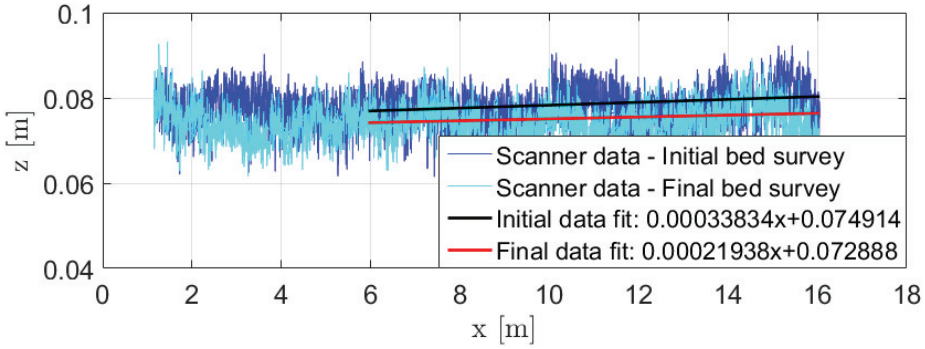

(b) Right side

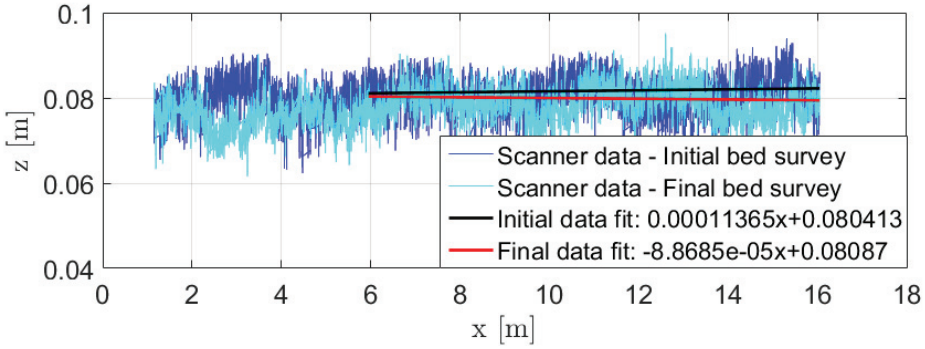

(c) Left side

Figure B.10.2: Longitudinal surveys of the bed surface before and after the experiment of sediment transport.

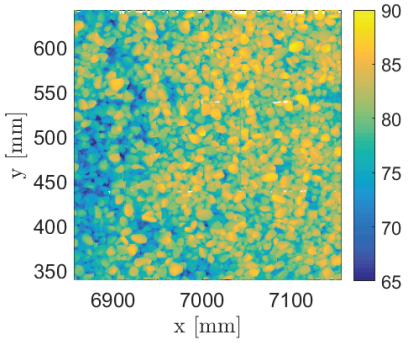

(a) Initial patch Z1

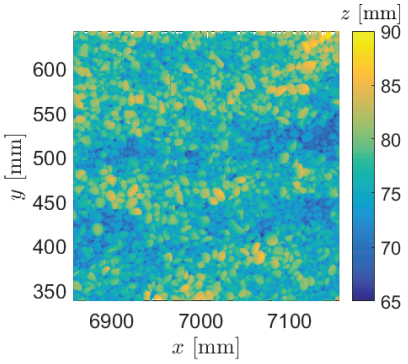

(b) Final patch Z1

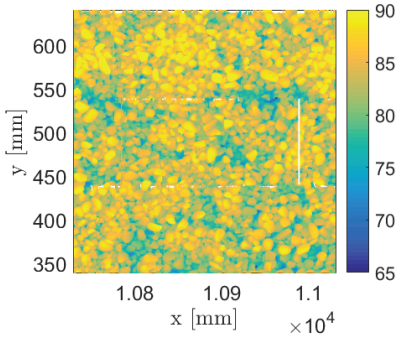

(c) Initial patch Z2

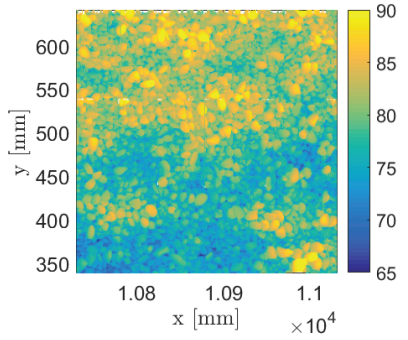

(d) Final patch Z2

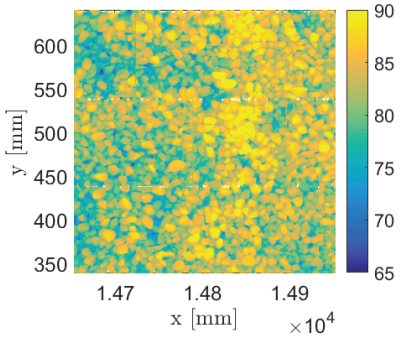

(e) Initial patch Z3

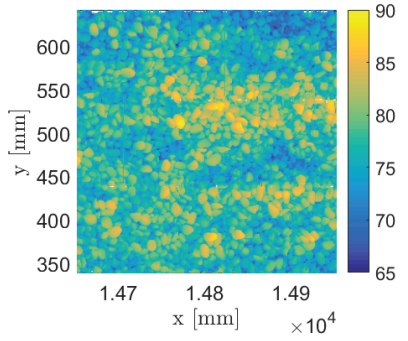

(f) Final patch Z3

Figure B.10.3: DEM of bed surface patches: left and right sides of this figure correspond to initial and final states of the bed surface, respectively.

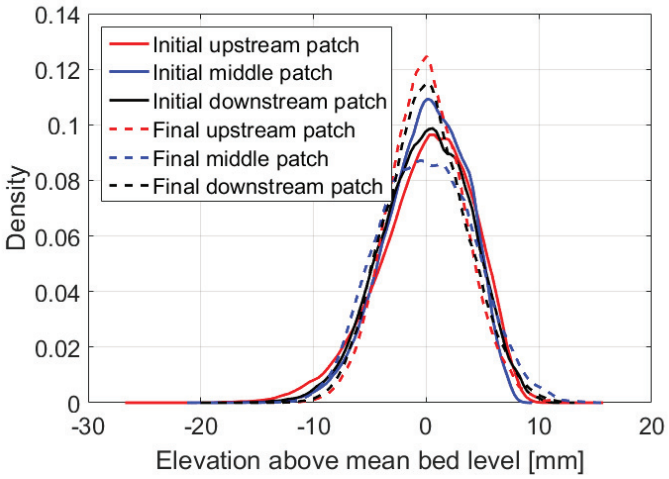

Figure B.10.4: PDF of the bed surface elevations for the 3 patches before and after the sediment transport experiment

Bed surface criteria

Table B.10a recaps all the bed surface criteria calculated for the three patches surveyed (initial and final states). Table B.10b reports the bed surface criteria computed at the scale of the entire bed surface, either by averaging data of the three patches or by using the transverse and longitudinal surveys of the bed.

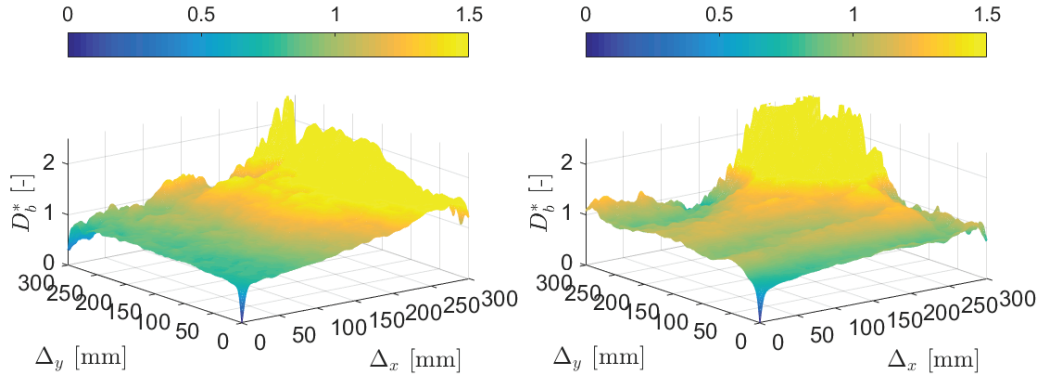

(a) Initial patch Z1

(b) Final patch Z1

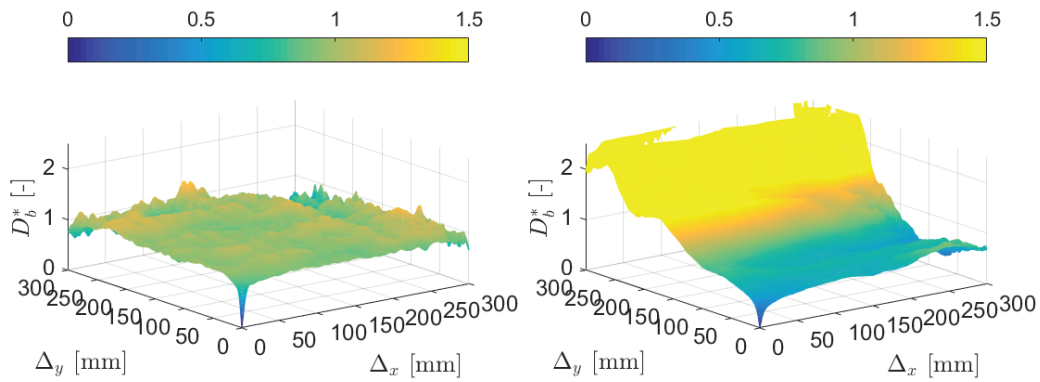

(c) Initial patch Z2

(d) Final patch Z2

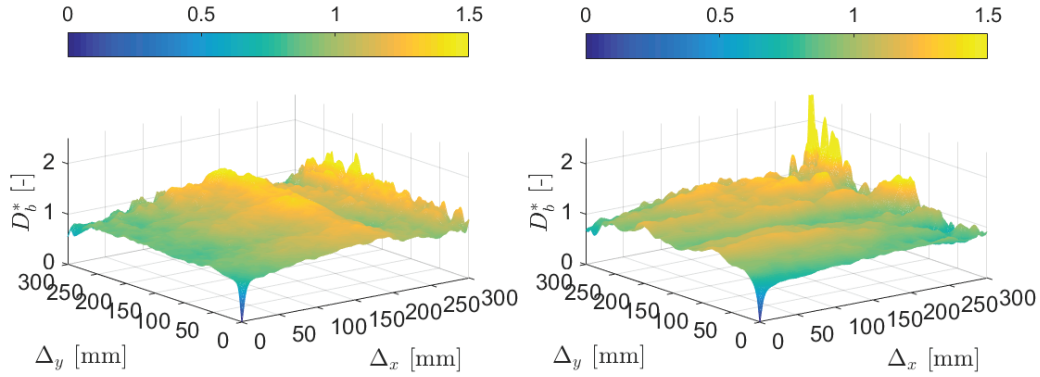

(e) Initial patch Z3

(f) Final patch Z3

Figure B.10.5: D_b^* plots for the three patches: left and right sides of this figure correspond to initial and final states of the bed surface, respectively.

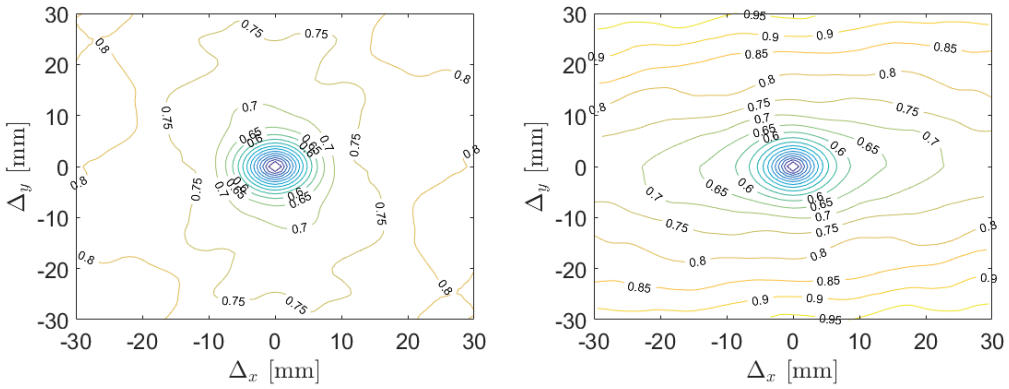

(a) Initial patch Z1

(b) Final patch Z1

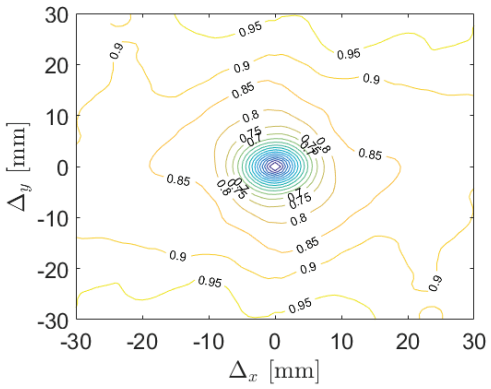

(c) Initial patch Z2

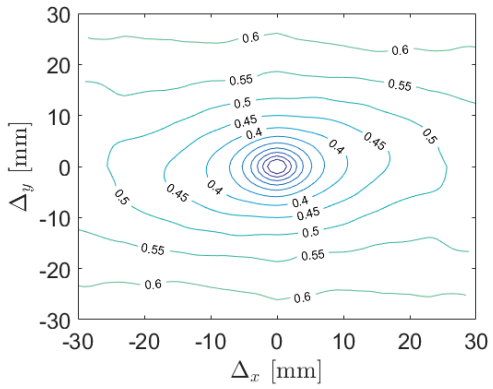

(d) Final patch Z2

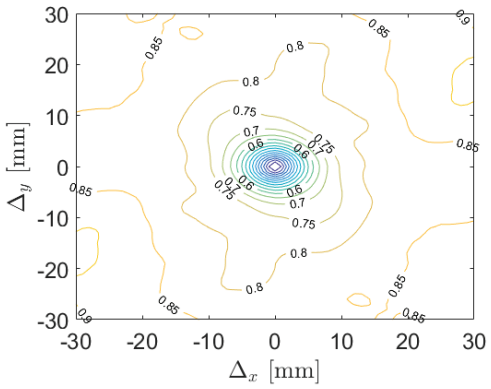

(e) Initial patch Z3

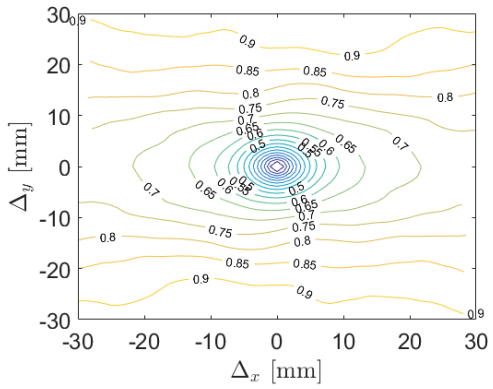

(f) Final patch Z3

Figure B.10.6: Contour plots for the three patches: left and right sides of this figure correspond to initial and final states of the bed surface, respectively.

Table B.10: Bed surface criteria of the 3 patches surveyed before and after the sediment transport experiment.

(a)

		σ_{zg} (mm)	S_k (mm^3)	K_u (mm^4)	Δ_{x0} (mm)	Δ_{y0} (mm)	H_x (-)	H_y (-)	x_0 (mm)	y_0 (mm)	a (mm)	b (mm)	$\frac{x_0}{y_0}$ (-)	$\frac{a}{b}$ (-)	ϕ (°)
Z1	Initial	4.2	-0.56	3.3	8.5	7.7	0.53	0.55	6.8	6.8	6.8	6.7	1.0	1.0	13.0
	Final	3.3	0.06	3.0	9.2	8.1	0.49	0.52	8.7	6.7	8.4	6.6	1.3	1.3	-2.0
Z2	Initial	3.6	-0.44	3.0	7.0	6.6	0.55	0.55	6.7	6.9	6.7	6.8	1.0	1.0	-11.2
	Final	4.2	0.08	2.7	15.6	13.2	0.49	0.52	8.9	6.9	8.9	6.7	1.3	1.3	-8.2
Z3	Initial	3.9	-0.24	2.9	7.7	7.1	0.54	0.56	7.4	6.8	7.6	6.6	1.1	1.2	28.4
	Final	3.6	0.09	2.9	9.7	8.6	0.51	0.53	8.5	6.8	8.3	6.7	1.2	1.2	-5.8

(b)

		σ_{zg} (mm)	S_k (mm^3)	K_u (mm^4)	σ_{zl} (mm)	σ_{zt} (mm)	Δ_{x0} (mm)	Δ_{y0} (mm)	H_x (-)	H_y (-)	$\frac{x_0}{y_0}$ (-)	$\frac{a}{b}$ (-)	ϕ (°)
General bed	Initial	3.9	-0.41	3.1	4.3	3.8	7.7	7.1	0.54	0.55	1.0	1.1	10.1
	Final	3.7	0.08	2.9	4.1	3.1	11.5	10.0	0.49	0.52	1.3	1.3	-5.3

B.11 P-G/Ms-6 experiment

General bed surface surveys

DEM of the entire bed surface channel is showed on figure B.11.1. Three longitudinal bed surface surveys are presented in B.11.2.

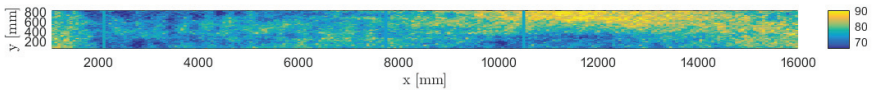

(a) Initial state

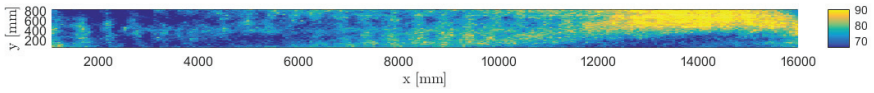

(b) Final state

Figure B.11.1: DEM of the entire bed surface channel before and after the experiment of sediment transport.

Surveys of bed surface patches

In the following, initial and final states mean before and after an experiment of sediment transport, respectively. Initial and final bed surface surveys were performed on 3 zones distributed along the channel: downstream (patch Z1), middle (patch Z2), and upstream (patch Z3). In this experiment, patches Z1, Z2 and Z3 were located at 7 m, 10.9 m, and 14.8 m from the downstream end of the flume, respectively.

Figure B.11.3 represents the resulting digital elevation models (DEM). Figure B.11.4 shows the probability density function of the bed surface elevations for the 3 patches. Two representations of the structure functions D_b associated to the 3 patches are given: one in 3D (Figure B.11.5) and one in contour plot (Figure B.11.6).

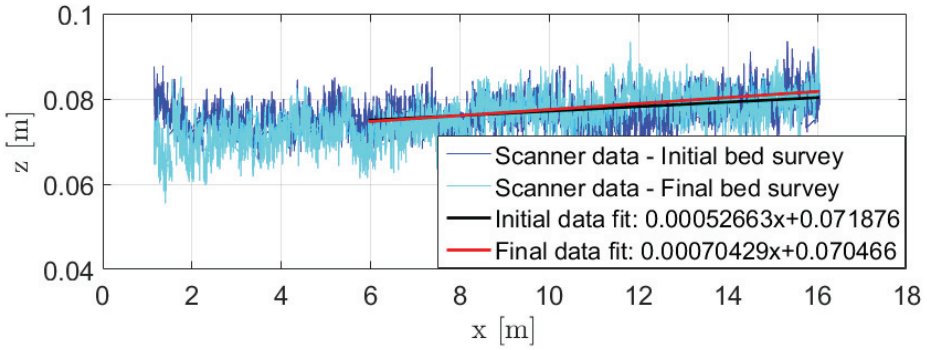

(a) Center line

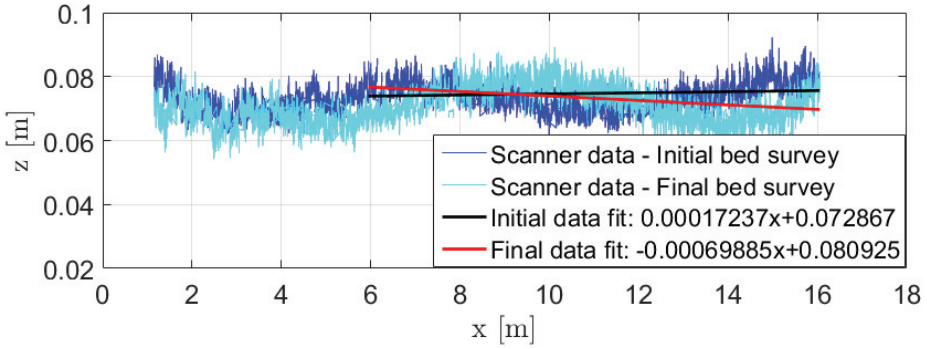

(b) Right side

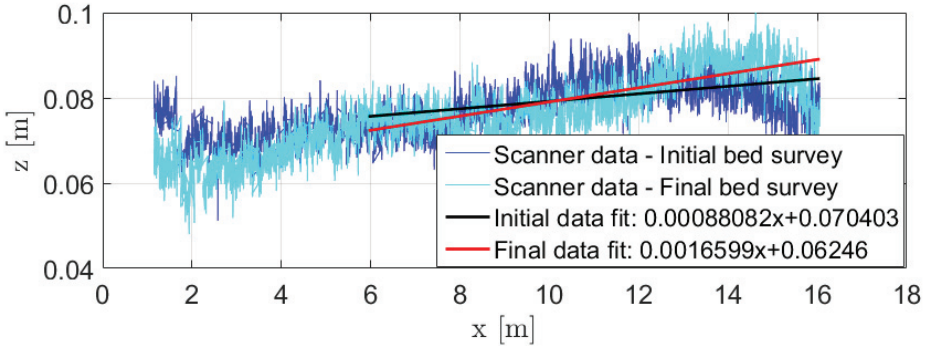

(c) Left side

Figure B.11.2: Longitudinal surveys of the bed surface before and after the experiment of sediment transport.

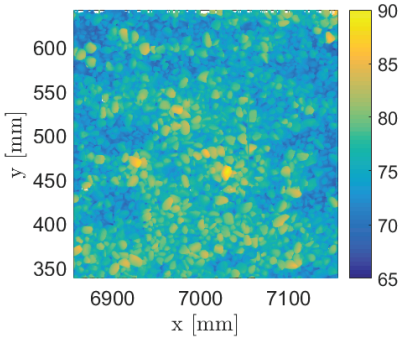

(a) Initial patch Z1

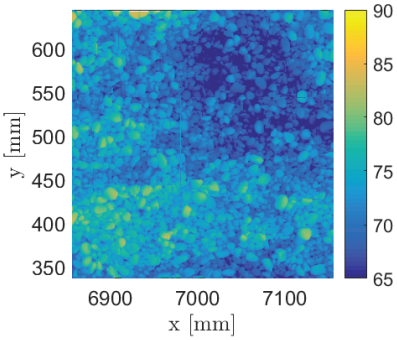

(b) Final patch Z1

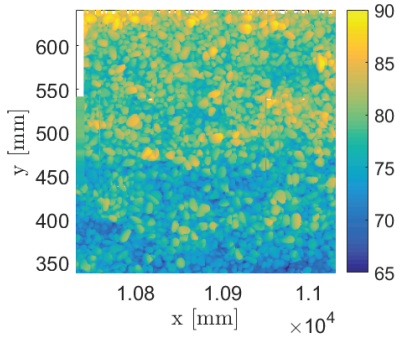

(c) Initial patch Z2

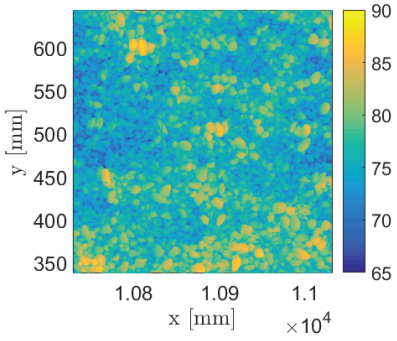

(d) Final patch Z2

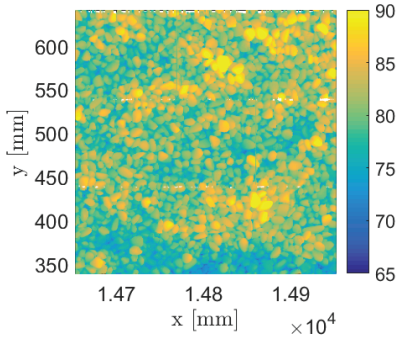

(e) Initial patch Z3

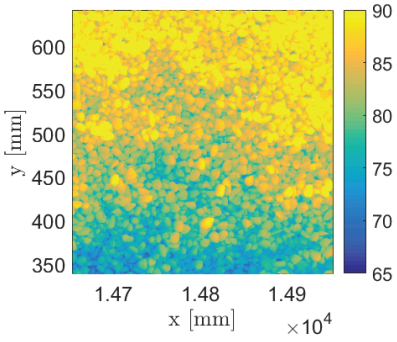

(f) Final patch Z3

Figure B.11.3: DEM of bed surface patches: left and right sides of this figure correspond to initial and final states of the bed surface, respectively.

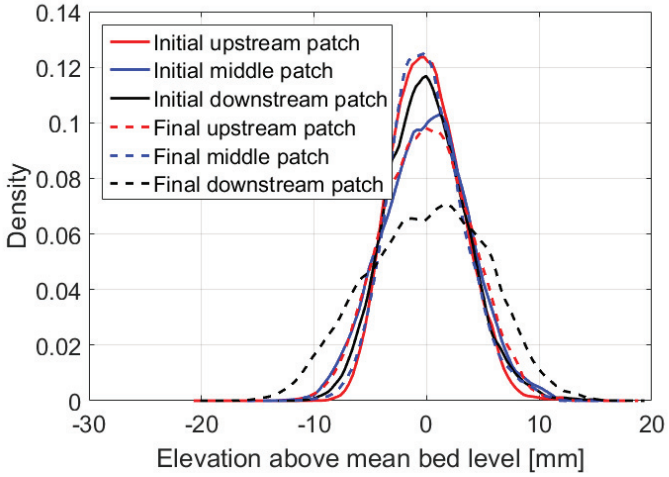

Figure B.11.4: PDF of the bed surface elevations for the 3 patches before and after the sediment transport experiment

Bed surface criteria

Table B.11a recaps all the bed surface criteria calculated for the three patches surveyed (initial and final states). Table B.11b reports the bed surface criteria computed at the scale of the entire bed surface, either by averaging data of the three patches or by using the transverse and longitudinal surveys of the bed.

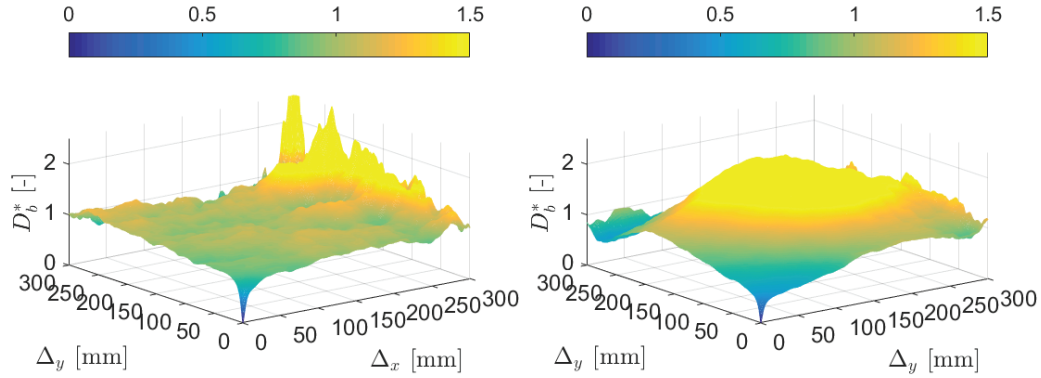

(a) Initial patch Z1

(b) Final patch Z1

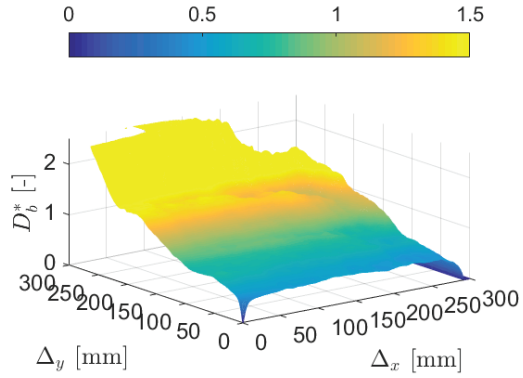

(c) Initial patch Z2

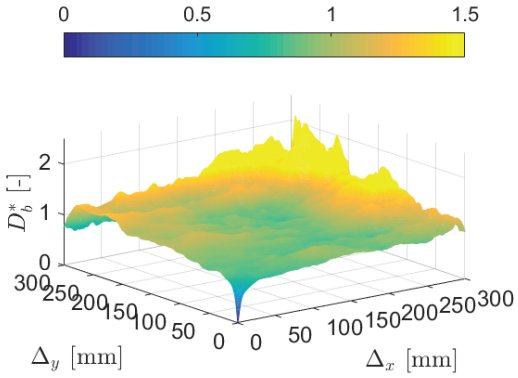

(d) Final patch Z2

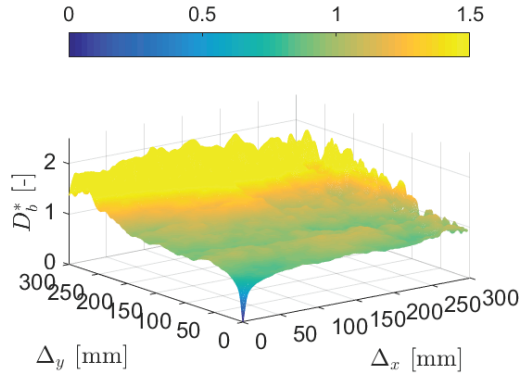

(e) Initial patch Z3

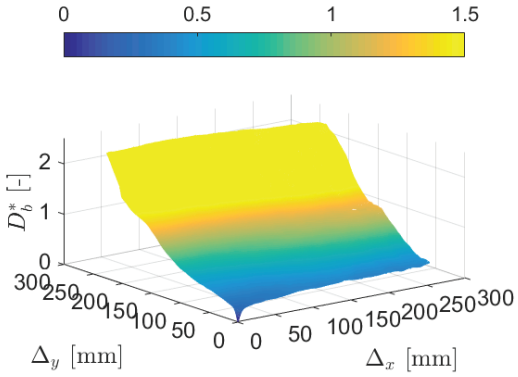

(f) Final patch Z3

Figure B.11.5: D_b^* plots for the three patches: left and right sides of this figure correspond to initial and final states of the bed surface, respectively.

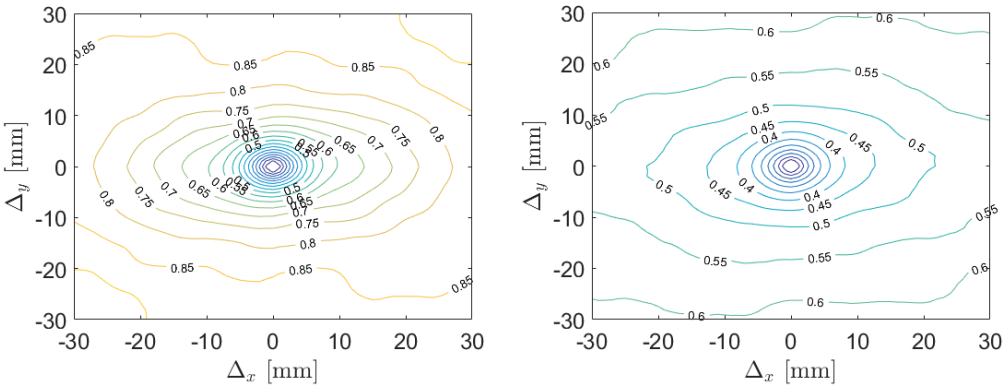

(a) Initial patch Z1

(b) Final patch Z1

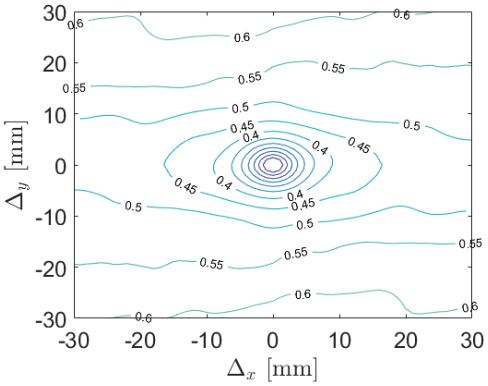

(c) Initial patch Z2

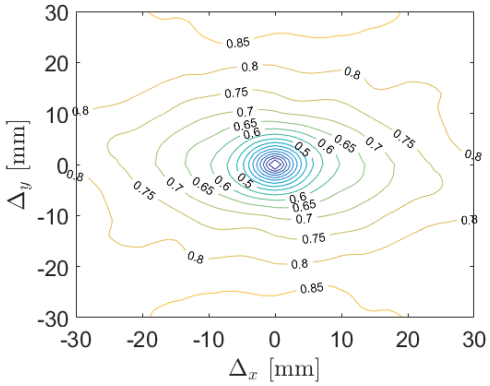

(d) Final patch Z2

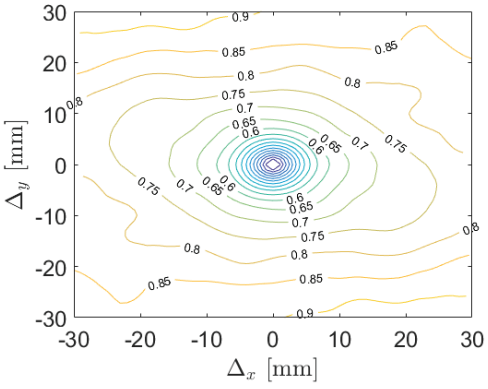

(e) Initial patch Z3

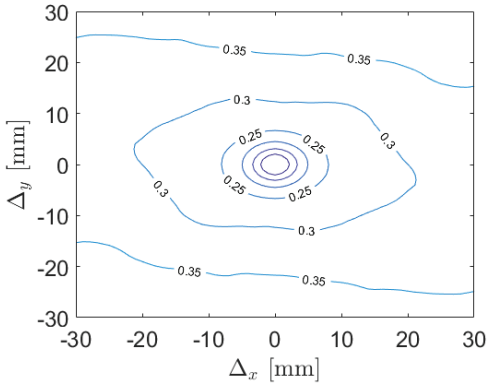

(f) Final patch Z3

Figure B.11.6: Contour plots for the three patches: left and right sides of this figure correspond to initial and final states of the bed surface, respectively.

Table B.11: Bed surface criteria of the 3 patches surveyed before and after the sediment transport experiment.

(a)

		σ_{zg} (mm)	S_k (mm^3)	K_u (mm^4)	Δ_{x0} (mm)	Δ_{y0} (mm)	H_x (-)	H_y (-)	x_0 (mm)	y_0 (mm)	a (mm)	b (mm)	$\frac{x_0}{y_0}$ (-)	$\frac{a}{b}$ (-)	ϕ (°)
Z1	Initial	3.1	0.26	2.9	9.4	8.2	0.54	0.57	9.1	6.7	9.0	6.6	1.4	1.4	-6.3
	Final	3.8	0.03	2.7	14.4	12.6	0.48	0.50	8.2	6.7	8.0	6.5	1.2	1.2	-7.7
Z2	Initial	3.8	0.02	2.8	12.8	11.3	0.54	0.56	8.9	6.6	8.7	6.4	1.4	1.4	-3.3
	Final	3.2	0.30	3.2	9.7	8.6	0.48	0.51	9.1	6.8	8.8	6.7	1.3	1.3	-1.4
Z3	Initial	3.5	0.28	3.3	8.9	8.1	0.54	0.56	8.0	6.8	7.9	6.8	1.2	1.2	2.7
	Final	5.3	-0.10	2.5	21.6	18.5	0.50	0.53	8.1	6.7	8.0	6.6	1.2	1.2	-1.0

(b)

		σ_{zg} (mm)	S_k (mm^3)	K_u (mm^4)	σ_{zl} (mm)	σ_{zt} (mm)	Δ_{x0} (mm)	Δ_{y0} (mm)	H_x (-)	H_y (-)	$\frac{x_0}{y_0}$ (-)	$\frac{a}{b}$ (-)	ϕ (°)
General bed	Initial	3.5	0.19	3.0	4.9	4.3	10.4	9.2	0.54	0.56	1.3	1.3	-2.3
	Final	4.1	0.08	2.8	6.4	5.2	15.2	13.2	0.49	0.51	1.3	1.3	-3.4

B.12 L-G-7 experiment

General bed surface surveys

DEM of the entire bed surface channel is showed on figure B.12.1. Three longitudinal bed surface surveys are presented in B.12.2.

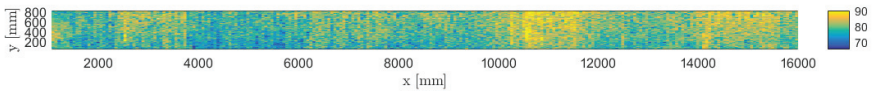

(a) Initial state

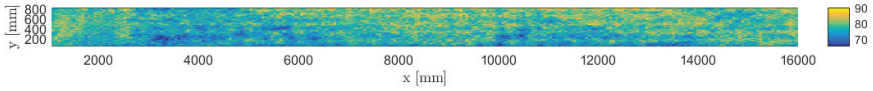

(b) Final state

Figure B.12.1: DEM of the entire bed surface channel before and after the experiment of sediment transport.

Surveys of bed surface patches

In the following, initial and final states mean before and after an experiment of sediment transport, respectively. Initial and final bed surface surveys were performed on 3 zones distributed along the channel: downstream (patch Z1), middle (patch Z2), and upstream (patch Z3). In this experiment, patches Z1, Z2 and Z3 were located at 7 m, 10.9 m, and 14.8 m from the downstream end of the flume, respectively.

Figure B.12.3 represents the resulting digital elevation models (DEM). Figure B.12.4 shows the probability density function of the bed surface elevations for the 3 patches. Two representations of the structure functions D_b associated to the 3 patches are given: one in 3D (Figure B.12.5) and one in contour plot (Figure B.12.6).

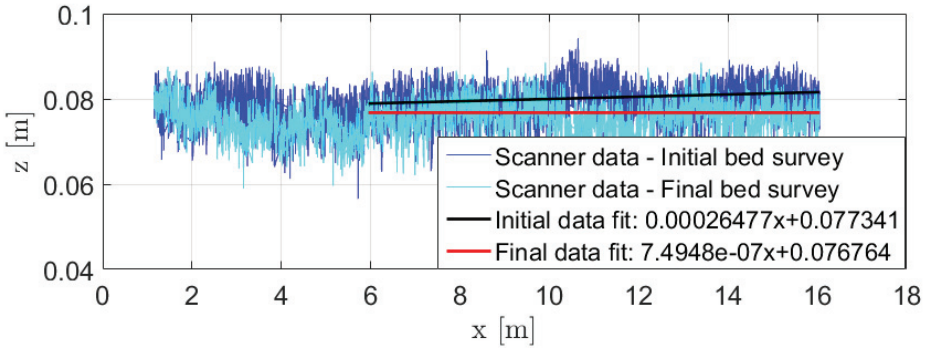

(a) Center line

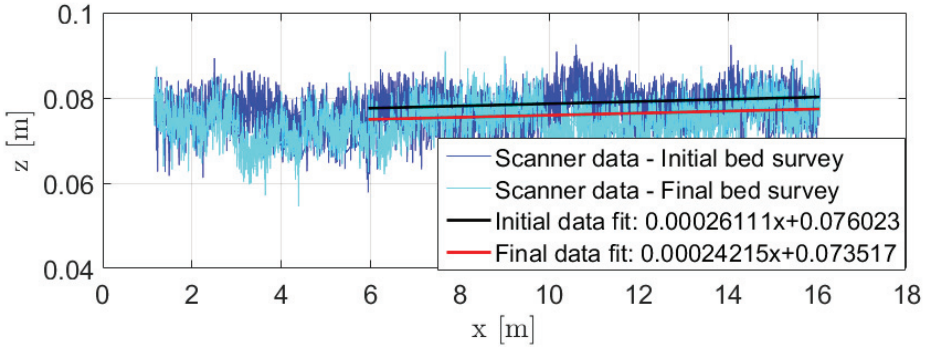

(b) Right side

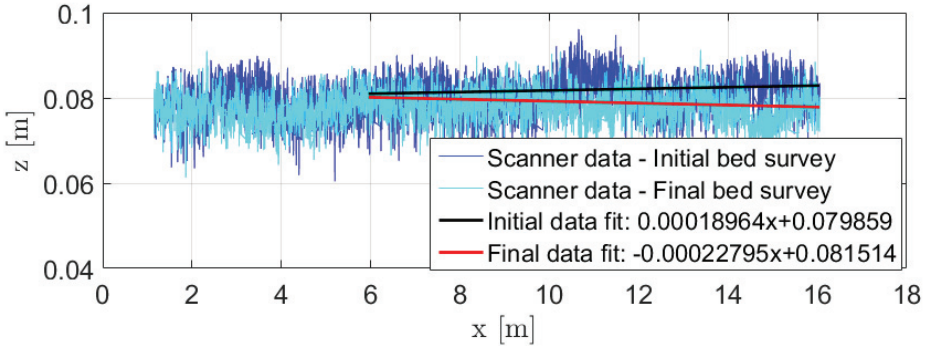

(c) Left side

Figure B.12.2: Longitudinal surveys of the bed surface before and after the experiment of sediment transport.

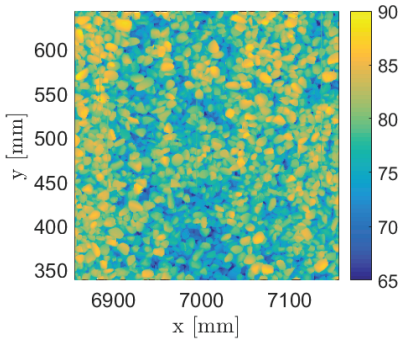

(a) Initial patch Z1

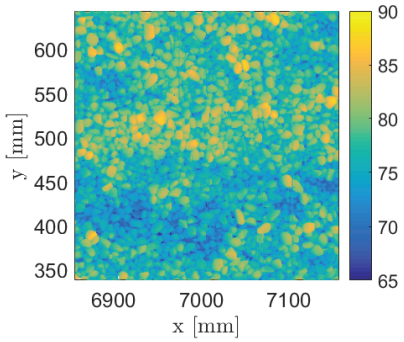

(b) Final patch Z1

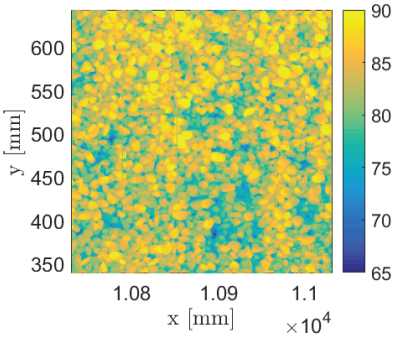

(c) Initial patch Z2

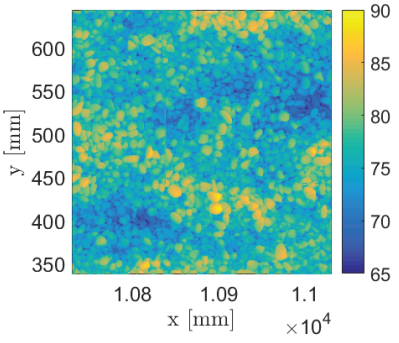

(d) Final patch Z2

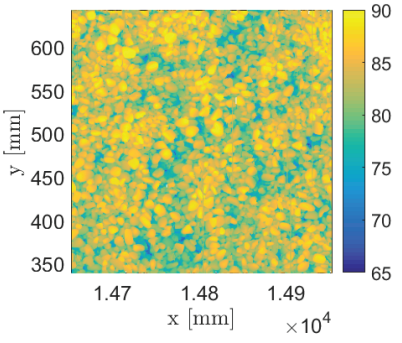

(e) Initial patch Z3

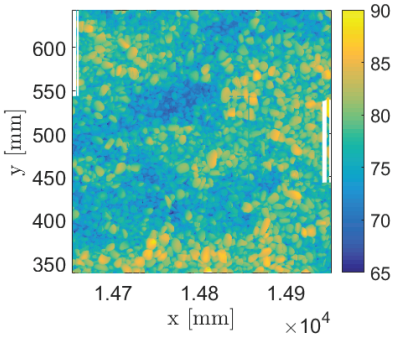

(f) Final patch Z3

Figure B.12.3: DEM of bed surface patches: left and right sides of this figure correspond to initial and final states of the bed surface, respectively.

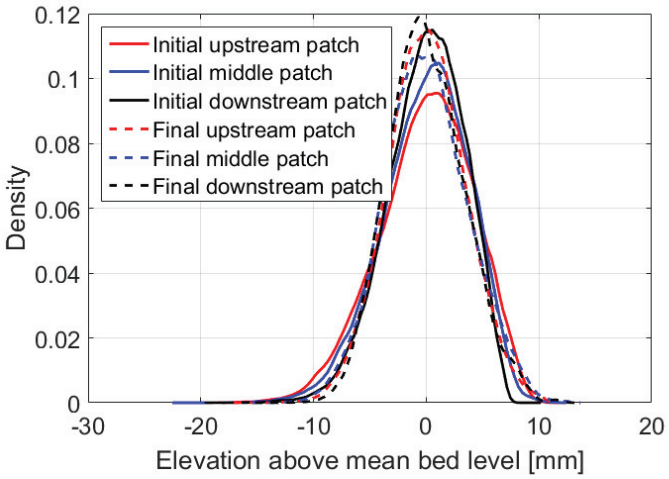

Figure B.12.4: PDF of the bed surface elevations for the 3 patches before and after the sediment transport experiment

Bed surface criteria

Table B.12a recaps all the bed surface criteria calculated for the three patches surveyed (initial and final states). Table B.12b reports the bed surface criteria computed at the scale of the entire bed surface, either by averaging data of the three patches or by using the transverse and longitudinal surveys of the bed.

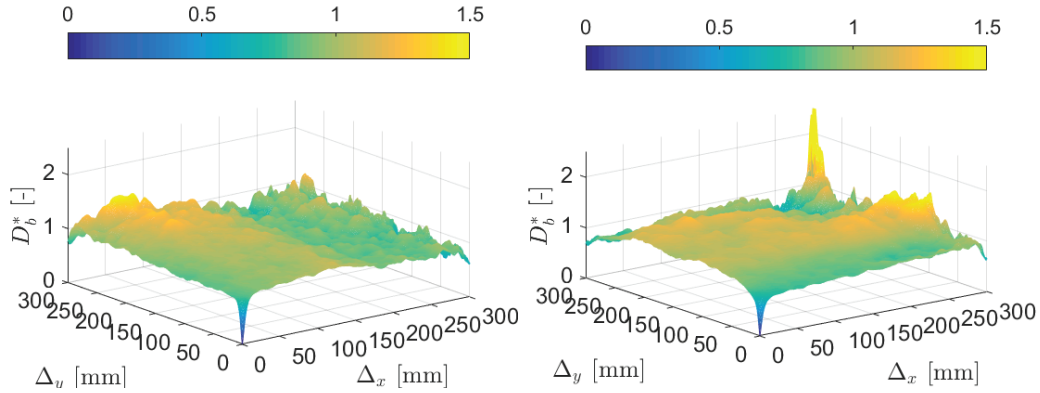

(a) Initial patch Z1 **(b)** Final patch Z1

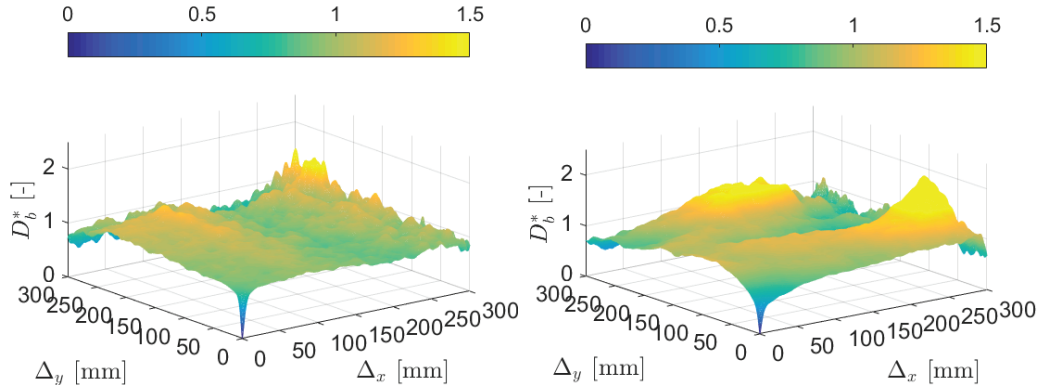

(c) Initial patch Z2 **(d)** Final patch Z2

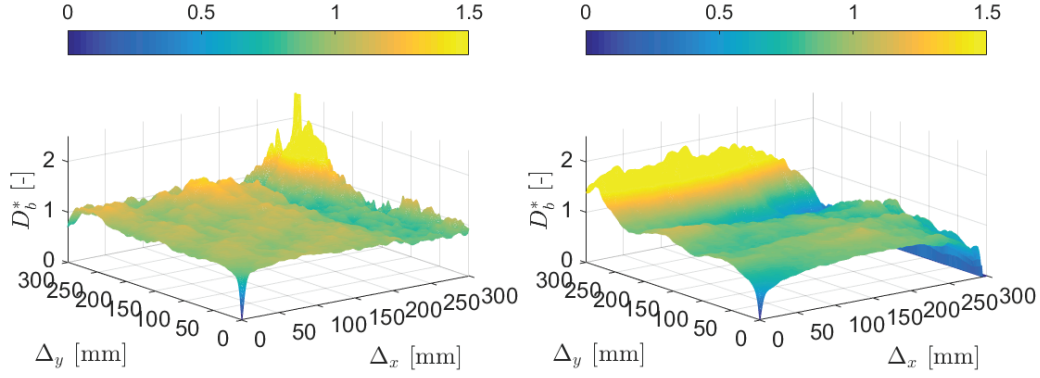

(e) Initial patch Z3 **(f)** Final patch Z3

Figure B.12.5: D_b^* plots for the three patches: left and right sides of this figure correspond to initial and final states of the bed surface, respectively.

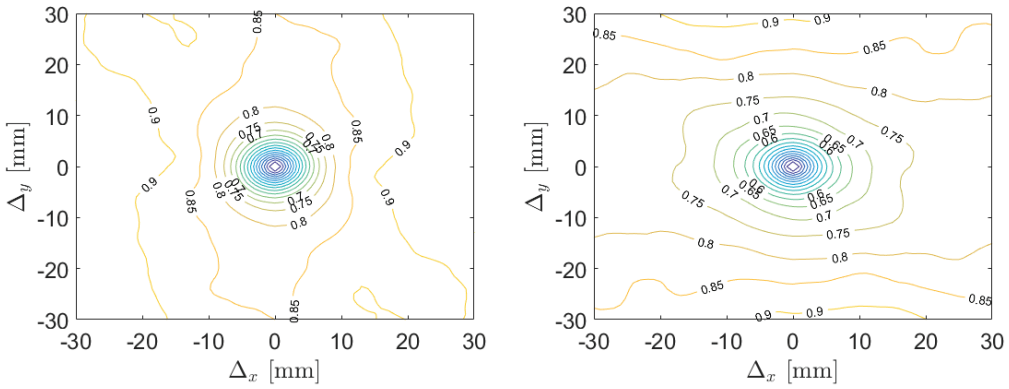

(a) Initial patch Z1

(b) Final patch Z1

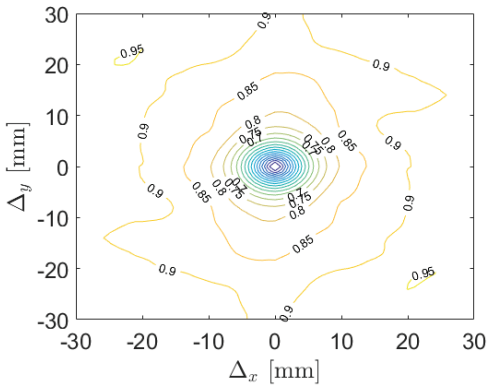

(c) Initial patch Z2

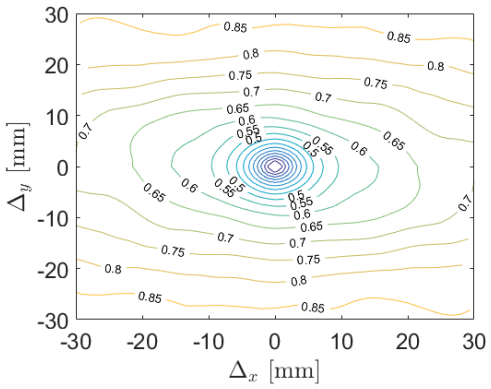

(d) Final patch Z2

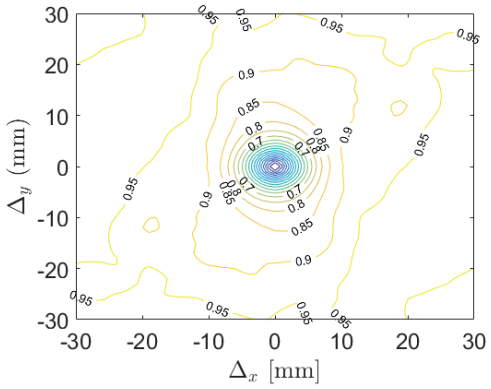

(e) Initial patch Z3

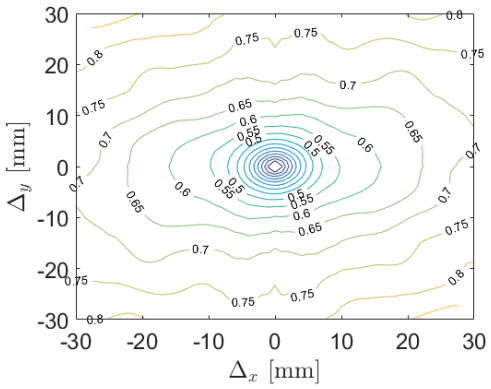

(f) Final patch Z3

Figure B.12.6: Contour plots for the three patches: left and right sides of this figure correspond to initial and final states of the bed surface, respectively.

Table B.12: Bed surface criteria of the 3 patches surveyed before and after the sediment transport experiment.

(a)

		σ_{zg} (mm)	S_k (mm^3)	K_u (mm^4)	Δ_{x0} (mm)	Δ_{y0} (mm)	H_x (-)	H_y (-)	x_0 (mm)	y_0 (mm)	a (mm)	b (mm)	$\frac{x_0}{y_0}$ (-)	$\frac{a}{b}$ (-)	ϕ (°)
Z1	Initial	4.1	-0.38	3.0	7.6	7.2	0.53	0.56	6.4	6.7	6.3	6.7	0.9	1.1	8.7
	Final	3.4	0.00	3.0	8.8	8.0	0.51	0.53	7.6	6.7	7.5	6.6	1.1	1.1	9.6
Z2	Initial	3.8	-0.39	3.1	7.4	6.7	0.53	0.55	6.8	6.7	6.8	6.6	1.0	1.0	-31.6
	Final	3.7	0.09	2.9	10.4	9.6	0.51	0.53	7.6	6.7	7.5	6.6	1.1	1.1	6.8
Z3	Initial	3.4	-0.43	3.1	6.6	6.4	0.54	0.54	6.1	6.8	6.0	6.8	0.9	1.1	0.7
	Final	3.4	0.19	2.9	10.4	9.6	0.50	0.52	7.5	6.7	7.5	6.7	1.1	1.1	-8.6

(b)

		σ_{zg} (mm)	S_k (mm^3)	K_u (mm^4)	σ_{zl} (mm)	σ_{zt} (mm)	Δ_{x0} (mm)	Δ_{y0} (mm)	H_x (-)	H_y (-)	$\frac{x_0}{y_0}$ (-)	$\frac{a}{b}$ (-)	ϕ (°)
General bed	Initial	3.8	-0.40	3.0	4.3	3.9	7.2	6.8	0.53	0.55	1.0	1.1	-7.4
	Final	3.5	0.09	2.9	3.9	3.9	9.9	9.1	0.51	0.53	1.1	1.1	2.6

B.13 H-G/S-7 experiment

General bed surface surveys

DEM of the entire bed surface channel is showed on figure B.13.1. Three longitudinal bed surface surveys are presented in B.13.2.

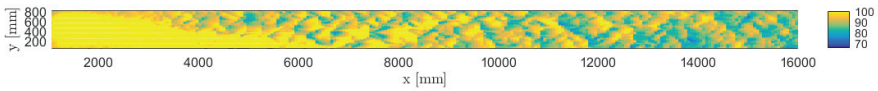

(a) Initial state

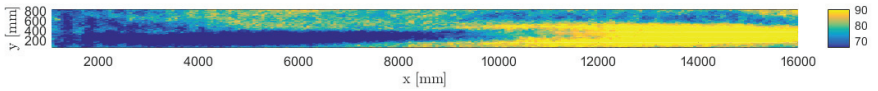

(b) Final state

Figure B.13.1: DEM of the entire bed surface channel before and after the experiment of sediment transport.

Surveys of bed surface patches

In the following, initial and final states mean before and after an experiment of sediment transport, respectively. Initial and final bed surface surveys were performed on 3 zones distributed along the channel: downstream (patch Z1), middle (patch Z2), and upstream (patch Z3). In this experiment, patches Z1, Z2 and Z3 were located at 7 m, 10.9 m, and 14.8 m from the downstream end of the flume, respectively.

Figure B.13.3 represents the resulting digital elevation models (DEM). Figure B.13.4 shows the probability density function of the bed surface elevations for the 3 patches. Two representations of the structure functions D_b associated to the 3 patches are given: one in 3D (Figure B.13.5) and one in contour plot (Figure B.13.6).

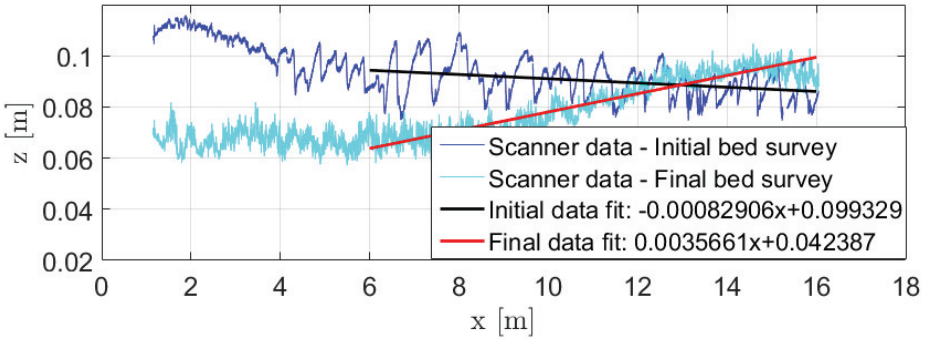

(a) Center line

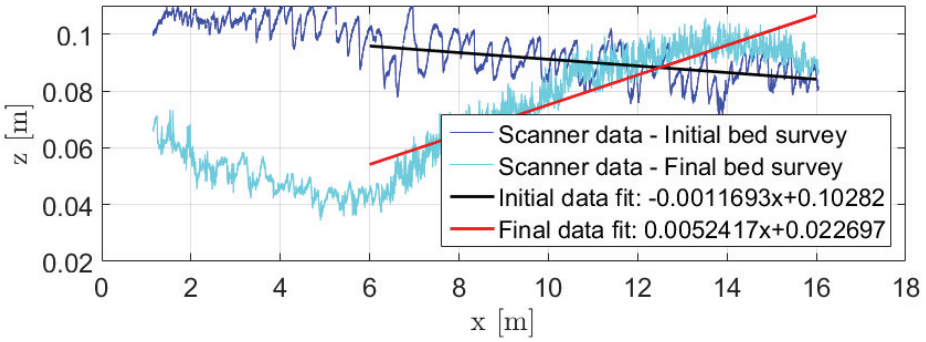

(b) Right side

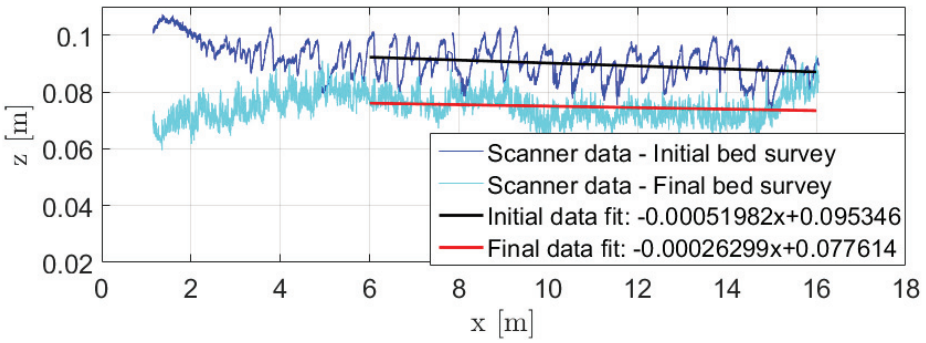

(c) Left side

Figure B.13.2: Longitudinal surveys of the bed surface before and after the experiment of sediment transport.

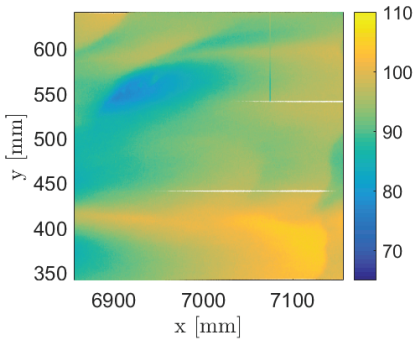

(a) Initial patch Z1

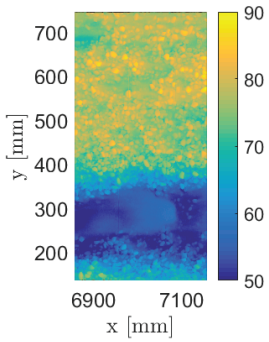

(b) Final patch Z1

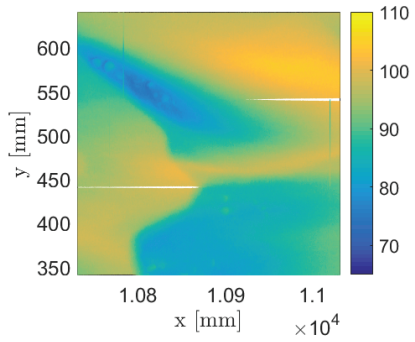

(c) Initial patch Z2

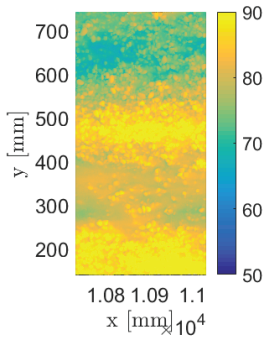

(d) Final patch Z2

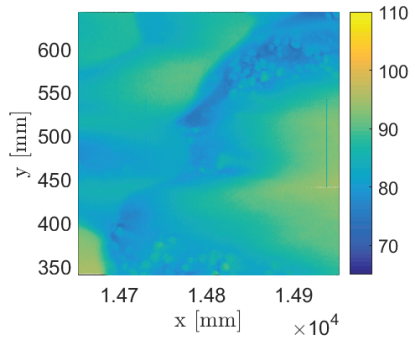

(e) Initial patch Z3

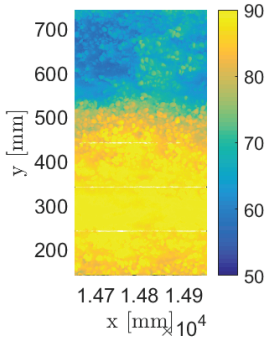

(f) Final patch Z3

Figure B.13.3: DEM of bed surface patches: left and right sides of this figure correspond to initial and final states of the bed surface, respectively.

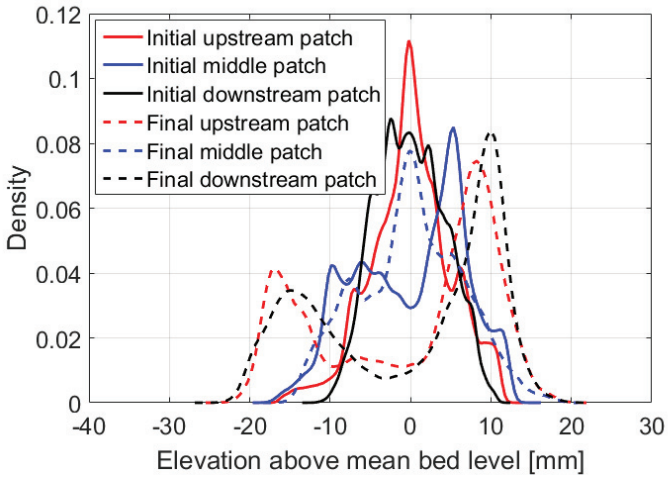

Figure B.13.4: PDF of the bed surface elevations for the 3 patches before and after the sediment transport experiment

Bed surface criteria

Table B.13a recaps all the bed surface criteria calculated for the three patches surveyed (initial and final states). Table B.13b reports the bed surface criteria computed at the scale of the entire bed surface, either by averaging data of the three patches or by using the transverse and longitudinal surveys of the bed.

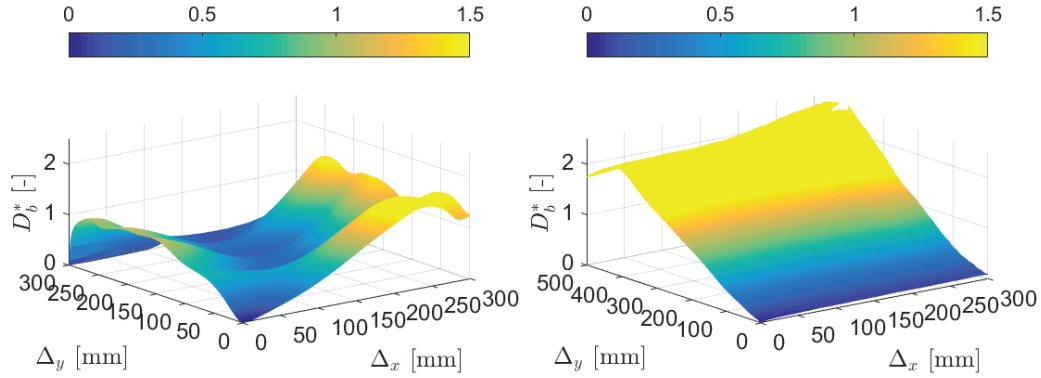

(a) Initial patch Z1

(b) Final patch Z1

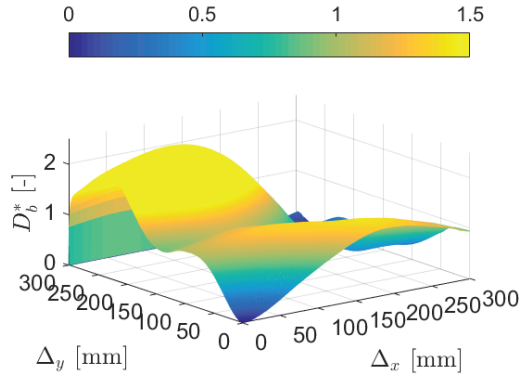

(c) Initial patch Z2

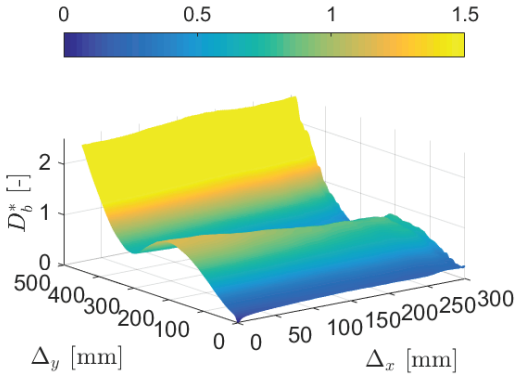

(d) Final patch Z2

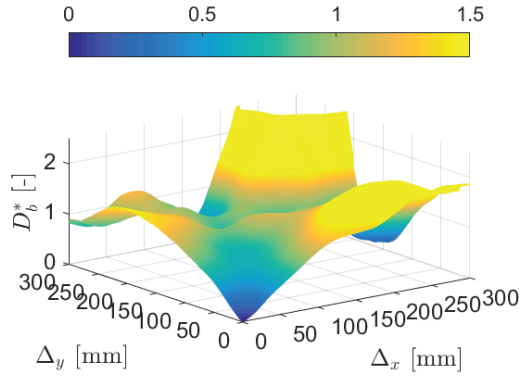

(e) Initial patch Z3

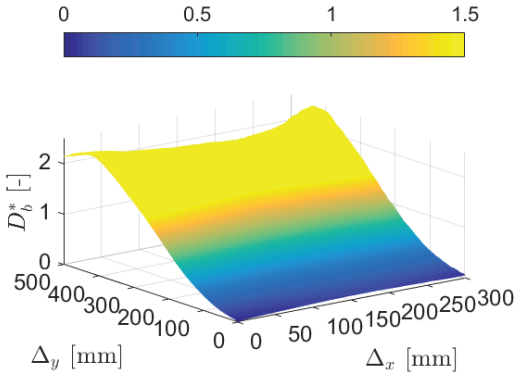

(f) Final patch Z3

Figure B.13.5: D_b^* plots for the three patches: left and right sides of this figure correspond to initial and final states of the bed surface, respectively.

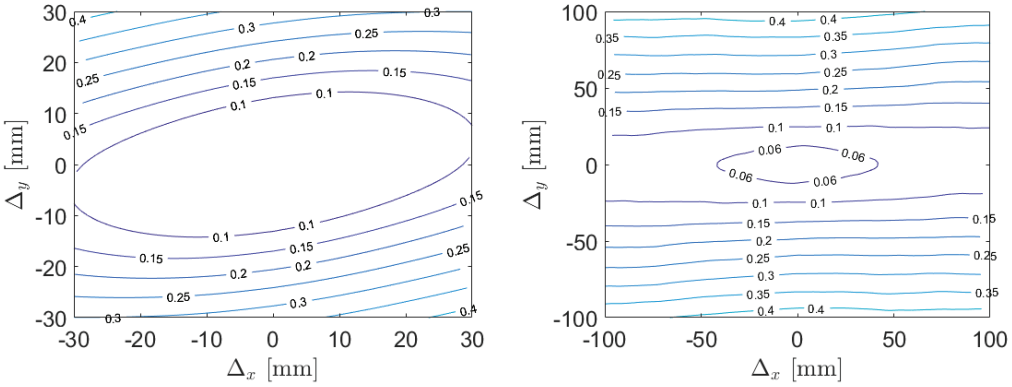

(a) Initial patch Z1

(b) Final patch Z1

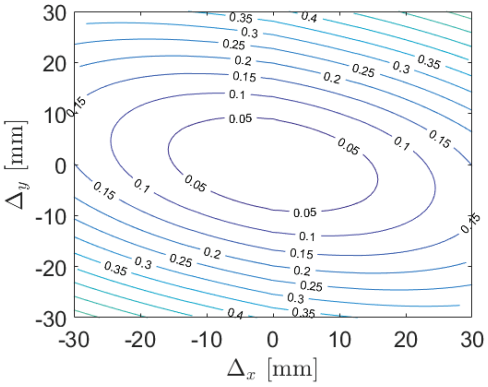

(c) Initial patch Z2

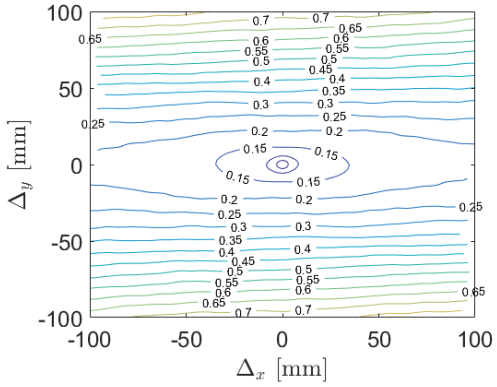

(d) Final patch Z2

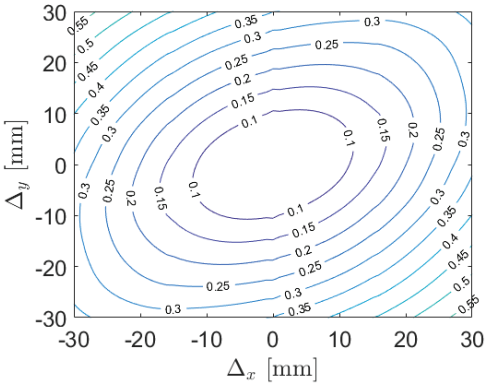

(e) Initial patch Z3

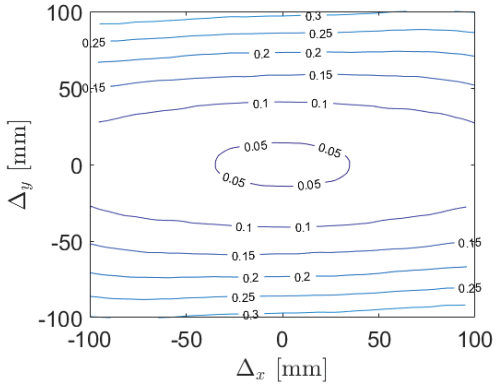

(f) Final patch Z3

Figure B.13.6: Contour plots for the three patches: left and right sides of this figure correspond to initial and final states of the bed surface, respectively.

Table B.13: Bed surface criteria of the 3 patches surveyed before and after the sediment transport experiment.

(a)

		σ_{zg} (mm)	S_k (mm^3)	K_u (mm^4)	Δ_{x0} (mm)	Δ_{y0} (mm)	H_x (-)	H_y (-)	x_0 (mm)	y_0 (mm)	a (mm)	b (mm)	$\frac{x_0}{y_0}$ (-)	$\frac{a}{b}$ (-)	ϕ (°)
Z1	Initial	5.0	-0.19	3.1	100.0	156.0	/	/	13.5	6.9	15.0	6.5	2.0	2.3	-14.0
	Final	10.9	-0.50	1.7	124.7	85.6	0.53	0.58	10.1	6.7	10.0	6.5	1.5	1.5	-0.7
Z2	Initial	6.8	-0.25	2.0	123.3	72.0	/	/	10.9	6.8	11.7	6.4	1.6	1.8	15.2
	Final	6.5	0.01	2.5	51.9	36.1	0.53	0.58	12.8	6.9	12.4	6.6	1.9	1.9	-1.8
Z3	Initial	4.2	0.10	2.3	88.0	98.8	/	/	7.3	6.9	8.1	6.1	1.1	1.3	-34.6
	Final	11.2	-0.44	1.6	148.0	105.0	0.54	0.58	10.5	6.7	10.3	6.6	1.6	1.6	0.5

(b)

		σ_{zg} (mm)	S_k (mm^3)	K_u (mm^4)	σ_{zl} (mm)	σ_{zt} (mm)	Δ_{x0} (mm)	Δ_{y0} (mm)	H_x (-)	H_y (-)	$\frac{x_0}{y_0}$ (-)	$\frac{a}{b}$ (-)	ϕ (°)
General bed	Initial	5.3	-0.11	2.5	8.9	5.8	103.8	108.9	/	/	1.5	1.8	-11.1
	Final	9.5	-0.31	1.9	12.1	9.1	108.2	75.5	0.53	0.58	1.6	1.7	-0.7

B.14 H-G/Ms-9 experiment

General bed surface surveys

DEM of the entire bed surface channel is showed on figure B.14.1. Three longitudinal bed surface surveys are presented in B.14.2.

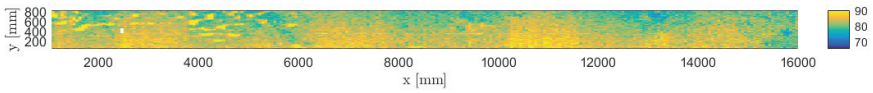

(a) Initial state

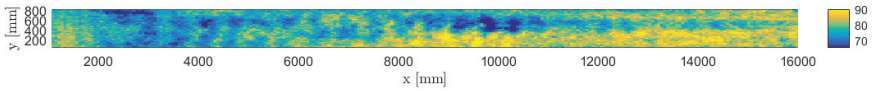

(b) Final state

Figure B.14.1: DEM of the entire bed surface channel before and after the experiment of sediment transport.

Surveys of bed surface patches

In the following, initial and final states mean before and after an experiment of sediment transport, respectively. Initial and final bed surface surveys were performed on 3 zones distributed along the channel: downstream (patch Z1), middle (patch Z2), and upstream (patch Z3). In this experiment, patches Z1, Z2 and Z3 were located at 7 m, 10.9 m, and 14.8 m from the downstream end of the flume, respectively.

Figure B.14.3 represents the resulting digital elevation models (DEM). Figure B.14.4 shows the probability density function of the bed surface elevations for the 3 patches. Two representations of the structure functions D_b associated to the 3 patches are given: one in 3D (Figure B.14.5) and one in contour plot (Figure B.14.6).

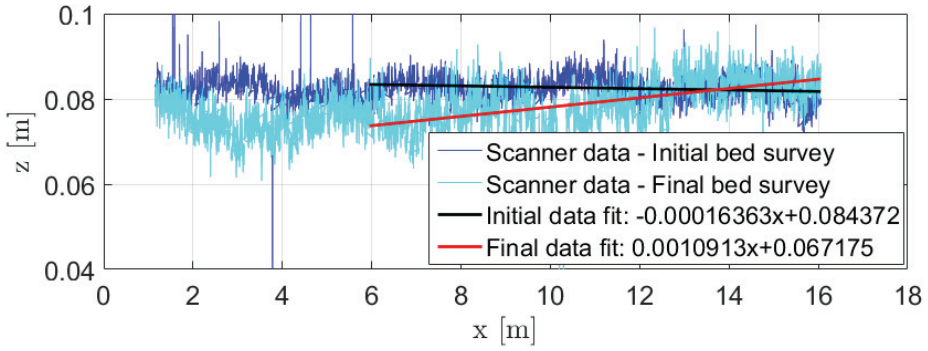

(a) Center line

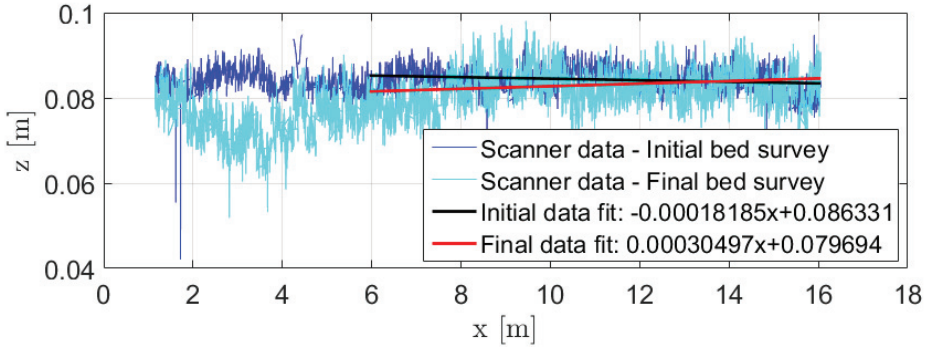

(b) Right side

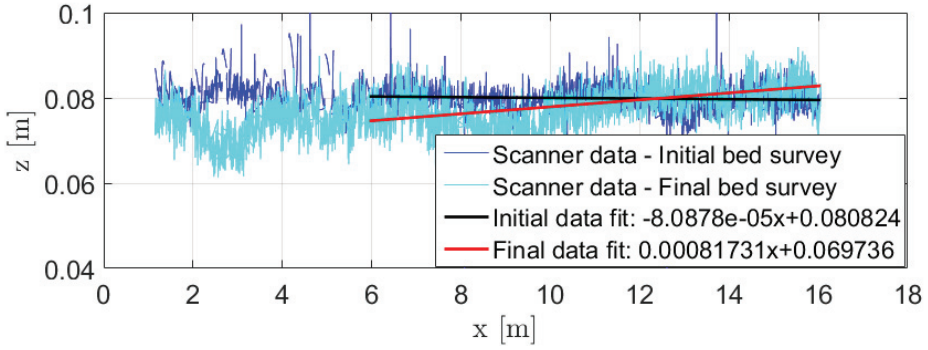

(c) Left side

Figure B.14.2: Longitudinal surveys of the bed surface before and after the experiment of sediment transport.

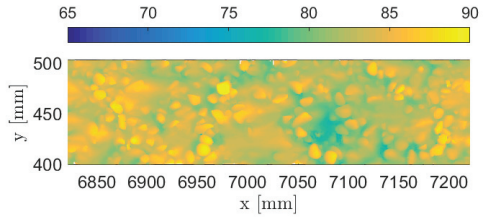

(a) Initial patch Z1

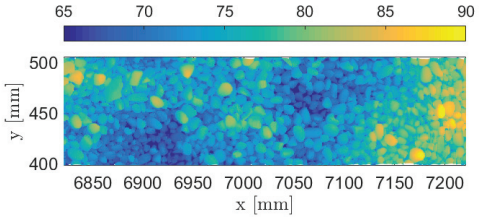

(b) Final patch Z1

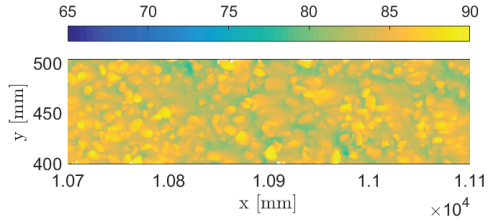

(c) Initial patch Z2

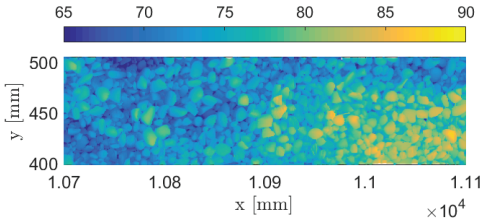

(d) Final patch Z2

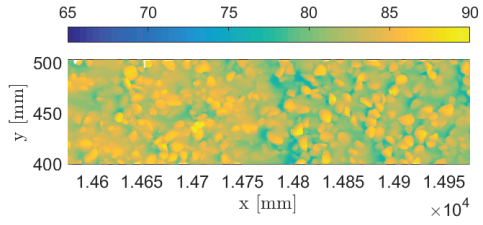

(e) Initial patch Z3

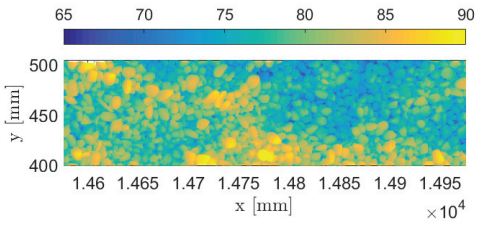

(f) Final patch Z3

Figure B.14.3: DEM of bed surface patches: left and right sides of this figure correspond to initial and final states of the bed surface, respectively.

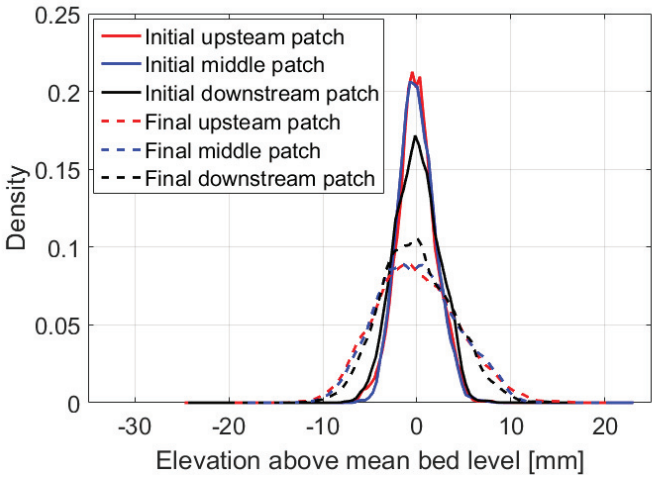

Figure B.14.4: PDF of the bed surface elevations for the 3 patches before and after the sediment transport experiment

Bed surface criteria

Table B.14a recaps all the bed surface criteria calculated for the three patches surveyed (initial and final states). Table B.14b reports the bed surface criteria computed at the scale of the entire bed surface, either by averaging data of the three patches or by using the transverse and longitudinal surveys of the bed.

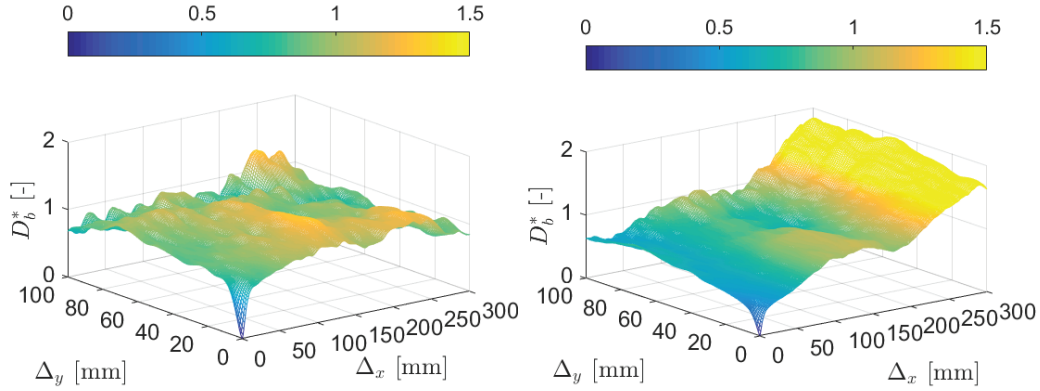

(a) Initial patch Z1

(b) Final patch Z1

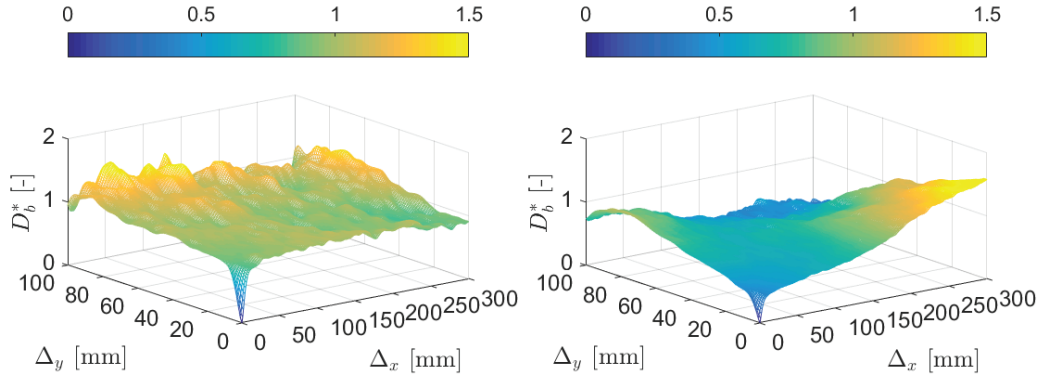

(c) Initial patch Z2

(d) Final patch Z2

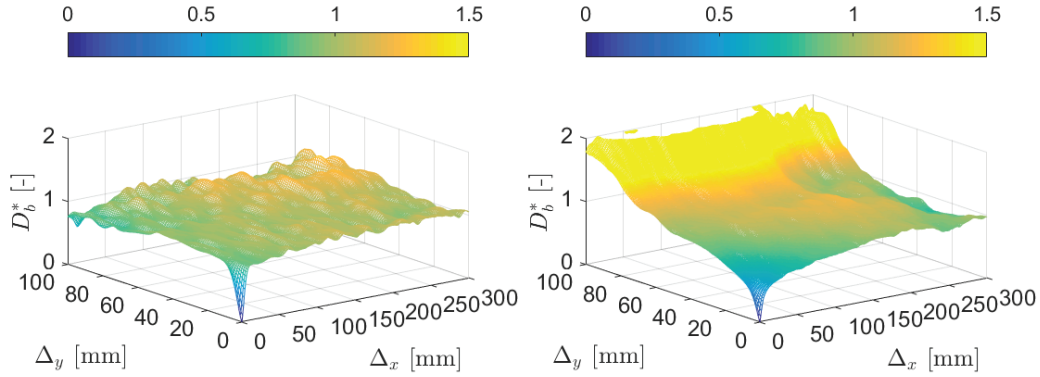

(e) Initial patch Z3

(f) Final patch Z3

Figure B.14.5: D_b^* plots for the three patches: left and right sides of this figure correspond to initial and final states of the bed surface, respectively.

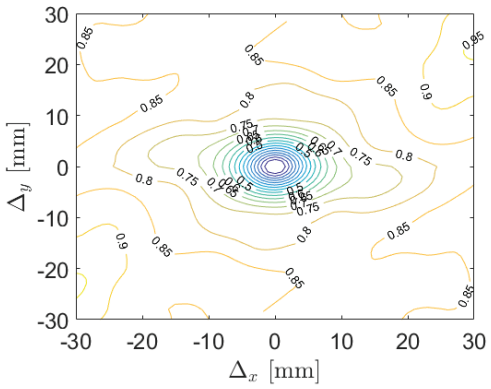

(a) Initial patch Z1

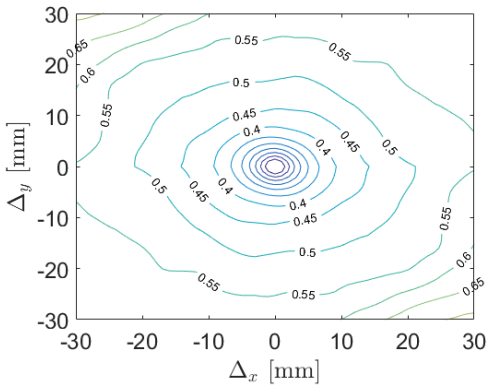

(b) Final patch Z1

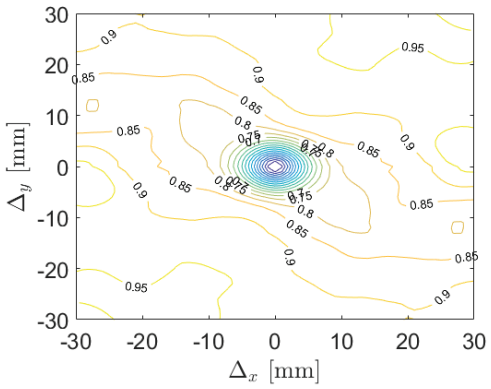

(c) Initial patch Z2

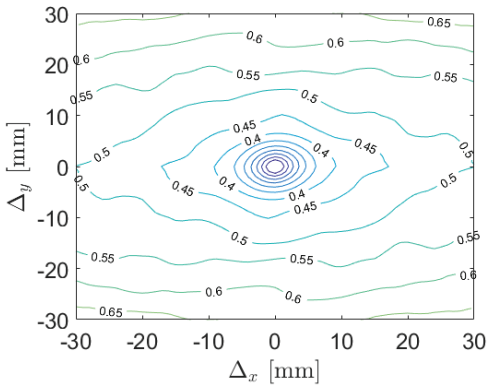

(d) Final patch Z2

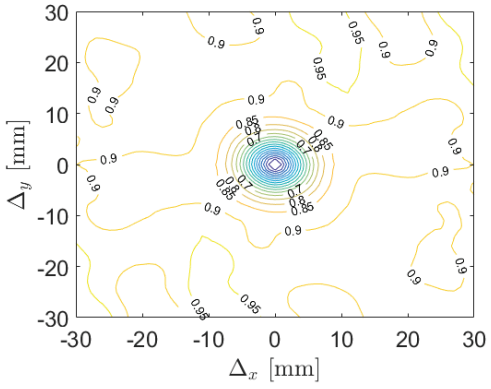

(e) Initial patch Z3

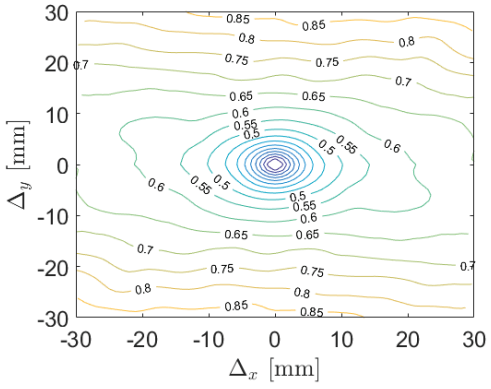

(f) Final patch Z3

Figure B.14.6: Contour plots for the three patches: left and right sides of this figure correspond to initial and final states of the bed surface, respectively.

Table B.14: Bed surface criteria of the 3 patches surveyed before and after the sediment transport experiment.

(a)

		σ_{zg} (mm)	S_k (mm^3)	K_u (mm^4)	Δ_{x0} (mm)	Δ_{y0} (mm)	H_x (-)	H_y (-)	x_0 (mm)	y_0 (mm)	a (mm)	b (mm)	$\frac{x_0}{y_0}$ (-)	$\frac{a}{b}$ (-)	ϕ (°)
Z1	Initial	2.1	0.10	3.4	8.6	7.6	0.68	0.68	9.0	6.9	8.8	6.8	1.3	1.3	-0.4
	Final	4.5	0.26	2.9	13.9	12.2	0.52	0.54	8.0	6.8	7.9	6.7	1.2	1.2	13.5
Z2	Initial	2.0	0.26	3.3	7.4	6.4	0.61	0.62	9.3	6.8	12.5	6.6	1.4	1.9	28.7
	Final	4.2	0.17	2.6	13.7	11.7	0.50	0.53	10.2	6.8	9.6	6.5	1.5	1.5	-4.2
Z3	Initial	2.4	0.04	3.1	6.7	6.6	0.60	0.62	6.6	6.8	6.5	6.9	1.0	1.1	-17.1
	Final	3.8	0.21	2.9	11.4	9.7	0.51	0.53	10.2	6.9	9.9	6.8	1.5	1.5	2.5

(b)

		σ_{zg} (mm)	S_k (mm^3)	K_u (mm^4)	σ_{zl} (mm)	σ_{zt} (mm)	Δ_{x0} (mm)	Δ_{y0} (mm)	H_x (-)	H_y (-)	$\frac{x_0}{y_0}$ (-)	$\frac{a}{b}$ (-)	ϕ (°)
General bed	Initial	2.1	0.13	3.3	2.8	3.0	7.6	6.9	0.63	0.64	1.2	1.4	3.7
	Final	4.2	0.21	2.8	5.5	4.7	13.0	11.2	0.51	0.53	1.4	1.4	3.9

Appendix C

Doppler noise and variance correction

This appendix shows how the variances can be expressed in function of the beam signals of the Vectrino II and the ones which are affected by Doppler noise.

$$\overline{u'}^2 = \frac{1}{4\sin^2(\alpha)}\left(\overline{b'_1}^2 + \overline{b'_3}^2 - 2\overline{b'_1 b'_3} + 2\sigma_{1\text{-}3}\right) \tag{C.1}$$

$$\overline{v'}^2 = \frac{1}{4\sin^2(\alpha)}\left(\overline{b'_2}^2 + \overline{b'_4}^2 - 2\overline{b'_2 b'_4} + 2\sigma_{2\text{-}4}\right) \tag{C.2}$$

$$\overline{w'_1}^2 = \frac{1}{4\cos^2(\alpha)}\left(\overline{b'_1}^2 + \overline{b'_3}^2 - 2\overline{b'_1 b'_3} + 2\sigma_{1\text{-}3}\right) \tag{C.3}$$

$$\overline{w'_2}^2 = \frac{1}{4\cos^2(\alpha)}\left(\overline{b'_2}^2 + \overline{b'_4}^2 - 2\overline{b'_2 b'_4} + 2\sigma_{2\text{-}4}\right) \tag{C.4}$$

$$\overline{u'w'_1}^2 = \frac{1}{2\sin(2\alpha)}\left(\overline{b'_1}^2 - \overline{b'_3}^2\right) \tag{C.5}$$

$$\overline{u'w'_2}^2 = \frac{1}{2\sin(2\alpha)}\left(\overline{b'_1 b'_2} + \overline{b'_1 b'_4} - \overline{b'_2 b'_3} - \overline{b'_3 b'_4}\right) \tag{C.6}$$

$$\overline{w'_1 w'_2}^2 = \frac{1}{4\cos^2(\alpha)}\left(\overline{b'_1 b'_2} + \overline{b'_1 b'_4} + \overline{b'_2 b'_3} + \overline{b'_3 b'_4}\right) \tag{C.7}$$

where $\sigma_{1\text{-}3}$ and $\sigma_{2\text{-}4}$ are Doppler noises associated with the beam couple 1-3 and with the beam couple 2-4, respectively, and α is the angle between the emitter and receiver of the Vectrino II.

Equation C.7 shows that $\overline{w_1' w_2'}^2$ is not contaminated by the Doppler noise and obtained with uncorrelated signals. That is why, it is often defined as the *true variance*.

Transport of moderately sorted gravels at low bed shear stresses : impact of bed arrangement and fine sediment infiltration

Abstract This PhD thesis aims to understand gravel dynamics in Alpine rivers at low bed shear stress using laboratory experiments. Alpine river beds are often poorly sorted and composed of sediments ranging from clay to pebble. To understand interactions between these classes is an issue for predicting bedload rate. Original laboratory experiments were performed in a 18 m long and 1 m wide flume, under unsteady flows. Two types of bed were investigated : unimodal and bimodal beds. A particular attention was paid to the bed construction, which was conducted in order to obtain a nature-like bed with different bed arrangements and degrees of clogging. Unimodal beds were made of moderately sorted gravels with different bed surface arrangements. Bimodal beds were made of moderately sorted gravels in which fine sediments (sand or silt) were infiltrated. Gravel rate was found to be impacted by the bed arrangement degree, the fine sediment concentration within the transport layer and the changes in bed properties due to fine sediment presence (bed cohesion, bed permeability). The more packed the bed is ; the more difficult it is to move gravels. The more concentrated in fine sediments the transport layer is ; the easier the transport of gravels is. The shape of fine sediments can also be an important factor for modifying the gravel rate. The presence of cohesive fine sediments within the bed matrix reduces significantly the gravel rate. A phenomenological diagram was built to recap the different processes controlling gravel transport. It provides a description of the overall bed responses to a hydrograph. Based on this diagram, a methodology and recommendations were proposed to help understanding, estimating and interpreting gravel transport in Alpine rivers. The methodology was discussed and applied to a field case made on the Arc River. We also suggest a new dimensionless analysis for the construction of a new bedload predicting model involving parameters describing bed arrangement, bed properties and fine sediment presence.

Keywords : sediment transport ; fine sediment clogging ; bed arrangement ; incipient motion ; laboratory experiments.

Transport de graviers à faibles contraintes : impact de l'arrangement et de l'infiltration du lit par des sédiments fins

Résumé Le but de cette thèse est de comprendre la dynamique des graviers au sein des rivières alpines à faibles contraintes en utilisant des expériences en laboratoire. Ces rivières sont souvent composées d'une large gamme de sédiments, allant des argiles aux galets. Ces différentes classes sédimentaires peuvent intéragir entre elles, ce qui peut rendre difficile l'estimation du transport solide. Des expériences en laboratoire ont été conduites en écoulements instationnaires dans un canal de 18 m de long et 1 m de large. Deux types de lits ont été étudiés : lits unimodaux et bimodaux. Une attention particulière a été portée sur la réalisation des lits de graviers dans notre canal. Ils ont été créés dans le but d'approcher au mieux la configuration des lits de rivières alpines, c'est-à-dire avec différents arrangements et degrés de colmatage du lit par des sédiments fins. Les lits unimodaux sont composés de graviers peu triés avec divers arrangements de surface. Les lits bimodaux sont composés d'une matrice de graviers peu triés dans laquelle des sédiments fins se sont infiltrés (sables ou limons). Les processus régissant le transport de graviers ont été mis en avant. Le transport de graviers est impacté par l'arrangement du lit, la concentration de sédiments fins dans la couche de charriage, et par le changement de propriétés du lit due à la présence de sédiments fins (cohésion, perméabilité du lit). Plus le lit est arrangé, plus le transport est difficile. Plus la couche de charriage est concentrée en sédiments fins, plus le transport est facile. La forme des sédiments fins est aussi un facteur important pouvant modifier le transport des graviers. La présence de sédiments fins cohésifs dans la matrice peut considérablement réduire le taux de graviers transportés. Un modèle phénoménologique a été développé pour résumer les différents processus contrôlant le transport de graviers. Il décrit le comportement des graviers dans les différentes configurations étudiées. Basé sur ce modèle, une méthode a été proposée pour aider à comprendre, estimer et interpréter le transport de graviers. Cette méthode a été appliquée et discutée sur un cas de terrain sur la rivière de l'Arc. Nos résultats nous ont également permis de proposer une nouvelle analyse dimensionnelle pour la construction d'un modèle de prédiction de transport solide prenant en compte des paramètres décrivant l'arrangement du lit, les propriétés géotechniques du lit et la présence de sédiments fins.

Mots-clefs : transport sédimentaire ; charriage ; colmatage ; arrangement du lit ; mise en mouvement ; laboratoire.